



Neutron-Assisted Modelling for Thermochemical Heat Storage

Karabanova, Anastasiia

Publication date:
2020

Document Version
Publisher's PDF, also known as Version of record

[Link back to DTU Orbit](#)

Citation (APA):
Karabanova, A. (2020). *Neutron-Assisted Modelling for Thermochemical Heat Storage*. Technical University of Denmark.

General rights

Copyright and moral rights for the publications made accessible in the public portal are retained by the authors and/or other copyright owners and it is a condition of accessing publications that users recognise and abide by the legal requirements associated with these rights.

- Users may download and print one copy of any publication from the public portal for the purpose of private study or research.
- You may not further distribute the material or use it for any profit-making activity or commercial gain
- You may freely distribute the URL identifying the publication in the public portal

If you believe that this document breaches copyright please contact us providing details, and we will remove access to the work immediately and investigate your claim.

**Neutron-Assisted Modelling for
Thermochemical Heat Storage**

Anastasiia Karabanova

PhD Thesis

Department of Energy Conversion and Storage

Technical University of Denmark

Kongens Lyngby 2020

Preface

The present thesis is submitted as a partial fulfilment of the requirements for the degree of a Doctor of Philosophy (Ph.D.) at the Technical University of Denmark (DTU).

The thesis was completed at the Section for Imaging and Structural Analysis at the Department of Energy Conversion and Storage. The work was carried out from July 1, 2017 until September 30, 2020 (including three months of research assistant) under the supervision of Senior Researcher Didier Blanchard and the co-supervision of Researcher Rune E. Johnsen.

The PhD project was funded by NordForsk Nordic Neutron Science Programme through the Neutrons for Heat Storage (NHS) project (No. 82206).

The thesis is written as a collection of articles.

Copenhagen, September 30, 2020

Anastasiia Karabanova

Acknowledgements

The present PhD thesis research has been carried out as a part of a Scandinavian project “Neutrons for Heat Storage” at the Department of Energy Conversion and Storage at Technical University of Denmark. I would like to say that I am very glad and happy for having had the opportunity to work and live in a Scandinavian environment, where honesty, respect to others, and trust are of great value, and when I say “Scandinavian environment” I mean people, who have the aforementioned principles. During my PhD journey, I have had an opportunity to meet such people and learn a lot from them professionally and personally, for which I am infinitely thankful.

First, I would like to thank my main supervisor, a senior researcher Didier Blanchard, for his kind guidance throughout my whole PhD. Didier could always find an appropriate word, when I was going through the lows of my PhD, and I always felt that he was on my side. His knowledge in different research areas and eagerness to understand the essence of phenomena gave me a great example of a researcher and supervisor, who I wish to become one day. Then, I would like to say many thanks to Rune E. Johnsen, who has been my co-supervisor for two years and seven months. Rune has patiently introduced me to the world of crystallography, which was completely new to me at the beginning of my PhD. His helpfulness and belief in me as a smart student helped me a lot in maintaining a cheerful state of mind during my studies. Another person, who I would like to express my sincere gratitude to in this “supervision section”, is a senior scientist Kenneth Dahl Knudsen from Institute of Energy Technology (IFE) (Norway). Even though Kenneth was not my official supervisor, I think about him in this way because he has contributed a lot to my knowledge on Small Angle Neutron Scattering through live and virtual meetings as well as long e-mails full of pieces of advice and insights.

I would like to acknowledge a researcher Michel van der Pal from TNO Energy Transition (the Netherlands) for his kind help with the preparation and characterization of the composite materials and modelling. I am thankful to Michel that he has introduced me to many researchers, working in the field of heat storage, among which are an assistant professor Huashan Bao and an assistant professor Ma Zhiwei from Durham University (the UK) and a professor Bob Critoph and a PhD student Sam Hinners from the University of Warwick (the UK). Discussions with these scientists helped me a lot to broaden my view on the topic of thermochemical heat storage.

I would also like to thank our project partners based at IFE and Royal Institute of Technology (KTH) (Sweden). I was fortunate to go to these two institutions for my external stays, as I received a warm welcome and was feeling like home there. From IFE, I am particularly very thankful to a senior researcher Stefano Deledda and a PhD student Perizat Berdiyeva for having performed the initial analysis of the neutron radiography data and for having been a great company during all the beamtime experiments. I also want to express my gratitude to Stefano for his support with the extension of my PhD project. From KTH, I am grateful to a professor Viktoria Martin and a researcher Saman Nimali Gunasekara, from whom I received many useful pieces of advice regarding the research and career as a scientist. Here, I would also like to mention that my cooperation with Viktoria and Saman started from a summer internship at KTH during my master studies, and I am very happy that I have continued working with these great scientists in the present project. I would like to extend my gratitude to postdoc Stefano Soprani, a professor Poul Norby, a professor Herbert Zondag from TNO Energy Transition (The Netherlands), an associate professor Andreas Kaiser, a PhD student Zeyu Li, and an associate professor Wenjing (Angela) Zhang for scientific discussions and fruitful collaboration on other short projects.

I am grateful to my former and current head of section, a professor Peter Holtappels and a professor Luise Theil Kuhn, for their support, encouragements and help during my whole PhD. I also want to express my gratitude to Luise for her support with the extension of my PhD project. I would like to thank the DTU secretaries, in particular Anne Heglingegård, Karina Ulvskov Frederiksen, and Marlene Daugaard Høyby, for their assistance with the administrative tasks and friendly talks.

My gratitude goes to the DTU team of technicians, who were always eager to help me “move mountains”. Without the help from Mike Wichmann, Ebtisam Abdellahi, Karl Tor Sune Thydén, Åsa Helen Persson, Ole Hansen, John Johnson, Jette Iversen, June Ruddle Flittner, and Annelise Mikkelsen, it would have been almost impossible to get the results presented in this thesis. I am also thankful to beamline scientists, who have helped our “neutron group” to prepare for neutron experiments and successfully conduct them. In particular, I want to acknowledge Leide Cavalcanti, Robert Dalgliesh, and Adam Washington from ISIS (the UK), Malgorzata Makowska, Thomas Bücherl, and Adrian Losko from FRM II (Germany), Lukas Helfen and Alessandro Tengattini from ILL (France), and Yun Liu and Cedric Gagnon from NIST (the US). In addition, I am very

grateful to Hilde Larson from COMSOL support team for the help with the modeling through e-mails and personal meetings.

I want to thank a group of interns - Ndeye Fatim Koundoul, Sôrameva Vahombey, Théodel Hrovatin, Lucie Mayé, Clémence Allard - who I had the pleasure to co-supervise. I am thankful for this experience of supervision as well as their contribution to the current work.

I am happy to say that I gained a lot from my colleagues through personal and academic interactions, for which I want to thank them - Mathias Kjærgård Christensen, Lev Martinez, Monica Lacatusu, Prasanna Kadirvelayutham, Tiago Ramos, Carlos Enrique Imbaquingo Muñoz, Zeyu Li, Christian Baur and many more. I would like to thank my friends, who always support me in my endeavors, inspire me to develop my personality and challenge my perception of the world with their own example: Ashkhen, Resul, Ljuba, nezhnii chelovek Julja, Sofia, Lev, Saman, and Katja. I would like to extend my gratitude to my spiritual teacher Ksenia Evgenievna Menshikova, who motivated me in a special way to start my career as a scientist.

I wish to give special thanks to my family – my Mama and Papa and my Sister. I am extremely thankful to my parents for transmitting to me this ability of theirs to think big and do job good. Their love, encouragements, and faith in me, since I was a child, have brought me to the point of my life, where my dreams come true. Luckily, I have a second, Italian family – Lucia, Bruno, Michele, zio Luca and zia Rita, zio Giacomo and zia Laura - whose love, support, and belief in me I appreciate very much, and I want to give a big thank to them and many kisses.

And last but not least, I want to express gratitude to my Amore Marco. Words cannot express how grateful I am to you for all your unconditional love and support that you gave me. For all the delicious breakfasts, lunches, and dinners that you have prepared for me. For all the beautiful surprises and presents that you made for me. And for all the lessons that you taught me, after which I believe I become a better, more loving and compassionate, person. All this has helped me a lot to keep my spirit strong during my PhD studies. Thank you very much and I love you.

Abstract

In the attempt to solve the problem of ever-increasing energy demand, thermochemical heat storage appears as a promising technology because it allows balance supply and demand of renewable energy power systems and recover low-grade waste heat. To construct a performant heat storage system, great attention should be given to the design of the thermal reactor, the core of the system, since it determines to a great extent its energy and power density, i.e. how much heat can be stored per unit volume and how fast this heat can be recovered. This has set the motivation to develop and validate a three-dimensional accurate numerical model of the reactor, coupling the kinetics of the chemical reaction with heat and mass transfer. In the present PhD project, such a model was developed for a reversible reaction between solid strontium chloride (SrCl_2) and gaseous ammonia (NH_3). This working pair allows storing large amount of heat at material level, 1579 kWh/m^3 , at relatively low cost, $3.9\text{-}4.9 \text{ \$/kWh}$. Moreover, SrCl_2 is environmentally benign and abundant.

As the first step of the work, the intrinsic kinetic parameters, constituents of the reaction rate equations, were experimentally determined for the sorption reactions between NH_3 and $\text{Sr}(\text{NH}_3)_z\text{Cl}_2$, where z varies between 1 and 8. The absorption and desorption kinetic curves were collected on a barometric Sieverts type apparatus using isothermal heating programs over a wide pressure-temperature range. To ensure that during the experiments the reaction kinetics was not limited by the heat and mass transfer, we used an optimal mass of solid SrCl_2 inserted into a heat conductive matrix of expanded natural graphite. As a result, the obtained rate equations predicted the experimental data with a good accuracy. Moreover, the results from numerical simulations performed using these equations were found to be in a good agreement with other experimental datasets, which had not been used for the determination of the kinetic parameters. For comparison, numerical simulations with the apparent kinetic equations from literature were found to deviate largely from the same datasets, underlying the importance of using intrinsic kinetic parameters for reactor modelling.

During the next step of this work, we developed and validated numerical model simulating NH_3 absorption into $\text{Sr}(\text{NH}_3)\text{Cl}_2$ and desorption from $\text{Sr}(\text{NH}_3)_8\text{Cl}_2$. The model was built in COMSOL Multiphysics environment. It was validated against experimental data obtained from neutron

radiography, and the results from the simulations were found to be in a very good agreement with the data. The originality of this study is that neutron radiography has been used for the purpose of model validation for the first time. Neutron radiography allowed following the spatio-temporal evolution of NH_3 within the reactive bed at each point of the reactor, which could not be achieved by other conventional methods of model validation, like temperature and flowmeter readings. The results from the absorption model were successfully crosschecked using the conventional methods. A distinctive feature of our model is that it is valid not only for the designed $\text{SrCl}_2\text{-NH}_3$ but also for other working pairs and different reactor configurations, as it utilizes intrinsic rather than apparent material properties.

The final step of the project focused on the optimization of the reactor by determining the main factors limiting its efficiency. A sensitivity study was performed on the thermal properties of the reactive bed and heat exchanger (thermal conductivity and specific heat capacity) as well as on the heat transfer coefficient between the reactive bed and heat exchanger. Based on the results of this study, practical recommendations for the improvement of the reactor design were made. To confirm and complement these recommendations, a set of sorption experiments, combined with neutron radiography measurements, were carried out using materials with superior and inferior thermal properties. The results revealed that all the studied thermal properties, except for the specific heat capacities of the reactive bed and heat exchanger, have an impact on the desorption rate and have to be considered when designing a reactor. For the absorption rate, the heat transfer coefficient was demonstrated to be the most influencing parameter among the heat transfer properties. In addition, it was also shown that absorption is a mass-driven process, and the parameter having the greatest impact on its rate is the permeability of the reactive bed.

Dansk resumé

For at imødekomme udfordringen med det evigt voksende behov for energi, er termokemisk varmelagring en lovende løsning, som kan udligne den forskel i produktion og forbrug, der er forbundet med bæredygtig energi. Samtidig vil et sådan system også kunne lagre restvarme fra industrielle processer. Et varmelagringsystem stiller store krav til designet af hovedkomponenten – den termiske reaktor. Det er denne, der i stor grad definerer det overordnede systems energi- og effekttæthed, altså hvor meget energi der kan lagres pr. enhedsvolume og hvor hurtigt varmen kan optages og afgives. For at udvikle et system med de mest optimale parametre, er der behov for at et varmelagringsystem kan simuleres i tre dimensioner, og at dette system bliver valideret. I denne ph.d.-afhandling er en sådan model blevet udviklet for en reversibel reaktion mellem Strontium Klorid (SrCl_2) og ammoniak (NH_3) på gasform, da disse materialer har intrinsisk høj varmekapacitet, 1579 kWh/m^3 og er relativt billige, $3.9\text{-}4.9 \text{ \$/kWh}$. Samtidig er SrCl_2 ufarligt for og normalt i naturen.

Som udgangspunkt for denne afhandling er de intrinsiske kinetiske parametre, konstanterne i ligningerne for reaktionshastighed, blevet eksperimentelt undersøgt for optagelsen af NH_3 i $\text{Sr}(\text{NH}_3)_z\text{Cl}_2$, hvor z kan variere mellem 1 og 8. Adsorption og desorption-hastigheder er blevet bestemt ved brug af et barometrisk Sieverts-apparat der brugte isotermisk opvarmning i et bredt temperaturvindue. For at sikre, at de kinetiske parametre ikke var begrænset af varme og masseoverførsel, blev de bestemt via forsøg, hvor SrCl_2 var indsat i en varmelende matrix af grafit. Derved blev det bestemt, at reaktionshastigheden fra simuleringerne stemte godt overens med den eksperimentelle data. Numeriske simulationer udført med disse ligninger stemte også overens med eksperimentelle data fra andre forsøg, der ikke havde til formål at bestemme hastighedskonstanterne. Til sammenligning, numeriske simulering fra litteraturen, viste store afvigelser fra de samme datasæt, hvilket understreger behovet for at bruge intrinsiske kinetiske parametre til reaktormodellering.

Det næste skridt var at udvikle og validerer en numerisk model, der simulerer NH_3 absorption i $\text{Sr}(\text{NH}_3)\text{Cl}_2$ og desorption fra $\text{Sr}(\text{NH}_3)_8\text{Cl}_2$. Modellen blev udviklet i COMSOL Multiphysics. Denne model blev valideret mod eksperimentelle data fra neutron-radiografi. Resultaterne fra simulering stemte godt overens med resultaterne fra disse eksperimenter. Brugen af neutron-

radiografi, som ikke er blevet anvendt før til dette formål, tillader rum og tidsopløsning af NH_3 i hele reaktoren som ikke kan opnås via andre konventionelle metoder, som temperatur og flowmålinger. Resultatet for absorptionsmodellen blev også fundet i overensstemmelse med disse konventionelle metoder. En vigtig egenskab ved vores model er, at den også kan benyttes til andre materialer og reaktor-konfigurationer, ud over dem, vi benytter heri, fordi den benytter intrinske parametre for de involverede materialer i stedet for værdier for systemet.

Den sidste del af projektet har været at optimere reaktordesignet ved at bestemme de forhold, der begrænser reaktorens effektivitet. En følsomhedsundersøgelse af termiske egenskaber af reaktoren og varmeveksleren blev udført med henblik på at bestemme varmeledningsevne og specifik varmekapacitet for disse. Samtidig blev koefficienten for varmeudvekslingen mellem disse komponenter også bestemt. Baseret på denne undersøgelse foreslås praktiske opgraderinger til reaktordesignet. For at verificere disse opgraderinger blev der udført en række adsorption og desorptions-eksperimenter, kombineret med neutron-radiografi som benyttede materialer med bedre og værre termiske egenskaber. Disse resultater viste, at alle de interessante termiske egenskaber, bortset fra specifik varmekapacitet af reaktoren og varmeveksleren, påvirkede desorptions-hastigheden og således skal der tages højde for dette i designet. For adsorptions-hastigheden blev det vist, at varmeudvekslingskoefficienten var den vigtigste parameter blandt de termiske egenskaber. Ydermere blev det demonstreret, at adsorption er en massedrevet proces, og den største påvirkning på effektiviteten af adsorption er fremkommeligheden i reaktoren.

List of publications

Journal papers

1. Karabanova A., Berdiyeva P., Pal M. van der, Johnsen R. E., Deledda S., Blanchard D. Importance of Using Intrinsic Kinetics in Modeling Thermochemical Heat Storage System: SrCl₂-NH₃ Case Study. Submitted to Applied Thermal Engineering in July 2020.
2. Karabanova A., Berdiyeva P., Soprani S., Johnsen R. E., Hauback B. C., Deledda S., Blanchard D. Neutron radiography for modeling thermochemical heat storage reactors: case study on SrCl₂-NH₃ system. To be submitted in December 2020.
3. Karabanova A., Berdiyeva P., Pal M. van der, Koundoul N. F., Deledda S., Blanchard D. Modeling and Neutron Radiography - Optimization of Heat Transfer for Thermochemical Heat Storage. To be submitted in December 2020.
4. Karabanova A., Knudsen K. D., Berdiyeva P., Deledda S., Johnsen R. E., Pal M. van der, Blanchard D. In-situ Nanostructural Characterization of SrCl₂-ENG Composite by Small Angle Neutron Scattering. Under preparation. To be submitted in December 2020.
5. Berdiyeva P., Karabanova A., Makowska M. G., Johnsen R. E., Blanchard D., Hauback B. C. and Deledda S. In-situ neutron imaging study of NH₃ absorption and desorption in SrCl₂ within a heat storage prototype reactor. J. Energy Storage, vol. 29, no. December 2019, p. 101388, 2020.
6. Berdiyeva P., Karabanova A., Blanchard D., Hauback B. C. and Deledda S. Sr(NH₃)₈Cl₂-Expanded Natural Graphite composite for thermochemical heat storage applications studied by in-situ neutron imaging. Submitted to Journal of Energy Storage in September 2020.

Peer-review conference papers

1. Karabanova A., Berdiyeva P., Soprani S., Johnsen R. E., Deledda S., Blanchard D. Comparison between Numerical Simulation and Neutron Radiography of Ammonia Absorption and Desorption in SrCl₂ for Application in Thermochemical Storage System for Waste

Heat Recovery. Eurotherm Seminar Advances in Thermal Energy Storage, University of Lleida, Lleida, Spain: 2019.

2. Gunasekara S. N., Soprani S., Karabanova A., Martin V. and Blanchard D. Numerical Design of a Reactor-Heat Exchanger Combined Unit for Ammonia-SrCl₂ Thermochemical Storage System. ISES Solar World Congress 2019 and IEA SHC conference 2019, Santiago, Chile: 2019

Contents

Preface.....	2
Acknowledgements.....	3
Abstract.....	6
Dansk resumé.....	8
List of publications	10
Journal papers	10
Peer-review conference papers	10
Contents	12
1 Chapter I: Introduction	17
1.1 Motivation.....	17
1.1.1 TES and its types	18
1.1.2 Comparison of TES types	20
1.1.3 Thermochemical heat storage	22
1.2 Thesis statement	27
1.3 Thesis outline	29
References.....	30
2 Chapter II: Methodology	35
2.1 System and reactor	35
2.2 Working pair SrCl ₂ -NH ₃	37
2.2.1 Basic principles of the sorption reactions	37
2.2.2 Structural changes during cycling.....	40
2.2.3 Composite materials.....	41
2.3 Neutron imaging.....	41
2.3.1 Basics of neutron imaging	42
2.3.2 Spatial and temporal resolution	47
2.4 Modelling	48
2.4.1 Heat transfer.....	49
2.4.2 Mass transfer.....	50
2.4.3 Kinetics	51
2.4.4 Modelling in COMSOL Multiphysics 5.5	58

References.....	59
3 Chapter III: Characterization of Parameters Governing the Reaction Rate	65
3.1 Paper I: Importance of Using Intrinsic Kinetics in Modeling Thermochemical Heat Storage System: SrCl ₂ -NH ₃ Case Study.....	67
3.1.1 Abstract.....	67
3.1.2 Introduction.....	68
3.1.3 Materials and Methods.....	70
3.1.4 Results and Discussions.....	80
3.1.5 Conclusion	93
3.1.6 References.....	94
4 Chapter IV. Validation of Thermochemical Reactor Modelling Using Neutron Radiography.	97
4.1 Paper II: In-situ neutron imaging study of NH ₃ absorption and desorption in SrCl ₂ within a heat storage prototype reactor	99
4.1.1 Introduction.....	100
4.1.2 Experimental.....	102
4.1.3 Results and discussion	104
4.1.4 Summary.....	115
4.1.5 Acknowledgements.....	116
4.1.6 Supplementary materials.....	116
4.1.7 References.....	116
4.2 Paper III: Comparison between Numerical Simulation and Neutron Radiography of Ammonia Ab- and Desorption in SrCl ₂ for Application in Thermochemical Storage System for Waste Heat Recovery	121
4.2.1 Introduction.....	122
4.2.2 Materials and methods	123
4.2.3 Results and discussion	130
4.2.4 Conclusions.....	133
4.2.5 Acknowledgements.....	133
4.2.6 References.....	133
4.3 Paper IV: Neutron Radiography for Modelling Thermochemical Heat Storage Reactors: Case Study on SrCl ₂ -NH ₃ System.....	135
4.3.1 Introduction.....	136

4.3.2	Materials and methods	139
4.3.3	Results and Discussions.....	153
4.3.4	Conclusion	160
4.3.5	Acknowledgements.....	161
4.3.6	Supplementary information	161
4.3.7	References.....	162
5	Chapter V: Modelling and Neutron Radiography – Optimization of Heat Transfer.....	165
5.1	Paper V: Modelling and Neutron Radiography - Optimization of Heat Transfer for Thermochemical Heat Storage	167
5.1.1	Abstract.....	167
5.1.2	Introduction.....	168
5.1.3	Experimental.....	169
5.1.4	Results and discussions.....	178
5.1.5	Conclusion	188
5.1.6	Acknowledgements.....	189
5.1.7	References.....	189
5.1.8	Supplementary information	193
5.2	Paper VI: Sr(NH ₃) ₈ Cl ₂ -Expanded Natural Graphite composite for thermochemical heat storage applications studied by <i>in-situ</i> neutron imaging.....	203
5.2.1	Abstract.....	203
5.2.2	Introduction.....	204
5.2.3	Experimental.....	205
5.2.4	Results and discussions.....	208
5.2.5	Conclusion	217
5.2.6	Acknowledgements.....	217
5.2.7	Appendix A. Supplementary data.....	218
5.2.8	References.....	221
6	Conclusion and Outlook	227
7	Supplementary Information.....	231
7.1	Paper VII: Small Angle Neutron Scattering Characterization of Composite SrCl ₂ -ENG for Thermochemical Heat Storage	231
7.1.1	Abstract.....	231

7.1.2	Introduction.....	232
7.1.3	Experimental.....	233
7.1.4	Results.....	242
7.1.5	Conclusion	258
7.1.6	Acknowledgements.....	259
7.1.7	References.....	259
7.1.8	Supplementary information	263
7.2	Paper VIII: Numerical Design of a Reactor-Heat Exchanger Combined Unit for Ammonia-SrCl ₂ Thermochemical Storage System.....	267
7.2.1	Abstract.....	267
7.2.2	Introduction.....	268
7.2.3	Methodology.....	269
7.2.4	Results and discussion	274
7.2.5	Concluding remarks	282
7.2.6	Acknowledgments.....	283
7.2.7	References.....	283



1 Chapter I: Introduction

1.1 Motivation

With all increasing population growth and rapid urbanization in developing countries, the modern energy system faces the challenge of providing more energy, in the form of electricity and heat, to larger amount of people. According to the global energy review published by the International Energy Agency [1], in 2019 the global energy mix was dominated by fossil fuels (coal, oil, gas), accounting for 80% of total primary energy demand. However, it was estimated that conventional fossil energy will not meet the continuous need for energy in the future due to the fact that these resources are limited [2]. Moreover, burning fossil fuels is responsible for most of the emissions of anthropogenic greenhouse gases (CO_2 , CH_4 , NO_x , etc.) [3], which cause the rise of the global temperature and hence global warming. One of the alternatives to the carbon-based fuels is renewable energy sources (mainly solar and wind energy) that are inexhaustible and low-carbon by their nature. Despite the obvious advantages, renewables exhibit inherent intermittency and low dispatchability, resulting in the gap between the supply and demand and hence their limited use. To balance the supply and demand, the energy extracted from renewables is to be stored in the form of electricity, in batteries [4] or fuel cells [5], or in the form of heat, by using thermal energy storage (TES) [6]–[12]. TES can also help in increasing the efficiency of already existing energy system by utilizing the heat generated during industrial processes, or so-called waste heat. Recent studies have shown that more than 45% of the global primary energy consumption accounts for low-grade waste heat, of the temperature below 100°C [13]. The industrial waste heat can be utilized either internally, within the industrial process, or externally, when the heat is supplied to other industrial processes or utility services, for example, district heating [14], [15]. In [16], the authors have shown that the district heating demand in Northern China can be covered, if 38 % of industrial low-grade waste heat is recovered. Beside maximizing the efficiency of the industrial processes (internal) or powering other processes, the waste heat recovery has other advantages, such as reduction of fossil fuel usage, carbon dioxide emissions, and water dissipation.

Taking into account that TES can help solving the problem of ever-increasing energy demand by equating production and consumption of the renewable energy as well as recovering waste heat

from industrial processes, the research community should pay particular attention to this technology.

1.1.1 TES and its types

There are three main types of TES technologies: sensible heat storage (SHS), latent heat storage (LHS), and thermochemical heat storage (TCHS). The three systems can exist in three modes: charging, storing, and discharging (see Figure 1).

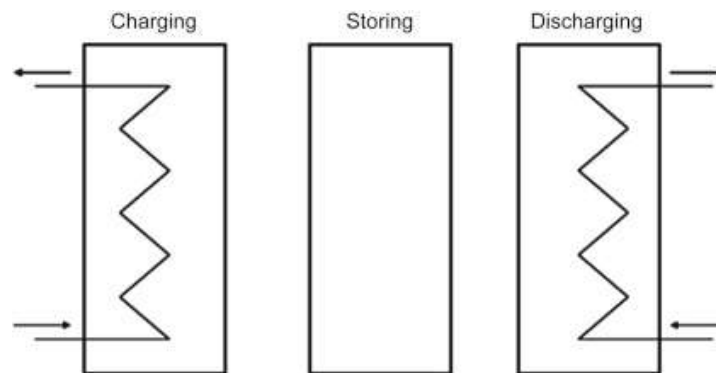


Figure 1. Steps during operation of Thermal Energy Storage systems: charging, storing, and discharging. Figure is taken from [17].

During the processes of charging and discharging, the heat is supplied and recovered to / from the system, respectively. During the storing step, the heat is stored.

1.1.1.1 Sensible heat storage (SHS)

In SHS systems, the heat is stored or released by heating or cooling a storage medium that can be in gaseous, liquid or solid state. The amount of stored heat depends on the specific heat capacity of the material, C_p , and the temperature difference between the initial and final states ΔT and can be calculated as follows [18]:

$$Q = m \cdot C_p \cdot \Delta T \quad \text{Eq. 1}$$

where m is the mass of the material.

Examples of materials for SHS are air, water, molten salts, oil, rocks etc. [19]. Generally, this type of energy storage is used for large applications, where large amount of heat needs to be stored, e.g.

aquifer TES [20]. The capital and operational expenditures (CAPEX and OPEX) are low compared to the other systems, and their operation is easy.

1.1.1.2 Latent heat storage (LHS)

LHS employs the phase change of a material, for example, from solid to liquid. For this reason, materials applied for LHS are called phase change materials (PCM). The energy that can be stored in a given amount of a PCM, m , is proportional to the phase change enthalpy ΔH and can be calculated using the following formula:

$$Q = m \cdot \Delta H \quad \text{Eq. 2}$$

where m is the mass of PCM.

Let us look at a solid-liquid LHS system. During charging, the heat is transferred to the system, which initiates melting of the material at melting temperature. Unlike sensible materials, the temperature of which always increases during charging, the temperature of the PCM keeps constant, equal to melting temperature, as long as there is still solid material present in the system (see Figure 2). This is the main difference between SHS and LHS.

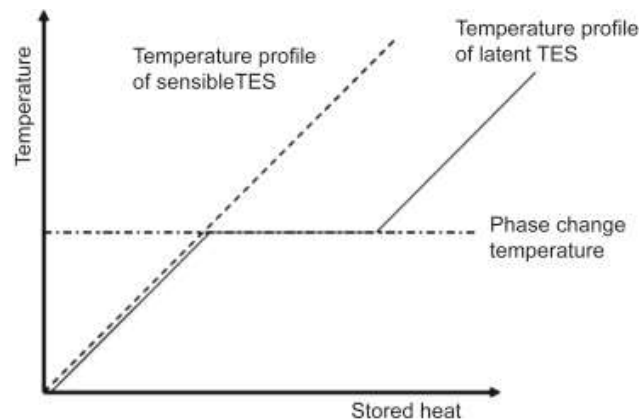


Figure 2. Heat profile for SHS and LHS. Figure is taken from [21].

During discharge mode, the process of solidification occurs at constant temperature with the release of the heat.

Extensive research has been done on different materials for LHS application (water-salt solutions, clathrates, paraffins, sugar alcohols, etc.); however, only a few have been commercialized due to

problems such as phase segregation, subcooling, corrosion, long-term stability, and low thermal conductivity [22].

1.1.1.3 Thermochemical heat storage (TCHS)

Thermochemical heat storage utilizes reversible reaction between a sorbent and a sorbate, which generally can be written as follows:



During the process of charging, the heat supplied to the system initiates desorption of the sorbate from the sorbent (endothermic reaction). When the two materials are not in contact, the heat is stored for any period of time. During the discharge mode, the sorbate reacts with the sorbent with the release of heat (exothermic reaction). The amount of heat released is proportional to the enthalpy of reaction.

1.1.2 Comparison of TES types

When comparing TES types, energy density is a key criterion. Thermochemical materials have higher energy density at material level compared to the other two types, meaning that for storing given amount of heat smaller volume of thermochemical material is required. This is shown in Figure 3, where the volume of each material type (sensible, latent, thermochemical) required for storing 10 GJ of heat is indicated. In addition, the energy density is shown with respect to the achievable temperature. It is worth noting that both chemical reactions (C) and sorption (S) represent thermochemical materials, and the difference between them is discussed further.

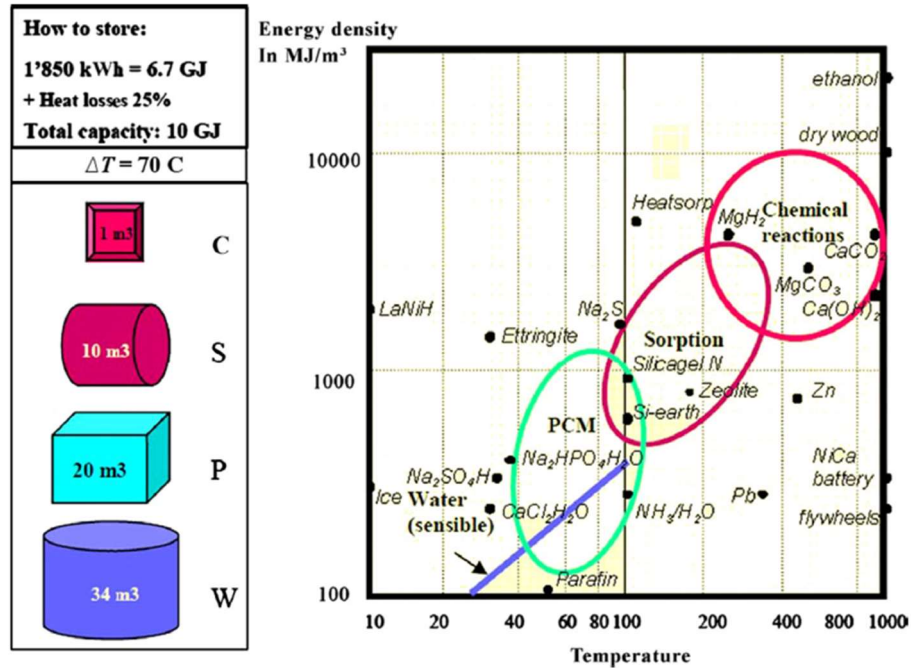


Figure 3. Energy storage density for different types of TES. C stands for Chemical reactions, S – Sorption, P – Phase change materials, W – water. Figure is taken from [23].

According to Figure 3, one can conclude that the energy density of chemical reactions is 20 and 34 times higher compared to PCM and water, respectively.

Besides higher energy density, thermochemical materials can store heat nearly with no losses for any period of time, provided sorbent and sorbate are not in contact. In contrast to TCHS, in SHS and LHS, stored heat dissipates with time. To prevent fast dissipation of heat, insulation materials are to be used; however, thick insulation layer leads to bulkier systems and lower energy densities with notably higher CAPEX.

In addition, input and output temperatures of thermochemical materials are determined by practical demands and working conditions. This is because equilibrium pressure p_{eq} , at which the forward and reverse reactions (see Eq. 3) occur at equal rate is dependent on the temperature of the sorbent in accordance with the van't Hoff equation:

$$p_{eq} = p_0 e^{-\frac{\Delta H + \Delta S}{RT + R}} \quad \text{Eq. 4}$$

where p_0 is a reference pressure equal to 1 Pa; ΔH and ΔS are the reaction enthalpy and entropy; R is the gas constant; and T is the temperature of the sorbent. By changing the pressure of the sorbate in the system, one can adjust the process temperature. Opposite to thermochemical materials, PCM can be operated only at specific temperatures, as their phase transition temperatures are definite.

Despite all the aforementioned advantages of TCHS, the technology is still under research and development due to critical drawbacks, among which are the complexity of the system (for closed configuration), the high capital cost and the low heat storage density at system level [10]. If solution emerge to solve these drawbacks, thermochemical materials have a great potential to offer compact heat storage systems with no heat losses. The combination of TCHS's distinctive features (compactness and loss-free) should play a central role in the recovery of waste heat in existing factories, with limited free space, and storing waste heat of industrial plants in mobilized form using so called thermal battery. The concept of thermal battery and its implementation has been discussed by Jarimi *et al.* [24], referring to a pilot study in Germany, where waste heat is transported from industrial plants to district heat networks with zeolite as a sorption material [25]. Long distance energy transportation using TCHS has been also covered in [15], [26]. Other applications of sorption systems are heat pump technologies and solar refrigeration [27], [28].

As the frame of this PhD project was to develop a compact TES system, the focus has been on thermochemical heat storage. Therefore, thermochemical heat storage is described in more detail here below.

1.1.3 Thermochemical heat storage

According to the latest classification [10], thermochemical storage is divided into four groups:

1. Liquid absorption. Absorption is defined as the process of sorbate incorporation into the bulk of sorbent material. In this case, the sorbate is gas, and sorbent – liquid.
2. Solid adsorption. Adsorption refers to the adhesion of a sorbate on the surface of a sorbent and, in case of solid adsorption, the sorbent is in solid state. One can distinguish between physical adsorption occurring due to intermolecular forces, or Van der Waals forces, and chemical adsorption involving valency forces. As chemical forces (valency forces) are

stronger than Van der Waals forces, chemisorption offers higher heat of sorption than physisorption.

3. Chemical reaction relates to sorption consisting of two main reaction types – coordination reaction of solid ammonia salts with gaseous ammonia and hydration reaction of solid salt hydrate with water vapour. The chemical reaction mechanism involves two steps: adsorption of the gaseous sorbate (ammonia, water) on the surface of the sorbent (ammines, hydrates) and absorption of the sorbate in the bulk of sorbent accompanied by the change of molecular structure of the latter. Recognizing the importance of one process over the other, different researchers recognize chemical reactions as either chemical adsorption [12], [27] or solid/gas absorption [29]. In this work, these reactions will be referred to as solid/gas absorptions because the diffusion of the sorbate in the bulk of the sorbent followed by the structural changes of molecules is the mechanism limiting the reaction rates.
4. Composite materials. These materials consists of a host matrix and an inorganic salt placed inside the matrix pores. This type of the material is discussed below.

The summary of the classification with the materials examples is presented in Figure 4.

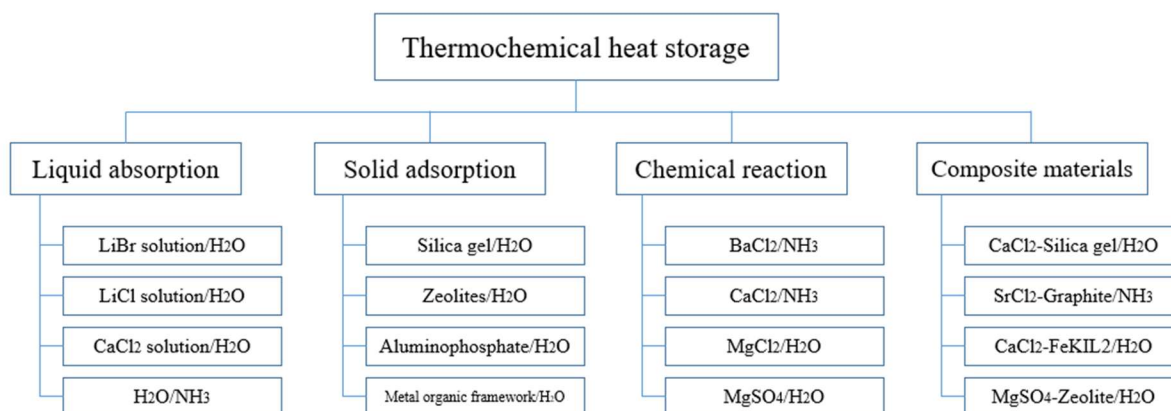


Figure 4. Sorption thermal storage classification. Adapted from [10].

1.1.3.1 Systems

Based on the system configuration, thermochemical heat storage systems can be divided into open and closed systems. While in the open systems the sorbent is exposed to the environment allowing the exchange of the sorbate, the closed system is isolated from the atmospheric environment.

The closed system is composed of two connected reservoirs: a reactor filled with a solid / liquid sorbent and a condenser / evaporator with a liquid sorbate (see Figure 5). During the charging mode, heat provided to the reactor initiates the detachment of the sorbate from the sorbent. The desorbed fluid in gaseous form turns into a liquid in the condenser, releasing heat of condensation. In storage mode, the two reservoirs are separated. There are nearly no heat losses at this stage. During the discharging mode, the liquid sorbate evaporates, absorbing heat of evaporation, and is adsorbed by the sorbent with the release of heat. Such a system can provide both heating and cooling, separately or simultaneously, thanks to the presence of the two reservoirs.

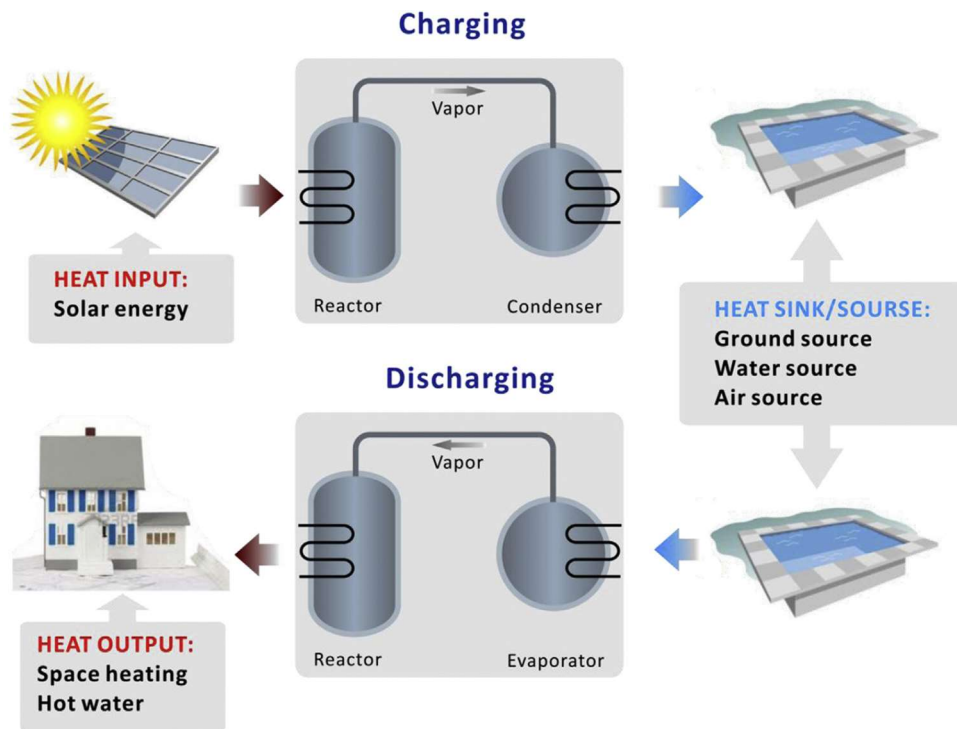


Figure 5. Operating principle of closed system. Figure is taken from [10].

Open systems contain a reactor only, as the atmospheric environment represents the other vessel, condenser / evaporator (see Figure 6). Needless to say that this type of systems can use only water as a sorbate.

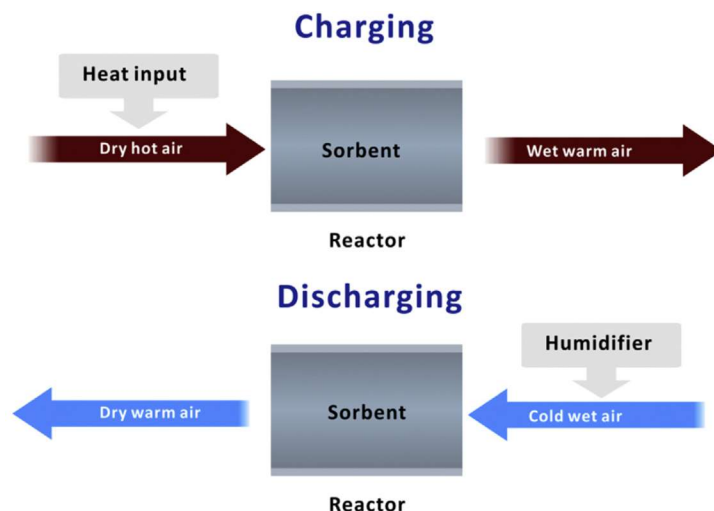


Figure 6. Operating principle of open system. Figure is taken from [10].

During the charging process, dry hot air enters the reactor filled with a sorbent resulting in water desorption. During the discharging, a stream of cold wet air passes through the sorbent bed with the release of ab/adsorption heat, which can be used for heating purposes.

In comparison to closed configuration, open systems are less complex and hence cheaper. However, when using open systems, one has to monitor the moisture level of the ambient air, as it could be insufficient for fast ab/adsorption, and the installation of a humidifier is required. In addition, such a system needs a fan, which also increase the cost of the system.

1.1.3.2 Thermochemical reactors

The thermochemical reactor used in TCHS systems can be divided into *integrated* and *separate* reactors. While the integrated reactors accommodate the reaction within the storage vessel, in the separate reactors the sorbent is transferred back to the storage vessel, once the reaction is complete. Although the separate reactors allow reducing the amount of heat required for inert metallic components, making them attractive for large scale storage applications [30], they have several drawbacks. For example, they require an additional power for driving the sorbent transport from the reactor to the storage reservoir and for handling the sorbent within the reactor. Furthermore,

the separate reactors cannot use the sorbents in the form of a consolidated composite material with superior heat and mass transfer properties, but in the form of powder only. Finally yet importantly, the separate reactors are complex to construct and require an additional vessel for the sorbent storage. For the aforementioned reasons, the integrated reactors are widely applied in thermochemical systems, in contrast to the separate reactors, and in our study, we have used this reactor type.

According to [31], thermochemical reactors can be categorized into *indirect* and *direct* reactors. In the indirect reactors, the heat absorbed and released by the sorbent is transferred to the heat transfer fluid (HTF) via the heat exchanger, avoiding the contact between the sorbent and the HTF. In the direct reactors, the HTF permeates the sorbent bed directly. Thus, the HTF can be a sorbate, but it is usually inert with respect to the sorbent, acting as a carrier only. The main advantage of the direct reactors is that the heat exchange between the sorbent and the HTF is not limited by the surface of the heat exchanger, as in case of the indirect reactors. However, in the direct reactors, an additional power is required to overcome pressure losses in low-permeable beds. Furthermore, the pressures of the sorbate and the HTF are interconnected and hence cannot be chosen independently. For these reasons, we chose an indirect reactor design, for which the choice of the heat exchanger is of great importance.

1.1.3.3 Heat exchanger types

According to several studies on the design of heat exchangers for thermal energy storage application [32]–[34], the heat exchangers are recommended to be as compact as possible, as the compactness of the heat exchangers results in a high area density, over $700 \text{ m}^2 \text{ m}^{-3}$ [35]. The area density is calculated as the ratio between the heat transfer surface and the volume. The high value of area density leads to small hydraulic diameter for sorbate flow and high heat transfer coefficient between the reactive bed and the heat exchanger [32]. The attempt of comparing three types of heat exchangers with high area density (helical coil [36], plate-fin ([32], [37], [38]), and honeycomb [39], [40]) for low-heat application using numerical modelling was made by Lele [41]. The results of the study revealed that the honeycomb heat exchanger exhibits much high heat transfer coefficient than the helical coil and plate-fin heat exchangers (182.2 vs. 53.2 and $75.9 \text{ W m}^{-2} \text{ K}^{-1}$). Furthermore, smaller pressure drop and higher temperature within the reactive bed was

observed in case of the honeycomb heat exchanger compared to the other options. Based on these results, we chose to use a honeycomb-type heat exchanger in our system.

1.1.3.4 Modeling of thermochemical reactor

There are two types of models, which can help predicting the behavior of thermochemical reactors: *lumped-parameter* (global) models and *spatially resolved* (local) models.

As name implies, “lumped models” lump the contribution of several spatially distributed phenomena into a limited set of variables and parameters. This type of models treats the reactor as a homogeneous control volume with an internally uniform state. The advantages of lumped system is that it is computationally cheap and gives the possibility of a rough dimensioning of the reactors. However, it does not allow a detailed modelling of the processes occurring inside the reactors and hence the optimization of the reactors is not possible. This task can be performed using “spatially resolved models”. These models calculate the spatio-temporal evolution of state variables (local pressure and temperature, reaction advancement) defined by locally formulated physical balance law and the dependency of the material properties on local thermophysical conditions. Local models for thermochemical heat storage systems were reviewed by Nagel *et al.* [31], where he listed models for metal halides – NH₃ working pairs [42]–[49]. Among the recommendation for future work, the authors advised to focus on reliable identification of the parameters, to which the reactor performance is more sensitive.

1.2 Thesis statement

The work presented in this thesis was performed in the frame of the Scandinavian project named “Neutrons for Heat Storage”. This project aimed at developing a cost effective and compact thermochemical heat storage (TCHS) system for low-grade waste heat recovery. A 2-3 kWh storage capacity was set as a target for the heat storage system.

To design a TCHS system of a given capacity, one has to carefully choose and size the auxiliary equipment, such as pumps, valves, evaporator, and condenser. To do this, it is necessary to have a good understanding of the processes occurring inside the thermochemical reactor. The thermochemical reactor, a core of the system, has to be designed and manufactured in a way that allows take full advantage of the high energy density of the sorbent material and produce high heat

power. Modelling comes as a natural tool to define such a performant reactor design. It allows test and study different reactor geometries and reactor materials together with different thermochemical material preparation while helping to identify the set of important parameters to optimize.

To develop a universal numerical model of thermochemical reactor has been the scope of this PhD work. The developed model, presented hereinafter, has been tested and validated using the $\text{SrCl}_2\text{-NH}_3$ working pair and a honeycomb heat exchanger, but is fully usable and applicable to other working pairs and reactor designs, as long as intrinsic or close-to-intrinsic material properties are provided.

The workflow has been divided into several subtasks as required for the development of this robust and versatile model:

1. Determine the close-to-intrinsic kinetic parameters of the working pair $\text{SrCl}_2\text{-NH}_3$.
The model is to be used for any working pair, and one have to use materials parameters independent of their configuration and environment – This requires careful characterization of the given material beforehand, but it should pay-off if an optimal reactor design is obtained.
2. Develop and validate the numerical model of the thermochemical reactor.
A three dimensional model of the thermochemical reactor has been developed using COMSOL Multiphysics. The model simulates the kinetics of the chemical reaction, as well as coupled heat and mass transfer. To validate the model, conventional techniques, such as temperature and ammonia flow readings, together with a much powerful validation tool, namely neutron radiography, have been used. Neutron radiography has been used for the first time on such a system for the numerical validation.
3. Perform a parametric study to identify the critical parameters, which may limit the performance of the thermochemical reactor and validate the results with conventional and neutron radiography experimental results.

1.3 Thesis outline

Chapter I is the introduction containing the motivation for the study, the thesis statement, and the thesis outline.

Chapter II presents the reactor prototype and the working pair $\text{SrCl}_2\text{-NH}_3$, which were studied throughout the thesis. In addition, basic principles of neutron radiography are described. Finally, a short description of processes occurring during the sorption reaction is given.

Chapter III describes the procedure for determining the intrinsic kinetics parameters of NH_3 absorption into $\text{Sr}(\text{NH}_3)\text{Cl}_2$ and desorption from $\text{Sr}(\text{NH}_3)_8\text{Cl}_2$. Moreover, the significance of using intrinsic kinetic parameters in reactor modeling is discussed (Paper I).

Chapter IV presents the results from the imaging studies obtained on the reactor prototype (Paper II). The results are then used for the validation of the numerical models presented in Paper III and IV. The model presented in Paper IV utilizes the kinetic parameters obtained in Chapter III.

Chapter V presents the results of the sensitivity analysis performed to find the critical parameters that could increase the absorption and desorption rates (Paper V). The study was carried out on the numerical model developed and validated in Chapter IV. In Paper VI, the results from the imaging studies, which were used in Paper V, are presented.

Chapter VI summarizes the most important findings of the thesis and gives suggestions for further work within the field.

Chapter VII contains the papers that were not included in the thesis, but are of relevance to the presented work. Paper VII presents the study on small angle neutron scattering, in which the attempt to correlate the nanostructural changes in SrCl_2 -expanded natural graphite composite during NH_3 cycling to the change in absorption and desorption rates was made. In Paper VIII, the design of the reactor unit, of 0.5 kWh capacity, is presented.

References

- [1] IEA (2020), “Global Energy Review 2019,” Paris.
- [2] A. Demirbas, “Electricity generation via unconventional methods,” *Energy Explor. Exploit.*, vol. 24, no. 1–2, pp. 131–138, 2006.
- [3] “Energy and the environment explained. Where greenhouse gases come from,” 2020. [Online]. Available: <https://www.eia.gov/energyexplained/energy-and-the-environment/where-greenhouse-gases-come-from.php>. [Accessed: 10-Sep-2020].
- [4] Y. Yang, S. Bremner, C. Menictas, and M. Kay, “Battery energy storage system size determination in renewable energy systems: A review,” *Renew. Sustain. Energy Rev.*, vol. 91, no. March, pp. 109–125, 2018.
- [5] V. T. Giap, Y. D. Lee, Y. S. Kim, and K. Y. Ahn, “A novel electrical energy storage system based on a reversible solid oxide fuel cell coupled with metal hydrides and waste steam,” *Appl. Energy*, vol. 262, no. September 2019, p. 114522, 2020.
- [6] A. Shukla, K. Kant, and A. Sharma, “Solar still with latent heat energy storage: A review,” *Innov. Food Sci. Emerg. Technol.*, vol. 41, pp. 34–46, 2017.
- [7] A. Crespo, C. Barreneche, M. Ibarra, and W. Platzer, “Latent thermal energy storage for solar process heat applications at medium-high temperatures – A review,” *Sol. Energy*, vol. 192, no. April 2018, pp. 3–34, 2019.
- [8] A. Gautam and R. P. Saini, “A review on sensible heat based packed bed solar thermal energy storage system for low temperature applications,” *Sol. Energy*, vol. 207, no. November 2018, pp. 937–956, 2020.
- [9] B. Koçak, A. I. Fernandez, and H. Paksoy, “Review on sensible thermal energy storage for industrial solar applications and sustainability aspects,” *Sol. Energy*, vol. 209, no. September, pp. 135–169, 2020.
- [10] N. Yu, R. Z. Wang, and L. W. Wang, “Sorption thermal storage for solar energy,” *Prog. Energy Combust. Sci.*, vol. 39, no. 5, pp. 489–514, 2013.

-
- [11] J. Xu, R. Z. Wang, and Y. Li, “A review of available technologies for seasonal thermal energy storage,” *Sol. Energy*, vol. 103, pp. 610–638, 2014.
- [12] K. E. N’Tsoukpoe, H. Liu, N. Le Pierrès, and L. Luo, “A review on long-term sorption solar energy storage,” *Renew. Sustain. Energy Rev.*, vol. 13, no. 9, pp. 2385–2396, 2009.
- [13] C. Forman, I. K. Muritala, R. Pardemann, and B. Meyer, “Estimating the global waste heat potential,” *Renew. Sustain. Energy Rev.*, vol. 57, pp. 1568–1579, 2016.
- [14] F. Huang, J. Zheng, J. M. Baleynaud, and J. Lu, “Heat recovery potentials and technologies in industrial zones,” *J. Energy Inst.*, vol. 90, no. 6, pp. 951–961, 2017.
- [15] Q. Ma, L. Luo, R. Z. Wang, and G. Sauce, “A review on transportation of heat energy over long distance: Exploratory development,” *Renew. Sustain. Energy Rev.*, vol. 13, no. 6–7, pp. 1532–1540, 2009.
- [16] H. Fang, J. Xia, K. Zhu, Y. Su, and Y. Jiang, “Industrial waste heat utilization for low temperature district heating,” *Energy Policy*, vol. 62, pp. 236–246, 2013.
- [17] A. Gil *et al.*, “State of the art on high temperature thermal energy storage for power generation. Part 1-Concepts, materials and modellization,” *Renew. Sustain. Energy Rev.*, vol. 14, no. 1, pp. 31–55, 2010.
- [18] A. H. Abedin, “A Critical Review of Thermochemical Energy Storage Systems,” *Open Renew. Energy J.*, vol. 4, no. 1, pp. 42–46, 2011.
- [19] K. Nielsen, “Thermal energy storage: A state-of-the-art,” *A Rep. within Res. Progr. Smart Energy-Efficient Build. Nor. Univ. Sci. Technol. SINTEF*, no. January 2003, 2003.
- [20] I. Dincer, S. Dost, and X. Li, “Performance analyses of sensible heat storage systems for thermal applications,” *Int. J. Energy Res.*, vol. 21, no. 12, pp. 1157–1171, 1997.
- [21] L. F. Cabeza and U. De Lleida, *Thermal energy storage for renewable heating and cooling systems* *. 2016.
- [22] L. F. Cabeza, I. Martorell, L. Miró, A. I. Fernández, and C. Barreneche, *Introduction to thermal energy storage (TES) systems*. Woodhead Publishing Limited, 2015.
-

-
- [23] D. Aydin, S. P. Casey, and S. Riffat, “The latest advancements on thermochemical heat storage systems,” *Renew. Sustain. Energy Rev.*, 2015.
- [24] H. Jarimi, D. Aydin, Z. Yanan, G. Ozankaya, X. Chen, and S. Riffat, “Review on the recent progress of thermochemical materials and processes for solar thermal energy storage and industrial waste heat recovery,” *Int. J. Low-Carbon Technol.*, vol. 14, no. 1, pp. 44–69, 2019.
- [25] A. Hauer, “Heat pumps and thermal energy storage. Zae Bayern.” [Online]. Available: <http://www.heatpumpcentre.org/en/hppactivities/hppworkshops/%0ANuremberg2012/Documents/S3 P10 ZAE Hauer.pdf>. [Accessed: 15-Sep-2020].
- [26] J. Berthiaud, N. Mazet, L. Luo, D. STITOU, and I. Descamps, “Long-distance transport of thermal energy using sorption cycles,” *Proc. ATI Conf. Milano, Italy*, vol. 34, pp. 14–17, Jan. 2006.
- [27] L. W. Wang, R. Z. Wang, and R. G. Oliveira, “A review on adsorption working pairs for refrigeration,” *Renew. Sustain. Energy Rev.*, vol. 13, no. 3, pp. 518–534, 2009.
- [28] X. Q. Zhai and R. Z. Wang, “A review for absorption and adsorption solar cooling systems in China,” *Renew. Sustain. Energy Rev.*, vol. 13, no. 6–7, pp. 1523–1531, 2009.
- [29] J. Cot-Gores, A. Castell, and L. F. Cabeza, “Thermochemical energy storage and conversion: A-state-of-the-art review of the experimental research under practical conditions,” *Renew. Sustain. Energy Rev.*, vol. 16, no. 7, pp. 5207–5224, 2012.
- [30] H. a. Zondag, V. M. Essen van, R. Schuitema, a. Kalbasenka, and M. Bakker, “Engineering Assessment of Reactor Designs for Thermochemical Storage of Solar Heat,” *Effstock 2009, Therm. Energy Storage Effic. Sustain.*, pp. 1–8, 2009.
- [31] T. Nagel, S. Beckert, C. Lehmann, R. Gläser, and O. Kolditz, “Multi-physical continuum models of thermochemical heat storage and transformation in porous media and powder beds—A review,” *Appl. Energy*, vol. 178, pp. 323–345, 2016.
- [32] Q. Li, G. Flamant, X. Yuan, P. Neveu, and L. Luo, “Compact heat exchangers: A review and future applications for a new generation of high temperature solar receivers,” *Renew.*
-

-
- Sustain. Energy Rev.*, vol. 15, no. 9, pp. 4855–4875, 2011.
- [33] Z. Luo, C. Wang, G. Xiao, M. Ni, and K. Cen, “Simulation and experimental study on honeycomb-ceramic thermal energy storage for solar thermal systems,” *Appl. Therm. Eng.*, vol. 73, no. 1, pp. 622–628, 2014.
- [34] F. Schaube, A. Wörner, and R. Tamme, “High temperature thermochemical heat storage for concentrated solar power using gas-solid reactions,” *J. Sol. Energy Eng. Trans. ASME*, vol. 133, no. 3, pp. 1–7, 2011.
- [35] L. Luo, *Heat and Mass Transfer Intensification and Shape Optimization. A Multi-scale Approach*. Springer, 2013.
- [36] M. Raju and S. Kumar, “Modeling of a Helical Coil Heat Exchanger for Sodium Alanate Based On-board Hydrogen Storage System,” *Sci. York*, no. January 2010, pp. 1–8, 2010.
- [37] A. M. Jacobi and R. K. Shah, “Heat transfer surface enhancement through the use of longitudinal vortices: A review of recent progress,” *Exp. Therm. Fluid Sci.*, vol. 11, no. 3, pp. 295–309, 1995.
- [38] L. Zhang, E. Hihara, F. Matsuoka, and C. Dang, “Experimental analysis of mass transfer in adiabatic structured packing dehumidifier/regenerator with liquid desiccant,” *Int. J. Heat Mass Transf.*, vol. 53, no. 13–14, pp. 2856–2863, 2010.
- [39] Y. Cadavid, A. Amell, and F. Cadavid, “Heat transfer model in recuperative compact heat exchanger type honeycomb: Experimental and numerical analysis,” *Appl. Therm. Eng.*, vol. 57, no. 1–2, pp. 50–56, 2013.
- [40] L. Zheng, D. Wu, B. Pan, Y. Wang, and B. Sun, “Experimental investigation and numerical simulation of heat-transfer properties of metallic honeycomb core structure up to 900 C,” *Appl. Therm. Eng.*, vol. 60, no. 1–2, pp. 379–386, 2013.
- [41] A. F. Lele, “A Thermochemical Heat Storage System for Households: Thermal Transfers Coupled to Chemical Reaction Investigations,” 2015.
- [42] V. Goetz and A. Marty, “A model for reversible solid-gas reactions submitted to
-

-
- temperature and pressure constraints: simulation of the rate of reaction in solid-gas reactor used as chemical heat pump,” *Chem. Eng. Sci.*, vol. 47, no. 17–18, pp. 4445–4454, 1992.
- [43] K. Castets and N. Mazet, “Optimization of the reactor configuration on the performance of the cyclic working mode of thermochemical transformers reactor miniaturization,” *Energy*, vol. 26, no. 3, pp. 271–286, 2001.
- [44] H.-B. Lu, N. Mazet, and B. Spinner, “Modelling of gas-solid reaction—Coupling of heat and mass transfer with chemical reaction,” *Chem. Eng. Sci.*, vol. 51, no. 15, pp. 3829–3845, 1996.
- [45] L. Hui-Bo, N. Mazet, O. Coudeville, and S. Mauran, “Comparison of a general model with a simplified approach for the transformation of solid-gas media used in chemical heat transformers,” *Chem. Eng. Sci.*, vol. 52, no. 2, pp. 311–327, 1997.
- [46] H. B. Lu and N. Mazet, “Mass-transfer parameters in gas-solid reactive media to identify permeability of IMPEX,” *AIChE J.*, vol. 45, no. 11, pp. 2444–2453, 1999.
- [47] N. Mazet and H. B. Lu, “Improving the performance of the reactor under unfavourable operating conditions of low pressure,” *Appl. Therm. Eng.*, vol. 18, no. 9–10, pp. 819–835, 1998.
- [48] K. Castets and N. Mazet, “Analysis and optimization of the cyclic working mode of thermochemical transformers,” *Appl. Therm. Eng.*, vol. 20, no. 17, pp. 1649–1666, 2000.
- [49] S. Dutour, N. Mazet, J. L. Joly, and V. Platel, “Modeling of heat and mass transfer coupling with gas-solid reaction in a sorption heat pump cooled by a two-phase closed thermosyphon,” *Chem. Eng. Sci.*, vol. 60, no. 15, pp. 4093–4104, 2005.
-

2 Chapter II: Methodology

2.1 System and reactor

As mentioned in the introduction, the goal of the project “Neutrons for Heat Storage” was to develop a cost-effective and compact thermochemical heat storage system for low-grade waste heat recovery. The first system and reactor prototypes were modelled before the actual start of the project. A simple modelling was performed by a postdoctoral researcher Stefano Soprani under the supervision of a senior researcher Didier Blanchard. The chosen system was of the closed type, and the reactor was of the integrated and indirect type. Taking into account the advantages of honeycomb heat exchanger over helical coil and plate-fin heat exchangers (see Introduction), the former was used. Figure 1 presents the schematic and the photograph of the system as well as the schematic of the reactor.

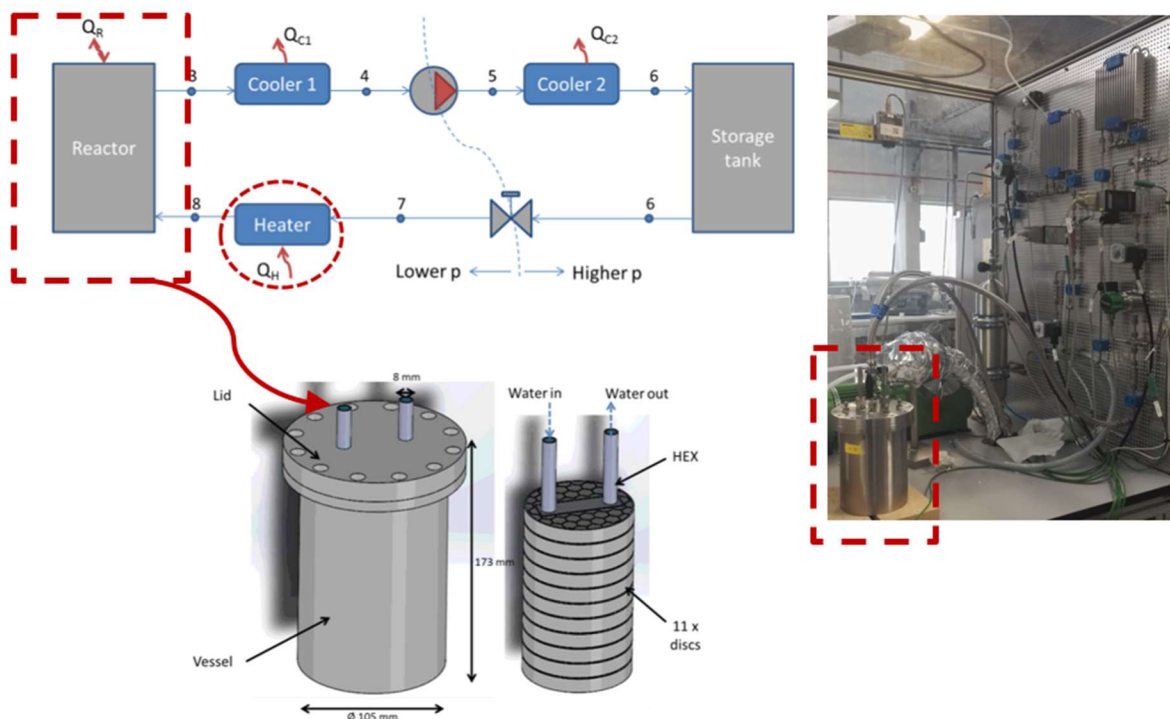


Figure 1. The system and reactor prototypes. The dashed red rectangle highlights the thermochemical reactor.

The reactor consisted of a stainless steel vessel, a U-shape tube with a heat transfer fluid (water, in this case), and 11 stainless steel honeycomb discs of 10 cm in diameter and 1 cm in height, with solid SrCl_2 powder embedded in their hexagon slots. Ammonia (NH_3) was chosen as a sorbent. The capacity of the system was estimated at 0.25 kWh.

Due to the lack of manpower, time constraints because of the laboratory relocation and collision with the COVID 19 lockdown, this TCHS system has been just commissioned and experimental data will be soon collected.

The presented reactor design and the materials served as a starting point of this PhD project. In order to optimize the reactor, one has first to obtain a good understanding of the processes occurring inside the reactor, and for this, a validated numerical model is required. There are two conventional methods of model validation. The first one is to compare model results to a reference solution published in literature. This method is not quite reliable, since commercial closed-source software can contain mistakes and user error cannot be excluded [1]. The other one is to validate a model against experimental data, which can be divided into local and global. Local data, like temperature readings, provides information about the state of the reaction at specific points, and global data, like flowmeter readings, gives an overall idea about the processes in a thermochemical reactor. Combining the two types of data gives a more complete picture of the phenomena happening inside the reactor; however, crucial information on the behavior of the reaction front is still overlooked, and the comparison between the model and the experiment is incomplete. Thus, we introduce neutron radiography, never used before for the purpose of model validation of such system. Neutron radiography is an imaging method, which gives an opportunity to follow spatio-temporal evolution of hydrogen and hence hydrogen-bearing molecules, e.g. NH_3 , at every point of the reactor. This owes to the fact that the attenuation coefficient for neutrons in hydrogen is significantly larger than in other elements, in contrast to X-rays, for which hydrogen is invisible. In addition, unlike X-rays, neutrons have high penetration power that makes it possible to study materials in bulk.

Since exposing the whole reactor prototype (see Figure 1) to neutron beam could not be achieved due to limited field of view at existing neutron instruments and the thick sample leading to low

transmission of neutron beam and therefore long exposure time, a half honeycomb disc was selected as a basic element that represents the system (see Figure 2).

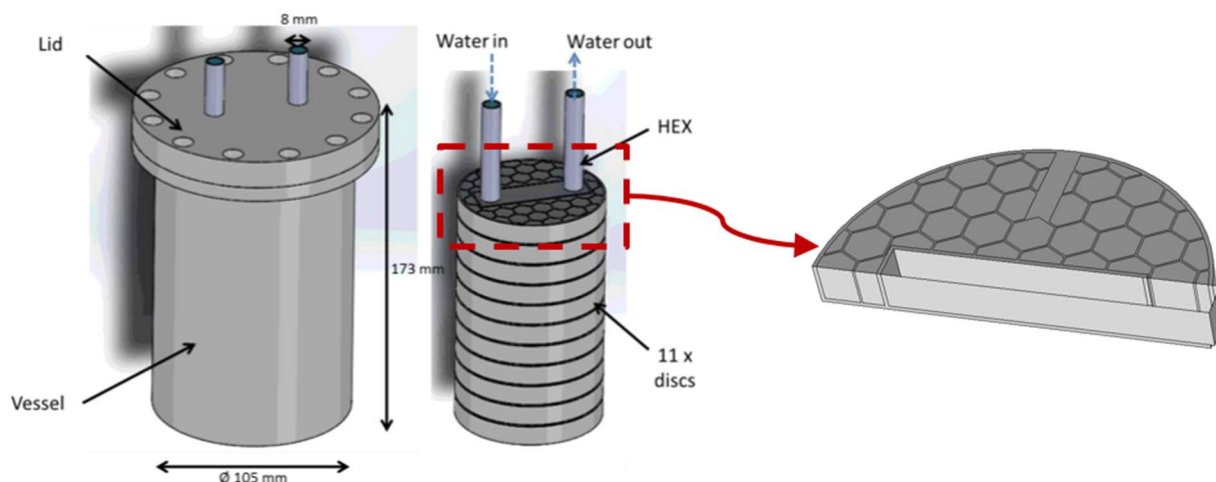


Figure 2. Reactor prototype and half honeycomb disc (basic element).

This representative element was inserted into an aluminum cell, a smaller reactor prototype, which we used during neutron imaging experiments. Hereinafter, reactor prototype or reactor will refer to this cell containing the half honeycomb disc. Besides the honeycomb element, with solid SrCl_2 powder embedded in its hexagonal slots, the reactor also included a heating element for desorption experiments. The schematic of the reactor prototype is presented in Chapter IV and Chapter V.

2.2 Working pair $\text{SrCl}_2\text{-NH}_3$

2.2.1 Basic principles of the sorption reactions

The expression that describes the complete reaction between gaseous ammonia (NH_3) and solid salt strontium chloride (SrCl_2) is:



where *s* and *g* refer to solid and gaseous state, respectively; ΔH is the enthalpy of the reaction.

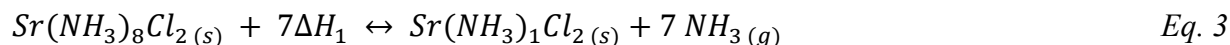
The equilibrium of the reaction is dependent on the pressure at which the reaction occurs. Absorption (\rightarrow) will occur, if the reaction pressure is higher than the equilibrium pressure p_{eq} , while desorption will occur (\leftarrow), if the reaction pressure is below p_{eq} .

The equilibrium pressure is dependent on the temperature and can be calculated through the Van't Hoff equation:

$$p_{eq} = p_0 e^{-\frac{\Delta H}{RT} + \frac{\Delta S}{R}} \quad \text{Eq. 2}$$

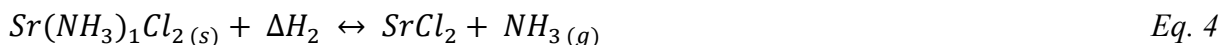
where p_0 is a reference pressure equal to 1 Pa, ΔH is the reaction enthalpy, ΔS is the reaction entropy, R is the ideal gas constant (8.314 J mole⁻¹ K⁻¹), and T is the temperature of the salt.

Desorption of NH₃ from SrCl₂ octaammine (Sr(NH₃)₈Cl₂) occurs in two steps. During the first step, one mole of Sr(NH₃)₈Cl₂ converts into one mole of SrCl₂ monoamine (Sr(NH₃)₁Cl₂), releasing 7 mole of NH₃:



where ΔH_1 is the enthalpy of the first desorption step.

Given the pressure of 1 bar, the reaction occurs at around 37-40°C. With further increase in the salt temperature, the last mole of NH₃ is desorbed in the vicinity of 130°C [2], resulting in the deammoniated salt:



where ΔH_2 is the enthalpy of the second desorption step.

As the enthalpy and entropy of the two reactions are different, different equilibrium pressure curves can be observed. For example, as reported in the study of Lysgaard *et al.* [3], the enthalpy and entropy of Eq. 3 are respectively 41.4 kJ (mole NH₃)⁻¹ and ~230 J mole⁻¹ K⁻¹. The last equivalent ammine (from Sr (NH₃)₁Cl₂ to SrCl₂) is characterized with the following values of the thermodynamic properties - 48.1 kJ (mole NH₃)⁻¹ and ~230 J mole⁻¹ K⁻¹ [3]. The equilibrium curves of the two reactions are presented in Figure 3.

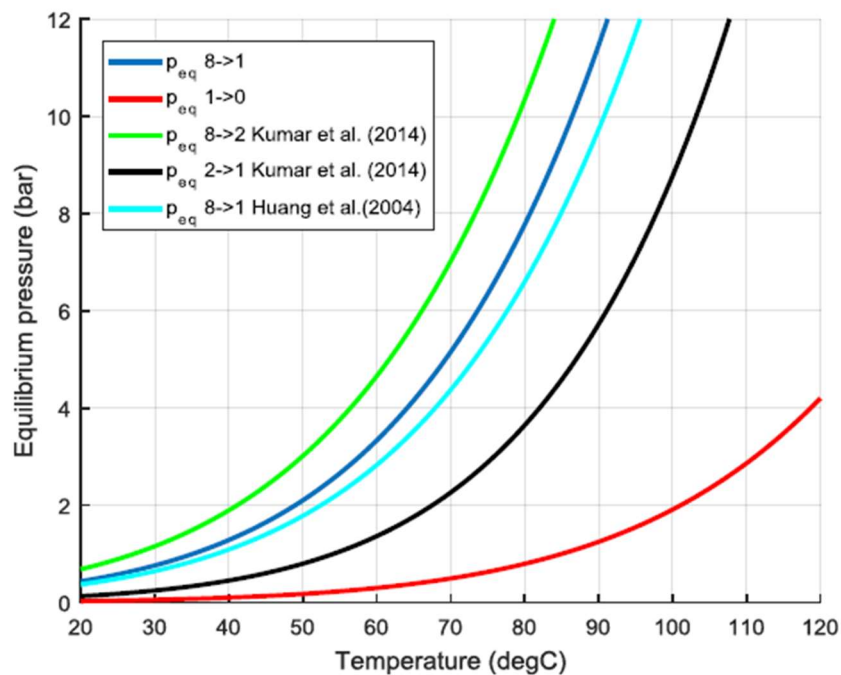


Figure 3. Representation of the equilibrium pressure trend vs. temperature, for different desorption mechanisms. Both calculated p_{eq} and trends from the literature are illustrated. Kumar et al. (2014) and Huang et al. (2004) are [4] and [5], respectively. Figure is taken from [6].

It can be noticed that the equilibrium pressure trend calculated with the data from [3] for the first seven moles of NH_3 (dark blue line in Figure 3) approximates well other trends reported in literature.

The equilibrium pressure for the last mole of NH_3 (red line in Figure 3), on the other hand, appears to be much lower than the one for the first seven. That means that, given certain desorption temperature, a significantly lower bed pressure is required to desorb the last ammine, compared to the first seven. Given a certain bed pressure, instead, a significantly higher bed temperature is necessary.

This makes the last mole of NH_3 more difficult and energy consuming to extract. This is even more relevant, if the TES system is designed for medium-low temperature heat sources (80-100 °C), as the salt bed would require desorption pressures below one bar. For these reasons, only the reaction with the first seven NH_3 moles (see Eq. 3) was considered in this work.

It is worth noting that several studies reported about the existence of SrCl_2 diamine for specific temperature-pressure conditions [3]; however, it will not be considered in the present work.

2.2.2 Structural changes during cycling

During NH_3 cycling, i.e. NH_3 absorption and desorption into and from SrCl_2 ammines, the crystal structure of the solid salt changes, as shown in Figure 4.

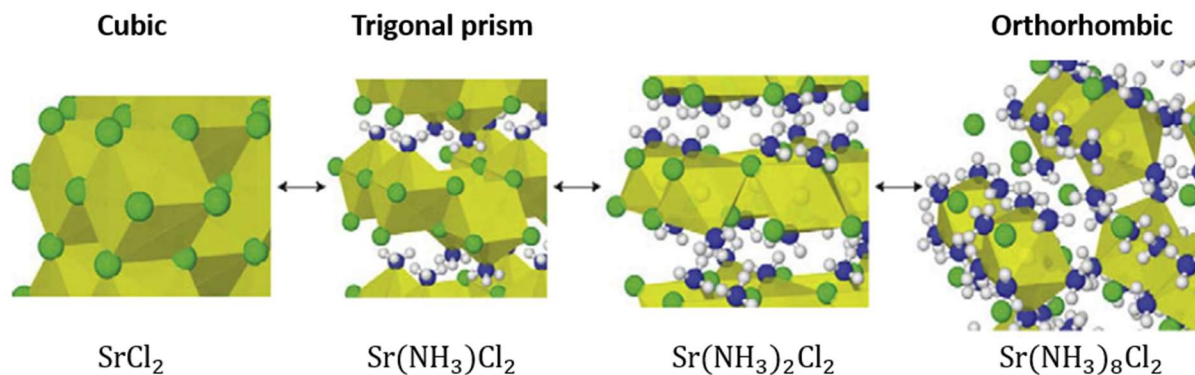


Figure 4. The structural changes of SrCl_2 ammines calculated with Density Functional Theory.

Figure is taken from [3].

During absorption, the crystal structure of the solid salt expands, while the opposite process of shrinking happens during desorption (see Figure 4). It can be also seen in the change of the crystallographic, or true, density of $\text{Sr}(\text{NH}_3)_x\text{Cl}_2$, where x varies between 0 and 8. For example, the density of SrCl_2 , $\text{Sr}(\text{NH}_3)_3\text{Cl}_2$, and $\text{Sr}(\text{NH}_3)_8\text{Cl}_2$ is 3108, 2440, and 1380 kg m^{-3} .

Thus, during the very first cycles, with the swelling and subsequent shrinking of the powder, a skeletal aggregate structure made of the salt particles appears [7]. This process is schematically presented in Figure 5.

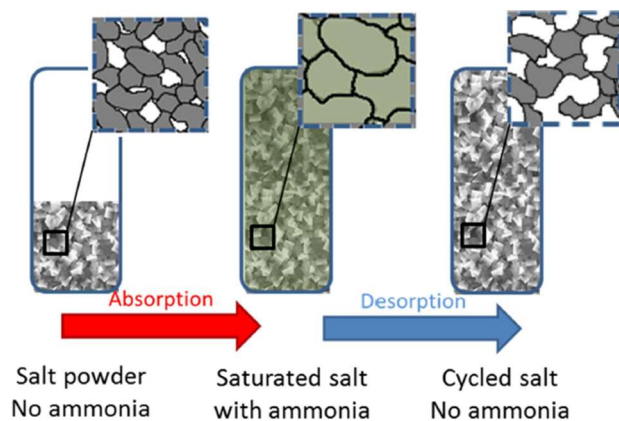


Figure 5. Schematic description of the formation of porous structure in the reactive bed.

Besides the development of the microporous structure, Jacobsen *et al.* [7] reported the formation of nanopores inside the salt particles during NH_3 desorption. These porous structures are advantageous for the ammonia diffusion in the powder beds, but detrimental to the heat conductivity.

2.2.3 Composite materials

The low heat conductivity of the reactive bed and agglomeration of the salt particles during NH_3 absorption limit the efficiency of the reactor and hence the whole system. To overcome these problems, research efforts to synthesize composite materials made of porous heat conductive matrix impregnated with particles of metal halide have been made. One of the candidates for a host matrix material is expanded natural graphite (ENG) [8]–[11]. Thanks to its high thermal conductivity and good gas permeability, it has been widely used for the intensification of heat and mass transfer within the reactive bed in thermochemical heat storage systems. In our work, we have also synthesized SrCl_2 -ENG composite material using impregnation method. The procedure of the material preparation is described in Chapter III.

2.3 Neutron imaging

Neutron imaging is a technique to visualize the interior structure of an object using its attenuation properties. Unlike in scattering experiments, where the information is obtained in reciprocal space and is averaged over the volume illuminated, in imaging experiments the data is derived in real

space. Among the methods of neutron imaging, one can distinguish between neutron radiography and neutron tomography. Neutron radiography results in two-dimensional (2D) images of the beam transmitted through the sample, while neutron tomography gives an opportunity to reconstruct a three-dimensional (3D) image of the object by combining multiple 2D images. In the present section, we will be focusing on the description of neutron radiography, since we have mainly used this technique. The neutron radiography data used in this research were collected at two instruments – NeXT at ILL (Grenoble, France) and NECTAR at FRM II (Munich, Germany). The technical data of these two instruments will serve as an example of the technique.

2.3.1 Basics of neutron imaging

The basic principle of neutron radiography is presented in Figure 6.

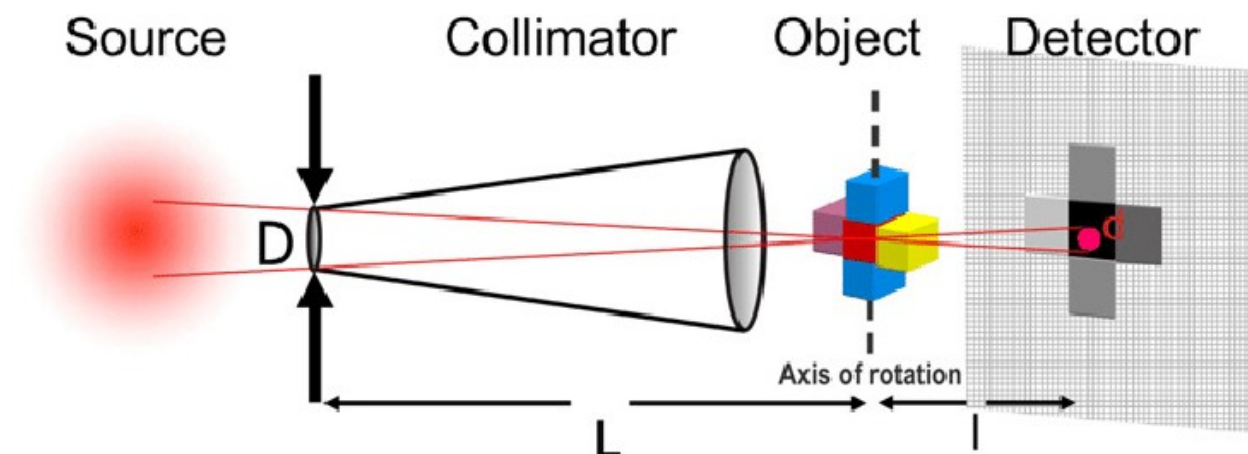


Figure 6. Typical geometry of a neutron imaging instrument. Figure is taken from [12].

The neutron beam generated by a source gets narrowed by a pinhole of the diameter D and a pinhole-sample distance of the length L . The collimated beam hits a sample and passes through it in accordance with the attenuation properties. The neutrons, which have passed through the sample, travel the distance l and are collected by a detector. Thus, four steps could be distinguished in a neutron radiography experiment, which are source, collimation, sample, and detector.

2.3.1.1 Source

Depending on how neutrons are produced, one can differentiate between two types of neutron sources: reactors and spallation sources. In the first case, neutrons are produced from chain reaction, interaction between neutrons and fissile isotopes (such as ^{235}U), whereas in the second case neutrons are generated from the collision of accelerated protons with a target consisting of material with heavy nuclei. Reactor sources are usually continuous (except pulsed reactor source at IBR-2, Dubna, Russia), while spallation sources typically produce pulsed neutron beam (except pseudo-continuous source at SINQ, Villigen, Switzerland). In modern instruments, neutron flux, i.e. neutrons per centimeter squared per second, measured at sample position varies between 10^6 and $10^9 \text{ cm}^{-2}\text{s}^{-1}$, and the neutron wavelength characterizing the energy of the beam ranges from one to 10 \AA [12]. Depending on the kinetic energy, neutrons are classified as presented in Table 1.

Table 1. Neutrons classification according to their kinetic energy. Table is taken from [13].

Neutrons	Energy range	Wavelength (Å)	Velocity
Ultra cold	$\leq 300 \text{ neV}$	≥ 500	≤ 8
Very cold	$300 \text{ neV} - 0.12 \text{ meV}$	$52.2 - 26.1$	$7.5 - 152$
Cold	$0.12 \text{ meV} - 12 \text{ meV}$	$26.1 - 2.6$	$152 - 1515$
Thermal	$12 \text{ meV} - 100 \text{ meV}$	$2.6 - 0.9$	$1515 - 4374$
Epithermal	$100 \text{ meV} - 1\text{eV}$	$0.9 - 0.28$	$4374 - 13.8 \cdot 10^3$
Intermediate	$1\text{eV} - 0.8\text{MeV}$		
Fast	$> 0.8\text{MeV}$		

The energy, wavelength, and velocity of neutron are interconnected and can be calculated with the following equations:

$$E_k = \frac{mv^2}{2} \quad \text{Eq. 5}$$

$$E_k = \frac{h^2}{2m} \cdot \frac{1}{\lambda^2} \quad \text{Eq. 6}$$

where E_k is neutron kinetic energy; m is the mass of neutron, $1.6749 \times 10^{-27} \text{ kg}$; v is neutron velocity; h is the Planck constant, $6.62607004 \times 10^{-34} \text{ m}^2 \text{ kg s}^{-1}$; λ is neutron wavelength.

For neutron imaging, thermal and cold neutrons are preferred due to their favorable detection reactions and due to their very useful contrast behavior.

At NECTAR, the neutron flux varies from 8.7×10^5 to 4.7×10^7 $\text{cm}^{-2}\text{s}^{-1}$ (depending on filter used), with a wavelength distribution centered at 1.81 Å [14]. The instrument is located at the neutron source FRM II, a beam tube reactor. The instrument NeXT, has a flux of around 2×10^8 $\text{cm}^{-2}\text{s}^{-1}$ (with L/D 400) with a spectrum of maximum intensity at 2.8 Å [15]. The instrument is located at the reactor neutron source Institute Laue-Langevin (ILL) in Grenoble, France, which provides one of the most intense neutron fluxes in the world.

2.3.1.2 Collimation

In order to narrow the neutron beam, meaning to make the directions of neutrons motion more aligned in specific direction, a pinhole of the diameter D , at a distance L from the sample, is used, giving a slightly convergent beam. This collimation is characterized with the ratio L/D . The collimation ratio restricts the spatial resolution as described further, in ‘Spatial and temporal resolution’. In modern instruments, the collimation ratio varies between several hundreds to thousands.

At NeXT instrument, the beam is collimated by pinholes of diameter from 30 to 1.5 mm, and with pinhole-sample distance of 10 m it gives collimation ratio in the range from 333 to 6667 [16]. During our experiment at NeXT, the results of which are reported in Chapter V, the pinhole diameter was 23 mm, resulting in a collimation ratio of 435. For comparison, at NECTAR, a less collimated beam was used with a collimation ratio substantially lower, $L/D \leq 233 \pm 16$ (depending on collimator) [17].

2.3.1.3 Sample

The intensity of the beam transmitted through the sample I can be calculated with the Beer-Lambert law:

$$I = I_0 e^{-\mu \cdot d} \tag{Eq. 7}$$

where I_0 is the incident neutron intensity, d the thickness of the sample, μ is the total linear attenuation coefficient of the sample. From Eq. 7, the transmission of the sample, $\frac{I}{I_0}$, can be derived.

The total attenuation is the sum of the absorption and scattering attenuation coefficients:

$$\mu = \mu_a + \mu_s \tag{Eq. 8}$$

where μ_a and μ_s are the absorption and scattering linear attenuation coefficients, respectively.

The linear attenuation coefficient of the sample can be calculated as follows:

$$\mu = \frac{\rho \cdot N_a}{M} \sigma = \frac{\rho \cdot N_a}{M} \cdot (\sigma_a + \sigma_s) \quad \text{Eq. 9}$$

where ρ is the sample apparent density (the porosity included), N_a is Avogadro's number, σ is the total cross section of the sample, M is the sample molar mass, and σ_a and σ_s are the absorption and scattering cross sections of the sample, respectively.

Figure 7 depicts absorption and scattering mass attenuation coefficients $\frac{\mu_a}{\rho}$ and $\frac{\mu_s}{\rho}$ depending on atomic number. For comparison, X-ray attenuation coefficients are also presented in the same graph.

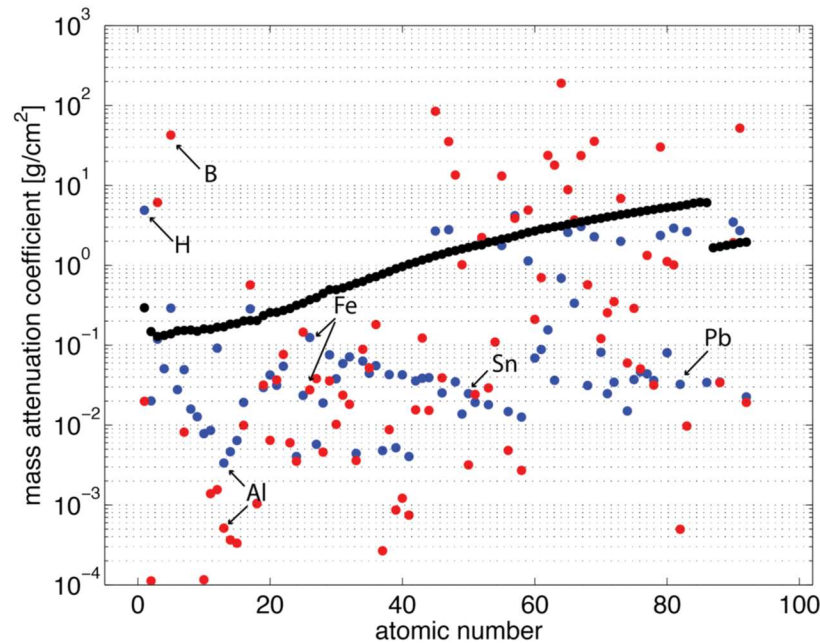


Figure 7. Absorption (red) and scattering (blue) coefficients for thermal neutrons with energy 25 meV, compared to the attenuation coefficient for X-rays with energy 100 keV (black). Figure is taken from [18].

As it can be observed from Figure 7, there is no dependency between atomic number and attenuation coefficients for neutrons, as in case of X-rays. Indeed, neutrons and X-rays interact

with matter differently. Neutrons interact with the atoms nuclei, whereas X-rays - with electrons. With the decrease in atomic number, and hence electron density, the ability of the atom in attenuating X-rays will deteriorate; however, it is not the case for neutrons. For example, the lightest element, hydrogen, has the lowest attenuation coefficient for X-rays but the highest scattering attenuation coefficient for neutrons indicating that hydrogen atoms are transparent to X-rays, but ‘highly visible’ in neutron radiography images. This characteristic of hydrogen-neutron interaction gives a possibility to study systems containing hydrogen, and in particular ammonia-based systems.

Quantitative analysis of radiography data can provide information on the sample composition, e.g. hydrogen content in case of ammonia-based systems. This analysis is performed using the simple exponential attenuation law, as shown in Eq. 7, given the thickness d of the sample is known. However, thick or strongly scattering samples show a deviation due to multiple scattering effect. In the present work, this effect was neglected in Chapter IV, but taken into account in Chapter V.

2.3.1.4 Detection

Figure 8 presents the basic principle of the detector, where a scintillator screen is coupled with a CCD (charge-couple-device) camera.

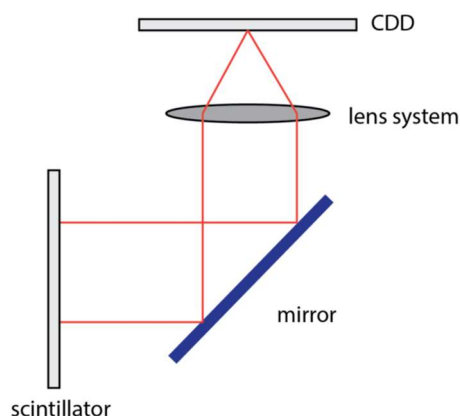


Figure 8. Schematic illustration of the scintillator screen coupled to a CCD camera. Figure is taken from [19].

The function of the scintillator is to absorb neutrons transmitted through the sample and convert them into light, which could be detected by a CCD camera. Since some of the neutrons impinging

on the scintillator screen may transmit through it, the CCD camera is not placed directly behind the scintillator screen, but instead a mirror reflecting the light through a lens system, as shown in Figure 8.

During the NeXT experiment, the sample was mounted in front of a Gadox scintillator screen with a field of view of 10 cm x 10 cm and a thickness of 50 μm . The scintillated light was captured by a CMOS camera (Hamamatsu Orca 4V2). At NECTAR, the transmitted neutron beam was converted into light by a 40 cm \times 40 cm scintillator screen $^6\text{LiF/ZnS}$. The light was then reflected by a mirror in a light-tight box and captured by CCD camera (Andor iKon-L-BV) with a 2048 \times 2048 pixels resolution.

2.3.2 Spatial and temporal resolution

There are two main criteria to be considered prior to performing a neutron imaging experiment the spatial and temporal resolutions. Spatial, or geometrical, resolution refers to the size of the smallest feature possible to resolve. Temporal resolution is an important parameter in kinetic studies because it is associated with the acquisition time, which is the total time to acquire one image. Acquisition time includes exposure time, image processing time, and sleeping time of the camera. The spatial and temporal resolutions are interdependent and are influenced by the source, the collimation, and the detector (see Figure 6).

2.3.2.1 The spatial resolution

The formula to determine the geometrical resolution can be derived from Figure 6 using trigonometry:

$$d = l \cdot (L/D)^{-1} \tag{Eq. 10}$$

where L/D is the collimation ratio and l the sample to detector distance . With higher collimation ratio, i.e. the lower divergence of the beam, the better the spatial resolution can be achieved for a given sample-detector distance l . For getting better spatial resolution, the sample-detector distance has to be as short as possible.

In addition to the collimation ratio and l , the spatial resolution also depends on the pixel size of the detection system. For example, it cannot be better than double the pixel size, as one neutron can be detected by two adjacent pixels.

2.3.2.2 Temporal resolution

For determining the required acquisition time, one has to take into account the signal-to-noise ratio described with the following formula:

$$\sigma(N) = \frac{N}{\sqrt{N}} \quad \text{Eq. 11}$$

where N is the number of counts in one pixel. Based on Eq. 11, to get higher signal-to-noise ratio one has to increase the number of counts in a single pixel by changing the following parameters:

1. Available neutron flux. The higher the intensity of the incident neutron beam, the higher the signal-to-noise ratio.
2. Collimation ratio. The decrease in the collimation ratio either by increasing the pinhole diameter or decreasing the detector-sample distance results in the magnification of the neutron flux and hence in the increase of the signal-to-noise ratio. This implies that the temporal and spatial resolutions are interdependent.
3. The attenuation properties of the sample.
4. The detector efficiency.
5. Additional detection noise, meaning dark current and read-out noise.

2.4 Modelling

Designing a thermochemical heat storage (TCHS) system requires a good knowledge of the transport phenomena (heat and mass exchange) occurring within the reactive bed. In case of TCHS system, the reactive bed is represented by a porous medium, a body consisting of a solid sorbent and micro- and nanopores filled with a gaseous sorbate. Recent studies in the field, at laboratory and prototype levels, formed the basis for further investigations of the phenomena, and several studies revealed a great interest in studying solid-gas reactions with the aim to optimize the work of the reactor and hence the system [20]–[26].

As already mentioned, the processes happening inside the reactive bed are mass-dependent phenomena, implying the heat and mass transfer. The dependence of these phenomena on mass lies in the fact that their effect on the overall reaction rate (how fast the overall reaction proceeds) is related to the size of the reactive bed. The larger is the reactive bed, the higher is the impact. In addition, the transfer properties are dependent on the material preparation, which includes its structure (size and shape of solid particles, size and shape of the pores inside the particles, material texture) as well as its compactness (porosity). Besides the heat and mass transfer, the rate of the chemical reaction has its impact on the overall reaction rate. The kinetic parameters constituting the reaction rate equation do not depend on the sample mass. In the following, a short description of each physics is given.

2.4.1 Heat transfer

Heat transfer can be realized through three mechanisms: convection, conduction, and radiation. Results of study conducted by Olives *et al.* [27] showed that thermal radiation can be neglected for TCHS systems with working temperature range between 10 and 90°C. In the work of Michel [28], it was reported that for TCHS systems, the effect from the convection is much smaller compared to the conduction and therefore can be neglected. Thus, the heat transfer in our system is represented by conduction defined by Fourier's law. The differential form of Fourier's law shows that the local heat flux density, \mathbf{q} , is a the product of thermal conductivity, k , and the negative local temperature gradient, $-\nabla T$:

$$\mathbf{q} = -k\nabla T \tag{Eq. 12}$$

The units of \mathbf{q} , k , ∇T are W m^{-2} , $\text{W m}^{-1} \text{K}^{-1}$, K m^{-1} . The heat flux density is defined as the amount of energy that flows through a unit area per unit time.

Thermal conductivity is a thermal property of the material, reflecting its intrinsic ability to conduct heat. The value of thermal conductivity tells us how much heat the material can conduct from one plate to another, if the distance between the plates is 1 m and the temperature difference is 1 K. The thermal conductivity of a porous medium is called effective thermal conductivity, which mainly depends on the thermal conductivities of the solid and the gas, the porosity, and the temperature.

Besides thermal conductivity, another important thermal parameter to mention is specific heat capacity. Specific heat capacity is determined as the amount of heat (J) that should be transferred to 1 kg of the material in order to cause an increase of 1 K in its temperature. Therefore, the standard units of the specific heat capacity is $\text{J kg}^{-1} \text{K}^{-1}$. The amount of thermal energy stored or released by the material with the change in the temperature can be calculated as follows:

$$Q = mc_p\Delta T \quad \text{Eq. 13}$$

The presence of heat exchanger in the reactor, performing the function of a heat conductor between the reactive bed and heat transfer fluid (or external source), includes another characteristics, which is heat transfer coefficient, h . Heat transfer coefficient can be calculated with the following equation:

$$h = \frac{q}{\Delta T} \quad \text{Eq. 14}$$

where q is a heat flux with the units of W m^{-2} , defined as a thermal power per unit contact area between the reactive bed and the heat exchanger; ΔT is the temperature difference between the reactive bed and the heat exchanger.

2.4.2 Mass transfer

The mass transfer in the TCHS systems is defined with the permeability of the reactive bed. Permeability is an important property of the porous medium that measures the capacity and ability of the reactive bed to transmit fluids [29]. The permeability of the reactive bed heavily depends on its porosity, and this correlation should be included in the modelling. There are different flow models that can describe the flow of fluid through a porous medium, among which are Darcy, Ergun, Forchheimer, turbulence models, etc. Depending on gas and pressure-temperature conditions used, the fluid behaviour can be described with compressible or incompressible equations of state, real or ideal gas laws [1].

2.4.3 Kinetics

The reaction rate, or the speed at which the sorption reaction takes place, can be generally described by the following equation [30]–[32]:

$$\frac{dx}{dt} = k_0 \cdot f(x) \cdot h(p) \cdot e^{-\frac{E_a}{RT}} \quad \text{Eq. 15}$$

where x is the reaction advancement varying between 0 and 1; t is time, in s; k_0 is a pre-exponential factor representing the frequency of collisions between reactant molecules at a standard concentration, in s^{-1} ; $f(x)$ is the function of the reaction model; $h(p)$ is the pressure function describing the dependency between the actual pressure in the system and the equilibrium pressure; E_a is the activation energy meaning the energy that must be provided to compounds to result in the chemical reaction, in $J \text{ mole}^{-1}$; R is the gas constant, in $J \text{ mole}^{-1} \text{ K}^{-1}$; T is the local temperature of the reactive bed, in K. A set of kinetic parameters and functions, namely k_0 , $f(x)$, $h(p)$, E_a , is called a kinetic tetrad.

2.4.3.1 Reaction models and pressure functions

There is a significant number of reaction models used in the solid-state kinetics, which could be divided into three main groups: accelerating, decelerating, and sigmoidal [30]. Accelerating models describe reactions, for which the rate increases continuously with the increase of the reaction advancement and reaches its maximum at the end of the reaction. This type of models is represented by power-law models:

$$f(x) = nx^{(n-1)/n} \quad \text{Eq. 16}$$

where n is a constant.

Opposite to accelerating models, decelerating models describe reactions, for which the rate decreases continuously with the increase in the reaction advancement and reaches its minimum at the end of the reaction. Models of this type can be represented by the reaction-order model:

$$f(x) = (1 - x)^n \quad \text{Eq. 17}$$

where n is the reaction order.

Sigmoidal models describe reactions, for which the rate reaches its maximum at some intermediate values of the reaction advancement. The most common example is the Avrami-Erofeev models:

$$f(x) = n(1 - x)[- \ln(1 - x)]^{(1-n)/n} \quad \text{Eq. 18}$$

Figure 9 presents reaction profiles, namely reaction advancement vs. time, for each type of models.

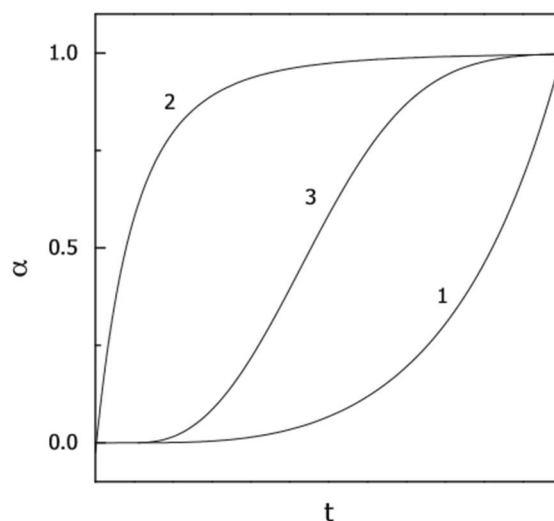


Figure 9. Reaction profiles for (1) accelerating, (2) decelerating, and (3) sigmoidal models.

Figure is taken from [30].

The type of the reaction model could be determined from the reaction profile taken at isothermal conditions. Some of the examples of the reaction models are presented in [30], [33].

Since pressure has a significant effect on the rate of solid-gas reactions, its effect must be included in the rate equation. The pressure function, $h(p)$, can be expressed in different mathematical forms, such as $(1-p/p_{eq})$ [34], [35], p/p_{eq} [36], $(1 - p/p_{eq})^n$ [37], $\ln(p/p_{eq})$ [34].

2.4.3.2 Kinetic measurements

In order to “solve” the kinetic tetrad, one has to obtain at least 3-5 reaction profiles [30] from sorption experiments. Prior to the start of the sorption experiments, there are three components of the experiments to optimize, which are the setup, the temperature program, and the sample. In the following, each of the components is described and their optimization is presented in Chapter III.

1. Setup.

There are several types of instruments that are used to obtain reaction profiles. The work of these instruments is based on the following techniques:

- Thermogravimetric analysis (TGA). When using this technique, one measures the mass of a sample over time as the temperature changes.
- Differential scanning calorimetry (DSC) is a technique in which the difference in the amount of heat required to increase the temperature of a sample is measured as a function of time.
- Differential thermal analysis (DTA). In this technique, the difference in temperature is measured as a function of time while the heat flow is kept constant.
- Barometric analysis using Sievert's type apparatus. When using this technique, one determine the change in gas pressure in a calibrated volume over time during sorption reaction.

2. Temperature program.

Profiles of heat driven reactions can be taken either by isothermal or nonisothermal measurements. The most common nonisothermal program is when a reference (e.g., furnace) temperature changes at a constant heating rate. Both isothermal and constant heating rate experiments have advantages and disadvantages, which are presented in Table 2.

Table 2. Pros and cons of isothermal and constant heating rate tests.

Type of experiment	Pros	Cons
Isothermal	<ul style="list-style-type: none"> - A type of a reaction model can be easily determined from a kinetic curve retrieved at isothermal conditions. Three reaction model types are presented in Figure 9. - A constant systematic error in temperature will affect the values of activation energy and pre-exponential factor insignificantly. 	<ul style="list-style-type: none"> - In the beginning of the measurement, some time (usually, a few minutes) is required to heat up the sample so that it reaches the reference temperature. - Limited temperature range because at lower temperatures it may be difficult to reach complete conversion over a reasonable time period but at high temperatures the heat-up time becomes comparable with the characteristic time of the process.
Constant heating rate	<ul style="list-style-type: none"> - There is no problem of heat-up time. 	<ul style="list-style-type: none"> - At least one isothermal run in addition to series of constant heating rates runs is required for selecting a proper reaction model. - A systematic error in a heating rate has a dramatic effect on an error in activation energy and pre-exponential factor; hence, the temperature calibration is required at every heating rate used in the measurements.

3. Sample

When looking at solid-gas reactions, e.g. the absorption and desorption of ammonia into / from SrCl₂ ammines (see Figure 10), one can distinguish four different processes occurring in the reactor:

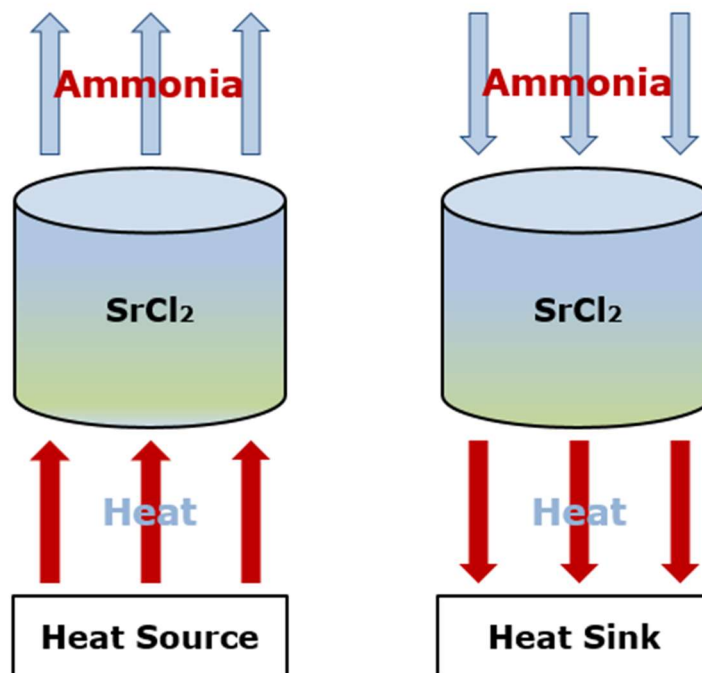


Figure 10. Schematic illustration of ammonia absorption and desorption into / from SrCl_2 .

1. Ammonia diffusion in the porous structure of the salt;
2. Heat transfer within the porous medium;
3. Heat transfer between the reaction medium and the heat source/sink.
4. Chemical reaction.

All the mentioned above processes contribute to the overall reaction rate to some extent. Figure 11 shows the weight of each of the four processes during sorption experiments for the determination of the apparent kinetics (a) and intrinsic kinetics (b).

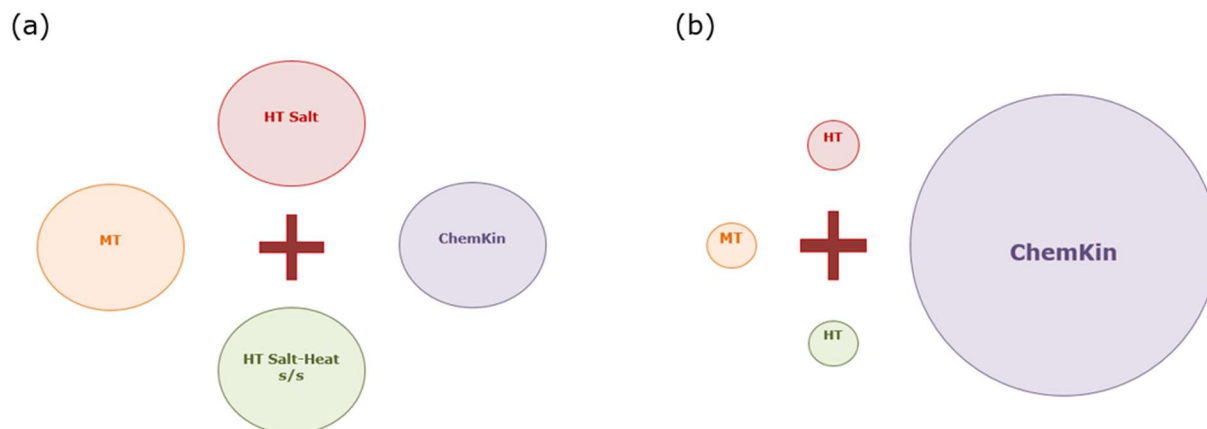


Figure 11. Contribution of four processes during gas-solid reaction for the determination of (a) apparent kinetics and (b) intrinsic kinetics. *MT* – mass transfer, *HT Salt* – heat transport within the porous reaction medium (salt), *HT Salt-Heat s/s* – heat transfer between the salt and the heat source/sink, *ChemKin* – chemical kinetics.

To determine the intrinsic kinetic parameters of the rate equation (*ChemKin* in Figure 11), one should eliminate the contribution from the heat and mass transfer processes. In practice, their complete removal is hard to reach, but the minimization of these factors, as shown in Figure 11(b), allows obtaining close-to-intrinsic kinetic parameters. In the following parts, the measures, which can be implemented to reach the close-to-intrinsic kinetics, are listed.

Heat transfer within reaction medium

Heat transfer within the reaction medium will have a profound impact on the reaction rate if the effective thermal conductivity, which is the thermal conductivity of the reaction medium including pores, is small. Low effective thermal conductivity leads to substantial self-heating/cooling of the reaction medium, and hence, deviation from the isothermal conditions, which in turn badly affects the kinetics measurements. Therefore, to intensify the heat transfer within the reaction medium, the thermal conductivity must be increased. There are two ways of doing so:

1. Decreasing the porosity.

With the increase of porosity, meaning the fraction of the volume of voids over the total volume, the heat transfer within porous reaction medium becomes limited. For example, highly porous

materials, like Styrofoam, are known for their exceptional insulation properties. This is because the thermal conductivity of gases is considerably lower when compared to the thermal conductivity of solids. On the contrary, low porosity supports the enhancement of heat conducting properties.

2. Increasing the thermal conductivity of the solid material.

This is especially applicable to the materials with low thermal conductivity, for example SrCl_2 , which thermal conductivity is below $1 \text{ W m}^{-1} \text{ K}^{-1}$ [38].

Mass transfer

In opposite to heat transfer, the decrease of the sample porosity makes mass transfer difficult. For instance, in accordance to the Carman-Kozeny equation, permeability, which is referred to the ability of a gas to penetrate through the porous medium, is proportional to the porosity of the sample [39]:

$$\kappa = \frac{\varepsilon^3}{180(1-\varepsilon)^2} d_p^2 \quad \text{Eq. 19}$$

where κ is the permeability, ε is the porosity, and d_p is the particle diameter.

Therefore, for the intensification of the mass transfer, higher porosity has to be provided.

Thus, speaking of porosity, it should have an optimal value to balance heat and mass transfer. One of the solutions in this case is to insert the particles of the active material, the salt, into a highly porous and heat conductive matrix. In our study, such a support material was expanded natural graphite (ENG).

Moreover, the contribution of the heat and mass transfer depends on the mass of the material used in the experiment, whereas the chemical reaction rate is an intrinsic characteristic of the material and does not depend on the sample mass. Given the same pressure-temperature conditions, the reaction should be equally fast for 1 milligram and 1 kilogram of the material, if there is no influence of the mass-dependent processes. In reality, due to the heat and mass transfer limitations, the reaction will be much faster for the lower mass. Therefore, to measure the close-to-intrinsic kinetics, one should minimize the impact of the heat and mass transfer processes by minimizing the sample mass within instrumental error. To find a compromise, one should determine a so-called “optimal mass”.

Heat transfer between the salt and the heat source/sink

Another parameter influencing the kinetics of the reaction is the heat transfer between the sample and the heat source/sink. When the two solid surfaces are in direct contact, surface roughness introduces gaps between them, which are filled with the gas (NH_3). This leads to the decrease in the conduction heat flux, resulting in decreased heat transfer coefficient.

2.4.4 Modelling in COMSOL Multiphysics 5.5

The listed above physics were modelled in COMSOL Multiphysics environment (version 5.5). COMSOL Multiphysics software is a powerful tool utilizing finite element method (FEM) for solving partial differential equations (PDEs). FEM is a numerical technique used to perform finite element analysis (FEA) of physical phenomena. The basic concept of FEM can be defined as splitting the computational domain (geometry) into small individual regions and finding local solutions that satisfy the PDEs within the boundaries of these regions [40].

COMSOL software contains add-on modules with already in-built equations. In our work, we have used the following modules: Heat Transfer in Porous Media, Free and Porous Media Flow, and Domain ODEs and DAEs to insert the reaction rate equation. PDEs for each physics and boundary conditions are listed in Chapter IV, Paper IV. The choice for the spatio-temporal discretization elements is also described there.

References

- [1] T. Nagel, S. Beckert, C. Lehmann, R. Gläser, and O. Kolditz, “Multi-physical continuum models of thermochemical heat storage and transformation in porous media and powder beds—A review,” *Appl. Energy*, vol. 178, pp. 323–345, 2016.
- [2] A. Bialy, P. B. Jensen, D. Blanchard, T. Vegge, and U. J. Quaade, “Solid solution barium-strontium chlorides with tunable ammonia desorption properties and superior storage capacity,” *J. Solid State Chem.*, vol. 221, pp. 32–36, 2015.
- [3] S. Lysgaard, A. L. Ammitzbøll, R. E. Johnsen, P. Norby, U. J. Quaade, and T. Vegge, “Resolving the stability and structure of strontium chloride amines from equilibrium pressures, XRD and DFT,” *Int. J. Hydrogen Energy*, vol. 37, no. 24, pp. 18927–18936, 2012.
- [4] S. Bacl, “Thermodynamic Analysis and Comparison for ‘COP’ In Solid Adsorption Refrigeration Systems ($\text{BaCl}_2\text{-NH}_3$ & $\text{SrCl}_2\text{-NH}_3$),” vol. 5, no. 3, pp. 444–450, 2014.
- [5] H. J. Huang, G. Bin Wu, J. Yang, Y. C. Dai, W. K. Yuan, and H. B. Lu, “Modeling of gas-solid chemisorption in chemical heat pumps,” *Sep. Purif. Technol.*, vol. 34, no. 1–3, pp. 191–200, 2004.
- [6] S. Soprani, “MODELING – TES system based on $\text{SrCl}_2 - \text{NH}_3$,” Roskilde, 2017.
- [7] H. S. Jacobsen *et al.*, “Nanoscale structural characterization of $\text{Mg}(\text{NH}_3)_6\text{Cl}_2$ during NH_3 desorption: An in situ small angle X-ray scattering study,” *Chem. Phys. Lett.*, vol. 441, no. 4–6, pp. 255–260, 2007.
- [8] M. M. Druske *et al.*, “Developed materials for thermal energy storage: Synthesis and characterization,” *Energy Procedia*, vol. 61, pp. 96–99, 2014.
- [9] S. Mauran, P. Prades, and F. L’Haridon, “Heat and mass transfer in consolidated reacting beds for thermochemical systems,” *Heat Recover. Syst. CHP*, vol. 13, no. 4, pp. 315–319, 1993.
- [10] L. Jiang, L. W. Wang, Z. Q. Jin, R. Z. Wang, and Y. J. Dai, “Effective thermal conductivity and permeability of compact compound ammoniated salts in the

- adsorption/desorption process,” *Int. J. Therm. Sci.*, 2013.
- [11] L. Jiang, R. Z. Wang, Y. J. Lu, A. P. Roskilly, L. W. Wang, and K. Tang, “Enquête sur l’utilisation de chlorure de strontium composite conducteur thermique innovant pour les machines de refroidissement à sorption à l’ammoniac,” *Int. J. Refrig.*, vol. 85, pp. 157–166, 2018.
- [12] M. Strobl, I. Manke, N. Kardjilov, A. Hilger, M. Dawson, and J. Banhart, “Advances in neutron radiography and tomography,” *J. Phys. D. Appl. Phys.*, vol. 42, no. 24, 2009.
- [13] “Neutron Physics.” [Online]. Available: <https://www.psi.ch/en/niag/neutron-physics>. [Accessed: 12-Sep-2020].
- [14] J. M. Campillo-Robles *et al.*, “Monitoring lead-acid battery function using operando neutron radiography,” *J. Power Sources*, vol. 438, no. April, p. 226976, 2019.
- [15] A. Tengattini *et al.*, “NeXT-Grenoble, the Neutron and X-ray tomograph in Grenoble,” *Nucl. Instruments Methods Phys. Res. Sect. A Accel. Spectrometers, Detect. Assoc. Equip.*, vol. 968, no. March, p. 163939, 2020.
- [16] “The neutron source.” [Online]. Available: <https://next-grenoble.fr/workinprogress/D50/>. [Accessed: 12-Sep-2020].
- [17] “MEDAPP & NECTAR.” [Online]. Available: <https://mlz-garching.de/medapp-nectar>. [Accessed: 12-Sep-2020].
- [18] “What is Neutron Imaging ?” [Online]. Available: <http://www.psi.ch/niag/what-is-neutron-imaging>. [Accessed: 12-Sep-2020].
- [19] K. Lefmann, J. Kirkensgaard, L. Arleth, B. Lebech, M. Strobl, and E. S. Source, “Neutron Scattering : and Simulation,” 2017.
- [20] Y. Azoumah, N. Mazet, and P. Neveu, “Constructal network for heat and mass transfer in a solid-gas reactive porous medium,” *Int. J. Heat Mass Transf.*, vol. 47, no. 14–16, pp. 2961–2970, 2004.
- [21] M. Ghommem, G. Balasubramanian, M. R. Hajj, W. P. Wong, J. A. Tomlin, and I. K.

-
- Puri, "Release of stored thermochemical energy from dehydrated salts," *Int. J. Heat Mass Transf.*, vol. 54, no. 23–24, pp. 4856–4863, 2011.
- [22] H. Ishitobi, K. Uruma, M. Takeuchi, J. Ryu, and Y. Kato, "Dehydration and hydration behavior of metal-salt-modified materials for chemical heat pumps," *Appl. Therm. Eng.*, vol. 50, no. 2, pp. 1639–1644, 2013.
- [23] H. Lahmidi, S. Mauran, and V. Goetz, "Definition, test and simulation of a thermochemical storage process adapted to solar thermal systems," *Sol. Energy*, vol. 80, no. 7, pp. 883–893, 2006.
- [24] H.-B. Lu, N. Mazet, and B. Spinner, "Modelling of gas-solid reaction—Coupling of heat and mass transfer with chemical reaction," *Chem. Eng. Sci.*, vol. 51, no. 15, pp. 3829–3845, 1996.
- [25] N. Mazet, M. Amouroux, and B. Spinner, "Analysis and experimental study of the transformation of a non-isothermal solid/gas reacting medium," *Chem. Eng. Commun.*, vol. 99, no. 1, pp. 155–174, 1991.
- [26] P. Neveu, S. Tescari, D. Aussel, and N. Mazet, "Combined constructal and exergy optimization of thermochemical reactors for high temperature heat storage," *Energy Convers. Manag.*, vol. 71, pp. 186–198, 2013.
- [27] R. Olives and S. Mauran, "A highly conductive porous medium for solid-gas reactions: Effect of the dispersed phase on the thermal tortuosity," *Transp. Porous Media*, vol. 43, no. 2, pp. 377–394, 2001.
- [28] B. Michel, "Procédé thermochimique pour le stockage intersaisonnier de l' énergie solaire : modélisation multi-échelles et expérimentation d' un prototype sous air humide," *Thesis*, p. 259, 2012.
- [29] G. Wałowski, "Assessment of gas permeability coefficient of porous materials," *J. Sustain. Min.*, vol. 16, no. 2, pp. 55–65, 2017.
- [30] S. Vyazovkin, A. K. Burnham, J. M. Criado, L. A. Pérez-Maqueda, C. Popescu, and N. Sbirrazzuoli, "ICTAC Kinetics Committee recommendations for performing kinetic
-

-
- computations on thermal analysis data,” *Thermochim. Acta*, vol. 520, no. 1–2, pp. 1–19, 2011.
- [31] M. Lebrun and B. Spinner, “Models of heat and mass transfers in solid-gas reactors used as chemical heat pumps,” *Chem. Eng. Sci.*, vol. 45, no. 7, pp. 1743–1753, 1990.
- [32] A. Fopah Lele, “A Thermochemical Heat Storage System for Households - Combined Investigations of Thermal Transfers Coupled to Chemical Reactions,” p. 202, 2016.
- [33] Q. Li, K. C. Chou, Q. Lin, L. J. Jiang, and F. Zhan, “Hydrogen absorption and desorption kinetics of Ag-Mg-Ni alloys,” *Int. J. Hydrogen Energy*, vol. 29, no. 8, pp. 843–849, 2004.
- [34] A. Chaise, P. De Rango, P. Marty, and D. Fruchart, “Experimental and numerical study of a magnesium hydride tank,” *Int. J. Hydrogen Energy*, vol. 35, no. 12, pp. 6311–6322, 2010.
- [35] S. S. Jahromy *et al.*, “Impact of partial pressure, conversion, and temperature on the oxidation reaction kinetics of Cu_2O to CuO in thermochemical energy storage,” *Energies*, vol. 12, no. 3, 2019.
- [36] M. Gaeini, S. A. Shaik, and C. C. M. Rindt, “Characterization of potassium carbonate salt hydrate for thermochemical energy storage in buildings,” *Energy Build.*, vol. 196, pp. 178–193, 2019.
- [37] R. Iwata, T. Yamauchi, Y. Hirota, M. Aoki, and T. Shimazu, “Reaction kinetics of ammonia absorption/desorption of metal salts,” *Appl. Therm. Eng.*, vol. 72, no. 2, pp. 244–249, 2014.
- [38] L. Jiang and A. P. Roskilly, “Thermal conductivity, permeability and reaction characteristic enhancement of ammonia solid sorbents: A review,” *Int. J. Heat Mass Transf.*, vol. 130, pp. 1206–1225, 2019.
- [39] F. J. Valdes-parada, J. A. Ochoa-tapia, and J. Alvarez-ramirez, “Validity of the permeability Carman – Kozeny equation : A volume averaging approach,” *Physica A*, vol. 388, no. 6, pp. 789–798, 2009.
-

[40] K. Wahyu, “Finite Element Method II” pp. 1–6, 2018.

3 Chapter III: Characterization of Parameters Governing the Reaction Rate

When designing a thermochemical reactor, one has to take into account three processes occurring within the reactive bed: the rate of chemical reaction, the heat transfer and the mass transfer. To build a numerical model of the reactor, one has to treat the three aforementioned phenomena independently to be able to assess their individual contribution to the overall sorption kinetic rate and hence to the reactor performance. The heat and mass transfer is characterized by the reactive bed properties (thermal conductivity, specific heat capacity, and mass diffusivity), and the chemical reaction is defined using the reaction rate equation. While the heat and mass transfer properties have to reflect the ability of the reactive bed to transfer and accumulate heat and to pass sorbate, the reaction rate equation should represent the dependency of the rate on the temperature of the solid sorbent, the pressure of the gas (sorbate), and the degree of the reaction progression with the kinetic parameters.

While the heat and mass transfer properties of SrCl_2 amines have been studied and reported in literature by several researchers, knowledge about the kinetic parameters of the working pair $\text{SrCl}_2\text{-NH}_3$ is missing. Indeed, the published kinetic parameters include the effect from the heat and mass transfer, meaning that they are dependent on the preparation of the reactive bed. Therefore, with the work presented in this chapter, we have defined a procedure for the determination of the intrinsic kinetic parameters of a solid-gas reaction and used $\text{SrCl}_2 - \text{NH}_3$ working pair as a study case. A distinctive feature of the used procedure is that the kinetic measurements were performed on a Sieverts type apparatus using isothermal heating programs, which allows resolving the common problem of heat-up time. In addition, instead of pure SrCl_2 salt, we used an “optimal” mass of solid SrCl_2 impregnated in a porous heat conductive matrix of expanded natural graphite, ensuring that the chemical reaction rate is not constrained by heat and mass transfer limitations. With such an approach, we obtained new absorption and desorption rate equations, which were shown to predict the experimental data over a wide pressure-temperature range. Afterwards, the obtained equations, as well as the ones found in literature, were implemented in a numerical model developed for the simulation of NH_3 sorption into SrCl_2 . In contrast to the literature parameters, the numerical results using the intrinsic equations were found

to be in a good agreement with the experimental results, confirming the importance of using intrinsic kinetic parameters in the modelling of solid-gas sorption process. As a result, besides the development of the procedure for defining close-to-intrinsic kinetic parameters of a solid-gas reaction, we have determined the kinetic parameters for SrCl₂ ammines, which can be used for modelling regardless the material preparation (mass and porosity) and reactor design.

This study resulted in a scientific paper submitted to the journal of Applied Thermal Engineering.

3.1 Paper I: Importance of Using Intrinsic Kinetics in Modeling Thermochemical Heat Storage System: SrCl₂-NH₃ Case Study

Anastasiia Karabanova¹, Perizat Berdiyeva², Michel van der Pal³, Rune E. Johnsen¹, Stefano Deledda², Didier Blanchard^{1*}

¹*Department of Energy Conversion and Storage, Technical University of Denmark, 2800 Kgs. Lyngby, Denmark;*

²*Department for Neutron Materials Characterization, Institute for Energy Technology, 2027 Kjeller, Norway;*

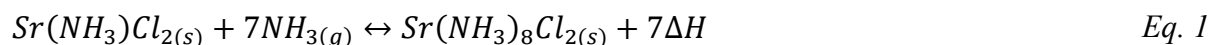
³*TNO Energy Transition, 1755 LE Petten, The Netherlands.*

3.1.1 Abstract

In the present study, intrinsic kinetic parameters of the sorption processes between ammonia (NH₃) and strontium chloride ammines Sr(NH₃)_zCl₂, where z varies between 1 and 8, were experimentally determined. Experimental data was collected on a Sieverts type apparatus using isothermal heating programs over a wide pressure-temperature range. During the kinetic experiments, the influence of heat and mass transfer limitations was minimized by impregnating SrCl₂ into the porous heat conductive matrix of expanded natural graphite (ENG). Using an optimal mass of the composite material, the close-to-intrinsic kinetic equations for absorption and desorption were obtained and found to predict the experimental data, from which these parameters were computed. Furthermore, numerical simulations using the obtained kinetic equations were found to be in a good agreement with another set of experimental data, not included in the kinetic computations, in contrast to simulations performed with kinetic parameters found in literature. Indeed, the published kinetic parameters are dependent on the environment and preparation of the active material and include the influence of the heat and mass transfer. In contrast, the kinetic tetrads given herein are more universal in nature and may be used independently of the environment.

3.1.2 Introduction

Over the past decade, energy storage has been identified by the European Commission as a topic of utmost importance for the ongoing transformation of the European energy system. Specifically, thermal energy storage is expected to play an important role in increasing the overall efficiency of energy systems [1,2]. This is particularly true for systems producing waste heat at temperatures below 100°C, so-called low-grade heat, which according to recent studies accounts for more than 45% of the global primary energy consumption [3]. Large quantities of low-grade heat can be stored reversibly in solid strontium chloride (SrCl_2) upon exo-/endothermal ab-/desorption of gaseous ammonia (NH_3) according to Eq. 1:



Where ΔH is the reaction enthalpy equal to 41.432 kJ/mole of NH_3 [4]. With such a reaction enthalpy, SrCl_2 offers a high heat storage capacity, of 0.51 kWh/kg SrCl_2 or 1579 kWh/m³ at material level. Furthermore, it is environmentally benign, abundant and of relatively low cost, 2000-2500 \$/ton giving a final price of 3.9-4.9 \$/kWh.

The basic operation of a thermochemical heat storage (TCHS) system utilizing the reversible sorption processes between NH_3 and SrCl_2 is shown in Figure 1.

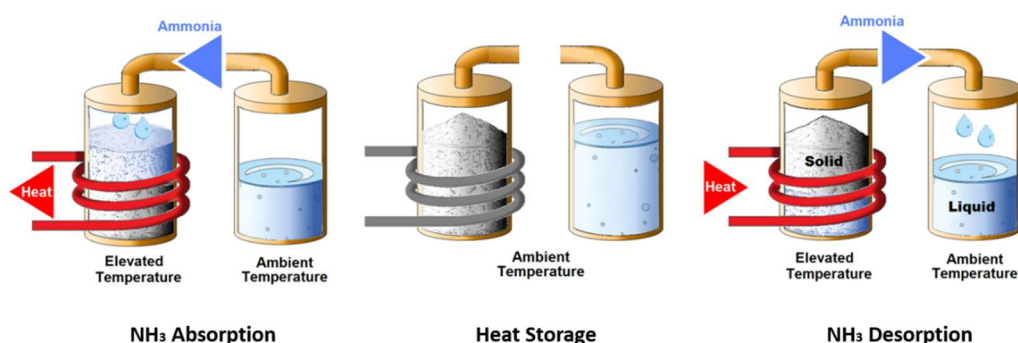


Figure 1. Sketch of a TCHS system operating in three working modes: NH_3 absorption, storage, and NH_3 desorption. The modes correspond to discharging, heat storage, and charging, respectively.

As shown in Figure 1, the TCHS system consists of two main vessels - a reactor containing SrCl_2 and a container enclosing liquefied NH_3 . In the storage mode, the connection between the two vessels is closed and the heat is stored for any period without losses. If the two vessels are connected, after expansion, gaseous NH_3 flows from the liquid NH_3 container into the reactor, where it gets absorbed by the salt and the heat of absorption is released. During charging, the molecules of NH_3 are detached from the salt by supplied heat and are condensed in the liquid NH_3 container. The system is considered to go through a full cycle upon the completion of two half-cycles, absorption and desorption.

Although the system is heat-driven, it has parasitic electricity use by ancillary equipment such as pumps and compressors, and to achieve the highest system performance it is of primary importance to accurately size these components. To achieve this, it is necessary to have a good understanding of the sorption processes taking place in the thermochemical reactor and determine the heat and mass flows. For such a task, a model describing the heat transfer, the diffusion of NH_3 , and the chemical reaction kinetics must be developed, and the accurate determination of the material parameters, including the kinetic parameters, is a prerequisite to obtain reliable simulations.

The kinetics of a chemical reaction can be described by a kinetic tetrad consisting of a pre-exponential factor, an activation energy, a reaction model, and a pressure impact model. The tetrad may be obtained for a material itself or for the material in a specific configuration. In the first case, the tetrad describes the intrinsic properties of the material, while in the second case the kinetic parameters describe the apparent properties, which include the effect of the heat and mass transfer and depend on the material volume, packing density, particle size etc. To develop a versatile simulation model giving the most accurate and reliable results it is required to apply the intrinsic kinetic parameters, since the use of the apparent tetrad may lead to wrong estimation of the reaction advancement, if the material packing and/or volume are modified.

In the literature, two studies reported the kinetic parameters of the reaction described by Eq. 1 [4,5]. In the work conducted by Huang *et al.* [7], the kinetic tests were performed on an IMPEX disk (150 mm in diameter and 100 mm in height) with a central hole of 8 mm in diameter. IMPEX is a composite material made of expanded natural graphite (ENG) and SrCl_2 . In the work carried out by Yuan *et al.* [8], the kinetics was also studied on a disc of the composite material made of

SrCl₂ and ENG. In this study, a disc of 52.5 mm in diameter with a central hole of 12 mm in diameter was used. Given the size of the samples used in both studies, it is clear that apparent rather than intrinsic kinetic parameters were found. The apparent kinetic parameters obtained in the two studies are different, which highlights that they are valid only for the specific material configurations. The knowledge of the apparent kinetics is sufficient for determining optimal pressure-temperature conditions in a given reactor filled with the material of given apparent density; however, it is insufficient when optimizing the reactor design and sizing the ancillary equipment as well as when predicting the impact of the material properties on the performance of the system. For such activity, accurate determination of the intrinsic or close-to-intrinsic kinetic parameters is essential. This statement was a motivation for the work presented herein, where the close-to-intrinsic kinetic parameters of the solid-gas reactions between the SrCl₂ ammines and NH₃ (Eq. 1) were determined. In addition, we compared results obtained from a developed numerical model, when using the obtained kinetics tetrads and the literature ones, with experimental data. Our findings confirmed the validity of our approach for determining the close-to-intrinsic kinetic parameters.

3.1.3 Materials and Methods

For determining the kinetic parameters of a sorption reaction, one has to obtain a series of reaction profiles, or, in other words, kinetic curves, which describe the dependence of the reaction advancement on time. Different types of techniques are commonly used to get kinetic curves: Thermo-Gravimetric Analysis (TGA), Differential Scanning Calorimetry (DSC), Differential Thermal Analysis (DTA), and volumetric analysis using a Sieverts type apparatus. Each of those techniques has advantages and disadvantages, and one should be aware of any limitations and precautions to take, to ensure reliable and accurate determination of the parameters of interest [9]. Together with the type of instrument, temperature program and sample preparation are the main components of the kinetics measurement to be optimized for obtaining reliable kinetic parameters.

In the present study, the kinetic parameters were determined using an in-house Sieverts type apparatus (see description below). In the apparatus, the temperature of the sample is measured by a thermocouple mounted at the bottom of the outer wall of the reactor, its tip being separated from the sample by 1 mm stainless steel wall. Such an instrument configuration, where the temperature

of the sample is measured indirectly, may lead to the systematic deviation between the thermocouple reading and the actual temperature of the sample, when carrying out constant heating rate experiments. As a result, this systematic error may have a profound effect on the values of obtained kinetic parameters. Therefore, in order to avoid this error, isothermal heating programs were selected, and sufficient time was given for the sample temperature to equilibrate before the start of any measurement.

The preparation of the sample and its mass also play an important role in obtaining accurate kinetic parameters, as these factors influence the rate at which heat and mass transfer occurs within the sample. To ensure that the transport processes have not biased the determination of the chemical reaction kinetics, they were intensified in this study, as described below.

3.1.3.1 Sieverts type apparatus

The operating principle of a Sieverts type apparatus is based on measuring the change in gas pressure in a calibrated volume during sorption processes. The principle diagram of the Sieverts apparatus used for performing the kinetics measurements is shown in Figure 2.

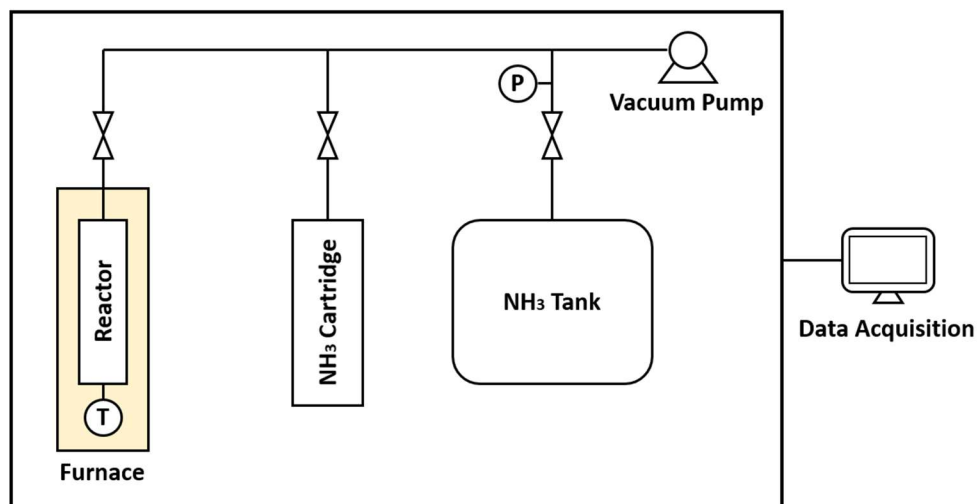


Figure 2. Schematic of the experimental setup used for the determination of the kinetic equations.

The setup mainly consists of a reactor embedded in a tubular furnace, an NH₃ cartridge, and an NH₃ tank. The three elements, connected to each other via gas lines, form a gas system of 4.86 l

total volume. The reactor, where the sample is placed, is a stainless steel tubular container of 10 mm in diameter and 30 mm in length with a wall thickness of 1 mm. The NH_3 cartridge filled with 132 g of ammoniated SrCl_2 serves as an NH_3 source to pressurize the system. The pressure is measured with a pressure transducer. The temperature of the sample is measured with a K-type thermocouple mounted at the bottom of the reactor. For the purpose of evacuation, the system is connected to a vacuum pump.

One of the main advantages of using the Sieverts apparatus is that the reactor and the NH_3 tank can be separated by a valve, which allows keeping the two reservoirs at different pressures. This resolves the problem of heat-up time for isothermal measurements preventing unwanted absorption or desorption during the heating of the sample up to the temperature chosen for the kinetic measurements.

Absorption mode

First, the sample was placed in the reactor, and the reactor closed tightly. These operations were performed in an argon glove box, where the level of water does not exceed 0.1 ppm, to avoid any water absorption by hydrophilic SrCl_2 . Then, the reactor was connected to the rest of the Sieverts apparatus, and all volumes, except the NH_3 cartridge, were evacuated for one hour using the vacuum pump. The value of residual pressure in the system after 1 h under active vacuum was usually of 4.5 mbar. Then, the NH_3 tank was filled with gaseous NH_3 by heating the cartridge until the desired pressure was reached. During the filling of the system with NH_3 , the valve between the reactor and the rest of the system was kept closed to avoid NH_3 absorption by the sample. The heat required for keeping the sample at constant temperature was supplied by the furnace. To ensure that the temperature of the sample had a set value during the absorption, the reaction was initiated one hour after the temperature measured by the thermocouple had reached the programmed value. The kinetic measurement was started by opening the valve connecting the reactor to the rest of the system and stopped with the stabilization of the pressure in the system. It has been shown that during the first absorption the morphology of the salt changes [10] and thus the absorption kinetics. For this reason, each sample was subjected to at least one NH_3 absorption and desorption prior to the kinetic measurement.

Desorption mode

In principle, the desorption measurements followed the absorption ones; therefore, the sample was already placed in the Sieverts apparatus as described above. Before the start of the desorption test, the temperature of the sample should reach the desired value; however, the rise in temperature may cause anticipatory decomposition of the ammoniated salt. Therefore, to avoid NH_3 desorption the pressure in the reactor was maintained above equilibrium pressure. Equilibrium pressure was determined using the Van't Hoff equation:

$$p_{eq} = p_0 e^{-\frac{\Delta H}{RT} + \frac{\Delta S}{R}} \quad \text{Eq. 2}$$

where p_0 is a reference pressure equal to 1 Pa; ΔH and ΔS are the reaction enthalpy and entropy equal to 41.432 kJ/mole of NH_3 and 228.6 J/(K · mole of NH_3), respectively [4]; R is the gas constant; and T is the temperature of the sample.

Once the sample temperature has stabilized (dwell of 1 h), the desorption was started by opening the valve between the reactor and the rest of the system. Desorption was finished when the pressure in the system got stable.

3.1.3.2 Composite material preparation and its characteristics

To ensure the determination of the close-to-intrinsic kinetic parameters, i.e. parameters independent of the sample configuration and environment, one should maximally eliminate the factors limiting NH_3 diffusion as well as heat transfer within the sample. Among these factors are: 1) low thermal conductivity of the sample; 2) low permeability of the sample; 3) large sample mass.

Recent studies have shown that inserting metal halides, and in particular SrCl_2 , into a porous heat conductive matrix of expanded natural graphite (ENG) allows intensifying heat and mass transfer within the reactive bed significantly [11]. Therefore, in this study SrCl_2 was impregnated into ENG. ENG boards (apparent density 75 kg/m³) were supplied by SGL carbon, and SrCl_2 (purity >98%) was delivered by Amminex, an industrial partner of the project. First, ENG pellets of 10 cm³ in volume dehydrated at 120°C for 8 h were immersed into ethanol for two hours to decrease the surface tension between non-polar ENG and polar water-based SrCl_2 solution. Then, the

samples were placed in SrCl₂ solution (33.3 % wt.) for two hours, after which they were dried in a ventilated oven at 90°C for 12 hours for the removal of the water. After that, the samples were further dried in a vacuum furnace at 300°C for 12 hours to eliminate the water absorbed by the crystals of the salt. It is worth to mention that after the impregnation and drying the volume of the samples decreased by 52%. The synthesized material has the following characteristics: the mass content of SrCl₂ is 55 %wt.; apparent density is 350 kg/m³.

The mass of the impregnated sample used herein, labelled as optimal mass in the following, was identified as the maximum mass to acquire unbiased and accurate kinetic tetrads, which are maximally independent of the effect from the heat and mass transfer and give readout numbers well above the instrumental noise. To determine the optimal mass, a series of kinetic experiments was performed at same pressure-temperature conditions using samples of various mass until the reaction profiles coincide. Such a sample mass independency analysis has been reported in several papers [12]–[14] for different metal halides.

3.1.3.3 Determination of the kinetic parameters

The equation of a solid-gas reaction kinetics is generally expressed as follows:

$$\frac{dx}{dt} = k \cdot f(x) \quad \text{Eq. 3}$$

where x is the reaction advancement at time t ; k is a rate constant; $f(x)$ is a function determining the reaction model.

The rate constant is a function of the salt temperature T and NH₃ pressure p over the sample and can be expressed as follows:

$$k = k_0 \cdot h(p) \cdot e^{-\frac{E_a}{RT}} \quad \text{Eq. 4}$$

where k_0 is a pre-exponential factor; E_a is an activation energy of the reaction; $h(p)$ is a pressure impact function expressing the degree of the discrepancy between the actual gas pressure in the system p and the equilibrium gas pressure over the salt p_{eq} (see Eq. 2).

Combining Eq. 3 and Eq. 4 results in the expanded form of the kinetics equation:

$$\frac{dx}{dt} = k_0 \cdot f(x) \cdot h(p) \cdot e^{-\frac{E_a}{RT}} \quad \text{Eq. 5}$$

In order to determine the coefficients and functions of Eq. 5, the following procedure was applied:

1. First, Pressure-Time curves were obtained from two series of kinetic experiments carried out at constant pressure and temperature. While one of the series was to be performed at the same temperature but different pressures, the other set was taken at different temperatures but fixed pressure.
2. Obtained in (1) Pressure-Time curves were converted into Reaction advancement-Time curves using the following formula:

- For absorption

$$x = \frac{p_{beg} - p}{p_{beg} - p_{end}} \quad \text{Eq. 6}$$

where x is the reaction advancement at time t ; p_{beg} is the pressure at the beginning of the experiment; p is the pressure at time t ; p_{end} is the pressure at the end of the experiment, when it reaches a plateau.

- For desorption

$$x = \frac{p - p_{beg}}{p_{end} - p_{beg}} \quad \text{Eq. 7}$$

3. Reaction advancement derived in Eq. 6 and Eq. 7 was inserted in the reaction models presented in the work of Vyazovkin *et al.* [9]. The function $g(x)$ is the integral form of $f(x)$:

$$g(x) = \int \frac{dx}{f(x)} = kt \quad \text{Eq. 8}$$

According to Eq. 8, the dependence of $g(x)$ on time should result in a straight line. Therefore, among the models listed in [9], the one with the highest coefficient of determination (R^2) to a linear trend line was selected. The slope of the line revealed the rate of the reaction k .

4. For the series of the kinetics experiments taken at constant temperature, a graph illustrating the dependence between the pressure impact function $h(p)$ and the rate

constant k was plotted. Eq. 9 shows a mathematical formula of this graph derived from Eq. 4:

$$h(P) = \frac{e^{\frac{E_a}{RT}}}{k_0} \cdot k \quad \text{Eq. 9}$$

Since the measurements were taken at the same temperature, the coefficient before the argument $\frac{e^{\frac{E_a}{RT}}}{k_0}$ is constant, and hence the dependence $h(p)$ - k should be as linear as possible. This was the criterion for the selection of the power function, the general form of which is presented in Eq. 10.

$$h(P) = \pm \left(\frac{p - p_{eq}}{p_{eq}} \right)^n \quad \text{Eq. 10}$$

where “+” is for absorption and “-” for desorption; p_{eq} is the equilibrium NH_3 pressure over the salt at the given temperature of the salt T . Equilibrium pressure was calculated from the Van't Hoff equation (Eq. 2).

5. In order to determine the values of the pre-exponential factor and the activation energy, $\ln \frac{k}{h(p)}$ was plotted as a function of inverse temperature for the set of the experiments obtained at constant pressure. This dependence can be derived from Eq. 4 and be expressed as follows:

$$\ln k - \ln(h(P)) = \ln k_0 - \frac{E_a}{RT} \quad \text{Eq. 11}$$

Thus, the pre-exponential factor was calculated from the intercept between the linear trend line to the data and y-axis, and the activation energy was retrieved from the slope of the trend line.

6. The goodness of the obtained tetrads was evaluated by comparing the kinetic curves from the obtained model with the experimental kinetics curves, from which the tetrads had been computed.

3.1.3.4 Comparison of simulation results with experimental data

A numerical model of the sorption processes was developed, and the model results were compared with experimental data. As an input for the model, we used the kinetic tetrads determined herein and the ones published in the literature [4,5].

Experimental data

A series of absorption and desorption experiments was performed on 466 mg of SrCl₂ using Sieverts type apparatus. To ensure good heat transfer between the sample and the heat source/sink, the salt was tightly wrapped in a piece of aluminum foil. To let ammonia in, an opening of 1 cm in length was made in the aluminum foil using a paper cutter. A series of absorption experiments was performed at same pressure (4.5 bar) and various temperature (25, 30, and 35°C). For desorption, one set of measurements was performed at same pressure and various temperature (50, 55, and 60°C), and another one was conducted at same temperature (55°C) and different pressure (0.5, 1, and 1.5 bar). As a result, curves showing the change in the pressure over time were obtained. The curves were then converted into kinetics curves using Eq. 6 and Eq. 7 for absorption and desorption, respectively.

Model

In the numerical model, a porous medium containing the salt and gaseous NH₃ was represented by a cube of 1 cm³. The volume of the cube was selected based on the value of apparent density of SrCl₂ (466 kg/m³). An aluminum layer of 0.016 mm in thickness was placed around the cube to represent the aluminum foil used during the Sieverts experiments. NH₃ inlet/outlet was made by cutting off a block (1 cm in length, 0.016 mm in depth, and variable width d) from one of the sides of the cube. The temperature of the outer wall of the aluminum layer was set equal to the temperature used during the experiment.

The absorption model developed in this study couples the kinetics of the chemical reaction with the heat and mass transfer. In case of the desorption model, the calculation of NH₃ diffusion and convective heat transfer was not included; it resulted in slightly less accurate model but with significant gain in computational time for the given desorption conditions.

The equation governing heat transfer in the porous medium can be written as follows:

$$(\rho c_p)_{eff} \frac{\partial T}{\partial t} + \rho_{NH_3} C_{p NH_3} \mathbf{u} \cdot \nabla T + \nabla(-k_{eff} \nabla T) = Q \quad Eq. 12$$

where $(\rho c_p)_{eff}$ is the effective volumetric heat capacity of the porous medium; T the temperature; ρ_{NH_3} the density of NH₃ calculated using the ideal gas law; $C_{p NH_3}$ the specific heat capacity of

NH_3 ; \mathbf{u} the velocity vector of NH_3 ; k_{eff} the effective thermal conductivity of the porous medium; Q the heat released/absorbed during absorption/desorption. The heat Q can be calculated using the following formula:

$$Q = \pm \frac{dx}{dt} \cdot N_s \cdot \Delta H \quad \text{Eq. 13}$$

where “+” and “-” are used for absorption and desorption, respectively; $\frac{dx}{dt}$ is the reaction rate; N_s is the molar density of NH_3 ; ΔH is the reaction enthalpy.

The heat flux transferred from the aluminum foil to the porous salt was calculated as follows:

$$q = h_w(T_{Al} - T) \quad \text{Eq. 14}$$

where h_w is the heat transfer coefficient between the aluminum foil and the porous medium; T_{Al} the temperature of the aluminum foil equal to the temperature applied during the experiment. For the desorption model, the heat transfer coefficient was assumed to change linearly from 265 till 65 $\text{W/m}^2/\text{K}$. On average, it gives a value of 165 $\text{W/m}^2/\text{K}$, reported by Huang *et al.* [17]. The change in the heat transfer coefficient reflects the change in the volume of the salt and the decrease in the contact area between the salt and the aluminum foil [18]. For the absorption model, the heat transfer coefficient was assumed constant and equal to 165 $\text{W/m}^2/\text{K}$, as the absorption is not driven by temperature but pressure.

The effective properties of the porous medium were calculated as follows:

$$(\rho C_p)_{eff} = \varepsilon \cdot \rho_{\text{NH}_3} \cdot C_{p \text{NH}_3} + (1 - \varepsilon) \cdot \rho_{\text{salt}} \cdot C_{p \text{salt}} \quad \text{Eq. 15}$$

$$k_{eff} = \varepsilon \cdot k_{\text{NH}_3} + (1 - \varepsilon) \cdot k_{\text{salt}} \quad \text{Eq. 16}$$

where ε is the salt porosity; $C_{p \text{NH}_3}$ and k_{NH_3} the specific heat capacity and the thermal conductivity of NH_3 taken from the database of Engineering Equation Solver (EES 2016); ρ_{salt} , $C_{p \text{salt}}$, k_{salt} the density, the specific heat capacity, and the thermal conductivity of the salt. All the properties of the salt depend on the reaction advancement and are assumed to change linearly between ammoniated and non-ammoniated states. The properties of the salt in ammoniated and non-ammoniated states are presented in Table 1.

Table 1. Properties of $Sr(NH_3)Cl_2$ and $Sr(NH_3)_8Cl_2$ used in modeling.

Property	Units	$Sr(NH_3)Cl_2$	$Sr(NH_3)_8Cl_2$
Porosity	n.a.	0.79*	0.37*
Density	kg/m ³	1380*	2440*
Specific heat capacity	J/kg/K	$649.8 + 3.524 \cdot T + 0.0021 \cdot T^2 + 0.00016 \cdot T^3$ [15]	$576.296 + 3.124 \cdot T + 0.07 \cdot T^2 + 0.00005 \cdot T^3$ [15]
Thermal conductivity	W/m/K	0.75 [16]	0.75 [16]

*: calculated based on the data used in this study.

The diffusion of NH_3 in the porous medium was described with the following equations:

$$\frac{\partial \varepsilon \rho_{NH_3}}{\partial t} + \nabla \cdot (\rho_{NH_3} \mathbf{u}) = Q_m \quad Eq. 17$$

$$Q_m = \pm \frac{dx}{dt} \cdot N_s \cdot M_{NH_3} \quad Eq. 18$$

$$\rho \frac{\partial \mathbf{u}}{\partial t} = \nabla \cdot \left[-p \mathbf{I} + \frac{\mu}{\varepsilon} (\nabla \mathbf{u} + (\nabla \mathbf{u})^T) - \frac{2\mu}{3\varepsilon} (\nabla \cdot \mathbf{u}) \mathbf{I} \right] - \left(\frac{\mu_{NH_3}}{\kappa} + \beta_F |\mathbf{u}| + \frac{Q_m}{\varepsilon^2} \right) \mathbf{u} + \mathbf{F} \quad Eq. 19$$

where Q_m is the mass of NH_3 absorbed/released during absorption/desorption per time and the reactive bed volume; M_{NH_3} is the molar mass of NH_3 ; p is local NH_3 pressure; μ_{NH_3} is the dynamic viscosity of NH_3 ; κ is the hydraulic permeability of the salt layer; β_F is the Forcheimer drag factor. In this case, domain forces \mathbf{F} were neglected. The hydraulic permeability of the porous salt can be calculated through the Carman-Kozeny equation [19], approximating the salt particles as spherical:

$$\kappa = \frac{\varepsilon^3}{180(1-\varepsilon)^2} d_p^2 \quad Eq. 20$$

where d_p is the salt particle diameter, which was set to 100 nm.

Equations describing the kinetics of the sorption processes are presented in Table 2.

Table 2. Kinetics equations and their elements for absorption and desorption of NH_3 obtained in this study and found in literature.

Source	Parameter	Absorption	Desorption
This study	Equation	$\frac{dx}{dt} = k_0 e^{-\frac{E_a}{RT}} \cdot f(x) \cdot \left(\frac{p - p_{eq}}{p_{eq}}\right)^n$	$\frac{dx}{dt} = k_0 e^{-\frac{E_a}{RT}} \cdot f(x) \cdot \left(\frac{p_{eq} - p}{p_{eq}}\right)^n$
	Reported in Results and Discussions		
Huang <i>et al.</i> [5]	Equation	$\frac{dx}{dt} = k_0 e^{-\frac{E_a}{RT}} (1 - x)^M \frac{p - p_{eq}}{p_{eq}}$	$\frac{dx}{dt} = k_0 e^{-\frac{E_a}{RT}} (1 - x)^M \frac{p_{eq} - p}{p_{eq}}$
	k_0, s^{-1}	0.0190	0.125
	$E_a, \text{J/mole}$	6921	9000
	M	2.96	3.02
Yuan <i>et al.</i> [6]	Equation	$\frac{dx}{dt} = Ar(1 - x)^M \left(1 - \frac{p_{eq}}{p}\right)$	$\frac{dx}{dt} = (Ar + A \cdot T) \cdot x^M \cdot \left(1 - \frac{p_{eq}}{p}\right)$
	Ar	0.001631	0.02413 ($x > 0.8$) 0.0004598 ($x < 0.8$)
	A	-	-6.2×10^{-8} ($x > 0.8$)
	M	2.071	1.1

3.1.4 Results and Discussions

3.1.4.1 Determination of the optimal mass

To determine the salt optimal mass for the kinetics measurements, four samples of the composite material made of ENG and SrCl_2 were tested. The mass of SrCl_2 in the composite material samples were 61, 70, 146, and 186 mg. All the prepared samples were of cubic shape. The desorption tests were performed under 1 bar of NH_3 and 45°C , and during the absorption measurements the samples were subject to NH_3 pressure of 2.5 bar at 20°C . As a result, Pressure-Time curves were obtained and then converted into kinetics curves using Eq. 6 and Eq. 7. The kinetics curves are shown in Figure 3(a) and Figure 4(a), and their comparison to each other, absolute difference, is plotted as a function of time in Figure 3(b) and Figure 4(b), respectively.

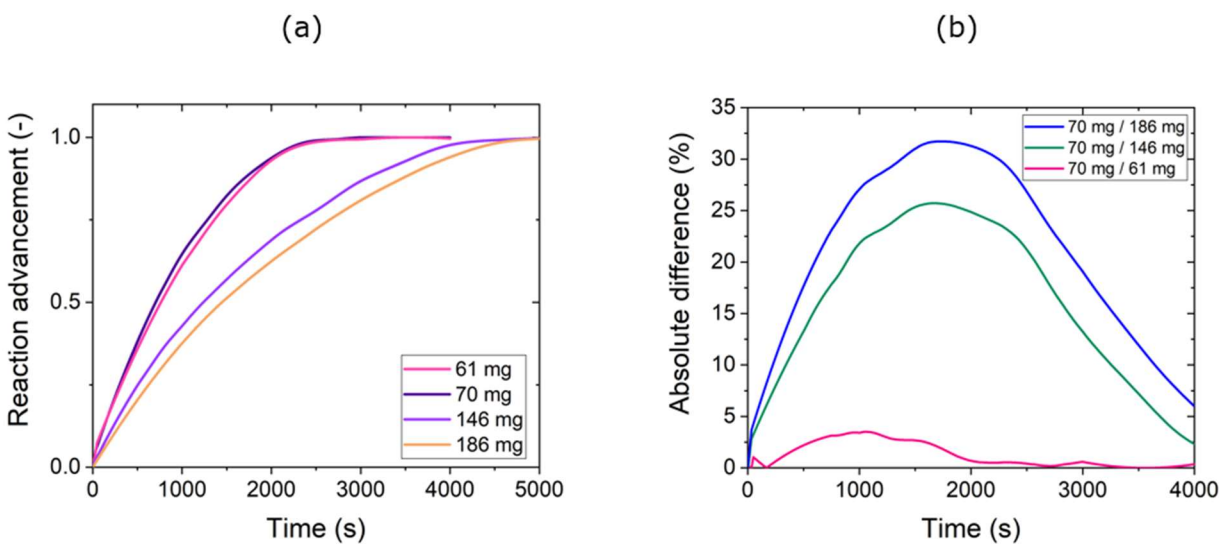


Figure 3. Determination of the optimal mass for desorption kinetic measurements: (a) kinetic curves obtained at one bar and 45°C for different masses of the composite material. In legend: the mass of SrCl₂ used; (b) Dependence of the absolute difference between the two curves, obtained for two different masses mentioned in legend, on time.

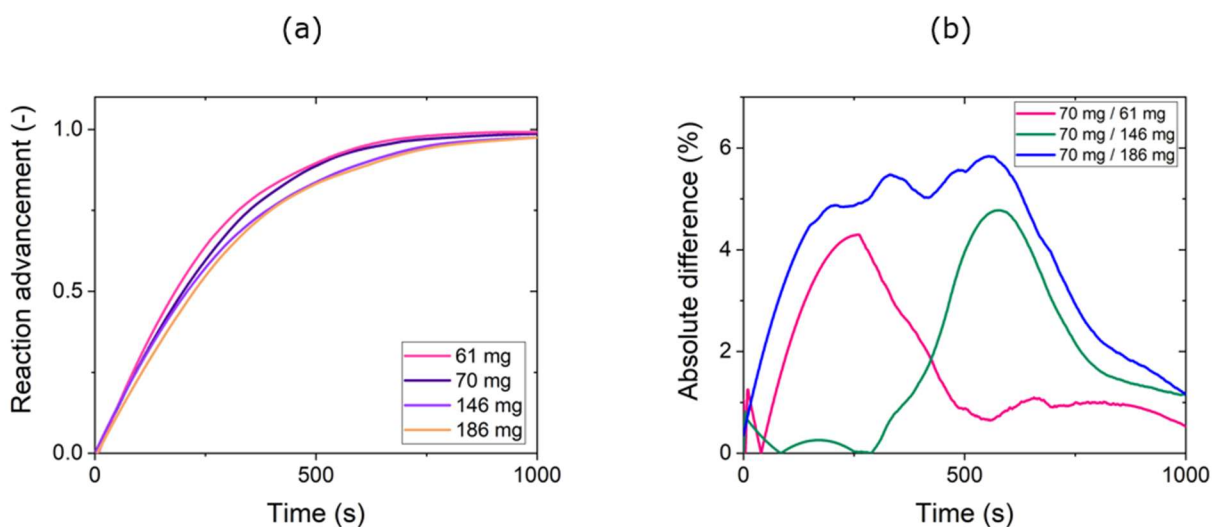


Figure 4. Determination of the optimal mass for the absorption measurements: (a) kinetic curves taken at 2.5 bar and 20°C for different masses of the composite material. In legend: the mass of SrCl₂ used in the test is indicated; (b) Dependence of the absolute difference between the two curves, obtained for two different masses mentioned in legend, on time.

Comparing the desorption curves in Figure 3(a), one can observe that the largest increase in the desorption rate occurred when the sample mass decreased from 146 to 70 mg. The absolute difference between the two desorption curves exceeded 24%. However, with further mass reduction, from 70 to 61 mg, the kinetics for the higher mass appeared to be faster. The reason for the faster kinetics of the higher mass sample may lay in higher contact area between the sample and the heat source. The contact area depends on the shape of the sample, as well as on the position of the sample relative to the heat source. In our experiment, it was easy to control the location of the sample, but making samples of exact same geometry, considering their small size ($\sim 0.4 \text{ cm}^3$), was challenging. Therefore, the difference in the sample geometry could explain such a behavior of the desorption curves. Despite this, the deviation between the curves appeared to be lower than acceptable variation set to 5%.

Compared to the results from the desorption, the deviation between the absorption curves is not that large (Figure 4(a)). For example, the 70 mg kinetic curve reproduces the other curves within 6% error, while in case of desorption the value of discrepancy surpasses 24%. This brings us to the conclusion that the mass of the sample has greater effect on the desorption rate compared to the absorption rate, at least for the used pressure-temperature conditions.

As a result, 70 mg of SrCl_2 was set to be the optimal mass, i.e. the maximum mass to be used to suppress any limitation from the mass and heat transfer while keeping a good accuracy of the kinetic measurements for the determination of the sorption tetrads.

3.1.4.2 Determination of the close-to-intrinsic kinetics

Desorption

For the first step of determining the close-to-intrinsic kinetics of NH_3 desorption from $\text{Sr}(\text{NH}_3)_8\text{Cl}_2$, two series of desorption measurements were carried out on the composite sample containing 70 mg of SrCl_2 . One of the desorption sets was performed at one bar and various temperature (45, 50, 55, and 60°C), and the other one was carried out at 55°C and various pressure (0.5, 1, 1.5, and 2 bar). The obtained Pressure-Time curves were converted into Reaction advancement-Time curves, using Eq. 7. Figure 5 shows the results of this step with the desorption curves at various temperature (Figure 5(a)) and various pressure (Figure 5(b)).

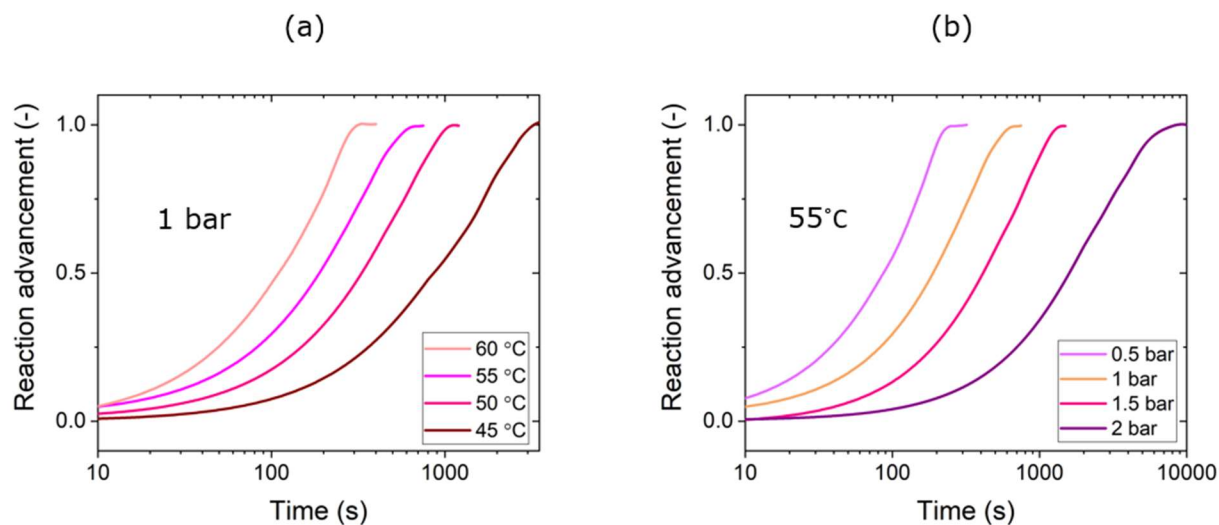


Figure 5. Desorption kinetic curves obtained on the composite material of the optimal mass (70 mg of SrCl_2) at (a) one bar and various temperature (45, 50, 55, and 60 °C) and (b) at 55 °C and various pressure (0.5, 1, 1.5, and 4.5 bar). X axis is plotted in log scale.

To determine the rate-limiting step of the desorption, the curves in Figure 5 were linearized with the models presented in [9]. The best accuracy of linearization ($R^2 > 0.99$) was reached using the contracting sphere reaction model described by the expression $g(x) = 1 - (1 - x)^{\frac{1}{3}}$. This equation is the integral form of $f(x) = 3 \cdot (1 - x)^{\frac{2}{3}}$. Figure 6 illustrates the linearized curves at various temperature (Figure 6(a)) and various pressure (Figure 6(b)).

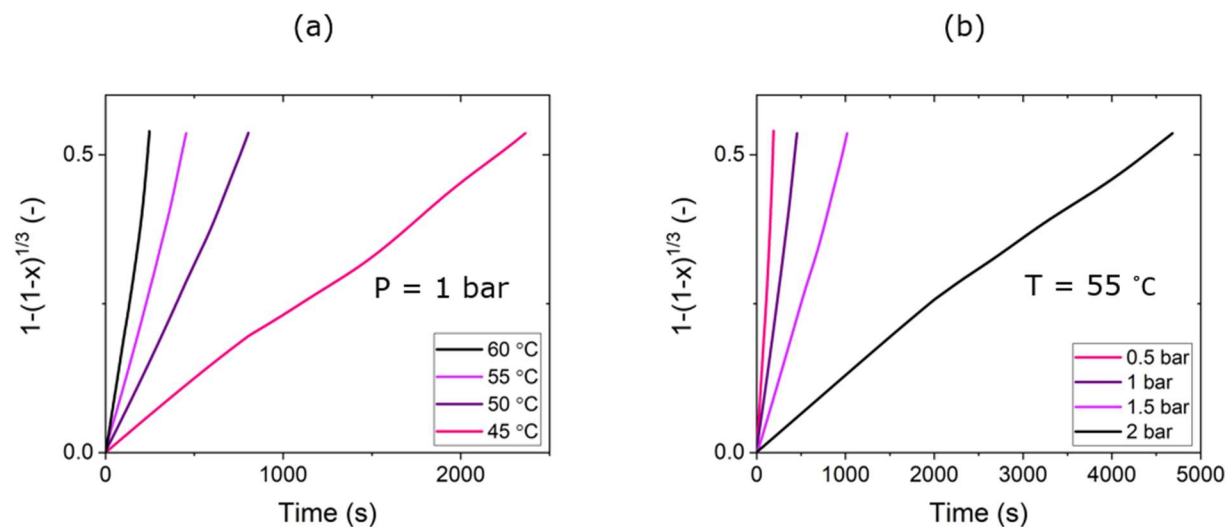


Figure 6. Linearization of desorption kinetic curves obtained on the composite material of the optimal mass (70 mg of SrCl_2) at (a) 1 bar and various temperature (45, 50, 55, and 60 °C) and (b) 55 °C and various pressure (0.5, 1, 1.5, and 2 bar). Chemical reaction mechanism used for the linearization is described with the function $g(x) = 1 - (1 - x)^{\frac{1}{3}}$. Reaction advancement x used is in the range $0 \div 0.9$.

Table 3 shows the values of the reaction rate k obtained as slope of the curves in Figure 6.

Table 3. Desorption rate constants obtained for various temperature and pressure.

1 bar				55 °C			
$T, ^\circ\text{C}$	p_{eq}/p	$k, 1/\text{s}$	R^2	p, bar	p_{eq}/p	$k, 1/\text{s}$	R^2
45	1.4	$2.272 \cdot 10^{-4}$	0.9983	0.5	4.2	$2.823 \cdot 10^{-3}$	0.9897
50	1.8	$6.67 \cdot 10^{-4}$	0.9988	1	2.2	$1.166 \cdot 10^{-3}$	0.9979
55	2.2	$1.181 \cdot 10^{-3}$	0.9979	1.5	1.5	$5.3 \cdot 10^{-4}$	0.9991
60	2.8	$2.183 \cdot 10^{-3}$	0.9929	2	1.1	$1.14 \cdot 10^{-4}$	0.9967

The rate constants at various pressure were plotted against pressure impact function expressed by Eq. 10.

The value of exponent n was set to 1.9, giving best fit to a straight line and an activation energy higher than the reaction enthalpy as expected for endothermic reactions. The dependence of the

pressure model $h(p)$ on the rate constant at various pressure is illustrated in Figure 7 together with a linear trend line, which coefficient of determination (R^2) is 0.9779.

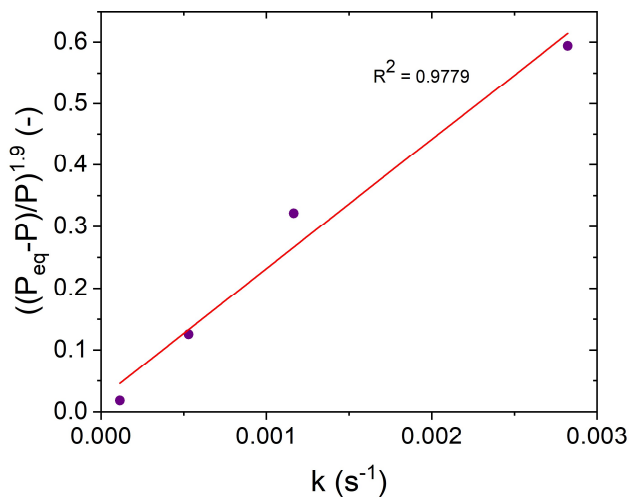


Figure 7. Pressure dependence function $h(P) = \left(\frac{p_{eq} - p}{p_{eq}}\right)^{1.9}$ versus reaction rate for close-to-intrinsic desorption kinetic study. p_{eq} is defined in Eq. 2.

Extracting the rate constants at various temperatures from Figure 6(a) allowed drawing Arrhenius plot, $\ln\left(\frac{k}{h(P)}\right)$ as a function of inverse temperature, as shown in Figure 8. The coefficient of determination (R^2) of the fitted linear trend line is 0.9877.

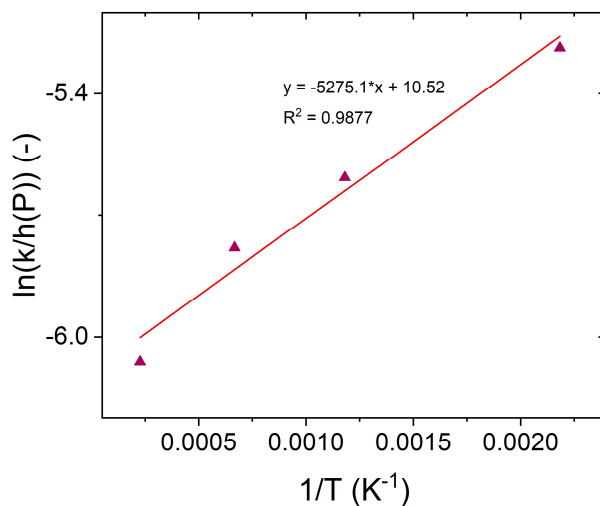


Figure 8. Arrhenius plot of NH_3 desorption from SrCl_2 .

From the Arrhenius plot, the intercept and the slope of the trend line were found to be 10.52 and -5275.1, respectively. These values correspond to $\ln k_0$ and $-\frac{E_a}{R}$, respectively. Thus, the pre-exponential factor k_0 and the activation energy E_a of the desorption were found to be 36754 s^{-1} and 43.9 kJ/mole , respectively.

The kinetic equation obtained in this analysis was computed for the experimental pressure-temperature conditions. Figure 9 depicts desorption profiles under various temperature and pressure. The kinetic model predicts the experimental data over a wide range of pressure and temperature. However, the predictions by the kinetic model slightly underestimates the desorption rate when the pressure in the system tends to the equilibrium one (Figure 9(b) – 2 bar).

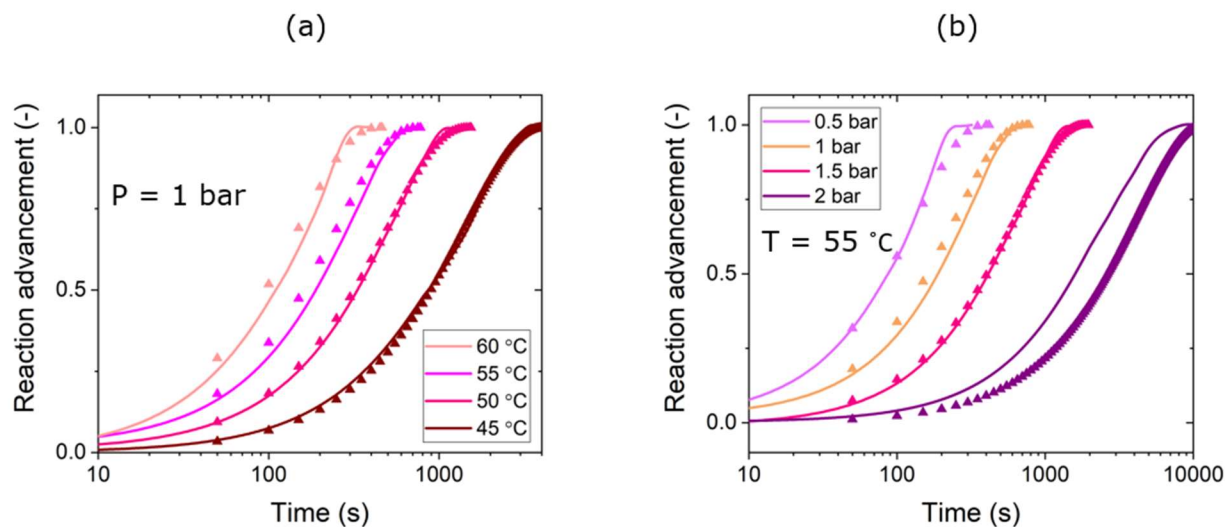


Figure 9. Desorption kinetic curves obtained experimentally and numerically. Computed kinetic curves are represented by triangles, while experimental curves are plotted as solid lines. X axis is plotted in log scale.

Absorption

To find the kinetic tetrad of NH_3 absorption into $\text{Sr}(\text{NH}_3)\text{Cl}_2$, the same steps as for the desorption analysis were taken.

The sample of the optimal mass (70 mg of SrCl_2) was subject to 2.5 bar of gaseous NH_3 at four different temperatures – 20, 25, 30, and 35 °C. In addition, the same sample was exposed to various pressure (1.5, 2, and 4.5 bar) of NH_3 , while the reactive bed temperature was kept at 30 °C. The results of the measurements at various temperature and various pressure are illustrated in Figure 10(a) and Figure 10(b), respectively.

After the seven absorption curves have been linearized, chemical reaction mechanism described by $g(x) = 1 - (1 - x)^{\frac{1}{3}}$ was chosen among the others. The selection was based on the value of the average R^2 of the linear trend lines fitted to the linearized curves. In case of the selected mechanism, average R^2 was equal to 0.98. Figure 11 shows the linearized curves.

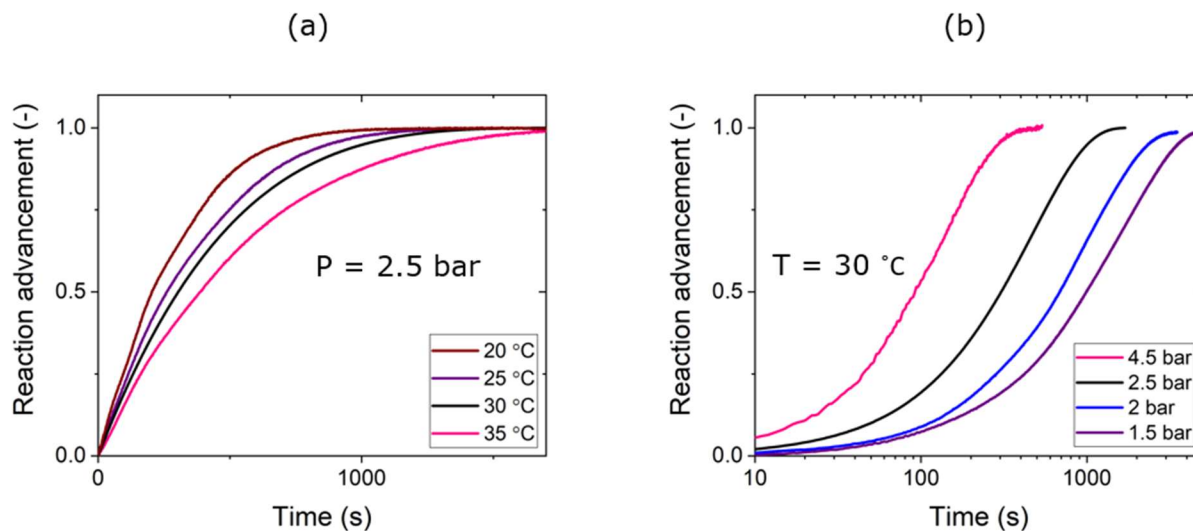


Figure 10. Absorption kinetic curves obtained on the composite material of the optimal mass (70 mg of SrCl_2) at (a) 2.5 bar and various temperature (20, 25, 30, and 35 °C) and (b) 30 °C and various pressure (1.5, 2, 2.5, and 4.5 bar).

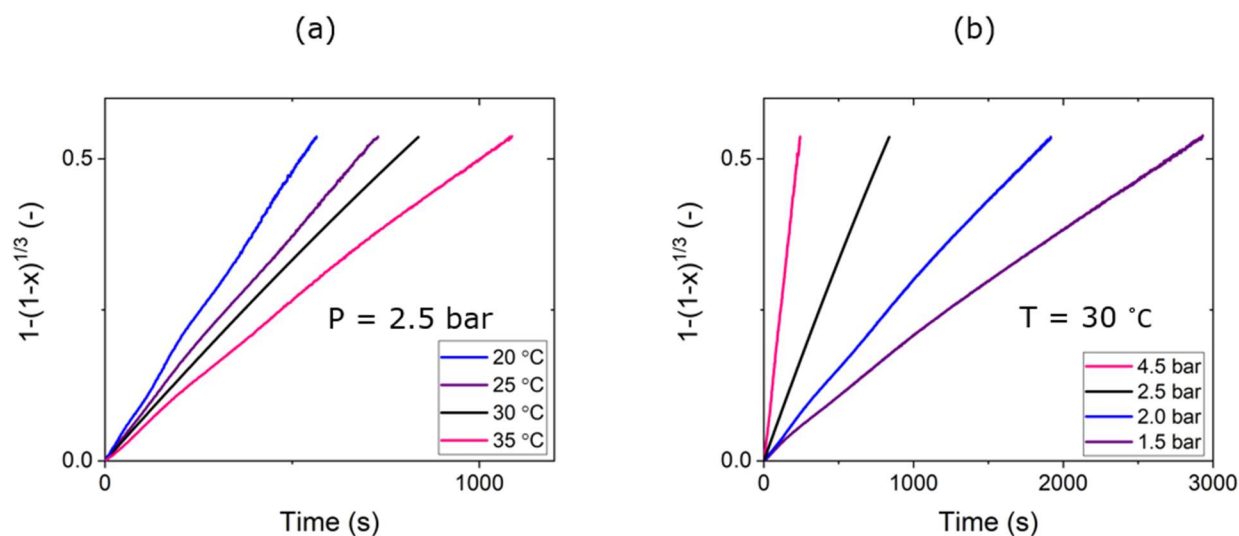


Figure 11. Linearization of absorption kinetic curves obtained on the composite material of the optimal mass (70 mg of SrCl_2) at (a) 2.5 bar and various temperature (20, 25, 30, and 35 °C) and (b) 30 °C and various pressure (1.5, 2, and 4.5 bar). Chemical reaction mechanism used is described with the function $g(x) = 1 - (1 - x)^{\frac{1}{3}}$. Reaction advancement x used is in the range $0 \div 0.9$.

Table 4 shows the values of the reaction rate obtained as slope of the curves in Figure 11.

Table 4. Absorption rate constants obtained for various temperature and pressure.

2.5 bar				30 °C			
$T, ^\circ\text{C}$	p/p_{eq}	$k, 1/\text{s}$	R^2	p, bar	p/p_{eq}	$k, 1/\text{s}$	R^2
20	6.7	$9.59 \cdot 10^{-4}$	0.9995	1.5	2.3	$1.8 \cdot 10^{-4}$	0.9979
25	5.0	$7.4 \cdot 10^{-4}$	0.9994	2	3.0	$2.8 \cdot 10^{-4}$	0.9985
30	3.8	$6.4 \cdot 10^{-4}$	0.994	2.5	3.8	$6.4 \cdot 10^{-4}$	0.994
35	2.9	$4.9 \cdot 10^{-4}$	0.9983	4.5	6.8	$2.2 \cdot 10^{-3}$	0.9995

The pressure dependence function, expressed in Eq. 10, was plotted against the rate constants at various temperature, as shown in Figure 12(a). The highest degree of linearization was achieved with n equal to 1.8. The coefficient of determination (R^2) in this case was found to be 0.9975.

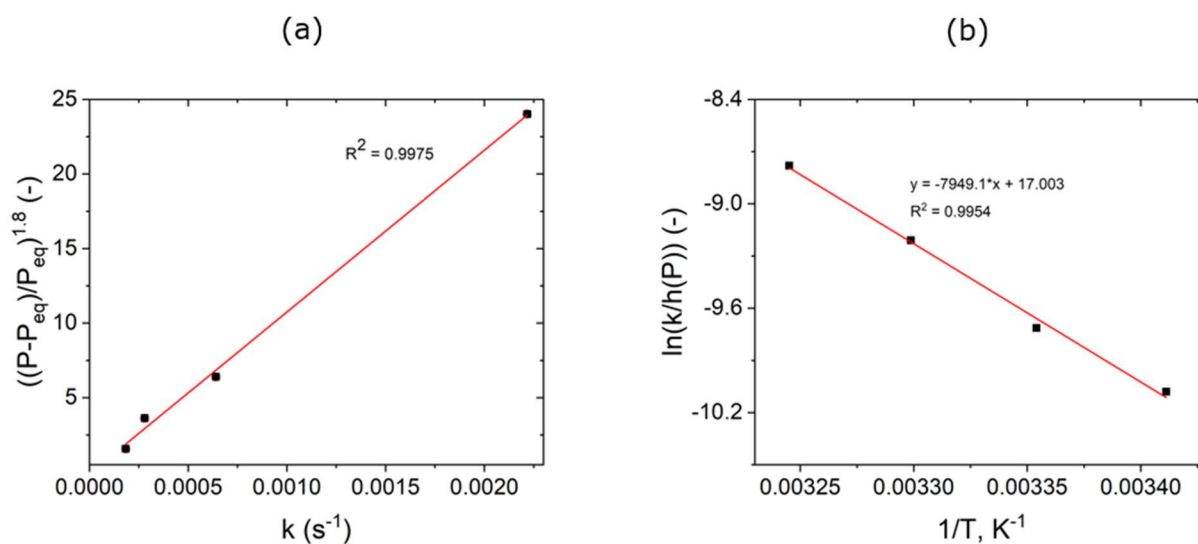


Figure 12. (a) Pressure dependence function over reaction rate for close-to-intrinsic absorption kinetics. (b) Arrhenius plot of NH_3 absorption into SrCl_2 – close-to-intrinsic kinetics.

Then, to find the kinetic parameters, such as pre-exponential factor and activation energy, the dependence of $\ln \frac{k}{h(P)}$ on inverse temperature were plotted together with a linear trend line ($R^2=0.9954$). Extracting the intercept and the slope of the trend line (17.003 and -7949.1

respectively) resulted in getting the following parameters: $k_0 = 2.423 \times 10^7 \text{ s}^{-1}$ and $E_a = 66.1 \text{ kJ/mole}$.

The determined absorption kinetic equation was computed for the pressure-temperature conditions used in the experiment. Figure 13 depicts absorption profiles under various temperature (a) and pressure (b). The computed kinetic curves are presented as triangles, while the experimental reaction profiles are illustrated as solid lines. From Figure 13, one can conclude that the absorption model is in a good agreement with the experimental data. However, as well as for the desorption, the numerical predictions slightly underestimate the absorption rate for small pressure difference, when actual pressure in the system tends to the equilibrium one (Figure 13(b) – 1.5 bar).

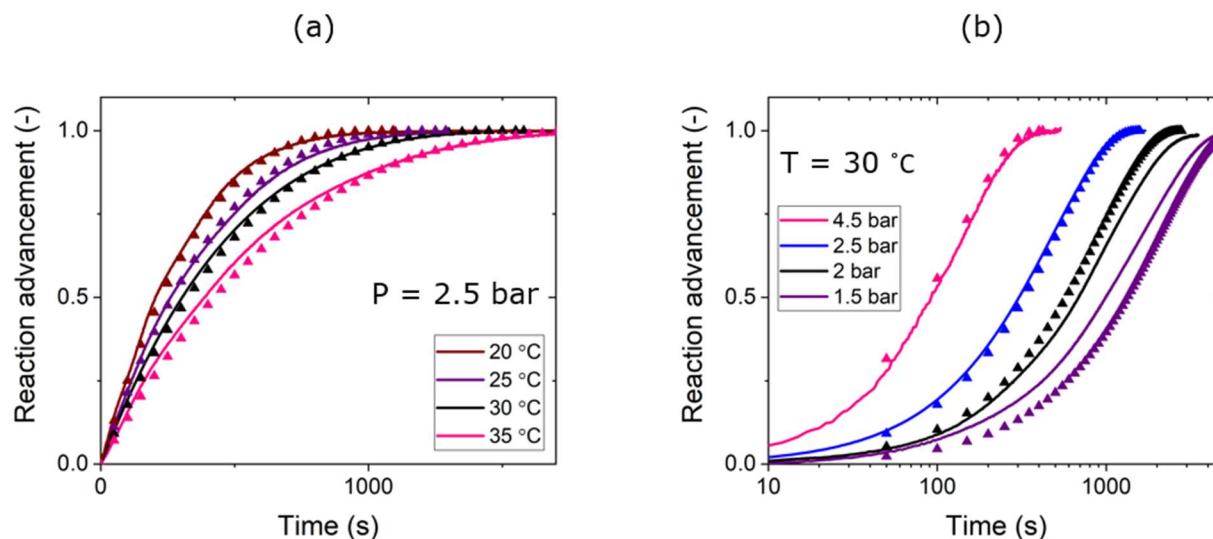


Figure 13. Absorption kinetic curves obtained experimentally and numerically. Computed kinetic curves are represented as triangles, while experimental ones are plotted as solid lines.

3.1.4.3 Experiment vs. Model

Experimental and numerical results for NH_3 absorption at 4.5 bar and various temperature (25, 30, and 35 °C) are presented and compared in Figure 14. As described above, the experimental data was collected for 466 mg StCl_2 wrapped in aluminum foil with an opening. As it was challenging to measure precisely the width of the opening, we investigated its effect on the absorption kinetics by computing the intrinsic model and the literature models using various opening size.

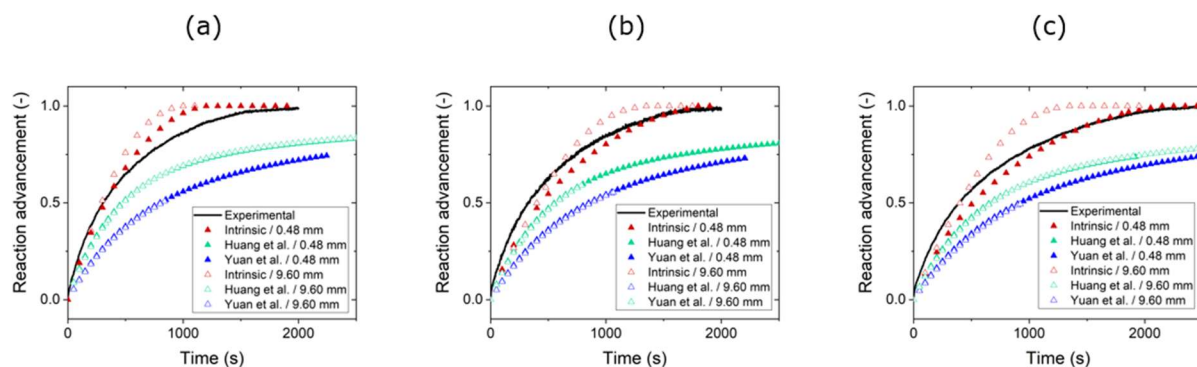


Figure 14. Kinetic curves of NH_3 absorption into 466 mg of SrCl_2 at 4.5 bar and (a) 25°C ; (b) 30°C ; and (c) 35°C . Experimental and numerical results are indicated as solid line and triangles, respectively. In the legend: the source from where the kinetic equation was taken / the width of the aluminum opening.

In case of the intrinsic kinetic equation, the increase in the size of the aluminum opening (from 0.48 to 9.6 mm) was found to speed up the absorption kinetics after the degree of absorption reaches 0.5, especially at higher absorption temperatures. This observation is reasonable, as in general the contribution from mass transfer should get more pronounced at higher absorption temperatures as well as at lower medium porosity and hence lower permeability. In addition, it was observed that further increase in the width does not lead to further acceleration of the reaction rate. Despite the fact that the intrinsic model becomes independent of the mass transfer at width of 9.6 mm, in practice the width was observed to be closer to the lower limit of the parametric range (0.48 mm). In contrast to the intrinsic model, the variation in the width size in the literature models did not result in any change of the reaction profile, indicating that such a contribution from the mass transfer is negligible for the apparent kinetics.

The absorption profiles computed with the use of the intrinsic tetrad at width of 0.48 mm reproduce nicely the experimental kinetic curves, while the kinetic curves simulated with the use of the tetrads found in the literature are much slower than the experimental ones. Since for the determination of the kinetic tetrads both Huang *et al.* and Yuan *et al.* used large composite samples, where NH_3 has to diffuse over long distances, it is reasonable to assume that the literature kinetic parameters include a rate limiting effect of the mass transfer, which results in slower simulated absorptions.

In addition to mass transfer, the literature kinetic equations include the contribution from the heat transfer, which also decelerates the overall kinetics.

The desorption kinetic curves obtained at 1 bar and various temperature (50, 55, and 60°C) and at 55°C and various pressure (0.5, 1.0, and 1.5 bar) are presented as markers for the numerical models and as solid lines for the experimental data in Figure 15.

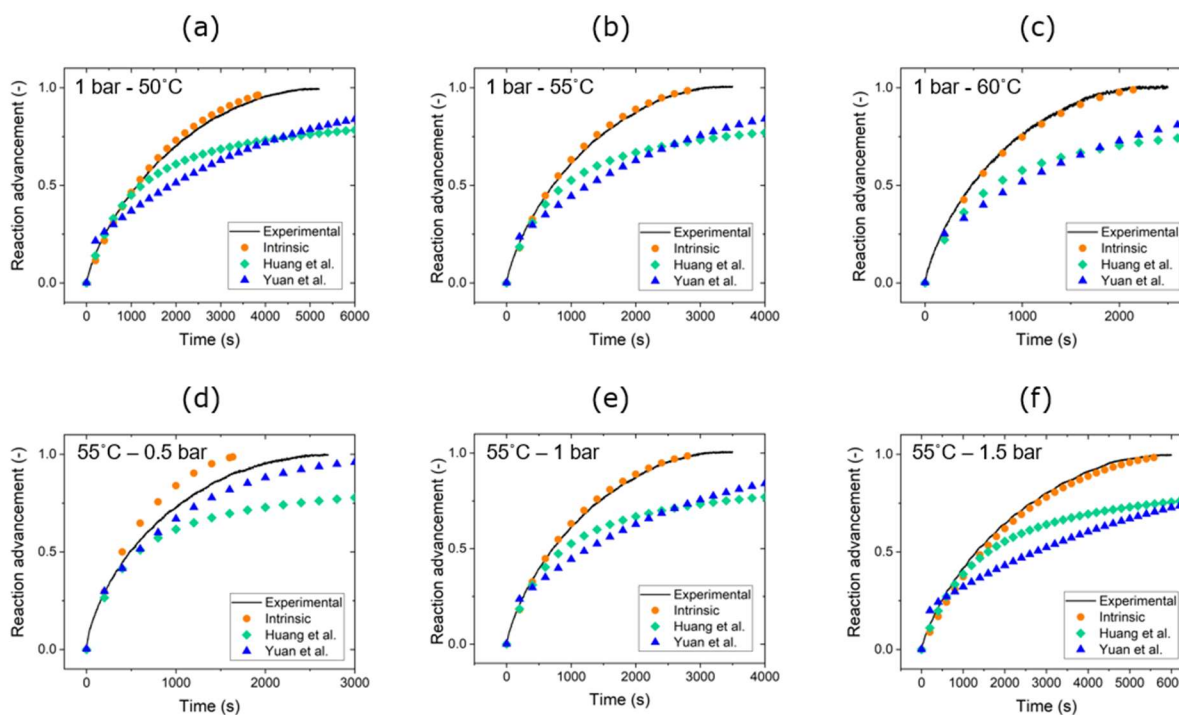


Figure 15. Kinetics curves of NH_3 desorption from SrCl_2 at: (a) 1 bar and 50°C; (b) 1 bar and 55°C; (c) 1 bar and 60°C; (d) 55°C and 0.5 bar; (e) 55°C and 1 bar; (f) 55°C and 1.5 bar. Experimental and numerical results are indicated as solid line and markers, respectively.

Similar to the absorption results, the desorption intrinsic model was found to be in a good agreement with the experimental data, and the kinetics parameters found in the literature resulted in slower reaction advancement. The same explanation as for the absorption holds for the slower desorption curves: the parameters determined by Huang et al. or Yuan et al. include a rate limiting effect from heat and mass transfer leading to slower apparent kinetics.

3.1.5 Conclusion

The aim of this study was to determine the close-to-intrinsic kinetics tetrads of the sorption processes between ammonia (NH_3) and Strontium Chloride (SrCl_2) ammines for performing later on an accurate numerical simulation of a thermochemical reactor.

In the first part of this paper, the close-to-intrinsic kinetic tetrads, including pre-exponential factor, activation energy, reaction model, and pressure impact function, of the absorption and desorption between gaseous NH_3 and solid SrCl_2 ammines were determined using volumetric method. The main influencing parameters of the kinetics measurements, i.e. temperature program and sample preparation, were optimized for obtaining accurate and reliable kinetics equations independent of the heat and mass transfer. The obtained kinetics equations predicted with a good accuracy the experimental data over wide pressure-temperature range. In the second part of this research, a 3D numerical model was developed and run in COMSOL Multiphysics to compare results from the model and the experiment. The model couples the chemical reaction and heat transfer for desorption, and in case of absorption mass transfer is added. As an input for the simulation, the kinetics tetrads determined herein and the ones found in the existing literature were used. As a result of the comparison, the following conclusions were drawn:

1. The model results calculated for the kinetics tetrads obtained herein are found to be in a good agreement with the experimental results;
2. The results of the model when computing for the literature kinetics equations are not consistent with the experimental data, especially by the end of the sorption reactions, which indicates that heat and mass transfer effect is already in-built in the literature kinetics equations.
3. The results of the study highlights the importance of using the close-to-intrinsic parameters when modeling sorption processes.

The kinetics tetrads given herein may be considered as “universal” and may be used by any researcher in the future, in any computational or experimental work, since they are independent of the environment of the active material.

3.1.6 References

- [1] G. Allan Schröder Pedersen, DTU (editor) Brian Elmegaard, DTU Claus Hviid Christensen, DONG Energy Claus Kjøller and R. A. Frank Elefsen, Danish Technological Institute John Bøgild Hansen, Haldor Topsøe A/S Jørgen Hvid, Rambøll A/S Per Alex Sørensen, PlanEnergi Søren Knudsen Kær, Aalborg University, Thomas Vangkilde-Pedersen, GEUS Thorkild Feldthusen Jensen, “Status and recommendations for RD&D on energy storage technologies in a Danish context,” *Danish energy Res. Program.*, no. February, 2014.
- [2] “Technology Roadmap,” *Encycl. Prod. Manuf. Manag.*, pp. 781–782, 2006.
- [3] C. Forman, I. K. Muritala, R. Pardemann, and B. Meyer, “Estimating the global waste heat potential,” *Renew. Sustain. Energy Rev.*, vol. 57, pp. 1568–1579, 2016.
- [4] L. Jiang and A. P. Roskilly, “Thermal conductivity, permeability and reaction characteristic enhancement of ammonia solid sorbents: A review,” *Int. J. Heat Mass Transf.*, vol. 130, pp. 1206–1225, 2019.
- [5] H. J. Huang, G. Bin Wu, J. Yang, Y. C. Dai, W. K. Yuan, and H. B. Lu, “Modeling of gas–solid chemisorption in chemical heat pumps,” *Sep. Purif. Technol.*, vol. 34, no. 1–3, pp. 191–200, 2004.
- [6] Y. Yuan, H. Bao, Z. Ma, Y. Lu, and A. P. Roskilly, “Investigation of equilibrium and dynamic performance of SrCl₂-expanded graphite composite in chemisorption refrigeration system,” *Appl. Therm. Eng.*, vol. 147, no. January 2018, pp. 52–60, 2019.
- [7] H. Huang, “Modeling of gas–solid chemisorption in chemical heat pumps,” *Sep. Purif. Technol.*, vol. 34, no. 1–3, pp. 191–200, Jan. 2004.
- [8] Y. Yuan, H. Bao, Z. Ma, Y. Lu, and A. P. Roskilly, “Investigation of equilibrium and dynamic performance of SrCl₂-expanded graphite composite in chemisorption refrigeration system,” *Appl. Therm. Eng.*, vol. 147, no. January 2018, pp. 52–60, 2019.
- [9] S. Vyazovkin, A. K. Burnham, J. M. Criado, L. A. Pérez-Maqueda, C. Popescu, and N. Sbirrazzuoli, “ICTAC Kinetics Committee recommendations for performing kinetic computations on thermal analysis data,” *Thermochim. Acta*, vol. 520, no. 1–2, pp. 1–19,

- 2011.
- [10] H. S. Jacobsen *et al.*, “Nanoscale structural characterization of $\text{Mg}(\text{NH}_3)_6\text{Cl}_2$ during NH_3 desorption: An in situ small angle X-ray scattering study,” *Chem. Phys. Lett.*, vol. 441, no. 4–6, pp. 255–260, 2007.
- [11] L. W. Wang, Z. Tamainot-Telto, S. J. Metcalf, R. E. Critoph, and R. Z. Wang, “Anisotropic thermal conductivity and permeability of compacted expanded natural graphite,” *Appl. Therm. Eng.*, vol. 30, no. 13, pp. 1805–1811, 2010.
- [12] M. Gaeini, A. L. Rouws, J. W. O. Salari, H. A. Zondag, and C. C. M. Rindt, “Characterization of microencapsulated and impregnated porous host materials based on calcium chloride for thermochemical energy storage,” *Appl. Energy*, vol. 212, no. May 2017, pp. 1165–1177, 2018.
- [13] M. Gaeini, S. A. Shaik, and C. C. M. Rindt, “Characterization of potassium carbonate salt hydrate for thermochemical energy storage in buildings,” *Energy Build.*, vol. 196, pp. 178–193, 2019.
- [14] R. Iwata, T. Yamauchi, Y. Hirota, M. Aoki, and T. Shimazu, “Reaction kinetics of ammonia absorption/desorption of metal salts,” *Appl. Therm. Eng.*, vol. 72, no. 2, pp. 244–249, 2014.
- [15] T. Roettinger, “PERFORMANCE TESTING AND EVALUATION OF SOLID ABSORPTION SOLAR COOLING UNIT,” vol. 61, no. 2, 1997.
- [16] L. Jiang, L. W. Wang, Z. Q. Jin, B. Tian, and R. Z. Wang, “Permeability and Thermal Conductivity of Compact Adsorbent of Salts for Sorption Refrigeration,” *J. Heat Transfer*, 2012.
- [17] H. J. Huang, G. Bin Wu, J. Yang, Y. C. Dai, W. K. Yuan, and H. B. Lu, “Modeling of gas-solid chemisorption in chemical heat pumps,” *Separation and Purification Technology*, vol. 34, no. 1–3, pp. 191–200, 2004.
- [18] P. Berdiyeva, A. Karabanova, M. G. Makowska, and R. E. Johnsen, “In-situ neutron imaging study of NH_3 absorption and desorption in SrCl_2 within a heat storage prototype reactor,” *J. Energy Storage*, vol. 29, no. December 2019, p. 101388, 2020.

- [19] F. J. Valdes-parada, J. A. Ochoa-tapia, and J. Alvarez-ramirez, “Validity of the permeability Carman – Kozeny equation : A volume averaging approach,” *Physica A*, vol. 388, no. 6, pp. 789–798, 2009.

4 Chapter IV. Validation of Thermochemical Reactor Modelling Using Neutron Radiography

This chapter presents the progression towards the validation of our numerical model. With the ambition of developing a model describing locally, down to the mm scale, the sorption reaction, we needed experimental data describing, at the same scale, the system. Typically, two types of experimental data are used to validate a numerical model of a thermochemical reactor – local and global. Local data, i.e. temperature readings, may reveal the degree of consistency between the model and the experimental results at specific points of the reactor. The use of global parameters, like the change in the mass or level of condensed fluid sorbate, gives an opportunity to compare the model and the experimental kinetics curves at a global scale. Combination of these two approaches gives a more complete picture of the processes occurring inside the reactor, but it still provides insufficient information, overlooking local behaviour, which may lead to biased simulations and eventually wrong optimization of the reactor design. Instead, our approach was to use neutron imaging, allowing getting local and global information on the sorbent state during absorption and desorption. Since with neutron imaging, it is not possible to study very large systems due to limited field of view of existing instruments, the validation of our model was conducted on a cell representing a basic element of a possible thermochemical reactor geometry.

In the first paper of this chapter, the reader is introduced to the first neutron imaging study performed on the cell. The cell consisted of a honeycomb heat exchanger with the active material, solid SrCl_2 in the form of powder, embedded in the hexagons of the honeycomb. To analyse spatio-temporal distribution of NH_3 within the reactive bed during NH_3 sorption into the salt, we have applied *in-situ* neutron radiography. The quantitative analysis of the radiography data using the Beer-lambert's law was not performed due to irregularities in the reactive bed thickness and expansion and contraction of the powder during cycling. Instead, to get the experimental kinetic curves, we analyzed the evolution of greyscale values of the images assuming the reactions to be complete. In addition, we have also performed neutron tomography experiments to acquire information on macrostructural changes in the salt bed during NH_3 cycling and on possible deformation of the heat exchanger. The obtained results provided crucial information for the continuation of the work, presented further in this chapter.

The next two papers focus on the development of the numerical model and its validation against neutron data. It is worth noting that the absorption results presented in the first paper were found unusable for the model validation. During the absorption experiments, argon was present in the reactor since the setup was not evacuated before the start of NH_3 cycling. The presence of other gas rather than NH_3 in the system might have caused the deceleration of the absorption rate, and hence the comparison of the numerical model with the absorption kinetics might have led to wrong conclusions. Other absorption results were collected later on, during another neutron beamtime carried out at the instrument NeXT at ILL and used as described in the third paper.

In the second paper, a conference paper, we present a numerical model of the NH_3 sorption into SrCl_2 . The model describes the kinetics of the chemical reaction and the heat transfer. The chemical reaction rate was defined with the kinetic parameters found in literature, and since the literature reaction rates are underestimated due to the heat and mass transfer limitations, the numerical sorption processes appeared to be slower compared to the experiment. This finding underlines the significance of using intrinsic kinetic parameters for accurate modelling. In addition, we learnt that the fluid dynamics cannot be neglected in case of absorption; otherwise, it results in significant change in the shape of the kinetic curve.

The third paper presents an advanced numerical model, simulating the chemical reaction kinetics and heat and mass transfer, with the mass transfer being applied only in case of absorption. In this model, the chemical reaction kinetics was described with the intrinsic kinetic parameters obtained as described in Chapter III, and the values of heat and mass transfer properties were taken from literature. The numerical results are in a good agreement with the neutron radiography data, and the results from neutron tomography gave us valuable insights on the behaviour of the kinetic curves.

4.1 Paper II: In-situ neutron imaging study of NH₃ absorption and desorption in SrCl₂ within a heat storage prototype reactor

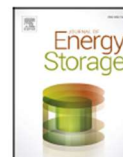
Journal of Energy Storage 29 (2020) 101388



Contents lists available at ScienceDirect

Journal of Energy Storage

journal homepage: www.elsevier.com/locate/est



In-situ neutron imaging study of NH₃ absorption and desorption in SrCl₂ within a heat storage prototype reactor



Perizat Berdiyeva^a, Anastasiia Karabanova^b, Malgorzata G. Makowska^c, Rune E. Johnsen^b, Didier Blanchard^b, Bjørn C. Hauback^a, Stefano Deledda^{a,*}

^a Department for Neutron Materials Characterization, Institute for Energy Technology, P.O. Box 40, NO-2027, Kjeller, Norway

^b Department of Energy Conversion and Storage, Technical University of Denmark, Fysikvej, DK-2800, Lyngby, Denmark

^c Photon Science Division, Paul-Scherrer Institute, Forschungsstrasse 111, 5232-Villigen, Switzerland

ARTICLE INFO

Keywords:
Metal halides
Heat storage
Ammonia absorption/desorption
Neutron radiography
Neutron tomography

ABSTRACT

Strontium chloride octaammine Sr(NH₃)₈Cl₂ offers high volumetric and gravimetric NH₃ densities and can store and release heat upon exo-/endothermal absorption and desorption of NH₃. Thus, it is a promising material for thermochemical heat storage (THS) applications.

In the present work, *in-situ* neutron imaging was applied to analyze spatio-temporal development of Sr(NH₃)₈Cl₂ powder in a thermochemical heat storage prototype reactor during NH₃ absorption and desorption processes. The powder was embedded in a stainless steel honeycomb for the efficient heat transfer during the NH₃ desorption process. 2D radiography images were obtained during NH₃ ab-/desorption cycles at selected temperatures. The swelling and formation of the porous structure in SrCl₂ is monitored during the first cycles. A powder bed expansion of up to 10% upon NH₃ absorption was observed. Neutron tomography experiment were also performed to acquire 3D information which revealed the deformation of the honeycomb. This neutron imaging experiment brought crucial information for optimizing the design of efficient and safe THS systems.

4.1.1 Introduction

To support the transition from conventional fossil fuel energy sources to decarbonized sources, a number of technologies have been identified and are expected to have major impacts. The technologies range from renewable energy sources to efficient energy use, where the excess of energy can be first stored and later supplied to meet the demands. The effective use of energy requires efficient storage, which can be achieved using different methods one of them being thermal energy storage [1]. Seasonal heat storage materials such as hydrates [2] and ammines have been studied as thermochemical heat storage materials for domestic heating applications [3]. However, most hydrates were found to have poor cyclability and degrade over multiple cycles at temperature higher than 50 °C [4]. Meanwhile sorption metal chloride and ammonia working pairs are reported to have a very good cyclability and high energy density [5].

Metal amines have more than 15 years been studied as an indirect storage of hydrogen due to their high volumetric and gravimetric hydrogen capacities [6–8]. $\text{Sr}(\text{NH}_3)_8\text{Cl}_2$ is one of the best metal halide ammines for NH_3 storage due to its high hydrogen density [9] and high theoretical volumetric NH_3 density of $642 \text{ kg}\cdot\text{m}^{-3}$ at RT [10]. It is obtained via absorption of NH_3 into SrCl_2 . The absorption reaction is exothermic, while the endothermic desorption is achieved by applying heat. These exothermic and endothermic absorption and desorption reactions are associated with good kinetics and make the $\text{SrCl}_2 / \text{Sr}(\text{NH}_3)_8\text{Cl}_2$ an interesting system for thermochemical heat storage (THS) applications [10,11]. In these applications, heat provided by an external source decomposes $\text{Sr}(\text{NH}_3)_8\text{Cl}_2$ into NH_3 gas and SrCl_2 . The NH_3 gas can then be condensed into liquid NH_3 in a separate reservoir. In storage mode the connection between liquid NH_3 and SrCl_2 is closed. To recovered the heat, NH_3 is transferred back to the container with SrCl_2 , where heat is released upon the absorption process and formation of $\text{Sr}(\text{NH}_3)_8\text{Cl}_2$. By controlling the applied pressure of the NH_3 gas, the heat release can be controlled and varied. Ideally, the exothermal and endothermal absorption and desorption of NH_3 in $\text{SrCl}_2 / \text{Sr}(\text{NH}_3)_8\text{Cl}_2$ can be employed for handling waste heat (40-80 °C) from industry and be reused for district heating [1]. The $\text{SrCl}_2/\text{NH}_3$ working pair was selected due to its high energy density and very good cyclability. SrCl_2 is rather cheap and non-toxic. Its working temperature corresponds to the target application, i.e. residential heating, taking advantage of low-price renewable electricity (heat-pump + heat storage) and / or low-grade waste heat recovery (<100 °C) readily available at most industrial production lines.

The crystal structures of $\text{Sr}(\text{NH}_3)_8\text{Cl}_2$, SrCl_2 and their intermediates have already been extensively studied and characterized [9,10]. However, the spatio-temporal evolution of the $\text{Sr}(\text{NH}_3)_8\text{Cl}_2$ and NH_3 transport in the system have not yet been investigated in detail. Neutrons are very well suited to determine the distribution of NH_3 molecules in the $\text{SrCl}_2 / \text{Sr}(\text{NH}_3)_8\text{Cl}_2$ system due to their unique properties of “seeing” hydrogen atoms and to the high hydrogen content in this system.

Neutron imaging is a powerful characterization technique which can provide 2D and 3D information about the inner structure of objects [12]. It is used as a characterization method for various energy storage materials and systems. The strong interaction of neutrons with hydrogen makes neutrons an attractive probe within hydrogen storage, where neutron radiography and tomography techniques can be used not only for qualitative, but also quantitative studies [13–16]. Furthermore, energy storage devices such as fuel cells or batteries are studied extensively by neutron imaging. The sensitivity of neutrons to hydrogen in water molecules allows detecting and visualizing water distribution in fuel cells [17–20]. Neutrons are also sensitive to lithium, which is a key element in commercial rechargeable batteries [21–25]. Further details about neutron imaging techniques, its accuracy, sensitivity, and its applications in various fields of research can be found in several review papers published in the last decade [12,26,27].

In this work, NH_3 uptake and release in the $\text{SrCl}_2 / \text{Sr}(\text{NH}_3)_8\text{Cl}_2$ system within a THS prototype reactor, was studied by neutron imaging. The specially designed THS prototype reactor contained SrCl_2 embedded in a stainless steel honeycomb structure. The designed THS reactor contains several honeycomb discs filled with SrCl_2 powder, which are placed on top of each other. In this work only the half of one whole disc was employed in order to examine the local NH_3 absorption and desorption. The honeycomb structure of the disc is used to provide an efficient heat transfer within the volume of the disc during the NH_3 desorption process, when heat is provided to the system. The high neutron scattering cross-section of hydrogen present in ammonia molecule allowed observation of the uptake and release of NH_3 within SrCl_2 . Absorption and desorption profiles for different regions of the honeycomb were obtained for each absorption and desorption cycle by *in-situ* neutron radiography. The results of image analysis are discussed with respect to the homogeneity of the absorption and desorption processes over the volume of the THS reactor and how it is affected by the degree of the compaction of the powder, as well as how efficiently the stainless-steel honeycomb structure conducts the heat during NH_3 desorption.

To the best of our knowledge this is the first time that neutron imaging is used to characterize a THS reactor, allowing a real-time visualization of the changes that the sorption material undergoes during charging and discharging. The neutron radiography data presented here will be used to validate results from numerical simulations. A COMSOL Multiphysics modelling was developed for the heat reactor, integrating, with a high degree of accuracy, the thermochemistry, the ammonia flow, the heat transfer to optimize the reactor design and achieve high heat power and maximum use of the heat generated [28]. Neutron imaging will help, on one hand, to validate the simulation model, and, on the other hand, to validate or invalidate our first assumption on the honeycomb effect on heat transfer and diffusion to the salt.

4.1.2 Experimental

4.1.2.1 The THS reactor prototype set-up

A special transportable THS reactor prototype (118 mm in length, 20 mm in width and 85 mm in height) was designed for the neutron imaging experiment (Figure 1). The THS reactor is made of 2 mm thick aluminum, in order to be as transparent as possible for neutrons to study the interior of the reactor. The THS reactor is tightly closed with a stainless-steel lid of 85 mm in diameter and an o-ring ensured the sealing. The lid had two gas inlets (only one of them was used during this experiment) and a cylindrical inlet which housed a heating element and a thermocouple.

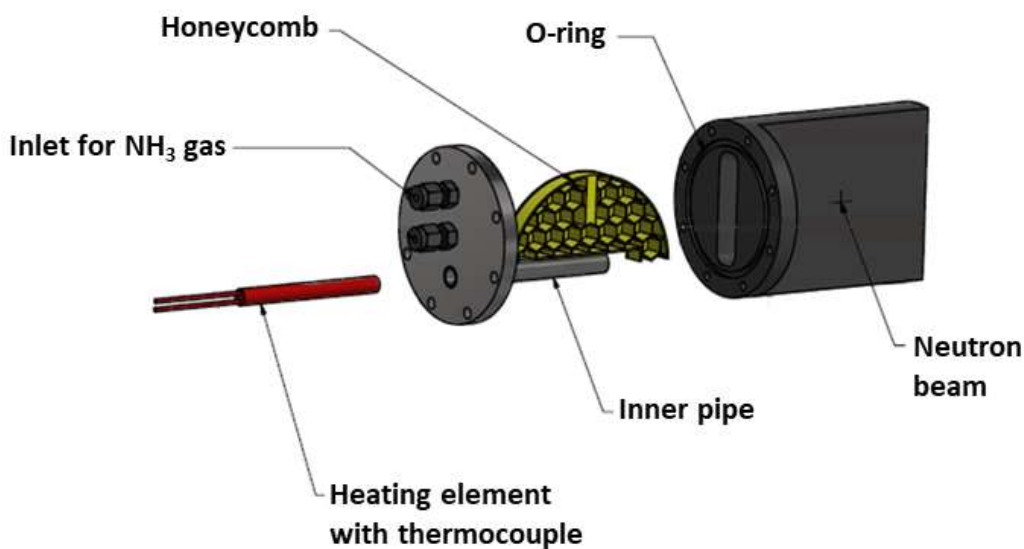


Figure 1. Detailed view of the THS prototype reactor with the honeycomb inside.

A honeycomb with the dimensions of 100 mm x 50 mm x 10 mm was filled with 10 g of SrCl_2 salt and placed inside the THS reactor in an inert argon gas filled glove box (<1 ppm of O_2 and H_2O). Two absorption and desorption cycles were performed on the SrCl_2 prior to the neutron imaging experiment in order to confirm the cyclability and suitability of the sample. The THS reactor was then connected through a stainless-steel tube to a reservoir, which contained 100 g of $\text{Sr}(\text{NH}_3)_8\text{Cl}_2$ powder that served as NH_3 source and reservoir during the experiment. Manual valves and a pressure reader (Figure 2) were included in the connection between the THS reactor and the reservoir. The reservoir and the prototype reactor were connected to a heating element and a thermocouple for controlling and monitoring the temperature.

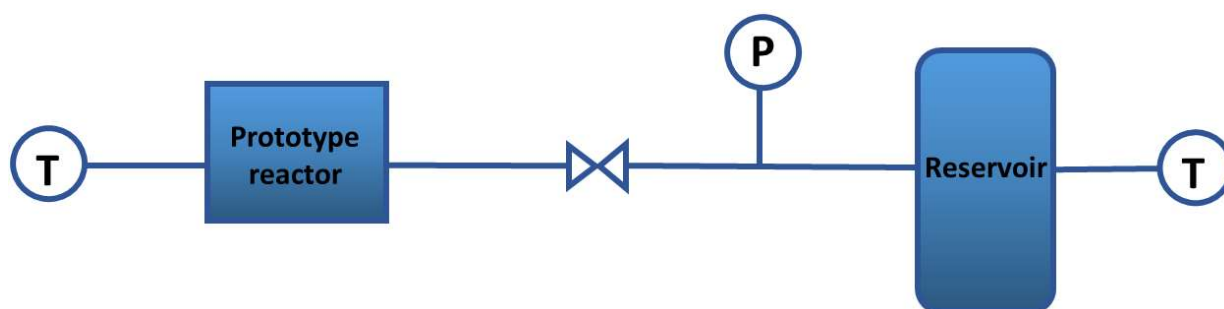


Figure 2. Schematic view of the setup used for the neutron imaging experiment. The letters *P* and *T* indicate the points where pressure and temperature were measured.

The $\text{Sr}(\text{NH}_3)_8\text{Cl}_2$ in the reservoir was heated up to 70°C during the experiment which then released NH_3 gas that was absorbed by the SrCl_2 salt in the honeycomb at RT. Upon heating the honeycomb in the THS reactor, NH_3 was released from the $\text{Sr}(\text{NH}_3)_8\text{Cl}_2$ powder and reabsorbed in the reservoir. The pressure of the system was remotely monitored and logged.

4.1.2.2 Neutron Imaging set-up

The neutron radiography and tomography experiments were performed at the NECTAR instrument, at the FRM-II research reactor in Garching, Germany using a white beam of thermal neutrons (mean energy 28 meV) [29]. The sample was mounted on a stage allowing translation along x, y and z-axes about 3 cm in case of radiography and about 10 cm for tomography from the scintillator screen. The thermal neutron beam transmitted through the sample impinged on a scintillator screen $\text{ZnS} / {}^6\text{LiF}$, which converted the neutrons into light. The light was then reflected by a mirror in a light-tight box and captured by CCD camera (Andor iKon-L-BV) with a 2048 x

2048 pixels resolution. The experiment did not require high spatial resolution, thus the collimation ratio L/D , which was about 230, provided sufficient image quality. Prior to each experiment open beam and dark current images were collected for normalization of the raw images using ImageJ [30]. The total acquisition time for each image including camera readout was 27 seconds and overall three absorption and two desorption processes were performed. Each absorption step, except the last one, was followed by desorption allowing us to investigate not only the absorption and desorption processes themselves, but also the difference between the first and next cycles. The honeycomb with SrCl_2 powder was open in the front side for free NH_3 and SrCl_2 powder interaction.

Neutron tomography measurements were carried out by placing the THS reactor in a vertical position and by rotating it over a 360° range. During the tomography experiment the THS reactor was disconnected from the reservoir. Several tomography scans, each with 1083 projections, were performed for different degrees of saturation of NH_3 in $\text{Sr}(\text{NH}_3)_8\text{Cl}_2$ and then 3D volume of the sample was reconstructed using MuhRec software [31] and visualized using Tomviz software[32]. The formation of $\text{Sr}(\text{NH}_3)_8\text{Cl}_2$, thus NH_3 concentration in the sample was defined by the normalized transmission $I(\lambda)$ (greyscale values between 0 and 1) in selected areas of the images, where I is the normalized intensity and λ is the neutron wavelength. The lower transmission $I(\lambda)$ represents the higher concentration of NH_3 while the higher transmission $I(\lambda)$ means lower NH_3 content in the sample.

4.1.3 Results and discussion

4.1.3.1 Absorption process

In-situ transmission images were obtained during NH_3 absorption and desorption processes in the SrCl_2 powder. The series of images in Figure 3 show the honeycomb at the end of absorption-1 (a), absorption-2 (b) and absorption-3 (c). These images were obtained by normalization of corresponding images by the image of the sample in the initial state. Therefore, the images show only the changes that occurred in the sample due to NH_3 absorption. The formation of $\text{Sr}(\text{NH}_3)_8\text{Cl}_2$ appears as dark areas during NH_3 uptake due to the high neutron attenuation of hydrogen atoms [19] contained in ammonia molecules.

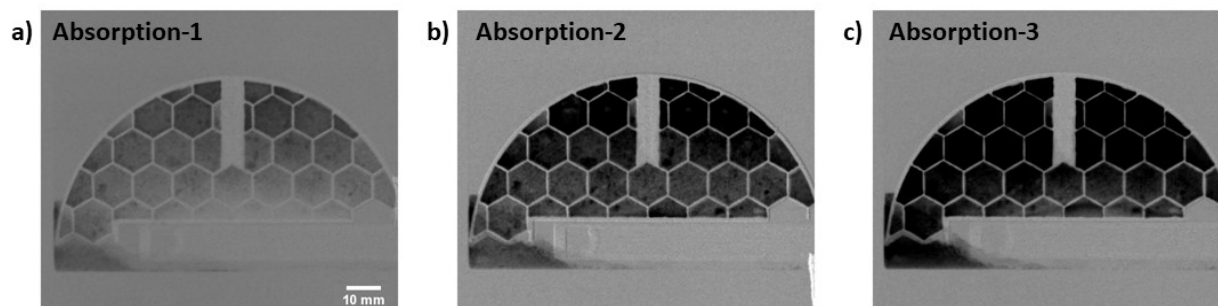


Figure 3. Neutron radiography images. The series of normalized images representing the sample after each absorption process **a)** absorption-1, **b)** absorption-2 and **c)** absorption-3.

The different transmission $I(\lambda)$ at the end of each NH_3 absorption process suggests a different extent of NH_3 uptake (see Figure 3). Transmission values $I(\lambda)$ were obtained by marking a hexagonal area in one cell of the honeycomb (cell-1, Figure 4a) and calculating the mean value over the selected area. Figure 4a presents the mean $I(\lambda)$ change over time in this cell. The graph shows a clear difference in transmission between the absorption-1, absorption-2 and absorption-3. During absorption-3, a lower greyscale value of 0.357 was reached compared to the absorption-1 and absorption-2, where the greyscale values were 0.622 and 0.551 at the end of absorption, respectively. This is the result of powder expansion during the NH_3 absorption processes and formation of macroporous structure [9], which creates paths for more NH_3 to diffuse into the powder bed during the following absorption processes. For this reason, absorption-2 and absorption-3 resulted in more ammoniated areas in the radiography images than those observed in absorption-1 (Figure 3). However, as seen in Figure 4, the change in the transmission $I(\lambda)$ with time, for a given absorption, does not stabilize to minimal values suggesting that the absorption processes were not completed.

The pressure in the system was monitored during the NH_3 absorption (see Figure 4b). As the reservoir was heated and NH_3 was released from the $\text{Sr}(\text{NH}_3)_8\text{Cl}_2$ salt in the reservoir, the pressure of the system increased to 2.5 bar, which is the equilibrium pressure of $\text{Sr}(\text{NH}_3)_8\text{Cl}_2$ at 70 °C. Once the NH_3 absorption process started in the THS reactor, the pressure was stabilized due to the equal rate of NH_3 release from $\text{Sr}(\text{NH}_3)_8\text{Cl}_2$ in the reservoir and the NH_3 absorption by SrCl_2 in the THS honeycomb structure.

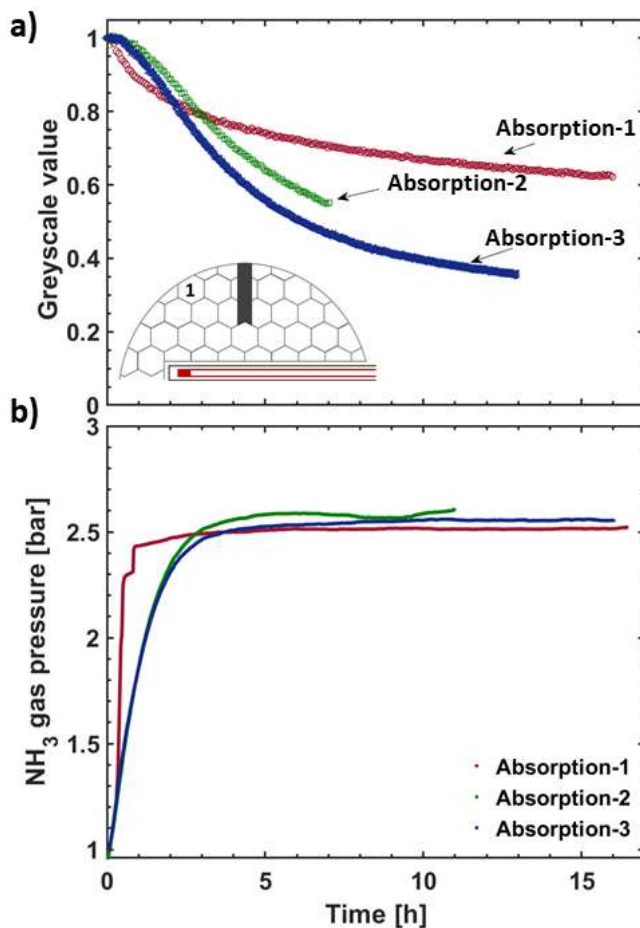


Figure 4. NH_3 gas absorption in SrCl_2 contained in the THS reactor. **a)** the change in transmission $I(\lambda)$ in the cell-1 and **b)** NH_3 gas pressure during the absorption processes.

A more detailed analysis of the $\text{Sr}(\text{NH}_3)_8\text{Cl}_2$ formation during absorption-2 and absorption-3 was performed on selected cells of the honeycomb. Mean transmission values $I(\lambda)$ were calculated by averaging over the area of the selected cells during the first 7 hours of absorption. The results are plotted in Figure 5 for absorption-2 (a) and absorption-3 (b), respectively. It can be observed that the formation of $\text{Sr}(\text{NH}_3)_8\text{Cl}_2$ is inhomogeneous over the honeycomb volume. The NH_3 distribution in the different cells of the honeycomb differs depending on their position within the honeycomb. Figure 5a shows that the topmost cells have the lowest mean greyscale value (higher concentration of NH_3) between 0.603 and 0.528 (cell-1, -2, -3 and -4) whereas the cells in the bottom (cell-9, -10, -11 and -12) have higher mean greyscale values (lower concentration of NH_3) between 0.756 and 0.744. The same trend can be seen during the third absorption process (Figure

5b). The lowest mean greyscale value calculated was 0.459 in the cell-3, whereas the highest value was 0.783 in the cell-11. Cell-5, -6, -7 and -8 located in the middle of the honeycomb show intermediate mean greyscale value between 0.579 and 0.613, which means that the NH_3 concentration in those cells is the intermediate between the NH_3 concentration in the top and bottom cells.

Several reasons might contribute to these results. Firstly, it should be noted that the NH_3 gas inlet was placed at the top right of the THS reactor, letting the powder particles on top cells absorb NH_3 gas earlier than the powder contained in the lower cells. Secondly, the free space between the THS reactor inner walls and the honeycomb allowed some powder to fall out of the honeycomb.

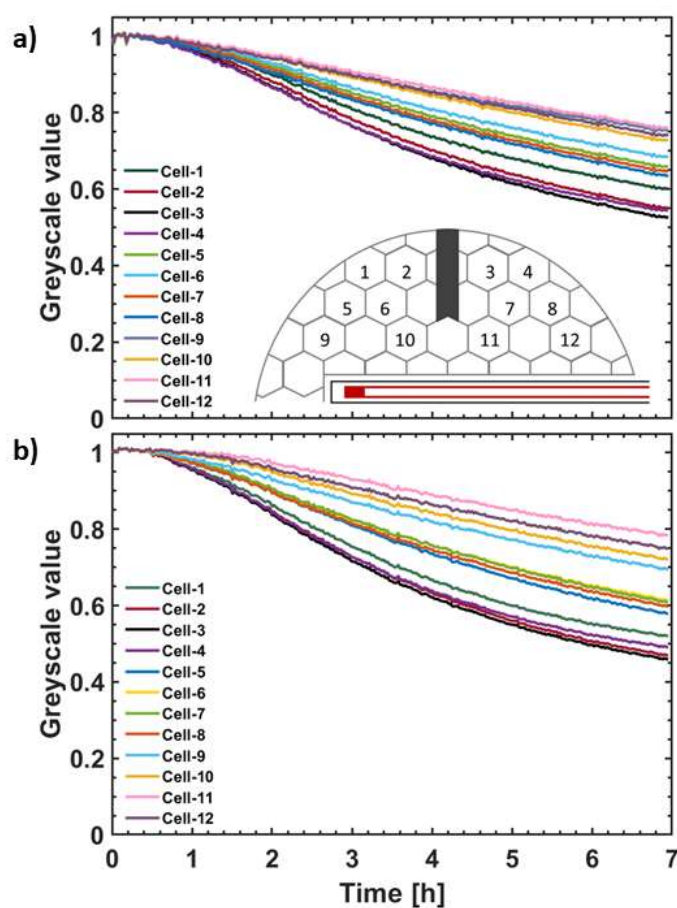


Figure 5. The change in transmission $I(\lambda)$ through the powder during **a)** absorption-2 and **b)** absorption-3. The schematic view of the honeycomb with selected and numbered cells is included in graph a.

Therefore, the powder thickness over the honeycomb was inhomogeneous, providing different amount of SrCl_2 salt in the different cells of the honeycomb and resulting in different NH_3 concentration. Finally, the honeycomb with the salt was prepared in an inert argon atmosphere, which filled the THS reactor prior to the start of the experiment. The THS reactor was not evacuated before the first NH_3 absorption process, so Ar gas was still present inside the reactor during absorption. The different densities of Ar and NH_3 gases, 1.661 kg/m^3 and 0.717 kg/m^3 at RT, respectively, might have created layers of NH_3 gas on the top and Ar on the bottom, preventing a homogeneous NH_3 gas flow towards the bottom of the THS reactor.

The expansion of $\text{Sr}(\text{NH}_3)_8\text{Cl}_2$ over time during the NH_3 uptake was studied by placing the honeycomb horizontally so that powder thickness change is perpendicular to the neutron beam. Side-view images were obtained while performing a NH_3 absorption process. The volume expansion of the $\text{Sr}(\text{NH}_3)_8\text{Cl}_2$ powder within the honeycomb is shown in Figure 6. The expansion of the $\text{Sr}(\text{NH}_3)_8\text{Cl}_2$ in axial direction with time can be observed. The packing within the honeycomb prevented the $\text{Sr}(\text{NH}_3)_8\text{Cl}_2$ powder from expanding in the radial direction, while free space between the honeycomb and THS reactor wall allowed the axial expansion. During this process NH_3 absorption over time produced a gradual expansion of the salt by up to 10% in height.

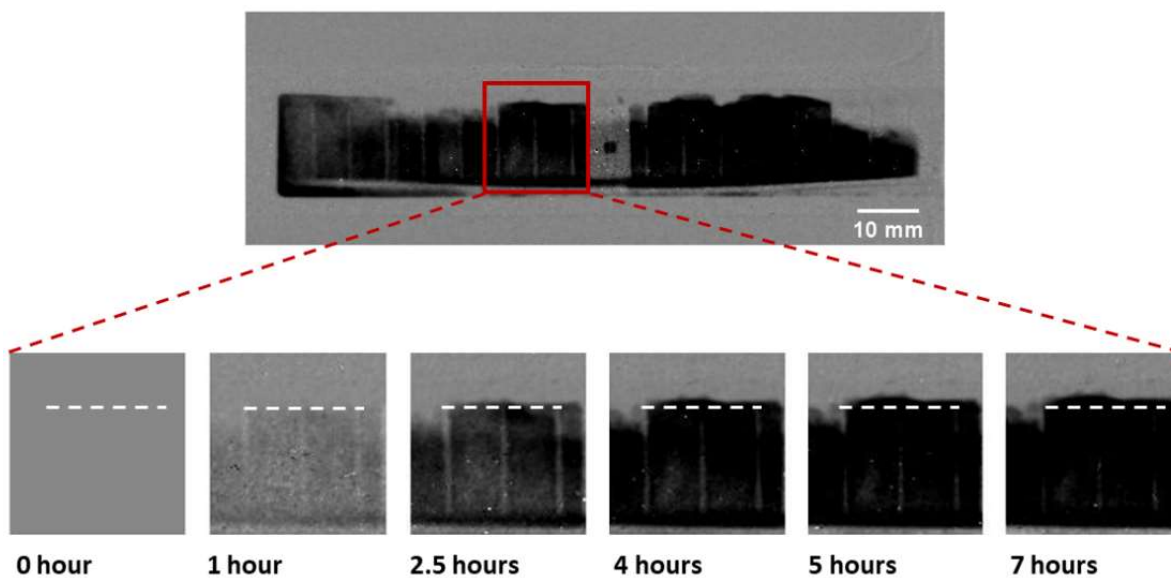


Figure 6. Series of images showing the expansion of the salt during the NH_3 absorption process with time in selected area of the honeycomb. The white dashed line shows the initial height of the powder. (Full-size image above the series was acquired at the 4th hour of absorption-4).

4.1.3.2 Desorption process

Neutron radiography was carried out on the THS reactor during the desorption processes at selected temperatures. The two desorption processes were performed at 220 °C and 100 °C at 1 bar of ammonia pressure, and full release of NH_3 was observed after 46 minutes and 3 hours 45 minutes, respectively. During desorption at 220 °C $\text{Sr}(\text{NH}_3)_8\text{Cl}_2$ was decomposed into SrCl_2 and NH_3 , while at 100 °C the end products were $\text{Sr}(\text{NH}_3)\text{Cl}_2$ and NH_3 . This is due to two-step desorption occurring in $\text{Sr}(\text{NH}_3)_8\text{Cl}_2$ at the given temperatures and ammonia pressure of 1 bar [6,9,10].

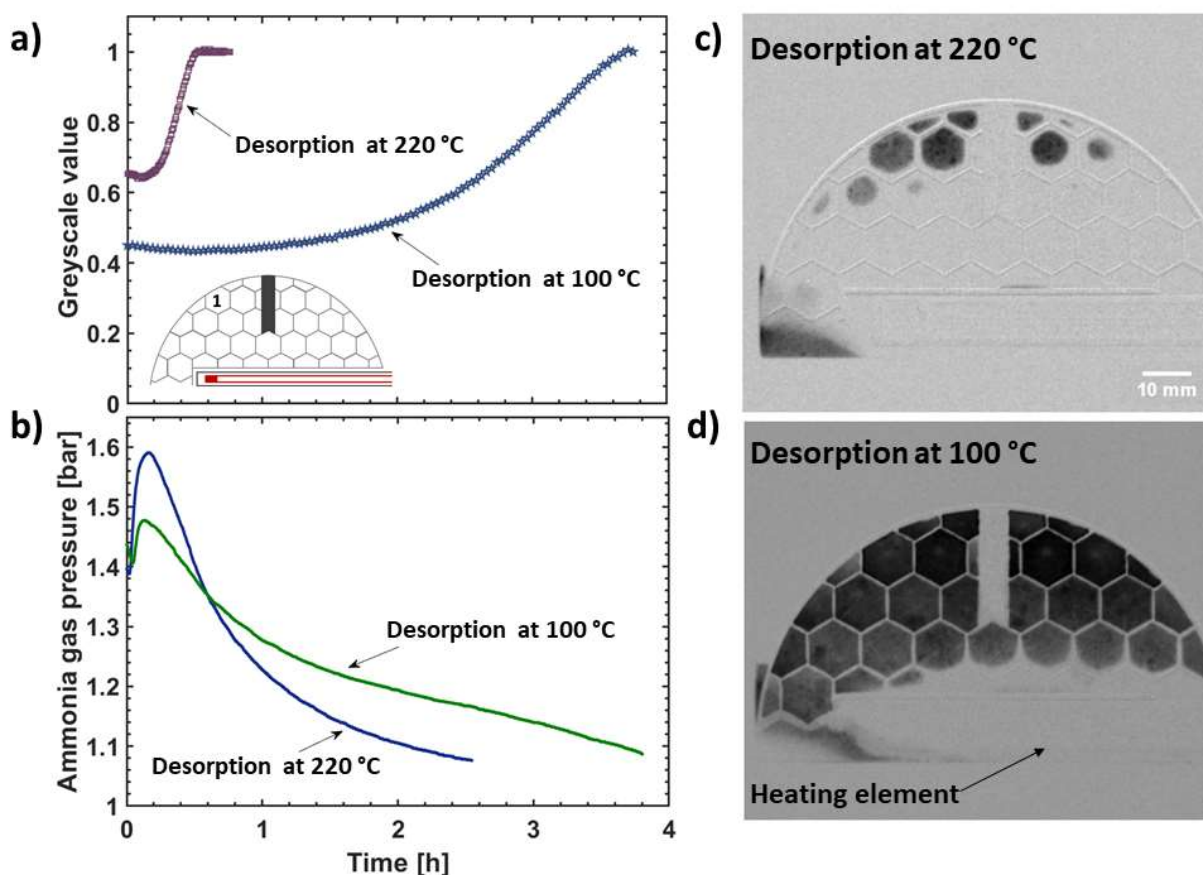


Figure 7. The desorption processes of $\text{SrCl}_2(\text{NH}_3)_8$ at 220 °C and 100 °C: **(a)** changes of the transmission $I(\lambda)$ and **(b)** corresponding pressure profile. Transmission images obtained after 20 minutes of NH_3 desorption processes performed at **(c)** 220 °C and **(d)** 100 °C.

Figure 7a and b show the change in transmission $I(\lambda)$ in the cell-1 and the pressure profile of the system during desorption processes. At 220 °C, the pressure increased drastically because of the large amount of NH_3 gas released in a short time and started decreasing after few minutes as NH_3 is absorbed in the reservoir. Figure 7c and d show the transmission images of the honeycomb 20 minutes after the start of the desorption processes. The decomposition of $\text{SrCl}_2(\text{NH}_3)_8$ into SrCl_2 and NH_3 is almost complete after 20 minutes at 220 °C. The powder in the cells closer to the heat source desorbed NH_3 faster than the powder in cells further away from the heating source. It should be mentioned that the special stainless-steel honeycomb was prepared to provide a higher heat transfer. The hexagon-shaped cells should provide efficient heat transmission from cell to cell and thus improving the NH_3 desorption efficiency of the whole plate. The images in Figure 7 show that heat conductivity of the stainless-steel was not sufficient for ensuring homogeneous NH_3 release. The NH_3 desorption process within all 12 cells was analyzed and included in the supplementary information (Figure A.1).

In order to observe the NH_3 release in detail, selected cells of the honeycomb were analyzed. The rate of desorption in each cell volume was studied by drawing lines parallel to the hexagon edges and measuring the transmission $I(\lambda)$ integrated along those lines and plotted as a function of time (see Figure 8). The lines are at distance of 2 mm from each edge of the hexagon. The NH_3 gas release over time at the sides of the cells gives us information about the heat efficiency of the total stainless-steel net since NH_3 release takes place only when $\text{Sr}(\text{NH}_3)_8\text{Cl}_2$ salt is heated.

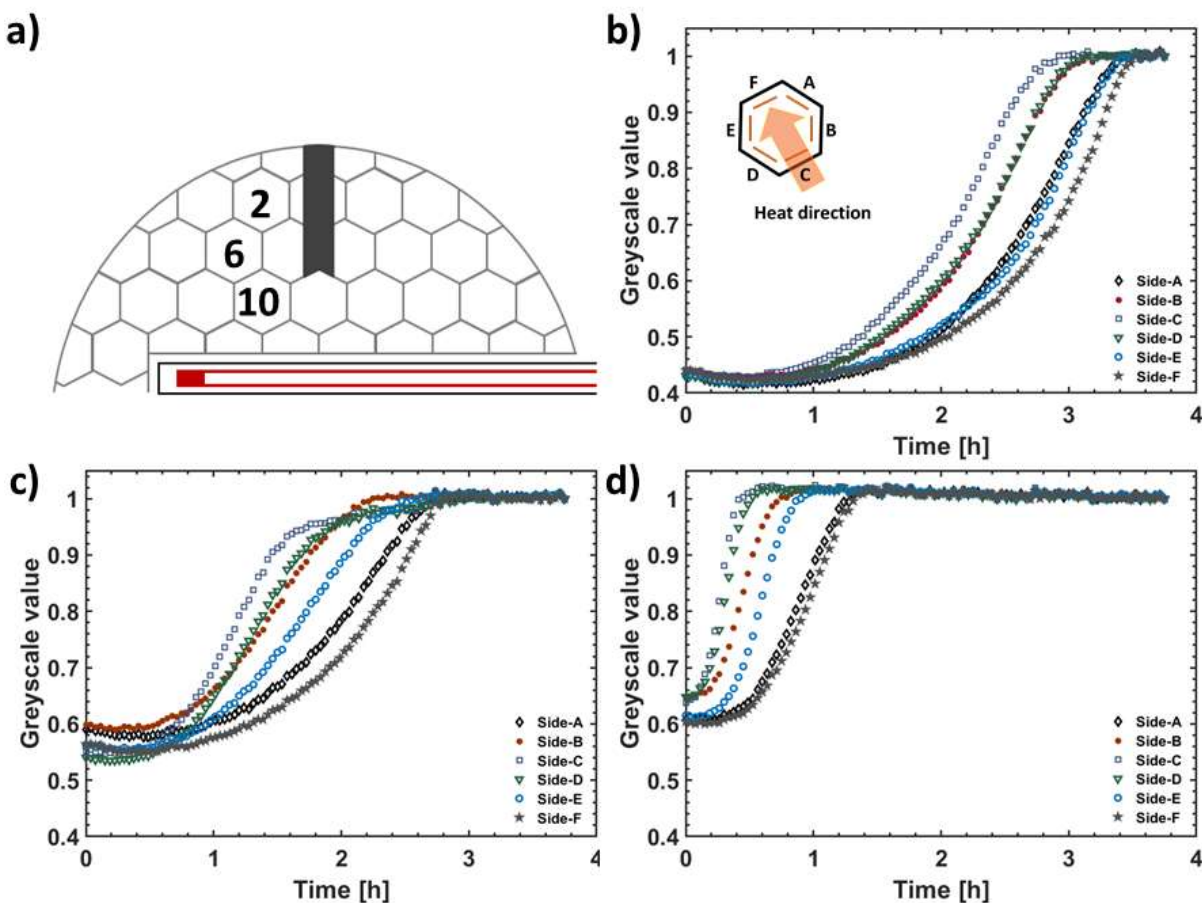


Figure 8. The change of transmission $I(\lambda)$ integrated along the selected volumes of the powder during desorption process at 100 °C **a)** a schematic view of the honeycomb with the selected cells and the changes in transmission $I(\lambda)$ along the lines drawn in cell-2 **(b)**, cell-6 **(c)** and cell-10 **(d)**. The heat direction is shown in the graph and is approximately the same in all three cases **(b)**.

Figure 8a shows a schematic view of the honeycomb and three cells selected for investigation of the change of NH_3 concentration during the desorption process at 100 °C. Figure 8b, c and d illustrate the drop of NH_3 content along the lines in the cell-2, 6 and 10, respectively.

In all three cells we see that the release of NH_3 is not uniform, and it changes according to the heat direction. The transmission through the absorbed NH_3 along the lines also strongly depends on the position of the analyzed area with respect to the relative distance from the heating element. The bottom-right edges, i.e. closer to the heat source (B, C and D) are those where NH_3 is released

earlier, indicating that they are the first to be heated. On the other hand, the top-left ones (A, E and F) are those where NH_3 is released later, pointing out they are heated later. Overall, the desorption of NH_3 from powder in the top parts of one cell happens mainly because of the heat is transferred through the salt inside the cell rather than from the cell walls. Besides, full NH_3 release happened within 1.5 hours in cell-10, which is the closest to the heating element, whereas NH_3 desorption was completed after about 3 and 3.5 hours in cell-6 and cell-2, the furthest from the heat source, respectively. The different time for NH_3 release in different areas of the honeycomb indicates that the stainless steel is not an ideal material for the efficient heat transfer, as the desorption process is inhomogeneous both along the honeycomb and within each cell. Similar calculations for other cells were performed and are included as supplementary information (Figure A.2).

4.1.3.3 Neutron Tomography

Ex-situ tomography studies were performed on the THS reactor, which was disconnected from the reservoir and placed vertically in front of the neutron beam. 3D images of the THS reactor after one absorption and desorption cycle (Figure 9a), after NH_3 absorption (Figure 9b) and after partial NH_3 desorption (Figure 9c) were obtained and visualized. A clear contrast between $\text{Sr}(\text{NH}_3)_8\text{Cl}_2$ and SrCl_2 can be observed. To visualize the partially desorbed state of the salt a desorption process during in-situ neutron radiography measurements was terminated after 30 minutes and the scan over 360° was performed on the sample.

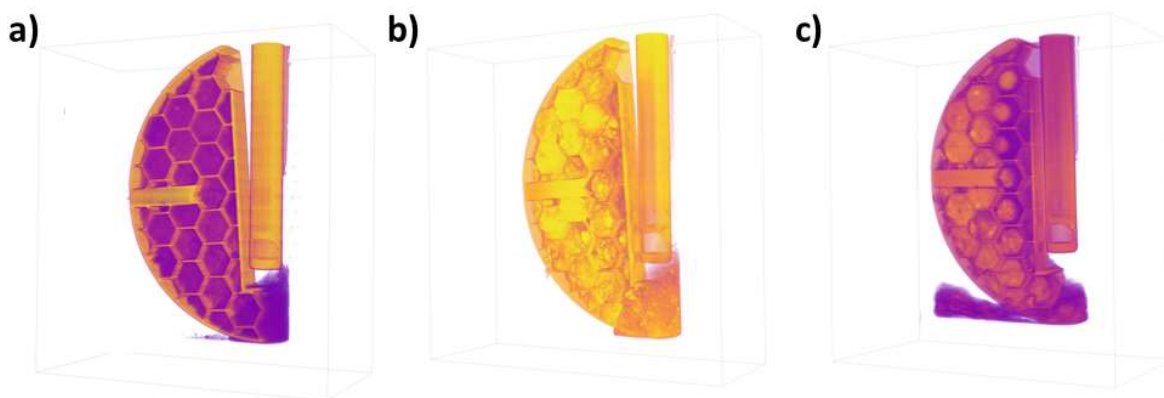


Figure 9. 3D visualization of the honeycomb created with Tomviz software a) fully desorbed SrCl_2 salt, b) $\text{Sr}(\text{NH}_3)_8\text{Cl}_2$ and c) the salt with partially desorbed NH_3 . The colors of the different states are arbitrary and represented by the transmission through the absorbed NH_3 intensities.

In all 3D visualizations sample powders outside the honeycomb can be noticed. This was also observed in the series of images acquired during absorption and shown in the Figure 3. The sample thickness irregularity in the honeycomb cells confirms that the powder was initially inside the cells. Each radiography/tomography switch during the experiments required the movement of the THS reactor from horizontal to vertical positions causing loose powder to fall from the honeycomb and movement of the honeycomb itself loosing contact with the heating element.

$\text{Sr}(\text{NH}_3)\text{Cl}_2$ in the Figure 9b shows that the powder occupies a slightly bigger volume in the cells compared to SrCl_2 (a), due to the SrCl_2 powder expansion during NH_3 absorption and shrinkage after NH_3 desorption. The 3D visualization of the partially desorbed state in Figure 9c confirms the direction of the desorption reaction discussed above (Figure 8) and that the $\text{Sr}(\text{NH}_3)_8\text{Cl}_2$ powder in the cells close to the heating element started releasing NH_3 first.

The 3D visualization of the $\text{Sr}(\text{NH}_3)_8\text{Cl}_2$ in Figure 9b was further analyzed by cutting orthogonal slices and studying the reactor in different planes. This allowed for a detailed view “inside” the investigated sample. This is shown in Figure 10, which displays the $\text{Sr}(\text{NH}_3)_8\text{Cl}_2$ powder in the honeycomb viewed through the XY and YZ-planes. The powder separated by the cell walls can be recognized and the irregular height of the powder both within each cell and over the honeycomb is confirmed. Additionally, a significant deformation of the honeycomb is observed by viewing the sample through two different planes.

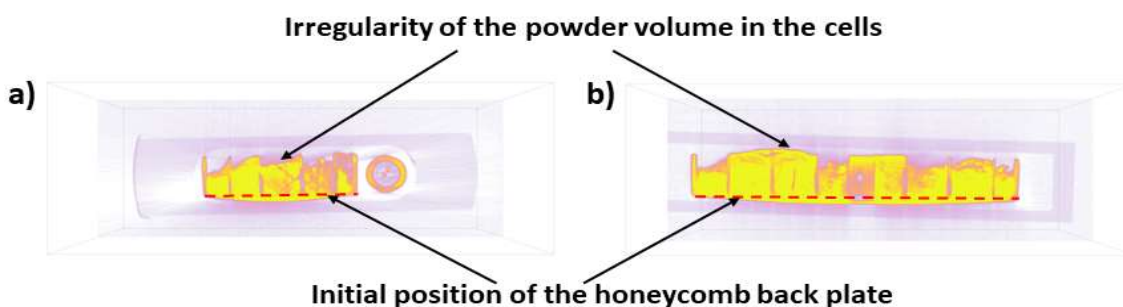


Figure 10. Deformation of the honeycomb back plate after the NH_3 absorption process a) XY-plane, slice $z=394$ and b) YZ-plane, slice $x=310$. The red dashed lines represent the position of the back plate before the absorption process.

In Figure 10 the red dashed line represents the original position of the honeycomb back plate, being flat before the experiments, but is found bended after the NH_3 absorption. This is likely caused by the SrCl_2 expansion occurring during NH_3 absorption and formation of $\text{Sr}(\text{NH}_3)_8\text{Cl}_2$. The stainless steel cell walls kept the powder from expanding in the radial direction, while the open front of the honeycomb allowed the powder to expand in the axial direction as displayed in Figure 6. This volume expansion caused stresses on the honeycomb back plate pushing it away from the honeycomb net. It should be noted that the back plate was welded to the honeycomb only along outer edges, but not to the entire net, making it vulnerable to potential stresses.

4.1.3.4 Feasibility of quantitative analysis of the acquired neutron imaging data

This work was focused only on the qualitative analysis of the obtained neutron imaging data. While it is generally possible to perform quantitative analysis from neutron imaging data, several uncertainties prevented us from quantifying in a reliable manner the NH_3 content in the investigated sample. In principle, the NH_3 content in the powder can be calculated from the neutron attenuation coefficient of NH_3 . When neutrons pass through the sample, they are attenuated according to the Beer-Lambert's law:

$$I(\lambda) = I_0 e^{-\mu(\lambda)x}$$

where I is an attenuated beam intensity, I_0 is an intensity behind a sample, μ is the neutron attenuation coefficient, λ is the neutron wavelength and x is the thickness of the sample. Here the dependence on neutron wavelength is neglected since the variation of the neutron attenuation coefficient of NH_3 and SrCl_2 for the herein used thermal spectrum does not affect the presented qualitative results. For a precise quantitative analysis, it would be proper to use monochromatic beam, which on the other hand would result in worse time resolution. Thus, for the presented experiment, using whole available spectrum was advantageous. The small sample thickness allows to neglect the beam hardening effect [34].

As seen from the 2D and 3D images, some amount of powder fell off the honeycomb causing irregularities in the powder thickness over the volume. The honeycomb was open on one side for facilitating the interaction between NH_3 and SrCl_2 . This allowed for some of the SrCl_2 to be displaced outside the honeycomb while mounting the reactor on the sample stage. As a result, the

initial thickness of the powder in the honeycomb changed and could not be determined accurately for further calculation of the NH_3 wt.%.

Finally, it should also be noted that the incoherent scattering from hydrogen contained in the NH_3 molecule results in additional errors. In particular, incoherent scattering causes the transmission behind the sample values to appear higher than the real value. This can lead to underestimate the thickness of the volume occupied by NH_3 and, in turn, the NH_3 concentration. A method for improving the quantification of neutron imaging measurements with scintillator-camera based detectors by correcting for biases introduced by scattered neutrons using reference measurement with a grid of neutron absorbers called black bodies (BB) was developed [35–37]. However, this method was not applied during the neutron imaging experiment discussed in this work.

4.1.4 Summary

Neutron imaging is an excellent method for evaluating NH_3 distribution in the $\text{SrCl}_2 / \text{Sr}(\text{NH}_3)_8\text{Cl}_2$ system. It offers a unique possibility to study simultaneously NH_3 spatial distribution and the structural changes in the sample such as volume expansion of the powder during NH_3 absorption, which in turn might produce mechanical stresses on the THS reactor. In this work, we showed the inhomogeneous formation of $\text{Sr}(\text{NH}_3)_8\text{Cl}_2$ during NH_3 absorption processes which was possibly due to the location of the NH_3 gas inlet in the reactor and the presence of Ar in the cell at the beginning of the experiment. The latter remained at the bottom of the cell preventing NH_3 absorption in some parts of the powder. It was also shown that the stainless-steel honeycomb structure was not efficient for transferring the heat from the heating element to the edges of the honeycomb during the NH_3 desorption processes, as slower desorption kinetics are observed in the regions farthest away from the heater. Additional investigations by neutron tomography showed that the back plate supporting the honeycomb structure was deformed after the volume expansion during NH_3 absorption in the powder.

The results presented here demonstrate that neutron imaging techniques are ideal and powerful tools for investigating thermochemical heat storage prototype systems and provided critical information on SrCl_2 powder behavior upon NH_3 absorption and desorption reactions. Based on these results, some improvements – e.g. a honeycomb disc made of a material with better heat

conductivity than stainless steel – will be implemented and tested. The outcome of those tests will be crucial for designing a safe and efficient THS reactor.

4.1.5 Acknowledgements

This work is funded by NordForsk Nordic Neutron Science Programme through the Neutrons for Heat Storage (NHS) project (No. 82206). The authors thank the Heinz Maier-Leibnitz Zentrum for neutron radiation beam time allocation and particularly Thomas Buecherl for experimental assistance. Furthermore, the Danish Research Council is greatly acknowledged for the financial support of the neutron measurements via DANSCATT.

4.1.6 Supplementary materials

Supplementary material associated with this article can be found, in the online version, at doi:10.1016/j.est.2020.101388.

4.1.7 References

- [1] D. Aydin, S.P. Casey, S. Riffat, The latest advancements on thermochemical heat storage systems, *Renew. Sustain. Energy Rev.* 41 (2015) 356–367.
<https://doi.org/10.1016/j.rser.2014.08.054>.
- [2] P.A.J. Donkers, L.C. Sogutoglu, H.P. Huinink, H.R. Fischer, O.C.G. Adan, A review of salt hydrates for seasonal heat storage in domestic applications, *Applied Energy*. 199 (2017) 45–68. <https://doi.org/10.1016/j.apenergy.2017.04.080>.
- [3] H. Jarimi, D. Aydin, Z. Yanan, G. Ozankaya, X. Chen, S. Riffat, Review on the recent progress of thermochemical materials and processes for solar thermal energy storage and industrial waste heat recovery, *Int. J. Low-Carbon Technol.* 14 (2019) 44–69.
<https://doi.org/10.1093/ijlct/cty052>.
- [4] L.C. Sogutoglu, P.A.J. Donkers, H.R. Fischer, H.P. Huinink, O.C.G. Adan, In-depth investigation of thermochemical performance in a heat battery: Cyclic analysis of K_2CO_3 , $MgCl_2$ and Na_2S , *Applied Energy*. 215 (2018) 159–173.
<https://doi.org/10.1016/j.apenergy.2018.01.083>.

-
- [5] T. Yan, Z.H. Kuai, S.F. Wu, Experimental investigation on a $\text{MnCl}_2\text{-SrCl}_2/\text{NH}_3$ thermochemical resorption heat storage system - ScienceDirect, 147 (2020) 874–883. <https://doi.org/10.1016/j.renene.2019.09.033>.
- [6] T. Vegge, R.Z. Sørensen, A. Klerke, J.S. Hummelshøj, T. Johannessen, J.K. Nørskov, C.H. Christensen, 19 - Indirect hydrogen storage in metal ammines, in: G. Walker (Ed.), Solid-State Hydrog. Storage, Woodhead Publishing, 2008: pp. 533–564. <https://doi.org/10.1533/9781845694944.4.533>.
- [7] C.H. Christensen, R.Z. Sørensen, T. Johannessen, U.J. Quaade, K. Honkala, T.D. Elmøe, R. Kähler, J.K. Nørskov, Metal ammine complexes for hydrogen storage, *J. Mater. Chem.* 15 (2005) 4106–4108. <https://doi.org/10.1039/B511589B>.
- [8] A. Klerke, C.H. Christensen, J.K. Nørskov, T. Vegge, Ammonia for hydrogen storage: challenges and opportunities, *J. Mater. Chem.* 18 (2008) 2304–2310. <https://doi.org/10.1039/B720020J>.
- [9] S. Lysgaard, A.L. Ammitzbøll, R.E. Johnsen, P. Norby, U.J. Quaade, T. Vegge, Resolving the stability and structure of strontium chloride amines from equilibrium pressures, XRD and DFT, *Int. J. Hydrog. Energy.* 37 (2012) 18927–18936. <https://doi.org/10.1016/j.ijhydene.2012.09.129>.
- [10] R.E. Johnsen, P.B. Jensen, P. Norby, T. Vegge, Temperature- and Pressure-Induced Changes in the Crystal Structure of $\text{Sr}(\text{NH}_3)_8\text{Cl}_2$, *J. Phys. Chem. C.* 118 (2014) 24349–24356. <https://doi.org/10.1021/jp508076c>.
- [11] A. Bialy, P.B. Jensen, D. Blanchard, T. Vegge, U.J. Quaade, Solid solution barium–strontium chlorides with tunable ammonia desorption properties and superior storage capacity, *J. Solid State Chem.* 221 (2015) 32–36. <https://doi.org/10.1016/j.jssc.2014.09.014>.
- [12] M. Strobl, I. Manke, N. Kardjilov, A. Hilger, M. Dawson, J. Banhart, Advances in neutron radiography and tomography, *J. Phys. Appl. Phys.* 42 (2009) 243001. <https://doi.org/10.1088/0022-3727/42/24/243001>.
- [13] A. Baruj, M. Ardito, J. Marín, F. Sánchez, E.M. Borzone, G. Meyer, Design and Characterization of a Hydride-based Hydrogen Storage Container for Neutron Imaging Studies, *Phys. Procedia.* 69 (2015) 491–495. <https://doi.org/10.1016/j.phpro.2015.07.069>.
-

-
- [14] Ł. Gondek, N.B. Selvaraj, J. Czub, H. Figiel, D. Chapelle, N. Kardjilov, A. Hilger, I. Manke, Imaging of an operating $\text{LaNi}_{4.8}\text{Al}_{0.2}$ -based hydrogen storage container, *Int. J. Hydrog. Energy*. 36 (2011) 9751–9757. <https://doi.org/10.1016/j.ijhydene.2011.05.089>.
- [15] F. Heubner, A. Hilger, N. Kardjilov, I. Manke, B. Kieback, Ł. Gondek, J. Banhart, L. Röntzsch, In-operando stress measurement and neutron imaging of metal hydride composites for solid-state hydrogen storage, *J. Power Sources*. 397 (2018) 262–270. <https://doi.org/10.1016/j.jpowsour.2018.06.093>.
- [16] M.G. Makowska, L.T. Kuhn, H.L. Frandsen, E.M. Lauridsen, S. De Angelis, L.N. Cleemann, M. Morgano, P. Trtik, M. Strobl, Coupling between creep and redox behavior in nickel - yttria stabilized zirconia observed in-situ by monochromatic neutron imaging, *J. Power Sources*. 340 (2017) 167–175. <https://doi.org/10.1016/j.jpowsour.2016.11.059>.
- [17] P. Boillat, E.H. Lehmann, P. Trtik, M. Cochet, Neutron imaging of fuel cells – Recent trends and future prospects, *Curr. Opin. Electrochem.* 5 (2017) 3–10. <https://doi.org/10.1016/j.coelec.2017.07.012>.
- [18] J. Zhang, D. Kramer, R. Shimoi, Y. Ono, E. Lehmann, A. Wokaun, K. Shinohara, G.G. Scherer, In situ diagnostic of two-phase flow phenomena in polymer electrolyte fuel cells by neutron imaging: Part B. Material variations, *Electrochimica Acta*. 51 (2006) 2715–2727. <https://doi.org/10.1016/j.electacta.2005.08.010>.
- [19] M. Siegwart, R.P. Harti, V. Manzi-Orezzoli, J. Valsecchi, M. Strobl, C. Grünzweig, T.J. Schmidt, P. Boillat, Selective Visualization of Water in Fuel Cell Gas Diffusion Layers with Neutron Dark-Field Imaging, *J. Electrochem. Soc.* 166 (2019) F149–F157. <https://doi.org/10.1149/2.1011902jes>.
- [20] D.S. Hussey, D.L. Jacobson, M. Arif, K.J. Coakley, D.F. Vecchia, In Situ Fuel Cell Water Metrology at the NIST Neutron Imaging Facility, *J. Fuel Cell Sci. Technol.* 7 (2010). <https://doi.org/10.1115/1.3007898>.
- [21] I. Manke, H. Markötter, C. Tötze, N. Kardjilov, R. Grothausmann, M. Dawson, C. Hartnig, S. Haas, D. Thomas, A. Hoell, C. Genzel, J. Banhart, Investigation of Energy-Relevant Materials with Synchrotron X-Rays and Neutrons, *Adv. Eng. Mater.* 13 (2011) 712–729. <https://doi.org/10.1002/adem.201000284>.
-

-
- [22] A. Senyshyn, M.J. Mühlbauer, K. Nikolowski, T. Pirling, H. Ehrenberg, “In-operando” neutron scattering studies on Li-ion batteries, *J. Power Sources*. 203 (2012) 126–129. <https://doi.org/10.1016/j.jpowsour.2011.12.007>.
- [23] G.V. Riley, D.S. Hussey, D. Jacobson, In Situ Neutron Imaging Of Alkaline and Lithium Batteries, *ECS Trans*. 25 (2010) 75–83. <https://doi.org/10.1149/1.3414005>.
- [24] Z. Nie, P. McCormack, H.Z. Bilheux, J.C. Bilheux, J.P. Robinson, J. Nanda, G.M. Koenig, Probing lithiation and delithiation of thick sintered lithium-ion battery electrodes with neutron imaging, *J. Power Sources*. 419 (2019) 127–136. <https://doi.org/10.1016/j.jpowsour.2019.02.075>.
- [25] K. Kino, M. Yonemura, Y. Kiyonagi, Y. Ishikawa, Joseph.Don. Parker, T. Tanimori, T. Kamiyama, First Imaging Experiment of a Lithium Ion Battery by a Pulsed Neutron Beam at J-PARC/MLF/BL09, *Phys. Procedia*. 69 (2015) 612–618. <https://doi.org/10.1016/j.phpro.2015.07.087>.
- [26] N. Kardjilov, I. Manke, A. Hilger, M. Strobl, J. Banhart, Neutron imaging in materials science, *Mater. Today*. 14 (2011) 248–256. [https://doi.org/10.1016/S1369-7021\(11\)70139-0](https://doi.org/10.1016/S1369-7021(11)70139-0).
- [27] N. Kardjilov, I. Manke, R. Woracek, A. Hilger, J. Banhart, Advances in neutron imaging, *Mater. Today*. 21 (2018) 652–672. <https://doi.org/10.1016/j.mattod.2018.03.001>.
- [28] S.N. Gunasekara, M. Laios, A. Karabanova, V. Martin, D. Blanchard, Numerical Design of a Reactor-Heat Exchanger Combined Unit for Ammonia-SrCl₂ Thermochemical Storage System, *ISES SWC2019-1551* (2019) 1-12.
- [29] T. Bücherl, S. Söllradl, NECTAR: Radiography and tomography station using fission neutrons, *J. Large-Scale Res. Facil. JLSRF*. 1 (2015) 19. <https://doi.org/10.17815/jlsrf-1-45>.
- [30] ImageJ2: ImageJ for the next generation of scientific image data | BMC Bioinformatics | Full Text, (n.d.). <https://bmcbioinformatics.biomedcentral.com/articles/10.1186/s12859-017-1934-z> (accessed October 23, 2019).
- [31] A.P. Kaestner, MuhRec—A new tomography reconstructor, *Nucl. Instrum. Methods Phys. Res. Sect. Accel. Spectrometers Detect. Assoc. Equip.* 651 (2011) 156–160. <https://doi.org/10.1016/j.nima.2011.01.129>.
-

-
- [32] M.D. Hanwell, C.J. Harris, A. Genova, J. Schwartz, Y. Jiang, R. Hovden, Tomviz: Open Source Platform Connecting Image Processing Pipelines to GPU Accelerated 3D Visualization, *Microsc. Microanal.* 25 (2019) 408–409. <https://doi.org/10.1017/S1431927619002770>.
- [33] E.H. Lehmann, P. Vontobel, N. Kardjilov, Hydrogen distribution measurements by neutrons, *Appl. Radiat. Isot.* 61 (2004) 503–509. <https://doi.org/10.1016/j.apradiso.2004.03.075>.
- [34] R. Hassanein, F. de Beer, N. Kardjilov, E. Lehmann, Scattering correction algorithm for neutron radiography and tomography tested at facilities with different beam characteristics, *Phys. B Condens. Matter.* 385–386 (2006) 1194–1196. <https://doi.org/10.1016/j.physb.2006.05.406>.
- [35] P. Boillat, C. Carminati, F. Schmid, C. Grünzweig, J. Hovind, A. Kaestner, D. Mannes, M. Morgano, M. Siegwart, P. Trtik, P. Vontobel, E.H. Lehmann, Chasing quantitative biases in neutron imaging with scintillator-camera detectors: a practical method with black body grids, *Opt. Express.* 26 (2018) 15769–15784. <https://doi.org/10.1364/OE.26.015769>.
- [36] P. Trtik, E.H. Lehmann, Progress in High-resolution Neutron Imaging at the Paul Scherrer Institut - The Neutron Microscope Project, *J. Phys. Conf. Ser.* 746 (2016) 012004. <https://doi.org/10.1088/1742-6596/746/1/012004>.
- [37] C. Carminati, P. Boillat, F. Schmid, P. Vontobel, J. Hovind, M. Morgano, M. Raventos, M. Siegwart, D. Mannes, C. Gruenzweig, P. Trtik, E. Lehmann, M. Strobl, A. Kaestner, Implementation and assessment of the black body bias correction in quantitative neutron imaging, *PLOS ONE.* 14 (2019) e0210300. <https://doi.org/10.1371/journal.pone.0210300>.

4.2 Paper III: Comparison between Numerical Simulation and Neutron Radiography of Ammonia Ab- and Desorption in SrCl₂ for Application in Thermochemical Storage System for Waste Heat Recovery



Eurotherm Seminar #112
Advances in Thermal Energy Storage



EUROTHERM112-O-269

Comparison between Numerical Simulation and Neutron Radiography of Ammonia Ab- and Desorption in SrCl₂ for Application in Thermochemical Storage System for Waste Heat Recovery

Anastasiia Karabanova^{1*}, Perizat Berdiyeva², Stefano Soprani¹, Rune E. Johnsen¹,
Stefano Deledda², Didier Blanchard¹

¹Department of Energy Conversion and Storage, Technical University of Denmark, Frederiksborgvej 399, DK-4000 Roskilde, Denmark

²Institute for Energy Technology, P.O. Box 40, NO-2027 Kjeller, Norway

*Corresponding author e-mail: anaka@dtu.dk

Abstract

To support the transition to a fossil-free society, energy storage and particularly thermal energy storage have been identified as strategic technologies. Large quantities of thermal energy – both per weight and price - can be stored reversibly in SrCl₂ upon exo-/endothermal ab-/desorption of ammonia. To achieve high efficiency of an ammonia-based heat storage system, the heat and mass transfer within the reactive salt bed must be well understood and analyzed. For this purpose, we combined theoretical and experimental methods. While a COMSOL Multiphysics 3D model was developed to study heat and mass transfer in the reactor, neutron radiography was used as an experimental imaging tool to study the ammonia ab-/desorption *in-situ* in the salt bed and validate the 3D model. The initial model is able to model some of the main features in the experimental kinetic ab-/desorption curves, but refinement of the model parameters is needed to further improve the model. The 3D model will be used to optimize the design of the reported reactor and may also be adopted to similar heat storage systems.

Keywords: Thermochemical Heat Storage (TCHS), Sr(NH₃)_xCl₂, COMSOL modelling, neutron radiography, model validation

4.2.1 Introduction

Over the past decade, energy storage has been identified by the European Commission as a topic of utmost importance for the ongoing transformation of the European energy system. Specifically, Thermal Energy Storage (TES) is expected to play an important role in increasing the overall efficiency of energy systems [1,2]. This is particularly true for systems producing waste heat at temperatures below 100°C, so-called low-grade waste heat, which according to the recent studies accounts for more than 45% of the global primary energy consumption [3].

Within the framework of the project “Neutrons for Heat Storage”, a first prototype of a thermochemical heat storage (TCHS) system, utilizing heat of the temperature up to 100°C, is constructed. The basic principle of the system operation is shown on a simple schematic with two vessels, one with a salt and another one with liquid ammonia (Figure 1).

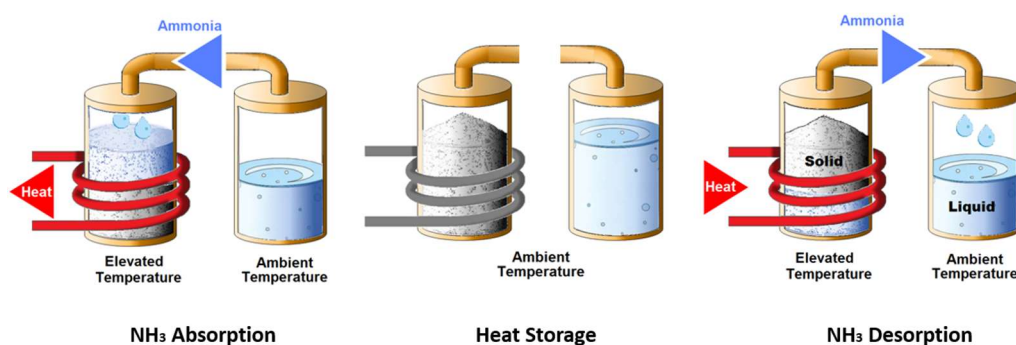
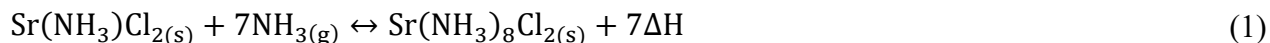


Figure 1. Sketch of a TCHS system working in three different modes: absorption, storage, and desorption, corresponding to heat production, heat storage, and heat adsorption, respectively.

In the heat storage mode, the connection between the two vessels is closed, and the heat can be stored for any period without significant energy losses. If the two vessels are connected, the ammonia flows from the liquid ammonia container into the reactor where it gets absorbed by the salt and the heat of absorption is released. During desorption, the molecules of ammonia are detached from the salt by the supplied heat and are condensed in the liquid ammonia container. The system is considered to go through a full cycle upon the completion of two half-cycles, which are absorption and desorption.

The heat is stored and recovered thanks to the reversible reaction between gaseous ammonia and solid SrCl₂. One molecule of SrCl₂ can absorb up to eight molecules of ammonia among which only seven can be desorbed at the temperature of low-grade heat:



where ΔH is the reaction enthalpy equal to 41.432 kJ/mole of NH₃ [4].

One of the main components of the system - the reactor - consists of a vessel containing a U-shape tube and eleven honeycomb structure discs filled with powdered SrCl₂ salt. In the effort of rationalizing the design of the reactor, the present study aims at investigating heat and mass transfer processes occurring in the honeycomb structure half-disc representing a basis element of the whole reactor. To study the transport processes in the TCHS system, neutron radiography was selected as a complementary technique to numerical modeling for two main reasons. First, ammonia (NH₃) contains hydrogen, and hydrogen has a neutron scattering cross section, which allows tracking the evolution of the ammonia concentration in the salt bed during ammonia cycling. Second, neutrons have high penetrating power giving the opportunity to study materials in bulky reactors. A numerical model was developed to investigate the transport processes in the reactor over ammonia cycling. The results from neutron radiography were used to calibrate and validate the model which may be used for rationalizing and optimizing the design of the TCHS reactor.

4.2.2 Materials and methods

4.2.2.1 Neutron imaging experiments: setup and operation

The set-up for the neutron imaging experiments consisted of a cell and a cartridge with ammoniated SrCl₂ used as an ammonia source during absorption and as an ammonia sink during desorption (Figure 2).

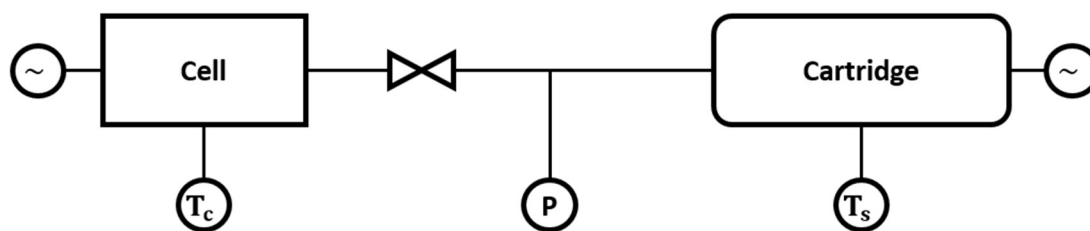


Figure 2. Schematic of experimental set-up for the neutron imaging experiments.

The cell comprised a stainless steel honeycomb structure half-disc of 10 cm diameter and 1 cm height with SrCl_2 embedded in its slots and a stainless steel heating element of 0.8 cm diameter and 8 cm length equipped with a thermocouple (Figure 3). Both the disc and the element were enclosed in an aluminum container. The aluminum container was closed with an aluminum lid connected to the cartridge with ammonia. Aluminum is almost transparent for neutrons. The cartridge could be replaced with a vacuum pump for the system evacuation. To follow and record the pressure evolution in the system during the ab-/desorption experiments, a pressure transducer P was installed in between the two parts of the system.

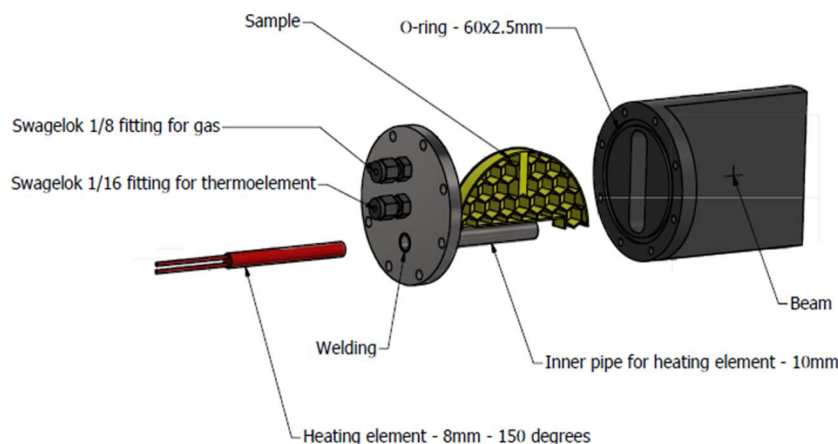


Figure 3. The cell for the neutron radiography experiments.

Given the fact that SrCl_2 swells up by three times after the first absorption, while it maintains the developed porous structure for the subsequent ab-/desorption cycles, the amount of the salt required for the full occupation of the honeycomb slots was calculated as one third of the total

volume of the slots. Knowing the mass of the salt and the total volume, the porosity of strontium chloride mono- and octaammine was quantified by calculating the change in the true density of the powdered salt over cycling. This variation was assumed linear with the advancement of the reaction. The true densities of $\text{Sr}(\text{NH}_3)\text{Cl}_2$ and $\text{Sr}(\text{NH}_3)_8\text{Cl}_2$ were calculated starting from the crystallographic data, i.e. the size of the unit cell and the sum of the weight of all atoms in the unit cell, as reported in [5]. The results of the calculation are presented in Table 1.

Table 1. Cell and materials parameters.

Total volume of the honeycomb slots, m^3	2.02×10^{-5}
True density of SrCl_2 , kg/m^3	3050
True density of $\text{Sr}(\text{NH}_3)\text{Cl}_2$, kg/m^3	2441
True density of $\text{Sr}(\text{NH}_3)_8\text{Cl}_2$, kg/m^3	1394
Tap density of SrCl_2 , kg/m^3	1525
Mass of SrCl_2 , kg	1.03×10^{-2}
Porosity of $\text{Sr}(\text{NH}_3)\text{Cl}_2$	0.79
Porosity of $\text{Sr}(\text{NH}_3)_8\text{Cl}_2$	0.38

Before the start of the experiments, the whole system was evacuated with the vacuum pump for 15 min. For the absorption, the temperature in the cartridge was set to 76°C to desorb its ammonia, while the cell was kept at room temperature to absorb the ammonia. Reverse procedure was applied during the desorption, the temperature of the heating element in the cell was set to 100°C , and the cartridge was kept at room temperature. The pressure in the cell was 1.2 ± 0.1 bar during the desorption. During the absorption, the initial pressure was 1 bar rising up to 2.6 bar by the end of the reaction.

4.2.2.2 COMSOL model

Geometry and Domains

For the numerical investigations, only the cell represented by the stainless steel honeycomb structure half-disc with SrCl₂ embedded in its slots is taken into consideration. The half-disc is enclosed in an insulating block filled with ammonia gas at the cell ammonia pressure P_{cell}. For the simulation reproducing the neutron results, the experimental values of P_{cell} are used as input values. Depending on whether the salt is subject to ammonia absorption or desorption, there is an ammonia inlet or outlet in the block. For the simplicity of the numerical model, the heating element is omitted in the geometry, and in case of desorption the temperature of the wall in contact with the heating element is set to 100°C.

The following assumptions were made while formulating the 3D numerical model:

1. Local thermal equilibrium exists between the gas and the solid particles;
2. Heat transfer through the bed is by conduction only;
3. Inside the honeycomb slots, the material is treated as a porous media composed of the three phases: NH₃, Sr(NH₃)Cl₂, and Sr(NH₃)₈Cl₂. Knowing the properties of each phase, the effective properties of the porous media have been defined (See below).

The geometry is divided into three domains, and each domain is characterized by different materials, the properties of which are presented in Table 2.

Material properties for ammonia such as thermal conductivity k_{NH_3} and specific heat capacity C_{p,NH_3} were taken from Engineering Equation Solver (EES 2016) and interpolated linearly. Ammonia density was derived based on the ideal gas law equation:

$$\rho_{NH_3}(p, T) = \frac{P_{cell} \cdot MW_{NH_3}}{RT} \quad (2)$$

where P_{cell} is the pressure in the cell, MW_{NH3} is ammonia molecular weight, R is the ideal gas constant, and T is the temperature of gaseous ammonia.

In the model the honeycomb slots domain was homogenized into a porous media, and in order to describe the behavior of the salt, effective material properties defined as the expressions below were used.

$$(\rho C_p)_{\text{eff}} = \varepsilon(x) \cdot \rho_{\text{NH}_3} \cdot C_{p, \text{NH}_3} + (1 - \varepsilon(x)) \cdot \rho_{\text{salt}}(x) \cdot C_{\text{salt}}(T, x) \quad (3)$$

Table 2. Modelled domain and materials properties. The full expressions are reported in Equations (2-10).

Domain	Component	Material	Density (kg/m ³)	Thermal conductivity (W/(m*K))	Specific heat capacity (J/(kg*K))
1	Ammonia	NH _{3(g)}	$\rho_{\text{NH}_3}(P, T)$	$k_{\text{NH}_3}(T)$	$C_{p, \text{NH}_3}(P, T)$
2	Honeycomb slots	NH ₃ Sr(NH ₃)Cl ₂ Sr(NH ₃) ₈ Cl ₂	$\rho_{\text{eff}}(P, T, x)$	$k_{\text{eff}}(T, x)$	$C_{p, \text{eff}}(P, T, x)$
3	Honeycomb structure	Stainless steel	7950	20	490

$$k_{\text{eff}} = \varepsilon(x) \cdot k_{\text{NH}_3} + (1 - \varepsilon(x)) \cdot k_{\text{salt}}(x) \quad (4)$$

where ε is the salt porosity, x is degree of desorption/absorption or reaction advancement, ρ_{salt} is the salt density, C_{salt} is the salt specific heat capacity, and k_{salt} is the salt thermal conductivity.

All the properties of the salt depend on the degree of the reaction x (desorption or absorption) defined in the following way:

Table 3. Definition of reaction advancement for absorption and desorption.

x=0	Absorption: the ammonia is fully desorbed, and the salt is in the form of $\text{Sr}(\text{NH}_3)\text{Cl}_2$ Desorption: the ammonia is fully absorbed, and the salt is in the form of $\text{Sr}(\text{NH}_3)_8\text{Cl}_2$
x=1	Absorption: the ammonia is fully absorbed, and the salt is in the form of $\text{Sr}(\text{NH}_3)_8\text{Cl}_2$ Desorption: the ammonia is fully desorbed, and the salt is in the form of $\text{Sr}(\text{NH}_3)\text{Cl}_2$

For the calculation of intermediate reaction advancement, the properties of the salt were assumed linear between the non-ammoniated and fully ammoniated states. For desorption, the equations describing the salt properties are listed below:

$$\rho_{\text{salt}} = x \cdot \rho_{\text{Sr}(\text{NH}_3)_1\text{Cl}_2} + (1 - x) \cdot \rho_{\text{Sr}(\text{NH}_3)_8\text{Cl}_2} \quad (5)$$

$$C_{\text{salt}} = \frac{x \cdot \rho_{\text{Sr}(\text{NH}_3)_1\text{Cl}_2} \cdot C_{\text{Sr}(\text{NH}_3)_1\text{Cl}_2} + (1-x) \cdot \rho_{\text{Sr}(\text{NH}_3)_8\text{Cl}_2} \cdot C_{\text{Sr}(\text{NH}_3)_8\text{Cl}_2}}{x \cdot \rho_{\text{Sr}(\text{NH}_3)_1\text{Cl}_2} + (1-x) \cdot \rho_{\text{Sr}(\text{NH}_3)_8\text{Cl}_2}} \quad (6)$$

$$k_{\text{salt}} = x \cdot k_{\text{Sr}(\text{NH}_3)_1\text{Cl}_2} + (1 - x) k_{\text{Sr}(\text{NH}_3)_8\text{Cl}_2} \quad (7)$$

$$\varepsilon(x) = x \cdot \varepsilon_{\text{Sr}(\text{NH}_3)_1\text{Cl}_2} + (1 - x) \cdot \varepsilon_{\text{Sr}(\text{NH}_3)_8\text{Cl}_2} \quad (8)$$

where $\rho_{\text{Sr}(\text{NH}_3)_1\text{Cl}_2}$, $C_{\text{Sr}(\text{NH}_3)_1\text{Cl}_2}$, $k_{\text{Sr}(\text{NH}_3)_1\text{Cl}_2}$, $\rho_{\text{Sr}(\text{NH}_3)_8\text{Cl}_2}$, $C_{\text{Sr}(\text{NH}_3)_8\text{Cl}_2}$, $k_{\text{Sr}(\text{NH}_3)_8\text{Cl}_2}$ are density, specific heat capacity, and thermal conductivity of strontium chloride monoamine and octaamine, respectively.

The listed above equations were used for the determination of the corresponding salt properties during absorption as well but with the correction for reversibility when x was substituted by (1-x) and (1-x) by x.

The expressions of specific heat capacities of strontium chloride mono- and octaamine were taken from [6] and are presented below:

$$C_{\text{SrCl}_2(\text{NH}_3)_1} = 649.8 + 3.524 \cdot T + 0.0021 \cdot T^2 + 0.00016 \cdot T^3 \quad (9)$$

$$C_{\text{SrCl}_2(\text{NH}_3)_8} = 576.296 + 3.124 \cdot T + 0.07 \cdot T^2 + 0.00005 \cdot T^3 \quad (10)$$

Since no experimental data was found for the thermal conductivity of strontium chloride mono- and octaammine, it was assumed to be 1.1 W/(m*K) for both of the salts consistently with the measurements reported in [7].

Mathematical modeling

Assuming no fluid dynamics, the equations governing heat transfer in the honeycomb structure and the honeycomb slots can be written as follows:

$$\rho_{ss} C_{ss} \frac{\partial T}{\partial t} + \nabla(-k_{ss} \nabla T) = 0 \quad (11)$$

$$(\rho c_p)_{\text{eff}} \frac{\partial T}{\partial t} + \nabla(-k_{\text{eff}} \nabla T) = Q \quad (12)$$

$$Q = \pm \frac{dx(t)}{dt} \cdot N_s \cdot \Delta H \quad (13)$$

where ρ_{ss} , C_{ss} , k_{ss} are the density, the specific heat capacity and the thermal conductivity of stainless steel, respectively. Q is the heat sink/source during desorption/absorption and N_s is the molar density of ammonia in honeycomb slots.

The reaction rate equation describing the kinetics of the gas-solid reaction was expressed as follows:

$$\frac{dx}{dt} = f(x) \cdot k(P, T) \quad (14)$$

where $f(x)$ is a function describing the rate-controlling step of reaction, $k(T,P)$ is a rate constant of reaction as a function of temperature and pressure:

$$k(P, T) = k_0 e^{-\frac{E_a}{RT}} \cdot g(P) \quad (15)$$

Where k_0 is the pre-exponential factor, E_a is the activation energy of reaction, and $g(P)$ is the pressure impact function expressing the degree of the discrepancy between the actual gas pressure in the system and the equilibrium gas pressure over the salt. This factor can be written as follows [8]: $g(P) = ((P - P_{\text{eq}})/P_{\text{eq}})^m$ for absorption and $g(P) = ((P_{\text{eq}} - P)/P_{\text{eq}})^m$ for desorption. P_{eq} is defined by the van't Hoff equation:

$$P_{eq} = P_0 e^{-\frac{\Delta H}{RT} + \frac{\Delta S}{R}} \quad (16)$$

Where P_0 is a reference pressure equal to 1 Pa, ΔS is the reaction entropy equal to 228.6 J/mole of NH_3 for Equation (1) [4].

The kinetic parameters and functions for the working pair $\text{SrCl}_2\text{-NH}_3$ were already defined by Huang *et al.* [9]. However, in the mentioned study the value of activation energy for the desorption is lower than the reaction enthalpy which is in contradiction with the endothermic nature of desorption. Thus, to correct this value a series of kinetics experiments were performed using a Sieverts-type apparatus. The kinetics curves obtained from the experiments were treated according to the procedure reported by Chaise *et al.* and Li *et al.* [10,11], and as a result new values of the kinetic parameters were obtained (Table 4).

Table 4. The literature and experimental values of the kinetics parameters.

Parameter	Absorption		Desorption	
	Literature	Experiment	Literature	Experiment
f(x)	$(1-x)^{2.96}$	$2(1-x)^{3/2}$	$(1-x)^{3.02}$	$4(1-x)^{1/4}$
k_0	0.019	28.1	0.125	$1.8 \cdot 10^8$
E_d	6921	31	9000	75000
m	1	1	1	0.44

4.2.3 Results and discussion

From neutron radiography, grayscale images showing ammonia distribution over the cell in time were obtained. During the absorption, the light-grey strontium chloride monoamine was reacting with ammonia and being converted into dark-grey strontium chloride octaamine. The reverse process was observed for the desorption: because of the supplied heat, dark-grey $\text{Sr}(\text{NH}_3)_8\text{Cl}_2$ was losing ammonia and being transformed into $\text{Sr}(\text{NH}_3)\text{Cl}_2$ appearing as light-grey.

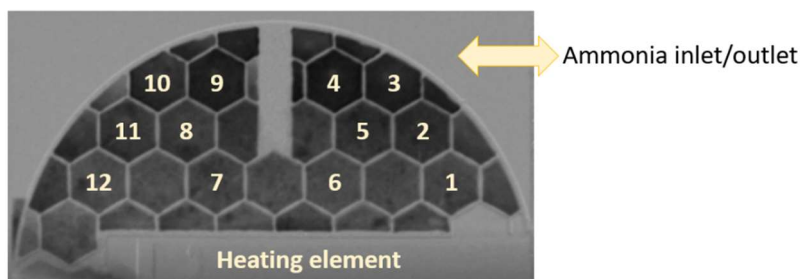


Figure 4. Neutron radiography image of desorption at $t = 0$ s with indexed hexagons.

Assuming that in the beginning and in the end of the half-cycles there was either pure monoamine or octaamine, experimental results presenting the dependence of the reaction advancement versus time were obtained and plotted as in Figure 5. While Figures 5a and 5c are the results obtained from a single hexagon of the honeycomb structure, Figures 5b and 5d show an average value of the numbered hexagons in Figure 4. The results obtained from the numerical model were also plotted in Figure 5 for comparison.

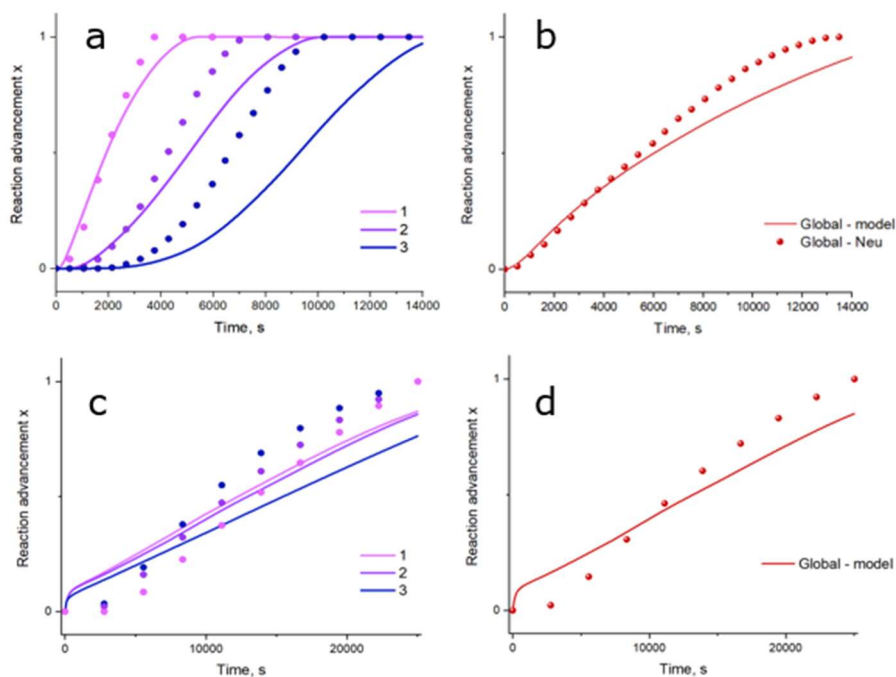


Figure 5. Kinetic curves of desorption (a, b) and absorption (c, d) shown as dotted line for experiments and as solid line for numerical model.

In Figure 5a, describing the desorption in the individual hexagons, while the sigmoidal shape of the experimental results is well captured by the model, a discrepancy appears when the desorption proceeds, which is even larger when the hexagon is further away from the heat source. As a result, the global kinetic curve (Figure 5b) obtained from the modelled desorption coincides with the experimental results until 4000 s. Thereafter, the model does not reproduce the experimental data with a good agreement, as the reaction appears to slow down. The reason for the observed mismatch could be due to errors in the value of the thermal conductivity or specific heat capacity of the porous media, or could originate from the poor description of the heat transfer between the honeycomb walls and the salt. This is the topic of further investigation.

For the absorption results showed in Figures 5c and 5d, the shape of the modelled curves do not correspond to the experimental ones at the beginning of the reaction. The modelled absorption starts sharply, which is consistent with our expectations, but the experimental data show that the absorption starts only after 3000 s. The explanation for the delay in the neutron imaging results could be that the initial cell pressure was inferior to the equilibrium pressure at room temperature or that the temperature of the salt bed was above the expected room temperature. Since the pressure was being recorded during the experiment, and it was made sure to be high enough for the start of the absorption at room temperature, it suggests that the reactive salt bed was not cooled down to room temperature after the preceding desorption, and the surplus of heat suppressed the reaction at the beginning. After 3000 s, the experimental reaction started and proceeded faster than what is predicted by the model. Again, as for the desorption, the discrepancy between the model and experimental results suggest that adjustment of the thermal properties of the porous media and/or introduction of the heat transfer coefficient between the salt and the honeycomb structure are needed. Another observation to make is that in the experiment the fastest reaction rate is observed for the hexagon closer to the ammonia inlet, while the opposite results were obtained for the model. The reasons for this could be that the fluid dynamics was not included in the model, and the pressure of ammonia was almost constant within the cell during the simulation. Therefore, the next step of this work will be to build a numerical model including fluid dynamics.

4.2.4 Conclusions

In the present study, the comparison between neutron radiography and numerical simulation of ammonia ab-/desorption in SrCl_2 is presented. While the numerical model coupling the reaction kinetic with heat transfer is in a reasonable agreement with the experimental data, discrepancies exist and call for improvement of the model:

1. Ammonia fluid dynamics is to be introduced in the model.
2. Thermal properties of the porous media have to be refined for a better description of the heat propagation during sorption processes.
3. Since in reality the contact between the porous media and the honeycomb structure is not ideal, thermal resistance in the contact area of the two domains have to be considered.

4.2.5 Acknowledgements

The authors would like to acknowledge the staff at the NECTAR beamline at FRM II for experimental assistance. NordForsk is acknowledged for financial support of the present work (project number 82206). The Danish Research Council is acknowledged for covering travel expenses in relation to the experiment (via DanScatt).

4.2.6 References

- [1] G. Allan Schrøder Pedersen, DTU (editor) Brian Elmegaard, DTU Claus Hviid Christensen, DONG Energy Claus Kjøller and R. A. Frank Elefsen, Danish Technological Institute John Bøgild Hansen, Haldor Topsøe A/S Jørgen Hvid, Rambøll A/S Per Alex Sørensen, PlanEnergi Søren Knudsen Kær, Aalborg University, Thomas Vangkilde-Pedersen, GEUS Thorkild Feldthusen Jensen, “Status and recommendations for RD&D on energy storage technologies in a Danish context,” *Danish energy Res. Program.*, no. February, 2014.
- [2] “Technology Roadmap,” *Encycl. Prod. Manuf. Manag.*, pp. 781–782, 2006.
- [3] C. Forman, I. K. Muritala, R. Pardemann, and B. Meyer, “Estimating the global waste heat potential,” *Renew. Sustain. Energy Rev.*, vol. 57, pp. 1568–1579, 2016.
- [4] L. Jiang and A. P. Roskilly, “Thermal conductivity, permeability and reaction characteristic

-
- enhancement of ammonia solid sorbents: A review,” *Int. J. Heat Mass Transf.*, vol. 130, pp. 1206–1225, 2019.
- [5] S. Lysgaard, A. L. Ammitzbøll, R. E. Johnsen, P. Norby, U. J. Quaade, and T. Vegge, “Resolving the stability and structure of strontium chloride amines from equilibrium pressures, XRD and DFT,” *Int. J. Hydrogen Energy*, vol. 37, no. 24, pp. 18927–18936, 2012.
- [6] T. Roettinger, “PERFORMANCE TESTING AND EVALUATION OF SOLID ABSORPTION SOLAR COOLING UNIT,” vol. 61, no. 2, 1997.
- [7] L. Jiang, L. W. Wang, Z. Q. Jin, R. Z. Wang, and Y. J. Dai, “Effective thermal conductivity and permeability of compact compound ammoniated salts in the adsorption/desorption process,” *Int. J. Therm. Sci.*, 2013.
- [8] R. Iwata, T. Yamauchi, Y. Hirota, M. Aoki, and T. Shimazu, “Reaction kinetics of ammonia absorption/desorption of metal salts,” *Appl. Therm. Eng.*, vol. 72, no. 2, pp. 244–249, 2014.
- [9] H. J. Huang, G. Bin Wu, J. Yang, Y. C. Dai, W. K. Yuan, and H. B. Lu, “Modeling of gas-solid chemisorption in chemical heat pumps,” *Separation and Purification Technology*, vol. 34, no. 1–3, pp. 191–200, 2004.
- [10] A. Chaise, P. De Rango, P. Marty, and D. Fruchart, “Experimental and numerical study of a magnesium hydride tank,” *Int. J. Hydrogen Energy*, vol. 35, no. 12, pp. 6311–6322, 2010.
- [11] Q. Li, K. C. Chou, Q. Lin, L. J. Jiang, and F. Zhan, “Hydrogen absorption and desorption kinetics of Ag-Mg-Ni alloys,” *Int. J. Hydrogen Energy*, vol. 29, no. 8, pp. 843–849, 2004.
-

4.3 Paper IV: Neutron Radiography for Modelling Thermochemical Heat Storage Reactors: Case Study on SrCl₂-NH₃ System

Anastasiia Karabanova¹, Perizat Berdiyeva², Stefano Soprani¹, Rune E. Johnsen¹, Bjørn C. Hauback², Stefano Deledda², Didier Blanchard^{1*}

¹*Department of Energy Conversion and Storage, Technical University of Denmark, Anker Engélunds Vej 301, DK-2800 Kgs. Lyngby, Denmark*

²*Department for Neutron Materials Characterization, Institute for Energy Technology, P.O. Box 40, NO-2027 Kjeller, Norway*

Abstract

Thermochemical heat storage (TCHS) may become a key technology in balancing intermittent renewables by regulating production and demand peaks as well as in increasing the efficiency of energy systems by reusing waste heat. Nowadays, there is a limited number of commercial products based on this technology, and for larger market penetration the improvement of the technology must be achieved. To advance a TCHS system, one has to pay a particular attention to studying the processes occurring inside the reactor. For the investigation of the sorption processes with further optimization of the reactor design, a numerical model of a thermochemical reactor, carefully validated at local and global levels, is of significant importance. In the present study, we propose a superior alternative to conventional techniques used for model validation, and this is neutron radiography. Using this techniques, we validated a three dimensional numerical model of a thermochemical heat storage reactor utilizing SrCl₂-NH₃ working pair. The results of the study demonstrate that the developed model describes the experimental neutron data, obtained at 2.6 bar and room temperature for absorption and at around 1.0 bar and 100°C for desorption, with a good agreement. In addition, the absorption model was successfully crosschecked using traditional experimental techniques (temperature and flowrate readings). The simulation model would be valid to describe any system, where gas-solid sorption processes are involved.

4.3.1 Introduction

In the effort of supporting the green energy transition in the next decades, thermal energy storage technologies are expected to play a major role in balancing supply and demand when intermittent renewable energy sources are used [1]. Moreover, these technologies can utilize waste heat, that is a product of industrial processes [2]. Among the three types of thermal energy storage - sensible, latent, and thermochemical - the latter has the advantage of achieving highest volumetric energy density with minor heat losses [3].

The processes occurring in a thermochemical heat storage (TCHS) system can be described with a general equation as follows:



where M is an absorbent/adsorbent in solid form (s); G is an absorptive/adsorptive in gaseous form (g), e.g. water vapor, hydrogen, ammonia; n is stoichiometric ratio; ΔH is the reaction enthalpy. The basics of a TCHS system are presented in Figure 1.

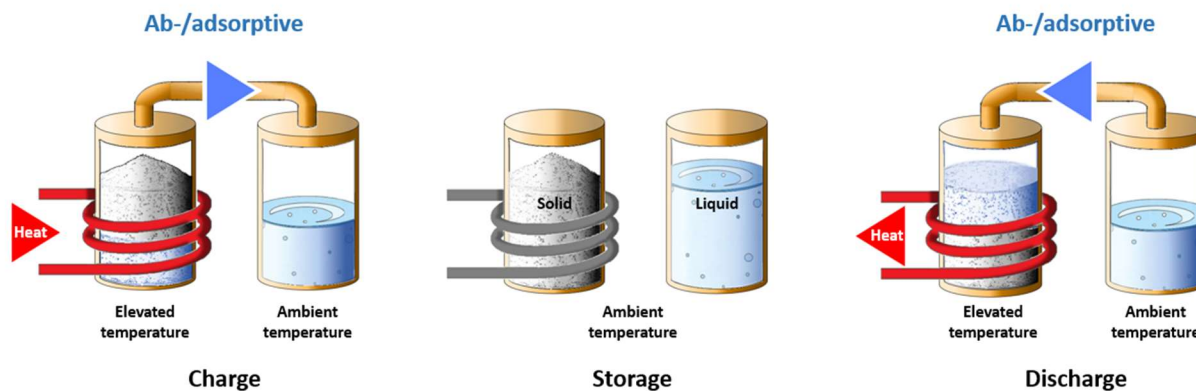


Figure 1. Sketch of a TCHS system operating in three working modes: charge, storage, and discharge.

As shown in Figure 1, the TCHS system has two main components – a reactor filled with a solid salt, i.e. an absorbent / adsorbent, and a tank with a liquid fluid, i.e. an absorptive / adsorptive. There are three modes, in which the system can exist – charge, storage, and discharge. During the process of charging, the heat supplied from outside initiates desorption of the fluid from the salt.

After desorption, the fluid in gaseous state condensates and is collected and stored in the tank. When the two materials are not in contact, the heat can be stored for any period (storage). During the discharge mode, the fluid converted from liquid to gaseous state reacts with the solid salt, which results in the release of absorption / adsorption heat. The system is considered to go through a full cycle upon the completion of two half-cycles, absorption and desorption.

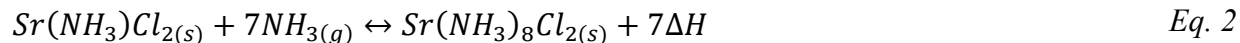
When developing the TCHS system, the design of a thermochemical heat reactor is of first importance, since it determines the dynamics of the system, i.e. the achievable heat power input and output. Therefore, an optimal reactor design should ensure optimal heat and mass transfer within the reactive bed to minimize the heat quantity needed in the charging mode while maximizing the heat power output in the discharge mode. Furthermore, the ultimate design should not impede the kinetics of the sorption reaction. To achieve this task, the standard approach is to build a numerical model of the reactor followed by its qualification with respect to experimental data.

There are several studies presenting numerical models of thermochemical reactors with validation against experimental data. In 2002, Huang *et al.* developed and validated a model coupling the kinetics of absorption/desorption between SrCl_2 and NH_3 with heat transfer [4]. Validation was conducted with respect to temperature data and global reaction advancement calculated as the change of liquid NH_3 level in an evaporator/condenser. In 2010, Chaise *et al.* developed a numerical model to investigate the charging and discharging performance of a MgH_2 packed bed reactor [5]. When validating the model, the authors used reading from seven thermocouples and global reaction advancement defined as pressure change during sorption processes. In another study published in 2019, Yuan *et al.* presented a numerical model of a reactor, where the kinetics of absorption and desorption between SrCl_2 and NH_3 is described. The model validation was conducted with respect to experimental tests, where the mass change of saturated NH_3 in a condenser / evaporator, referring to global reaction advancement, was measured [6]. Additionally, in 2019, the desorption process of $\text{Mg}(\text{OH})_2$ in a macroscale reactor was simulated with a model coupling chemical reaction with heat and mass transfer. The authors validated the model by comparing the temperature at two points in the reactor with experimental data [7].

Based on the conducted literature review, one can conclude that there are two types of experimental data used for validating a numerical model of a thermochemical reactor – local and global. Using local data, i.e. temperature readings, can reveal the degree of consistency between the model and the experimental results at specific points of the reactor, while utilizing global parameters like the change in the mass or in the level of condensed fluid, gives an opportunity to compare the model and the experimental kinetics curves within the reactive bed. Combining the two types of data gives a more complete picture of the processes occurring inside the reactor, which helps building models that are more reliable. However, when using this approach, crucial information on the behavior of the reaction front is still overlooked, and the comparison between the model and the experiment is incomplete, which may lead to biased simulations and eventually to wrong optimization of the reactor design.

To address these issues, neutron radiography can be a technique of choice for two main reasons. First, the fluid molecules used in TCHS systems, i.e. ammonia (NH_3), water (H_2O), or hydrogen (H_2), contain hydrogen atoms, and hydrogen atoms have one of the highest neutron scattering cross sections, which allows tracking the evolution of the fluid concentration in the salt bed during cycling. Second, neutrons have high penetrating power giving the opportunity to study materials in bulky reactors and sample environments. The viability of neutron radiography for studying hydrogen-based systems has been already demonstrated by several researches. For example, in 2018, the successful analysis of the spatio-temporal hydrogen content within metal hydride composites was presented by Heubner *et al.* [8]. In another research, conducted by Berdiyeva *et al.* [9] in 2020, *in-situ* neutron radiography was applied to investigate the distribution of NH_3 within SrCl_2 powder during absorption and desorption processes. In the present study, *in-situ* neutron radiography data is used for validating a numerical model of a thermochemical reactor at micro- and macroscopic scales for the first time.

We have used neutron radiography to confirm results obtained from a numerical model for a prototype of a TCHS reactor, in which heat is stored and recovered thanks to the reversible reaction between gaseous NH_3 and solid SrCl_2 . One mole of SrCl_2 can absorb up to eight moles of NH_3 , among which only seven can be desorbed at the temperature of low-grade heat:



where ΔH is the reaction enthalpy.

The prototype consists of a vessel containing eleven honeycomb structure discs (diameter: 10 cm; thickness: 1 cm) filled with powdered SrCl_2 salt, the active material volume being 0.5 l. Here, we present the results from neutron radiography and 3D simulation for a honeycomb half-disc, which represents a basic element of the reactor. The developed numerical model validated against neutron radiography results can be used for optimizing the design of the reactor as well as for modeling any gas-solid sorption reactors, of any geometry and active material, as long as material properties are reasonably described.

4.3.2 Materials and methods

To perform in-situ neutron radiography experiments, a gas setup suitable for absorption/desorption studies was constructed. Using this setup, in-situ absorption and desorption experiments have been performed at two different neutron facilities – ILL (Grenoble, France) and FRM II (Munich, Germany), respectively. The absorption was conducted at 2.60 bar and room temperature, while the desorption was carried out at around 1 bar and 100°C. The experimental conditions were used as an input for a 3D numerical model. The model couples chemical reaction with heat and mass transfer.

4.3.2.1 Sorption experiments

The gas setup for the neutron imaging experiments mainly consists of two vessels - a reactor and a cartridge with ammoniated SrCl_2 , the later being used as an NH_3 source during absorption and as an NH_3 sink during desorption in the reactor (Figure 2).

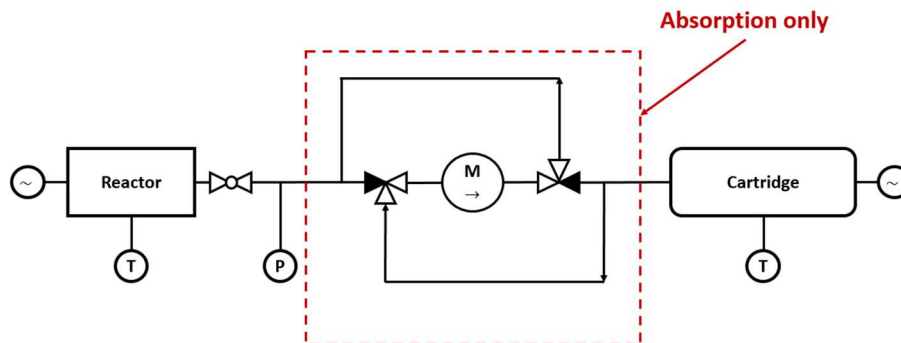


Figure 2. Schematic of the experimental setup for the neutron radiography experiments, where T is a thermocouple, P is a pressure transducer, and M is a flowmeter.

To follow and record the evolution of the pressure in the system during the ab-/desorption experiments, a pressure transducer was installed in-between the two vessels. For the absorption experiments, the setup was also equipped with a flowmeter (measuring range between 0 and 200 ml/min) for keeping track of the amount of NH_3 passing from the cartridge to the reactor. The cartridge could be replaced with a vacuum pump for the system evacuation. Data logging was performed via LabVIEW environment at regular intervals.

The reactor consisted of a cell containing a sample holder filled with powdered SrCl_2 and a stainless steel heating element equipped with a K-type thermocouple (Figure 3). In case of absorption experiment, another thermocouple, with its tip placed in the middle of the hexagon (see Figure 3), measured the temperature in the powder.

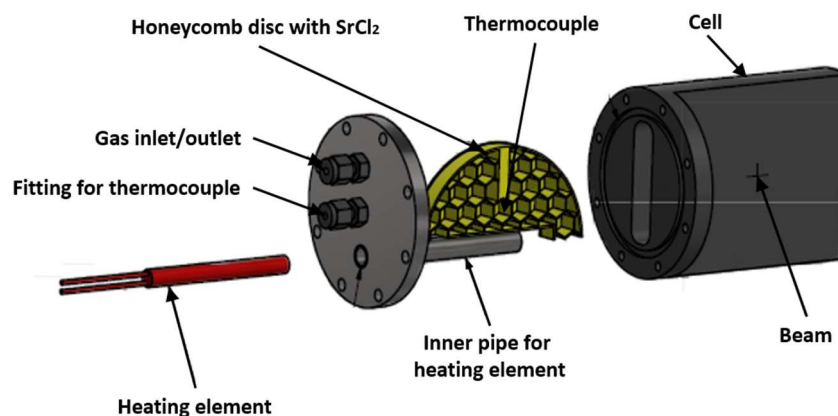


Figure 3. Schematic of the reactor for the neutron radiography experiments.

The cell was a rectangular prism container with the following dimensions: 110 mm in length, 21 mm in width, and 85 mm in height. The cell was made of aluminum, as this material is almost “transparent” for neutrons. The sample holder was the stainless steel honeycomb half-disc of 10 cm in diameter and 1 cm in height with SrCl₂ powder embedded in its slots. To make sure that the powder remains “seated” in the honeycomb slots, a stainless steel back plate was welded to one of the sides of the half-disc. The heating element was a stainless steel rod of 0.8 cm in diameter and 8 cm in length. The reactor was tightly closed with an aluminum lid connected to the rest of the gas system via Swagelok fittings.

Prior to loading the powder into the sample holder, it was left in a vacuum furnace for dehydration at 300°C for 12 h. Then, the dehydrated powder was evenly distributed within the half-disc, as shown in Figure 4. To avoid the contamination of the sample with water, its handling took place in an argon filled glove-box, where the monitored concentration of water was kept below 1 ppm.

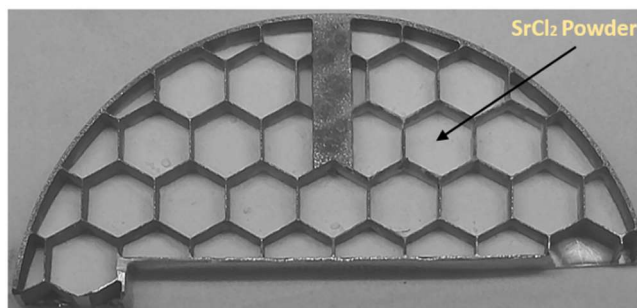


Figure 4. Sample holder filled with SrCl₂ powder before NH₃ cycling

The maximum amount of the salt required for full occupation of the honeycomb slots was calculated as one third of the total volume of the slots. This is because after the first absorption SrCl₂ swells up to three times its original volume and maintains the developed porous structure during the subsequent ab-/desorption cycles. Assuming no porosity in the pure powder, its maximum mass was calculated using Eq. 3:

$$m_{SrCl_2,max} = \frac{V_{total}}{3} \cdot \rho_{SrCl_2} \quad Eq. 3$$

where $m_{SrCl_2,max}$ is the maximum mass of SrCl₂; V_{total} is the volume of SrCl₂ after the first NH₃ cycle; ρ_{SrCl_2} is the true density of SrCl₂.

Assuming that the salt occupies the total volume of the slots after the first absorption, the porosities of $\text{Sr}(\text{NH}_3)\text{Cl}_2$ and $\text{Sr}(\text{NH}_3)_8\text{Cl}_2$ were quantified using the following formulae:

$$\varepsilon_{\text{Sr}(\text{NH}_3)\text{Cl}_2} = 1 - \frac{\rho_{\text{Sr}(\text{NH}_3)\text{Cl}_2\text{-app}}}{\rho_{\text{Sr}(\text{NH}_3)\text{Cl}_2}} \quad \text{Eq. 4}$$

$$\varepsilon_{\text{Sr}(\text{NH}_3)_8\text{Cl}_2} = 1 - \frac{\rho_{\text{Sr}(\text{NH}_3)_8\text{Cl}_2\text{-app}}}{\rho_{\text{Sr}(\text{NH}_3)_8\text{Cl}_2}} \quad \text{Eq. 5}$$

where $\varepsilon_{\text{Sr}(\text{NH}_3)\text{Cl}_2}$, $\varepsilon_{\text{Sr}(\text{NH}_3)_8\text{Cl}_2}$, $\rho_{\text{Sr}(\text{NH}_3)\text{Cl}_2\text{-app}}$, $\rho_{\text{Sr}(\text{NH}_3)_8\text{Cl}_2\text{-app}}$, $\rho_{\text{Sr}(\text{NH}_3)\text{Cl}_2}$, $\rho_{\text{Sr}(\text{NH}_3)_8\text{Cl}_2}$ are the porosities, the apparent densities, and the true densities of $\text{Sr}(\text{NH}_3)\text{Cl}_2$ and $\text{Sr}(\text{NH}_3)_8\text{Cl}_2$, respectively. The true densities were calculated starting from the crystallographic data, as reported in [10]. The apparent densities of the salts were defined as follows:

$$\rho_{\text{Sr}(\text{NH}_3)\text{Cl}_2\text{-app}} = \rho_{\text{SrCl}_2\text{-app}} \cdot \frac{M_{\text{Sr}(\text{NH}_3)\text{Cl}_2}}{M_{\text{SrCl}_2}}$$

$$\rho_{\text{Sr}(\text{NH}_3)_8\text{Cl}_2\text{-app}} = \rho_{\text{SrCl}_2\text{-app}} \cdot \frac{M_{\text{Sr}(\text{NH}_3)_8\text{Cl}_2}}{M_{\text{SrCl}_2}}$$

where M_{SrCl_2} , $M_{\text{Sr}(\text{NH}_3)\text{Cl}_2}$, $M_{\text{Sr}(\text{NH}_3)_8\text{Cl}_2}$ are the molar masses of SrCl_2 , $\text{Sr}(\text{NH}_3)\text{Cl}_2$, and $\text{Sr}(\text{NH}_3)_8\text{Cl}_2$, respectively. The apparent density of the salt $\rho_{\text{SrCl}_2\text{-app}}$ was computed as the ratio between the mass of SrCl_2 m_{SrCl_2} used in the experiment and the total volume of the honeycombs.

The summary of the preparation for the neutron imaging experiments is presented in Table 1.

Table 1. Summary of the preparation for the neutron imaging experiments.

Parameter	Absorption	Desorption
Total volume of the honeycomb slots V_{total} (m ³)	2.12x10 ⁻⁵	
Maximum mass of SrCl ₂ $m_{SrCl_2_{max}}$ (g)	21.946	
True density (kg/m ³):		
- ρ_{SrCl_2}	3108	
- $\rho_{Sr(NH_3)Cl_2}$	2440	
- $\rho_{Sr(NH_3)_8Cl_2}$	1380	
Mass of SrCl ₂ used in the experiment m_{SrCl_2} (g)	12.250	10.252
Apparent density (kg/m ³):		
- $\rho_{SrCl_2_{app}}$	578	484
- $\rho_{Sr(NH_3)Cl_2_{app}}$	641	536
- $\rho_{Sr(NH_3)_8Cl_2_{app}}$	1075	900
Porosity:		
- $\epsilon_{Sr(NH_3)Cl_2}$	0.74	0.78
- $\epsilon_{Sr(NH_3)_8Cl_2}$	0.22	0.35

After the setup was assembled, the reactor and the gas lines were evacuated with the vacuum pump for 15 min to remove any gases.

During the absorption experiment, SrCl₂ in the reactor absorbed NH₃ provided by the cartridge filled with 300 g of ammoniated SrCl₂. The NH₃ flow and hence the pressure in the system were adjusted by setting the temperature in the cartridge via a variable power supply. The temperature in the cartridge was set to 58°C, which corresponds to NH₃ equilibrium pressure of 2.6 bar, while the reactor was kept at room temperature. During the desorption experiments, the reverse procedure was applied. The temperature of the heating element in the reactor was set to 100°C, while the cartridge was kept at room temperature. Due to the difference in temperature and hence NH₃ equilibrium pressure in the two vessels, NH₃ was desorbed in the reactor and reabsorbed in

the cartridge. Since the mass of the salt in the cartridge was much larger than the one in the reactor, no limitation could compromise the desorption from the reactor. The pressure curves for the absorption and desorption experiments are shown in Figure 5.

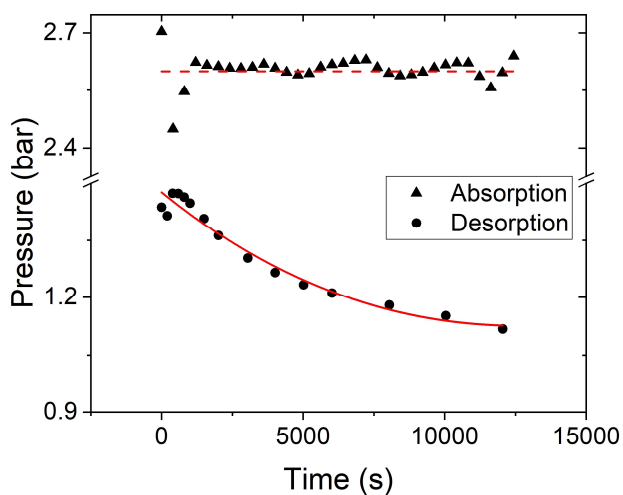


Figure 5. Pressure evolution during absorption and desorption experiments.

A third order polynomial was used to fit the desorption pressure curve. The polynomial will serve as an input for the pressure evolution in the desorption simulation (see Supplementary information). The average pressure during the absorption experiment was 2.6 bar.

Using the flowrate readings, the degree of absorption was calculated as follows:

$$x = \frac{V_t}{V_{tot}} \quad \text{Eq. 6}$$

where x is the degree of absorption at time t ; V_t is the amount of NH_3 that has passed from the cartridge to the reactor by time t ; V_{tot} is the total volume of NH_3 that has reacted with the salt. The values of V_t and V_{tot} were calculated as areas under the curve “Flowrate-Time” from 0 to t and from 0 to the end of the absorption, respectively. While the fluctuations of NH_3 pressure was accounted in the calculations, the temperature of passing through the flowmeter NH_3 was assumed constant.

It is worth noting that prior to conducting neutron imaging experiments, the sample was subject to five NH_3 cycles for both the absorption and desorption studies.

4.3.2.2 Neutron radiography

Prior to the operation of the gas system, the reactor was mounted on a stage in a way that the sample holder was perpendicular to the direction of incident neutron beam, as shown in Figure 6.

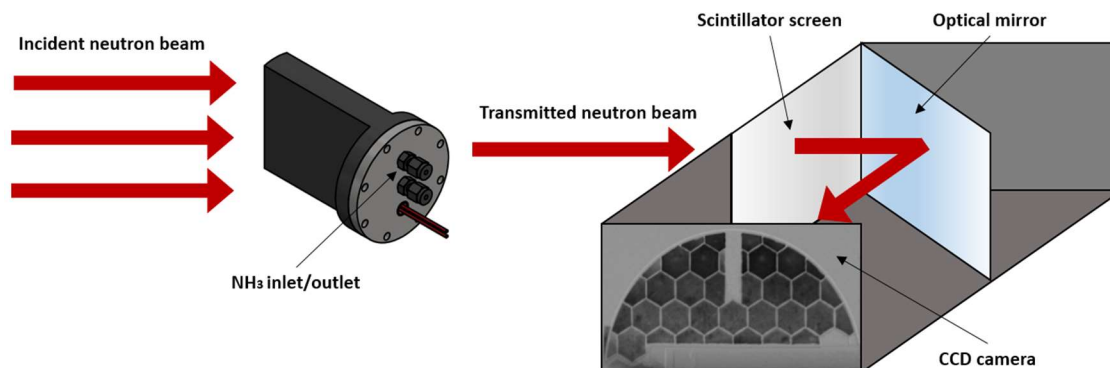


Figure 6. Simplified drawing depicting the configuration used for neutron radiography studies.

With the start of the reaction (absorption or desorption), a neutron shutter was opened, and a thermal neutron beam started to hit the reactor. The incident neutron beam passing through the sample was attenuated in accordance with the Beer-Lambert's law:

$$I(\lambda) = I_0 e^{-\mu(\lambda)y} \quad \text{Eq. 7}$$

where I is an attenuated beam intensity, λ is a neutron wavelength, I_0 is an intensity behind a sample, μ is a neutron attenuation coefficient depending on neutron wavelength, sample, and its apparent density, and y is the thickness of the sample.

After that, the transmitted neutron beam impinging on a scintillator screen was converted into light. The light was reflected from an optical mirror onto a CCD camera, which resulted in radiographs. To remove white spots and reduce noise level in the final images, a median filtering was applied to a number of consecutive radiographs. Based on this number and the time resolution of the detector, the total acquisition time for one image including camera readout was calculated. The reaction was considered to be finished when there were no further changes in several consecutive images. By the end of the reaction, a stack of the raw images was obtained. The details of the neutron instruments for absorption and desorption experiments are presented in Table S 1.

To perform the data analysis, the raw images were normalized by open beam and dark current images using ImageJ [11]. The open beam and dark current images were obtained in the beginning of the absorption and desorption experiments. Then, the stack of the normalized images were divided by the first image in case of absorption and by the last image in case of desorption. By doing this, one removes the contribution of $\text{Sr}(\text{NH}_3)\text{Cl}_2$ and the reactor components from the normalized images, and the amount of NH_3 absorbed/desorbed can be estimated in the obtained reduced images. Assuming that the reactions was completed when the image acquisition had stopped, the reaction advancement x at time t was computed as follows:

$$x = \frac{a_{beg} - a_t}{a_{beg} - a_{end}} \quad \text{Eq. 8}$$

where a_{beg} , a_{end} are mean greyscale values of a selected area obtained from the first and last reduced image, respectively; a_t is a mean greyscale value of the selected area obtained from the reduced image taken at time t .

The qualitative analysis of the neutron radiography data described above was also applied in the work of Berdiyeva *et al.* [9], from which the desorption dataset used in this study was taken. The authors argued that the quantitative analysis using the Beer-Lambert's law (see Eq. 7) was problematic to perform due to several uncertainties, like irregularities in the powder thickness (see Figure 8), expansion and contraction of the powder over cycling, and additional error due to incoherent scattering from hydrogen.

4.3.2.3 Numerical model

Geometry, Domains, and Boundary Conditions

To simulate NH_3 absorption and desorption into/from SrCl_2 inside the reactor, a 3D Time-Dependent numerical model was build and computed in COMSOL Multiphysics environment. Similar to the neutron imaging experiment, the geometry of the model includes a honeycomb half disc enclosed in an aluminum rectangular prism with a circular ($\varnothing=3$ mm) NH_3 inlet/outlet (see Figure 3). To simplify the numerical model, the heating element is omitted in the geometry. Instead, in the desorption model the temperature of the heating element is assigned to the surface of the honeycomb disc in contact with the heating element. The temperature of the heating element was assumed to change from an initial temperature of 20°C till the set temperature of 100°C within 450 s from the start of the desorption. To simulate the atmospheric cooling of the outer surface of

the reactor, convective heat flux, characterized with a heat transfer coefficient of $5 \text{ W/m}^2/\text{K}$ [12], is applied to the sides of the aluminum prism. The honeycomb slots are fully loaded with a porous media, composed of $\text{Sr}(\text{NH}_3)\text{Cl}_2$, $\text{Sr}(\text{NH}_3)_8\text{Cl}_2$, and gaseous NH_3 . The rest of the prism interior is filled with gaseous NH_3 . A uniform pressure of 2.6 bar is applied to the NH_3 inlet in the absorption model. In the desorption model, the outlet pressure is described using the polynomial fit mentioned above (see Eq. 35 in Supplementary information). In the beginning of the absorption and desorption, the value of pressure in the reactor is set to 2.60 and 1.48 bar, respectively. The initial temperature of 20°C was used for the absorption and desorption models.

The geometry was divided into four domains: 1) gaseous NH_3 ; 2) honeycomb slots loaded with the porous media (honeycomb slots); 3) honeycomb disc; 4) aluminum cell. Properties of each domain are listed in Table 2.

Table 2. Modelled domains and materials properties. The full expressions of the properties are reported in Eq. 9-Eq. 12.

#	Domain	Material	Molar mass (kg/kmole)	Density (kg/m ³)	Thermal conductivity (W/(m*K))	Specific heat capacity (J/(kg*K))
1	Gaseous NH_3	$\text{NH}_3(\text{g})$	17.031	ρ_{NH_3}	k_{NH_3}	$C_{p \text{NH}_3}$
2	Honeycomb slots	$\text{NH}_3(\text{g})$ $\text{Sr}(\text{NH}_3)\text{Cl}_2$ $\text{Sr}(\text{NH}_3)_8\text{Cl}_2$	17.031 175.561 294.778	ρ_{eff}	k_{eff}	$C_{p_{eff}}$
3	Honeycomb disc	Stainless steel	-	7950	16.3	490
4	Aluminum cell	Aluminum 6063-T83	-	2700	201	900

Material properties of gaseous NH_3 such as thermal conductivity k_{NH_3} , specific heat capacity $C_{p \text{NH}_3}$, and dynamic viscosity μ_{NH_3} were taken from Engineering Equation Solver (EES 2016) and interpolated linearly:

$$k_{\text{NH}_3} = (0.138 \cdot T + 16.58) \cdot 10^{-3} \quad \text{Eq. 9}$$

$$C_{p \text{NH}_3} = 1.96 \cdot T + 1531 \quad \text{Eq. 10}$$

$$\mu_{\text{NH}_3} = 4 \cdot 10^{-8} \cdot T - 10^{-6} \quad \text{Eq. 11}$$

where T is the temperature of gaseous NH_3 in K.

The density of gaseous NH_3 ρ_{NH_3} was derived from the ideal gas law equation, valid in the used range of pressure and temperature:

$$\rho_{\text{NH}_3} = \frac{p \cdot M_{\text{NH}_3}}{RT} \quad \text{Eq. 12}$$

where p is NH_3 pressure; M_{NH_3} is NH_3 molar mass taken from Table 2; R is the ideal gas constant.

As mentioned before, inside the honeycomb slots, the material was treated as the porous medium constituted of the two phases: gaseous NH_3 and the solid salt, a mixture of $\text{Sr}(\text{NH}_3)\text{Cl}_2$ and $\text{Sr}(\text{NH}_3)_8\text{Cl}_2$. Knowing the properties of each phase, the effective properties of the porous medium was defined as follows:

$$(\rho C_p)_{eff} = \varepsilon \cdot \rho_{\text{NH}_3} \cdot C_{p \text{NH}_3} + (1 - \varepsilon) \cdot \rho_{salt} \cdot C_{p salt} \quad \text{Eq. 13}$$

$$k_{eff} = \varepsilon \cdot k_{\text{NH}_3} + (1 - \varepsilon) \cdot k_{salt} \quad \text{Eq. 14}$$

where $(\rho C_p)_{eff}$ and k_{eff} are the effective volumetric heat capacity and the effective thermal conductivity of the porous medium, respectively; ε , ρ_{salt} , $C_{p salt}$, k_{salt} are the salt porosity, true density, specific heat capacity, and thermal conductivity, respectively.

All the properties of the salt depend on the degree of the reaction x , the definition of which is expressed in Table 3.

Table 3. Definition of reaction advancement for absorption and desorption.

$x=0$	Absorption: the ammonia is fully desorbed, and the salt is in the form of $\text{Sr}(\text{NH}_3)\text{Cl}_2$ Desorption: the ammonia is fully absorbed, and the salt is in the form of $\text{Sr}(\text{NH}_3)_8\text{Cl}_2$
$x=1$	Absorption: the ammonia is fully absorbed, and the salt is in the form of $\text{Sr}(\text{NH}_3)_8\text{Cl}_2$ Desorption: the ammonia is fully desorbed, and the salt is in the form of $\text{Sr}(\text{NH}_3)\text{Cl}_2$

For the calculation of the salt properties at intermediate reaction advancement, they were assumed linear between the non-ammoniated and fully ammoniated states. For desorption, the equations describing the salt properties were computed as follows:

$$\rho_{salt} = x \cdot \rho_{\text{Sr}(\text{NH}_3)_1\text{Cl}_2} + (1 - x) \cdot \rho_{\text{Sr}(\text{NH}_3)_8\text{Cl}_2} \quad \text{Eq. 15}$$

$$C_{p\ salt} = \frac{x \cdot \rho_{\text{Sr}(\text{NH}_3)_1\text{Cl}_2} \cdot C_{p\ \text{Sr}(\text{NH}_3)_1\text{Cl}_2} + (1-x) \cdot \rho_{\text{Sr}(\text{NH}_3)_8\text{Cl}_2} \cdot C_{p\ \text{Sr}(\text{NH}_3)_8\text{Cl}_2}}{x \cdot \rho_{\text{Sr}(\text{NH}_3)_1\text{Cl}_2} + (1-x) \cdot \rho_{\text{Sr}(\text{NH}_3)_8\text{Cl}_2}} \quad \text{Eq. 16}$$

$$k_{salt} = x \cdot k_{\text{Sr}(\text{NH}_3)_1\text{Cl}_2} + (1 - x) k_{\text{Sr}(\text{NH}_3)_8\text{Cl}_2} \quad \text{Eq. 17}$$

$$\varepsilon = x \cdot \varepsilon_{\text{Sr}(\text{NH}_3)_1\text{Cl}_2} + (1 - x) \cdot \varepsilon_{\text{Sr}(\text{NH}_3)_8\text{Cl}_2} \quad \text{Eq. 18}$$

where $\rho_{\text{Sr}(\text{NH}_3)_1\text{Cl}_2}$, $C_{p\ \text{Sr}(\text{NH}_3)_1\text{Cl}_2}$, $k_{\text{Sr}(\text{NH}_3)_1\text{Cl}_2}$, $\varepsilon_{\text{Sr}(\text{NH}_3)_1\text{Cl}_2}$, $\rho_{\text{Sr}(\text{NH}_3)_8\text{Cl}_2}$, $C_{p\ \text{Sr}(\text{NH}_3)_8\text{Cl}_2}$, $k_{\text{Sr}(\text{NH}_3)_8\text{Cl}_2}$, $\varepsilon_{\text{Sr}(\text{NH}_3)_8\text{Cl}_2}$ are the true densities, specific heat capacities, intrinsic thermal conductivities, and porosities of $\text{Sr}(\text{NH}_3)\text{Cl}_2$ and $\text{Sr}(\text{NH}_3)_8\text{Cl}_2$, respectively. The true densities and porosities of the materials are presented in Table 1.

The listed above equations (Eq. 15-Eq. 18) were also used for the determination of the salt properties in the absorption model with the correction for reversibility, when x was substituted by $(1-x)$ and $(1-x)$ was replaced by x .

The expressions of the specific heat capacities of $\text{Sr}(\text{NH}_3)\text{Cl}_2$ and $\text{Sr}(\text{NH}_3)_8\text{Cl}_2$ were retrieved from [13] and are presented below:

$$C_{SrCl_2(NH_3)_1} = 649.8 + 3.524 \cdot T + 0.0021 \cdot T^2 + 0.00016 \cdot T^3 \quad Eq. 19$$

$$C_{SrCl_2(NH_3)_8} = 576.296 + 3.124 \cdot T + 0.07 \cdot T^2 + 0.00005 \cdot T^3 \quad Eq. 20$$

The intrinsic thermal conductivities of $Sr(NH_3)Cl_2$ and $Sr(NH_3)_8Cl_2$ were assumed to be equal to the one of $SrCl_2$ (0.75 W/m/K), which was calculated based on the value of the apparent density of $SrCl_2$ reported in [14].

Mathematical modeling

Heat transfer

The equations governing heat transfer in gaseous NH_3 , aluminum cell, honeycomb disc, and honeycomb slots domains were defined as follows:

$$\rho_{NH_3} C_{p NH_3} \frac{\partial T}{\partial t} + \rho_{NH_3} C_{p NH_3} \mathbf{u} \cdot \nabla T + \nabla(-k_{NH_3} \nabla T) = 0 \quad Eq. 21$$

$$\rho_{Al} C_{p Al} \frac{\partial T}{\partial t} + \nabla(-k_{Al} \nabla T) = 0 \quad Eq. 22$$

$$\rho_{ss} C_{p ss} \frac{\partial T}{\partial t} + \nabla(-k_{ss} \nabla T) = 0 \quad Eq. 23$$

$$(\rho C_p)_{eff} \frac{\partial T}{\partial t} + \rho_{NH_3} C_{p NH_3} \mathbf{u} \cdot \nabla T + \nabla(-k_{eff} \nabla T) = Q \quad Eq. 24$$

$$Q = \pm \frac{dx}{dt} \cdot N_s \cdot \Delta H \quad Eq. 25$$

where \mathbf{u} is the fluid velocity vector; ρ_{Al} , $C_{p Al}$, k_{Al} , ρ_{ss} , $C_{p ss}$, k_{ss} are the density, the specific heat capacity and the thermal conductivity of aluminum and stainless steel, respectively. All these properties are presented in Table 2. Q is the heat absorbed (“+” sign in Eq. 25) or released (“-” sign in Eq. 25) by the porous medium during desorption and absorption, respectively. N_s is the molar density of NH_3 in the honeycomb slots and was calculated as follows:

$$N_s = \frac{\rho_{SrCl_2 app}}{M_{SrCl_2}} \cdot N_{st} \quad Eq. 26$$

where $\rho_{SrCl_2 app}$ and M_{SrCl_2} are the molar mass and the apparent density of $SrCl_2$. The values of these properties are listed in Table 1. N_{st} is the number of NH_3 moles reacting with one mole of $SrCl_2$. In our study, N_{st} is equal to seven.

The heat flux transferred between the stainless steel honeycomb disc and the porous medium was calculated as follows:

$$q = h_w(T_{hc} - T_p) \quad \text{Eq. 27}$$

where h_w is the heat transfer coefficient between the honeycomb disc and the porous medium; T_{hc} is the temperature of the honeycomb disc; T_p is the temperature of the porous medium. During desorption, the heat transfer coefficient was assumed to change linearly from 265 till 65 W/m²/K, due to swelling and shrinking of the sorbent bed [15], as reported by [9]. On average, it gives a value of 165 W/m²/K, which was reported by Huang *et al.* [16]. The change in the heat transfer coefficient reflects the change in volume of the salt and the decrease in the contact area between the salt and the honeycomb disc [9]. During absorption, the heat transfer coefficient was assumed constant and equal to 165 W/m²/K.

Chemical reaction

The reaction rate equation describing the kinetics of the gas-solid reaction was expressed as follows:

$$\frac{dx}{dt} = f(x) \cdot k(p, T) \quad \text{Eq. 28}$$

where $f(x)$ is a function describing the rate-controlling step of the reaction and $k(p, T)$ is a rate constant of the reaction:

$$k(p, T) = k_0 \cdot e^{-\frac{E_a}{RT}} \cdot g(p) \quad \text{Eq. 29}$$

where k_0 is the pre-exponential factor, E_a is the activation energy of the reaction, and $g(p)$ is the pressure impact function expressing the degree of the discrepancy between the actual gas pressure in the system p and the equilibrium gas pressure over the salt p_{eq} . This factor can be written as follows [17]: $g(p) = ((p - p_{eq})/p_{eq})^m$ for absorption and $g(p) = ((p_{eq} - p)/p_{eq})^m$ for desorption. p_{eq} is defined by the van't Hoff equation:

$$p_{eq} = p_0 e^{-\frac{\Delta H}{RT} + \frac{\Delta S}{R}} \quad \text{Eq. 30}$$

where p_0 is a reference pressure equal to 1 Pa; ΔH is the reaction enthalpy equal to 41.432 kJ/(mole of NH₃) [18]; ΔS is the reaction entropy equal to 228.6 J/(K · mole of NH₃) [18].

The absorption and desorption kinetics tetrads for the working pair SrCl₂-NH₃ was defined in another study, which was submitted for a publication [19]. The tetrads are listed in Table 4.

Table 4. Kinetics tetrads for NH₃ absorption/desorption into/from SrCl₂.

Function / Parameter	Absorption	Desorption
$f(x)$	$3 \cdot (1 - x)^{\frac{2}{3}}$	$3 \cdot (1 - x)^{\frac{2}{3}}$
k_0 , 1/s	$2.423 \cdot 10^7$	36754
E_a , kJ/mole	66.1	43.9
m	1.8	1.9

Mass transfer

The diffusion of NH₃ in the porous medium was described with the following equations:

$$\frac{\partial \varepsilon \rho_{NH_3}}{\partial t} + \nabla \cdot (\rho \mathbf{u}) = Q_m \quad Eq. 31$$

$$Q_m = \pm \frac{dx}{dt} \cdot N_s \cdot M_{NH_3} \quad Eq. 32$$

$$\rho \frac{\partial \mathbf{u}}{\partial t} = \nabla \cdot \left[-p\mathbf{I} + \frac{\mu}{\varepsilon} (\nabla \mathbf{u} + (\nabla \mathbf{u})^T) - \frac{2\mu}{3\varepsilon} (\nabla \cdot \mathbf{u})\mathbf{I} \right] - \left(\frac{\mu_{NH_3}}{\kappa} + \beta_F |\mathbf{u}| + \frac{Q_m}{\varepsilon^2} \right) \mathbf{u} + \mathbf{F} \quad Eq. 33$$

where Q_m is the source/sink term, positive for desorption and negative for absorption; κ is the hydraulic permeability of the salt layer; β_F is the Forchheimer drag factor. In this case, domain forces \mathbf{F} were neglected. The hydraulic permeability of the porous salt was calculated through the Carman-Kozeny equation [20], approximating the salt particles are spherical:

$$\kappa = \frac{\varepsilon^3}{180(1-\varepsilon)^2} d_p^2 \quad Eq. 34$$

where d_p is the salt particle diameter, which was set to 100 nm.

Spatial and temporal discretization

The governing equations of chemical reaction, heat transfer, and mass transfer, coupled with each other, were solved in COMSOL Multiphysics environment. To calculate the evolution of the system over time, segregated solver was used. Applied in this study time and space discretization, determined based on the results of the simulations with different time step and mesh sizes, offers

an optimum compromise between the accuracy (within 1 % absolute error in kinetic curve) and computational time. For the desorption model, we have applied a time step of 5 s with a convergence criterion set to 0.01. For the spatial discretization of the domains, we have used free tetrahedrals, and the dimensions of the elements are presented in Table S 2. For the absorption model, the same spatial discretization was used but with a fine mesh for the “Honeycomb slots” domain. The time stepping was free in this case, meaning that the solver takes as large a timestep as possible, but reduces the timestep size if the solution starts to vary rapidly in time. As in case of the desorption model, the convergence criterion was set to 0.01.

4.3.3 Results and Discussions

To validate the numerical model presented in this study, kinetics curves obtained from the simulation and the experiment were plotted for absorption and desorption, and the deviation between the curves was evaluated. The absorption was carried out at 2.60 bar and room temperature, while the desorption was performed at around 1 bar and 100°C. The experimental reaction advancement for a hexagon was calculated using *Eq. 8*, while the model reaction advancement was computed as an average degree of desorption over the hexagon. It should be noted that the desorption model did not include the calculation of the fluid flow and neglected the convective heat transfer in the honeycomb slots and gaseous NH₃ domains. For the given desorption conditions, this resulted in slightly less accurate model (discrepancy within 3%) with significant gain in computational time.

4.3.3.1 Desorption

The detailed results of the desorption studies are shown in Figure 7, where global kinetics curves (Figure 7(b)) and individual kinetics curves (Figure 7(c-d)) are presented as dots and solid lines for the experiment and for the model, respectively. The individual kinetics curves were obtained for the hexagons numbered as shown in Figure 7(a). The value of global reaction advancement was calculated as an average of the 10 individual hexagons.

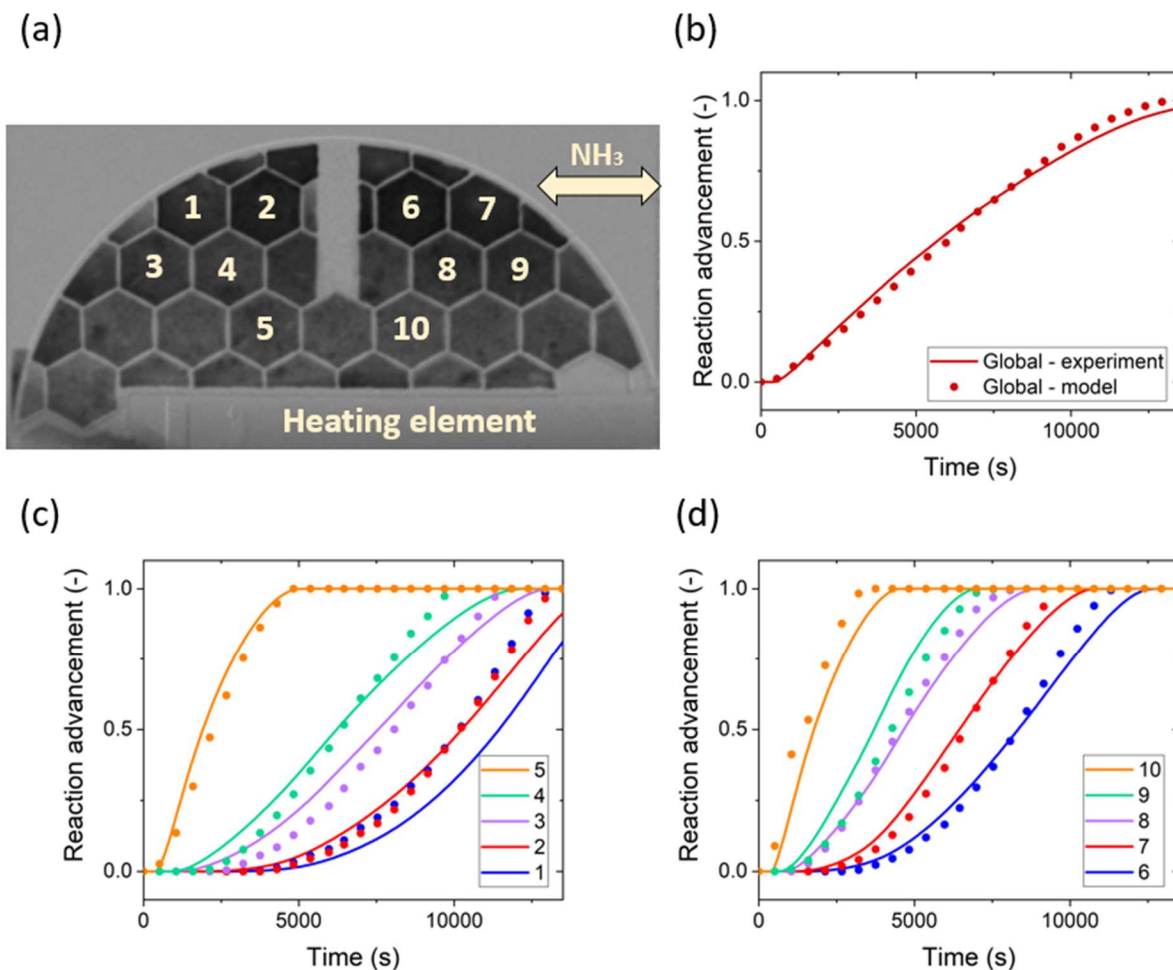


Figure 7. Results of desorption studies for hexagons: (a) Neutron radiograph with indexed hexagons and designated heating element and NH_3 inlet/outlet; (b) Global kinetics curves obtained as an average of 10 hexagons indexed in (a); (c) Individual kinetics curves for hexagons 1-5; (d) Individual kinetics curves for hexagons 6-10. The kinetics curves illustrated in (b)-(d) are derived from experimental measurement (dots) and numerical simulation (solid lines).

From the comparison between the global curves from Figure 7(b), one can conclude that the model nicely follows the experimental data, as maximum deviation between the two curves does not exceed 5%. When comparing the individual kinetics curves presented in Figure 7(c-d), it appears that the sigmoidal shape of the experimental curves is well captured by the model and that the experimental progression of the desorption from hexagon to hexagon is modelled by the

simulation. However, larger discrepancy between the model and the experimental data sets is observed in case of individual hexagons when compared to the global results. For example, a maximum deviation of 27% is noticed for hexagon 1, the model curves being slower than the experimental one. The fact that the most distant from the heating element hexagon has the highest discrepancy among all the studied hexagons may originate from a non-accurate description of heat transfer within the reactor, provided that the deviation is systematic and scales up with the distance between hexagons and the heating element. However, the discrepancy does not seem to be systematic, as desorption occurs faster for further hexagon 3 compared to closer hexagon 4 (Figure 7(c)). The same observation can also be made for hexagons 8 and 9 (Figure 7(d)). Consequently, non-accurate modelling of heat transfer does not appear to be a reason of the deviation for individual hexagons. Instead, this discrepancy may arise from the deviation between the perfect system described in the simulation and the actual experimental setup. Indeed, as shown and discussed in Berdiyeva *et al.* [9], the powder was not evenly distributed among the honeycombs during the experiments, since some of the powder had fallen out of the half-disc during the mounting of the reactor on the neutron stage (Figure 8).

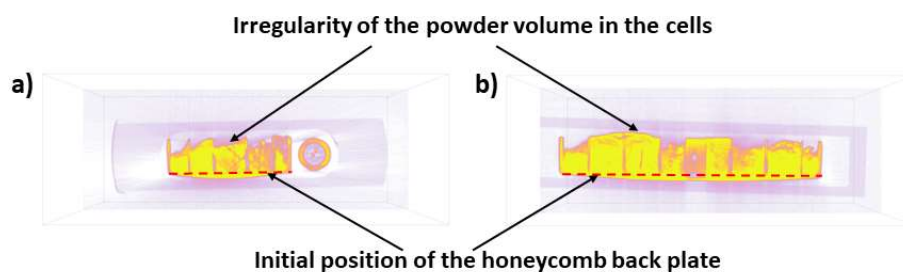


Figure 8. Irregularity of the powder thickness and deformation of the honeycomb back plate after NH_3 absorption in a) XY-plane and b) YZ-plane. The red dashed lines represent the position of the back plate before the first absorption. Figure is taken from [9].

In addition to that, the authors reported that taking side-view images of the reactor while performing sorption processes revealed the change of the powder thickness by 10%. In the simulation, these features of the experiment were not modelled, and thickness of the powder was assumed homogeneous within the reactive bed and constant throughout the sorption processes. Furthermore, neutron tomography analysis, the results of which are also reported in [9], has shown

that the back plate of the half-disc was bended presumably due to both the thermal stresses and the expansion of the salt during the first absorption cycles (Figure 8). In the desorption simulation, the back plate was omitted; however, the presence of the back plate could have affected the experimental results especially on the edges of the honeycomb half-disc. Therefore, all the deviations between the experimental setup and the model mentioned above may have contributed to the discrepancy between the experimental and model results.

In order to study how the reaction front proceeds within individual hexagons, the degree of desorption along the sides of the hexagons was computed, and the results are illustrated in Figure 9. The numbering of the hexagons used in this study and the indexing of their sides are illustrated in Figure 9(a). Figure 9(b), (c), and (d) represents the desorption advancement curves for hexagons 2, 4, and 5, respectively. In the graphs, the experimental data is represented as dots, while the results from the model are shown as solid lines.

When comparing experimental and model curves illustrated in Figure 9(b-d), the shape of the model curves is observed to be in a good agreement with the experimental data. However, some inconsistency between the simulation and experimental heat propagation, which corresponds to the reaction propagation in case of desorption, can be noticed. For instance, in case of the experimental data, desorption starts from the lower-right side and finishes at the upper-left side for all the studied hexagons. In case of the simulation, this heat distribution pattern is fully relevant for the hexagon furthest from the heating element (hexagon 2), but it does not describe the heat transfer within the closest hexagon 5. Inside hexagon 5, the heat flows from the bottom of the hexagon to its top, resulting in the mirroring between the right and left halves of the hexagon. For middle hexagon 4, a pattern combining the two discussed models could be applied. The increase in the inconsistency in the heat transfer distribution from the furthest to the closest to the heating element cell is seen to lead to the growth of the absolute deviation. The value of maximum absolute deviation has reached 17, 40, and 42% for hexagon 2, 4, and 5, respectively. This disparity may come from the fact that the heating element was not in close contact with the honeycomb structure disc, in particularly, at its end. Moreover, the effect of the bended back plate, mentioned above, may have contributed to this discrepancy, too.

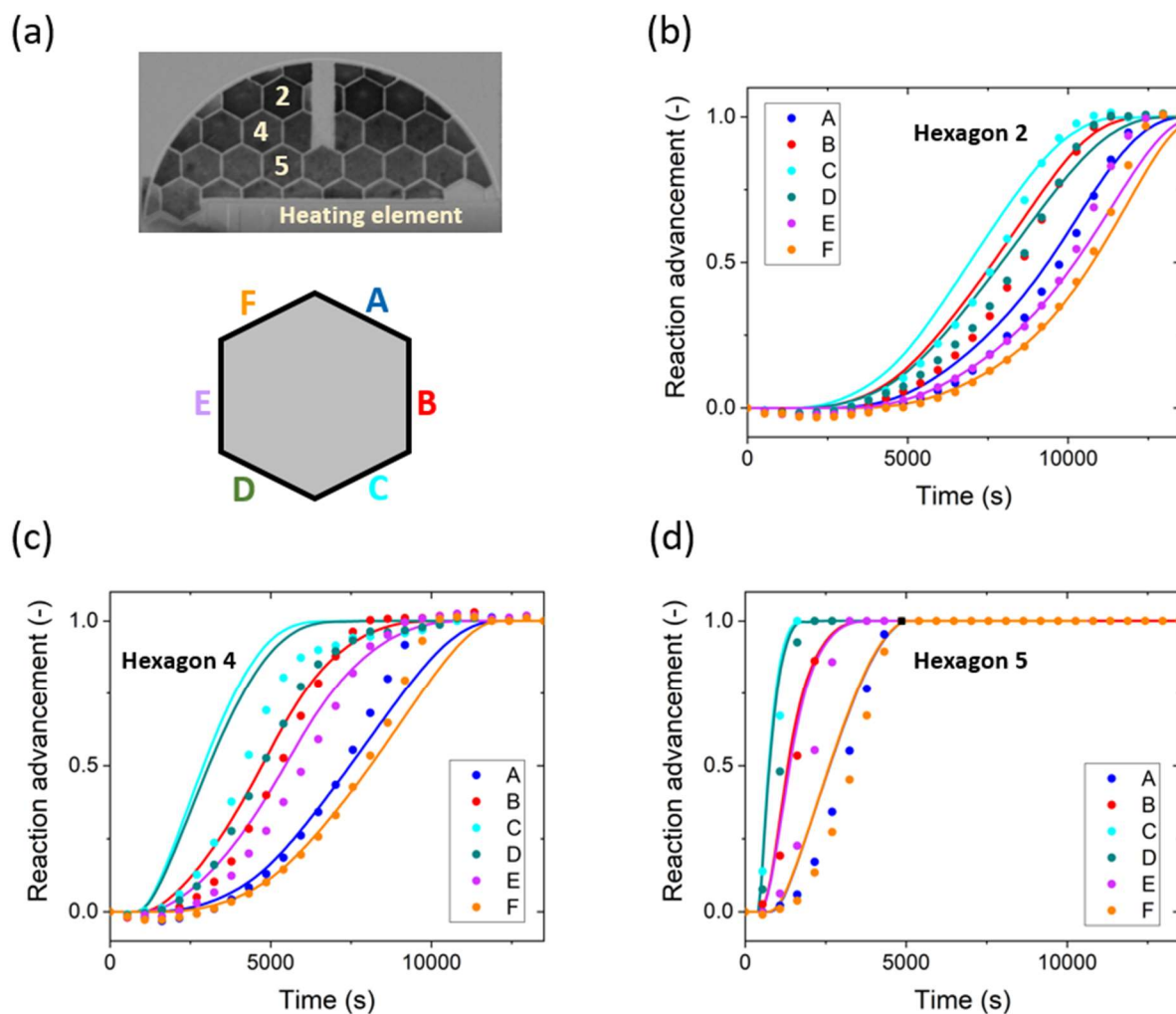


Figure 9. Results for desorption studies for hexagon sides: (a) Neutron radiograph with indexed hexagons and hexagon with indexed sides. Kinetics curves obtained for sides of (b) hexagon 2, (c) hexagon 4, and (d) hexagon 5. Kinetics curves in (b)-(d) are represented as dots for experimental measurement and solid lines for model.

4.3.3.2 Absorption

The results of the absorption study are shown in Figure 10 as solid lines for the model and as dots for the experiment. Kinetics curves for the individual hexagons indexed as illustrated in Figure 7(a) are plotted in Figure 10(a-b). In Figure 10(c), the global advancement curve obtained from the model results is compared with the ones derived from the flowmeter readings and neutron measurements. The value of global reaction advancement for the neutron and model results was

calculated as an average of the 10 individual hexagons. Figure 10(d) represents temperature profiles at the point of the reactive bed shown in Figure 3.

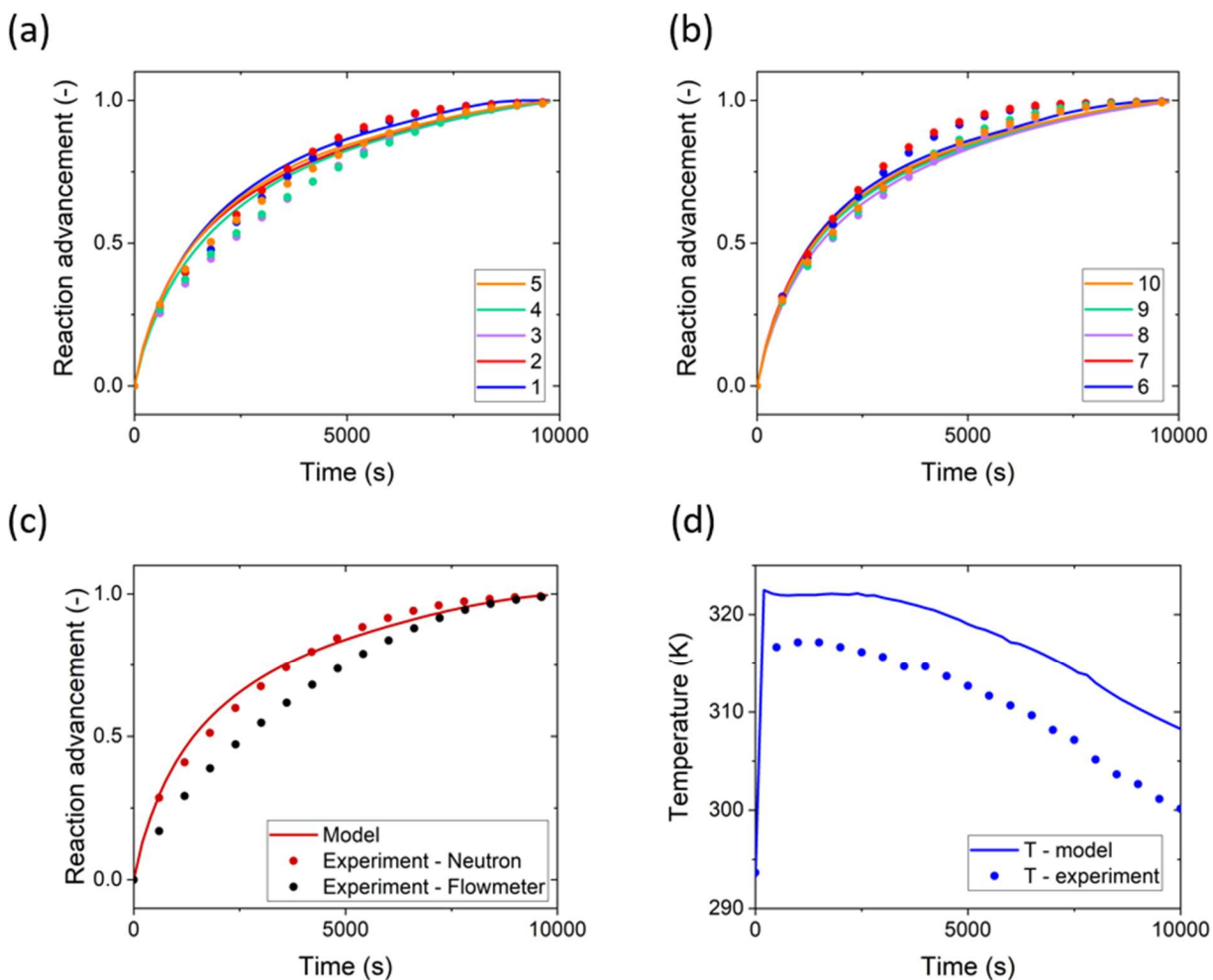


Figure 10. Results of absorption studies “hexagons”: (a) Individual kinetics curves for hexagons 1-5; (b) Individual kinetics curves for hexagons 6-10; (c) Global kinetics curves obtained as an average of 10 hexagons from simulation results and neutrons and flowmeter; (d) Temperature profile at the point shown in Figure 3. The curves illustrated in (a)-(d) are derived from experimental measurement (markers) and numerical simulation (solid lines).

As could be observed from Figure 10(a-b), the deviation between the model curves is much smaller compared to the one between the experimental curves. It means that in case of the model, absorption proceeds in a more homogeneous way within the reactive bed when compared to the

experiment. Indeed, during the experiment the reaction kinetics is fastest in the upper part of the honeycomb half-disc (hexagons 1, 2, 6 and 7), and slowest in its middle part (hexagons 3, 4, 8, and 9). In the lower part of the disc, hexagons 5 and 10 are characterized with intermediate reaction progress. This dependency indicates that the absorption rate does not solely depend on the location of the salt relative to the NH_3 inlet but also on the availability of heat sink material around the salt. The same tendency but less pronounced could be noticed in case of the model, which resulted in 10% of maximum absolute deviation between the experiment and the model for hexagon 1. However, in case of global reaction advancement curves, this value is lower and equal to 5% (Figure 10(c)). This suggests that the neutron experiment and the simulation are in a good agreement on global and local levels.

Interestingly, the curves derived from the flowmeter readings and neutron measurement have same reaction time but different shape which leads to a deviation of 13% (Figure 10(c)). There are two possible reasons for why the reaction rate is faster in case of the neutron measurement compared to the flowmeter ones. First, when calculating the actual flowrate, the indicated flowrate was corrected for pressure but not temperature, as the temperature of NH_3 gas passing through the flowmeter was not measured. Thus, the deviation in the NH_3 gas temperature might have resulted in the reshape of the flowmeter curve. Second, in the beginning of the absorption the flowrate of the gas surpassed the maximum flowrate of the flowmeter for a short period of time (150 s). This was not accounted for in the calculations of the flowmeter reaction rate, which should eventually translate the flowmeter curve up.

When comparing the temperature profiles of the salt in Figure 10(d), one may notice a good agreement in their shape. However, the measured temperature is on average 5 degrees lower than the one obtained from the model. This is not surprising because the tip of the thermocouple cannot be in perfect contact with the porous reactive media, while the model gives the temperature within a grain of the salt.

Based on the absorption and desorption results presented above, the model was confirmed to reproduce the neutron experimental data well. In the future, the model will be compared with experimental data obtained over wider range of pressure and temperature. Here arises a major drawback of neutron radiography technique, which is limited availability of neutron facilities, both

in the facility cost and portability [21]. Moreover, depending on the neutron facility, the period between planning a neutron experiment and carrying it out may take up to a year. However, the construction of new neutron facilities, like the European Spallation Source [22], will contribute to making the technique more accessible in the world and, in particular, in Nordic Europe.

Besides applying the model in a wider range of temperature and pressure, another direction for future work is computing the model for working pairs other than $\text{SrCl}_2\text{-NH}_3$ and other reactor configurations to confirm its [model] versatility. Carrying out new experiments will also give an opportunity to investigate the origin of the discrepancy between the flowmeter and neutron experimental data in more detail.

4.3.4 Conclusion

The aim of this study was to show the possibility of verifying a numerical model of a TCHS reactor using neutron radiography technique. To achieve this, we have developed a 3D COMSOL model of a reactor utilizing absorption and desorption between SrCl_2 and NH_3 and have compared the simulation results with neutron experiment obtained on the identical reactor. As neutron radiography was applied for the first time for the verification of a TCHS reactor model, the procedure of the detailed comparison between the experiment and the model was developed.

From the model validation, the following conclusions were drawn:

1. The numerical model describes the neutron radiography experiments with a good accuracy, and it will be further applied for the optimization of the reactor design. In addition, the developed model may be used not only for the designed $\text{SrCl}_2\text{-NH}_3$ system, but also for other materials in other reactor configurations, as it utilizes intrinsic rather than apparent material properties as an input.
2. Neutron radiography is a powerful tool for validating numerical models of TCHS reactors, as it gives insight into how the reaction proceeds inside the reactor at local and global levels. As well as for the TCHS systems, the procedure of model validation developed in this study can be also successfully applied for other systems utilizing hydrogen containing absorptive – heat pumps, H_2 and NH_3 storage systems etc.

4.3.5 Acknowledgements

This work is funded by NordForsk Nordic Neutron Science Programme through the Neutrons for Heat Storage (NHS) project (No. 82206). The authors thank the neutron facilities FRM II and ILL for the allocation of neutron radiation beam times. Particularly, Thomas Buecherl and Malgorzata G. Makowska (FRM II) and Lukas Helfen and Alessandro Tengattini (ILL) are acknowledged for experimental assistance during the beamtimes. Additionally, the Danish Research Council is greatly acknowledged for the financial support via Danscatt. Moreover, the authors thank Hilde Larsson for giving valuable pieces of advice during modeling in COMSOL software.

4.3.6 Supplementary information

Polynomial fit for the pressure evolution curve during the desorption experiment:

$$y = 1.4766 - 5.9925 \cdot 10^{-5}x + 2.90752 \cdot 10^{-9}x^2 - 2.84936 \cdot 10^{-14}x^3 \quad \text{Eq. 35}$$

where y refers to the pressure of gaseous NH_3 in the reactor, and x stand for the reaction time t .

Table S 1. Details of neutron setup configuration for absorption and desorption studies.

	Absorption	Desorption
Instrument/Neutron source	D50/ILL (Grenoble, France)	NECTAR/FRM-II (Munich, Germany)
Wavelength λ , Å	2.8	1.81
L/D ratio	435	230
Sample – detector distance, mm	42.5-52.5	
Acquisition time, s	5	27

Table S 2. Mesh parameter and dimensions for each domain for desorption model.

Domain	Name of element size	Max. element size, m	Min. element size, m	Max. element growth rate	Curvature factor	Resolution of narrow regions
Gaseous NH ₃	Fine	0.008	0.001	1.45	0.5	0.6
Honeycomb slots	Extremely fine	0.002	2×10^{-5}	1.3	0.2	1
Honeycomb disc	Normal	0.01	0.0018	1.5	0.6	0.5
Aluminum cell						

4.3.7 References

- [1] L. F. Cabeza and U. De Lleida, *Thermal energy storage for renewable heating and cooling systems* *. 2016.
- [2] C. Forman, I. K. Muritala, R. Pardemann, and B. Meyer, “Estimating the global waste heat potential,” *Renew. Sustain. Energy Rev.*, vol. 57, pp. 1568–1579, 2016.
- [3] et al. Andreas Hauer, “IEA-ETSAP and IRENA © Technology Brief E17-Thermal Energy Storage ENERGY TECHNOLOGY SYSTEMS ANALYSIS PROGRAMME,” no. January, 2013.
- [4] H. J. Huang, G. Bin Wu, J. Yang, Y. C. Dai, W. K. Yuan, and H. B. Lu, “Modeling of gas-solid chemisorption in chemical heat pumps,” *Sep. Purif. Technol.*, vol. 34, no. 1–3, pp. 191–200, 2004.
- [5] A. Chaise, P. De Rango, P. Marty, and D. Fruchart, “Experimental and numerical study of a magnesium hydride tank,” *Int. J. Hydrogen Energy*, vol. 35, no. 12, pp. 6311–6322, 2010.
- [6] Y. Yuan, H. Bao, Z. Ma, Y. Lu, and A. P. Roskilly, “Investigation of equilibrium and dynamic performance of SrCl₂-expanded graphite composite in chemisorption refrigeration system,” *Appl. Therm. Eng.*, vol. 147, no. January 2018, pp. 52–60, 2019.

-
- [7] C. Zeng, S. Liu, L. Yang, X. Han, M. Song, and A. Shukla, "Investigation of a three-phase thermochemical reactor through an experimentally validated numerical modelling," *Appl. Therm. Eng.*, vol. 162, no. March, p. 114223, 2019.
- [8] F. Heubner *et al.*, "In-operando stress measurement and neutron imaging of metal hydride composites for solid-state hydrogen storage," vol. 397, no. June, pp. 262–270, 2018.
- [9] P. Berdiyeva, A. Karabanova, M. G. Makowska, and R. E. Johnsen, "In-situ neutron imaging study of NH₃ absorption and desorption in SrCl₂ within a heat storage prototype reactor," *J. Energy Storage*, vol. 29, no. December 2019, p. 101388, 2020.
- [10] S. Lysgaard, A. L. Ammitzbøll, R. E. Johnsen, P. Norby, U. J. Quaade, and T. Vegge, "Resolving the stability and structure of strontium chloride amines from equilibrium pressures, XRD and DFT," *Int. J. Hydrogen Energy*, vol. 37, no. 24, pp. 18927–18936, 2012.
- [11] C. A. Schneider, W. S. Rasband, and K. W. Eliceiri, "NIH Image to ImageJ: 25 years of image analysis.," *Nat. Methods*, vol. 9, no. 7, pp. 671–675, Jul. 2012.
- [12] P. Kosky, R. Balmer, W. Keat, and G. Wise, "Mechanical Engineering," *Explor. Eng.*, pp. 259–281, 2013.
- [13] T. Roettinger, "PERFORMANCE TESTING AND EVALUATION OF SOLID ABSORPTION SOLAR COOLING UNIT," vol. 61, no. 2, 1997.
- [14] L. Jiang, L. W. Wang, Z. Q. Jin, B. Tian, and R. Z. Wang, "Permeability and Thermal Conductivity of Compact Adsorbent of Salts for Sorption Refrigeration," *J. Heat Transfer*, vol. 134, no. 10, p. 104503, 2012.
- [15] R. Z. Wang and R. G. Oliveira, "Adsorption refrigeration-An efficient way to make good use of waste heat and solar energy," *Prog. Energy Combust. Sci.*, vol. 32, no. 4, pp. 424–458, 2006.
- [16] H. J. Huang, G. Bin Wu, J. Yang, Y. C. Dai, W. K. Yuan, and H. B. Lu, "Modeling of gas-solid chemisorption in chemical heat pumps," *Separation and Purification Technology*, vol. 34, no. 1–3, pp. 191–200, 2004.
-

- [17] R. Iwata, T. Yamauchi, Y. Hirota, M. Aoki, and T. Shimazu, "Reaction kinetics of ammonia absorption/desorption of metal salts," *Appl. Therm. Eng.*, vol. 72, no. 2, pp. 244–249, 2014.
- [18] L. Jiang and A. P. Roskilly, "Thermal conductivity, permeability and reaction characteristic enhancement of ammonia solid sorbents: A review," *Int. J. Heat Mass Transf.*, vol. 130, pp. 1206–1225, 2019.
- [19] A. Karabanova, P. Berdiyeva, M. van der Pal, R. E. Johnsen, S. Deledda, and D. Blanchard, "Importance of Using Intrinsic Kinetics in Modeling Thermochemical Heat Storage System: $\text{SrCl}_2\text{-NH}_3$ Case Study," *Appl. Therm. Eng. - subm. July 2020*.
- [20] F. J. Valdes-parada, J. A. Ochoa-tapia, and J. Alvarez-ramirez, "Validity of the permeability Carman – Kozeny equation : A volume averaging approach," *Physica A*, vol. 388, no. 6, pp. 789–798, 2009.
- [21] J. S. Brenizer, "The 7 th International Topical Meeting on Neutron Radiography A review of significant advances in neutron imaging from conception to the present," *Phys. Procedia*, vol. 43, pp. 10–20, 2013.
- [22] K. H. Andersen *et al.*, "Nuclear Inst . and Methods in Physics Research , A The instrument suite of the European Spallation Source," *Nucl. Inst. Methods Phys. Res. A*, vol. 957, no. January, p. 163402, 2020.

5 Chapter V: Modelling and Neutron Radiography – Optimization of Heat Transfer

In the previous chapter, we have presented and validated the model of the NH_3 sorption occurring in the honeycomb reactor. Such a model should allow developing optimal reactor design, in terms of achievable heat power and cycling efficiency. The reactor geometry and the materials can be examined in detail with further identification of factors limiting the sorption reactions, by performing a sensitivity analysis. In this chapter, we present the results of a parametric study performed on the same reactor prototype used for the validation of the model.

The first paper of this chapter presents the results of the parametric study. We identified the influence of the thermal properties of the reactive bed and heat exchanger on the reaction rate by evaluating the time required to complete 95% of the sorption reactions. Based on the results of the study, practical recommendations regarding the selection of materials for the reactive bed and the heat exchanger were made. To confirm and complement these recommendations, we performed a series of sorption tests using materials with superior and inferior thermal properties. The tests were carried out in combination with neutron radiography measurements to follow the spatio-temporal evolution of NH_3 within the reactive bed during absorption and desorption. The quantitative analysis of the radiography data was performed using the exponential attenuation law, with a scattering component taken into account.

In the second paper, we present a detailed description of one of the sorption / neutron imaging experiments mentioned and briefly described in the first paper of this chapter. This experiment was performed in the same reactor prototype described in Chapter IV, but instead of pure SrCl_2 , we used a composite material made of SrCl_2 and expanded natural graphite, to increase the thermal conductivity of the sorbent bed.

5.1 Paper V: Modelling and Neutron Radiography - Optimization of Heat Transfer for Thermochemical Heat Storage

Anastasiia Karabanova¹, Perizat Berdiyeva², Michel van der Pal³, Ndeye Fatim Koundoul¹,
Stefano Deledda², Didier Blanchard^{1*}

¹*Department of Energy Conversion and Storage, Technical University of Denmark, Anker Engelds Vej 301, DK-2800 Kgs. Lyngby, Denmark;*

²*Department for Neutron Materials Characterization, Institute for Energy Technology, P.O. Box 40, NO-2027 Kjeller, Norway;*

³*TNO Energy Transition, 1755 LE Petten, The Netherlands.*

5.1.1 Abstract

In the present study, a parameter sensitivity analysis was performed on a three-dimensional model of a thermochemical reactor utilizing a reversible reaction between solid strontium chloride (SrCl_2) and gaseous ammonia (NH_3). The analysis was carried out to determine the most critical parameters for the reactor efficiency among thermal properties of the reactive bed and heat exchanger. To confirm and complement the simulation results, a series of sorption experiments assisted with neutron radiography were performed using materials with superior and inferior thermal properties. The study revealed that all the studied properties, except specific heat capacities, play an important role in the desorption rate, and could not be neglected when designing a reactor. For the absorption rate, the most influencing thermal parameter was demonstrated to be the heat transfer coefficient between the reactive bed and heat exchanger. It was also shown that the absorption is a process driven by fluid dynamics, and the permeability of the reactive bed is the major factor defining the efficiency of the system.

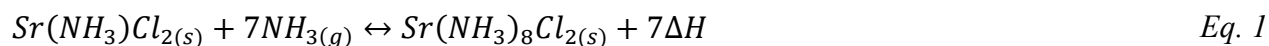
Keywords: thermochemical heat storage, neutron radiography, COMSOL modelling, ammonia-based heat storage system.

5.1.2 Introduction

Resolving the mismatch between the supply and demand of intermittent renewable energy sources and reutilizing waste heat are among the most important problems of the modern energy system. These issues can be addressed with thermal energy storage [1], [2]. There are three types of heat storage systems – sensible [3], latent [4], and thermochemical [5]. Thermochemical storage is considered as a promising technology because it offers greater energy density with no heat loss [6]. Besides, it can also be used for heat upgrade [7].

In order to achieve highly efficient thermochemical heat storage (THS) system, particular attention must be paid to the design of the heat reactor, as it would determine the specific amount of heat that can be charged and discharged per unit of time. To design an optimal reactor, one has to determine the parameters, which have a major impact on the efficiency of the system. This can be done by conducting a parametric study on a numerical model of the thermochemical reactor. This approach has been used by Huang et al. [8], but without an experimental validation of their parametric sensitivity analysis.

In the present paper, we have performed a parametric study on the thermal properties of a reactive bed and heat exchanger, to identify the parameters influencing the rate of the sorption processes to the greatest extent. The parametric sweep was carried out using the three dimensional (3D) absorption and desorption models, previously validated [9]. In [9], the models simulated a reactor prototype with a stainless steel heat exchanger and a reactive bed of SrCl₂ powder. In the reactor, the salt interacts with gaseous NH₃ according to the following equation:



where (*s*) and (*g*) indicate solid and gaseous forms, respectively; ΔH is the enthalpy of the reaction, equal to 41.432 kJ (mole of NH₃)⁻¹ [10].

Based on the results of the parametric study, we have determined the important thermal parameters to be optimized and selected materials for the reactive bed and heat exchanger. Thereafter we have performed a series of real-life experiments to confirm the predictions of the parametric sweep study.

5.1.3 Experimental

5.1.3.1 Numerical model

Geometry, domains, boundary conditions and materials

The geometry of the absorption and desorption models reproduce a reactor prototype, consisting of a honeycomb half-disc (heat exchanger) and a heating element enclosed in an aluminum rectangular prism with a circular NH_3 inlet/outlet. Figure 1(a) depicts the geometry used for modeling, and Figure 1(b) shows the numbering of the hexagons inside the half-disc. For detailed description of the reactor prototype, the reader is referred to [9].

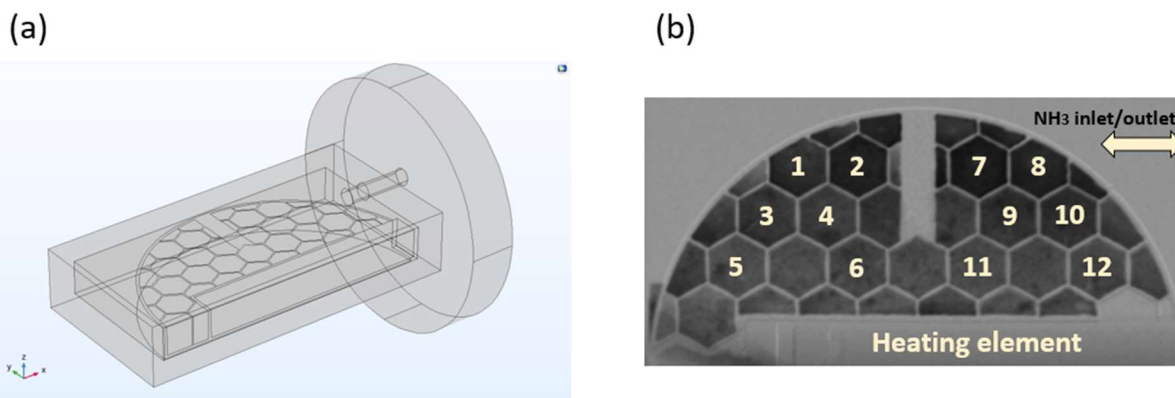


Figure 1. (a) Geometry of reactor prototype in absorption and desorption models. (b) Numbering of hexagons inside reactor prototype.

The model geometry was divided into four domains:

1. Gaseous NH_3 ;
2. Honeycomb slots (hexagons) with embedded reactive sorbent material;
3. Honeycomb half-disc;
4. Aluminum cell.

For the absorption and desorption models, the initial temperature T_{ini} was applied to all the domains. To account for losses to ambient, a convective flux with a heat transfer coefficient h_1 was assigned to the outer surface of the aluminum prism. Thermal insulation boundary condition (no heat flux) was assigned to the upper face of the honeycomb half-disc to prevent heat being

instantly transferred at the points where domains 1-3 coexist in the models. To simulate the thermal resistance between domains 2 and 3, thermal contact boundary condition, characterized with a heat transfer coefficient h_2 , was applied to the contact surface between the two domains. During desorptions, the pressure p_{des} was assumed constant within the reactor, and the temperature of the half-disc surface adjacent to the heating element was set to a desorption temperature T_{des} . It is worth noting that T_{des} is different from the temperature set for the heating element T_{he} due to the thermal resistance between the heating element and the half-disc resulting from the roughness and geometrical imperfection of the contact surfaces. Time required for reaching T_{des} from T_{ini} was programmed using a step function. In the absorption model, a uniform pressure p_{abs} was applied to the NH_3 inlet, and no special temperature conditions were used. Domain 2 represents a heat source during absorption (exothermic reaction Eq. 1 – reverse) and heat sink during desorption (endothermic reaction Eq. 1 – direct).

Table 1 presents the domains with their constituting materials.

Table 1. Domains and corresponding materials with their properties.

#	Domain	Material	Molar mass (kg kmole ⁻¹)	Density (kg m ⁻³)	Thermal conductivity (W m ⁻¹ K ⁻¹)	Specific heat capacity (J kg ⁻¹ K ⁻¹)
1	Gaseous NH_3	$\text{NH}_3(\text{g})$	$M_{\text{NH}_3}^*$	ρ_{NH_3}	$k_{\text{NH}_3}^*$	$C_{p\text{NH}_3}^*$
2	Honeycomb slots	$\text{NH}_3(\text{g})$ $\text{Sr}(\text{NH}_3)\text{Cl}_2(\text{s})$ $\text{Sr}(\text{NH}_3)_8\text{Cl}_2(\text{s})$ Matrix	$M_{\text{NH}_3}^*$ M_1^* M_8^* -	ρ_{eff}	k_{eff}	$C_{p_{eff}}$
3	Honeycomb half-disc	To be selected	-	ρ_{hc}	k_{hc}	$C_{p_{hc}}$
4	Aluminum cell	Aluminum 6063- T83	-	ρ_{cell}^*	k_{cell}^*	$C_{p_{cell}}^*$

* The values of the properties are listed in Table 6 in Supplementary information.

The density of gaseous NH_3 was computed based on the ideal gas law using the following formula:

$$\rho_{\text{NH}_3} = \frac{p \cdot M_{\text{NH}_3}}{RT} \quad \text{Eq. 2}$$

where p is pressure, R is the gas constant, and T is temperature.

The “Honeycomb slots” domain represents a porous medium consisting of the reactive sorbent material in different ammoniated states and gaseous NH_3 . The modification of the reactive bed properties was performed by adding an inert matrix with superior thermal properties to form a composite material consisting of expanded natural graphite (ENG) and $\text{Sr}(\text{NH}_3)_y\text{Cl}_2$, where y varies between 1 and 8.

The properties of the porous medium, called effective properties, can be determined with the following equation:

$$(\rho C_p)_{eff} = \varepsilon \cdot \rho_{\text{NH}_3} \cdot C_{p \text{NH}_3} + (1 - \varepsilon) \cdot \rho_{comp} \cdot C_{p \text{comp}} \quad \text{Eq. 3}$$

where ε is the porosity of the composite material, ρ_{comp} and $C_{p \text{comp}}$ are the density and specific heat capacity of the composite material, respectively.

The porosity of the reactive bed was calculated as follows:

$$\varepsilon = 1 - \frac{\rho_{app \text{comp}}}{\rho_{comp}} \quad \text{Eq. 4}$$

where $\rho_{app \text{comp}}$ is the apparent density of the composite material calculated as shown below:

$$\rho_{app \text{comp}} = \frac{\rho_{app \text{s}}}{1 + \frac{1-w_s}{w_s}} \cdot \left(\frac{(1-x) \cdot M_1 + x \cdot M_8}{M_s} + \frac{1-w_s}{w_s} \right) \quad \text{Eq. 5}$$

where $\rho_{app \text{s}}$ is the apparent density of the composite material with no NH_3 present; w_s is the weight fraction of SrCl_2 in deammoniated composite material; M_1 , M_8 , and M_s are the molar masses of $\text{Sr}(\text{NH}_3)_1\text{Cl}_2$, $\text{Sr}(\text{NH}_3)_8\text{Cl}_2$, and SrCl_2 , respectively; x is the degree of the reaction progression, or reaction advancement, which varies between 0 and 1. In case of absorption, x is equal to 0 and 1, when the salt is in the form of $\text{Sr}(\text{NH}_3)_1\text{Cl}_2$ and $\text{Sr}(\text{NH}_3)_8\text{Cl}_2$, respectively. The opposite applies to desorption: $x=0$ and $x=1$ correspond to $\text{Sr}(\text{NH}_3)_8\text{Cl}_2$ and $\text{Sr}(\text{NH}_3)_1\text{Cl}_2$, respectively.

The properties of the composite materials, ρ_{comp} and $C_{p \text{com}}$, are dependent on both the weight fraction of the matrix w_{matr} and the degree of the reaction progression as indicated below:

$$\rho_{comp} = w_{matr} \cdot \rho_{matr} + (1 - w_{matr}) \cdot ((1 - x) \cdot \rho_1 + x \cdot \rho_8) \quad Eq.6$$

$$C_{p\ comp} = w_{matr} \cdot C_{p\ matr} + (1 - w_{matr}) \cdot ((1 - x) \cdot C_{p\ 1} + x \cdot C_{p\ 8}) \quad Eq. 7$$

where ρ_{matr} , ρ_8 and ρ_1 are the true densities of the matrix, $Sr(NH_3)_8Cl_2$, and $Sr(NH_3)_1Cl_2$, respectively; $C_{p\ matr}$, $C_{p\ 8}$, and $C_{p\ 1}$ are the specific heat capacities of the matrix, $Sr(NH_3)_8Cl_2$, and $Sr(NH_3)_1Cl_2$, respectively. The weight fraction of the matrix w_{matr} was calculated as follows:

$$w_{matr} = \frac{\frac{1-w_s}{w_s}}{\frac{1-w_s}{w_s} + \frac{(1-x)M_1 + xM_8}{M_s}} \quad Eq. 8$$

In case of $SrCl_2$ powder, w_{matr} is null, which leads to zeroing of the first term in Eq. 6 and Eq. 7. It should be noted that Eq. 5-Eq. 8 are adapted for the absorption model. To apply these equations to the desorption model, one has to substitute x and $(1-x)$ with $(1-x)$ and x , respectively.

The effective thermal conductivity of the reactive bed was calculated as follows:

$$k_{eff} = \varepsilon \cdot k_{NH_3} + (1 - \varepsilon) \cdot k_{comp} \quad Eq. 9$$

where k_{comp} is the thermal conductivity of the composite.

Physics

The absorption model couples the kinetics of the chemical reaction with the heat and mass transfer. The desorption model does not include the NH_3 mass transfer and convective heat transfer in domains 1 and 2, which results in substantial gain in computational time without loss in the results accuracy in case of pressure-temperature conditions used in the present study.

- Heat transfer

Eq. 10-Eq. 14 describe heat transfer in the four domains:

$$\rho_{NH_3} C_{p\ NH_3} \frac{\partial T}{\partial t} + \rho_{NH_3} C_{p\ NH_3} \mathbf{u} \cdot \nabla T + \nabla(-k_{NH_3} \nabla T) = 0 \quad Eq. 10$$

$$\rho_{hc} C_{p\ hc} \frac{\partial T}{\partial t} + \nabla(-k_{hc} \nabla T) = 0 \quad Eq. 11$$

$$\rho_{cell} C_{p\ cell} \frac{\partial T}{\partial t} + \nabla(-k_{cell} \nabla T) = 0 \quad Eq. 12$$

$$(\rho C_p)_{eff} \frac{\partial T}{\partial t} + \rho_{NH_3} C_{p, NH_3} \mathbf{u} \cdot \nabla T + \nabla(-k_{eff} \nabla T) = Q \quad Eq. 13$$

$$Q = \pm \frac{dx}{dt} \cdot N_s \cdot \Delta H \quad Eq. 14$$

where \mathbf{u} is the fluid velocity vector and ΔH is the reaction enthalpy equal to 41.432 kJ (mole of NH_3)⁻¹ [10]. Q is the heat absorbed (“-”) during desorption or released (“+”) during absorption by domain 2. N_s is the molar density of NH_3 , calculated as follows:

$$N_s = N_{st} \cdot \frac{\rho_{app,s}}{M_s \cdot (1 + \frac{1-w_s}{w_s})} \quad Eq. 15$$

where N_{st} is the stoichiometric coefficient for NH_3 in Eq. 1, equal to 7.

Heat losses to ambient due to atmospheric cooling was calculated using the following equation:

$$q_1 = h_1 \cdot (T_{ext} - T) \quad Eq. 16$$

where q_1 is the convective heat flux; T_{ext} is external temperature.

The heat flux between domains 2 and 3 was computed as follows:

$$q_2 = h_2 \cdot (T_u - T_d) \quad Eq. 17$$

where T_u and T_d are temperatures upside and downside, respectively.

- Chemical reaction

The kinetics of the sorption processes was expressed with the reaction rate equation:

$$\frac{dx}{dt} = f(x) \cdot k_0 \cdot e^{-\frac{E_a}{RT}} \cdot g(p) \quad Eq. 18$$

where $f(x)$ is the reaction model, k_0 is the pre-exponential factor, E_a is the activation energy of the reaction. $g(p)$ is the pressure function describing the degree of the discrepancy between the actual gas pressure and the equilibrium gas pressure p_{eq} :

$$g(p) = (\pm(p_{eq} - p)/p_{eq})^m \quad Eq. 19$$

where m is a number; “+” and “-” are applied in case of desorption and absorption, respectively.

The equilibrium pressure solely depends on the temperature of the salt and can be defined using the Van't Hoff equation:

$$p_{eq} = p_0 e^{-\frac{\Delta H}{RT} + \frac{\Delta S}{R}} \quad \text{Eq. 20}$$

where p_0 is a reference pressure equal to 1 Pa; ΔS is the reaction entropy equal to 228.6 J (mole of NH_3)⁻¹ K⁻¹ [10].

A set of functions and parameters $f(x)$, k_0 , E_a , and $g(p)$ is called kinetic tetrad. The intrinsic kinetic tetrads for the working pair $\text{SrCl}_2\text{-NH}_3$, determined by Karabanova *et al.* [11], were implemented in the present study. The tetrads are presented in Table 2.

Table 2. Kinetic tetrads for NH_3 absorption and desorption by SrCl_2 amines.

Function / Parameter	Units	Absorption	Desorption
$f(x)$	-	$3 \cdot (1 - x)^{\frac{2}{3}}$	$3 \cdot (1 - x)^{\frac{2}{3}}$
k_0	s ⁻¹	$2.423 \cdot 10^7$	36754
E_a	kJ mole ⁻¹	66.1	43.9
m	-	1.8	1.9

- Mass transfer

The diffusion of NH_3 in the porous medium was described with the Brinkman equations:

$$\frac{\partial \varepsilon \rho_{\text{NH}_3}}{\partial t} + \nabla \cdot (\rho_{\text{NH}_3} \mathbf{u}) = \pm Q_m \quad \text{Eq. 21}$$

$$\rho_{\text{NH}_3} \frac{\partial \mathbf{u}}{\partial t} = \nabla \cdot \left[-p \mathbf{I} + \frac{\mu_{\text{NH}_3}}{\varepsilon} (\nabla \mathbf{u} + (\nabla \mathbf{u})^T) - \frac{2}{3} \frac{\mu_{\text{NH}_3}}{\varepsilon} (\nabla \cdot \mathbf{u}) \mathbf{I} \right] - \left(\frac{\mu_{\text{NH}_3}}{\kappa} + \beta_F \varepsilon \rho_{\text{NH}_3} |\mathbf{u}| + \frac{Q_m}{\varepsilon^2} \right) \mathbf{u} + \mathbf{F} \quad \text{Eq. 22}$$

where Q_m is the source/sink term, positive for desorption and negative for absorption; κ is the hydraulic permeability of the reactive bed; β_F is the Forchheimer drag factor. In the present study, domain forces \mathbf{F} were neglected and β_F was set to 0. Q_m depends on the reaction rate and thus was calculated using the following equation:

$$Q_m = \pm \frac{dx}{dt} \cdot N_s \cdot M_{\text{NH}_3} \quad \text{Eq. 23}$$

5.1.3.2 Material preparation and characterization

As will be further shown in the section Results - Parametric sweep, the ability of the reactive bed to conduct heat plays an important role in increasing the rate of sorption processes. To improve the thermal conductivity of the reactive bed, we have prepared a composite material made of SrCl₂ and porous heat conductive matrix of expanded natural graphite (ENG). The composite material SrCl₂ - ENG was synthesized by impregnation method, widely used for the preparation of metal halides – ENG composites [12]–[14]. The synthesis procedure consisted of three steps. First, ENG board (SGL Carbon, apparent density 75 kg m⁻³) was soaked in ethanol to lower the surface tension of water. Then, the ENG board was immersed in 33.3 % wt. aqueous solution of SrCl₂ (Amminex, purity > 98%) for 72 h. After that, the sample was placed in a ventilated oven for 12 h at 90°C with further drying at 300°C for 12 h in a vacuum furnace. The synthesized composite material has 76 % wt. of SrCl₂ and the apparent density is 543 kg m⁻³. Hexagonal pellets with a side of around 5.8 mm and a height of 10 mm were fabricated from the synthesized material in a way that the ENG sheets were parallel to the height of the hexagons to allow NH₃ gas flow freely within the reactive bed.

The effective thermal conductivity of the deammoniated composite material was determined using a Xenon Flash Analyzer. As the properties of the ENG-based materials are anisotropic, the thermal conductivity of the composite was measured in parallel and perpendicular directions relative to the ENG sheets [15]. As a result, in-plane and through plane thermal conductivities were obtained. The thermal conductivities of the sample (10 mm × 10 mm × 2 mm) were tested over a temperature range from 25 till 150°C at 13 different points.

5.1.3.3 Gas setup and experiments

The gas setup for sorption experiments and its operation is described in more detail elsewhere [9]. Using this setup, we performed three sets of measurements with different materials as reactive bed (sample) and honeycomb half-disc. The materials were selected based on the results of the parametric study, presented below. The details of the experiments are presented in Table 3.

Table 3. Experiments and materials used.

#	Experiment name	Sample	Honeycomb half-disc	Sample mass m_{sample} (g)	Apparent density $\rho_{app,s}^*$ (kg m ⁻³)
1	Comp + SS	Composite material	Stainless Steel (type 316)	8.4	543
2	Comp + Al	Composite material	Aluminum 3003-H18		
3	SrCl ₂ + Al	SrCl ₂ powder (Amminex, purity > 98%)	Aluminum 3003-H18	7.28	366

* The apparent density of the sample (composite material or SrCl₂ powder) prior to NH₃ cycling was calculated using the following formula:

$$\rho_{app,s} = \frac{m_{sample}}{V_{total}} \quad Eq. 24$$

where V_{total} is the volume of the reactive bed, equal to around 19.9 cm³ for the three experiments.

Stainless steel and aluminum honeycomb discs were fabricated using a water jet cutter and a three dimensional (3D) printer, respectively. The difference in manufacturing method resulted in different degree of roughness of the two half-discs. While the surface of the stainless steel sample holder is relatively smooth, the one made of aluminum is rather rough.

Each experiment includes one sorption cycle consisting of absorption and desorption. Absorptions were carried out at room temperature, and during desorptions, the temperature of a heating element, located inside the reactor prototype, was set to 100°C.

Based on the values of the corrected flowrate, the reaction advancement x was calculated as shown below:

$$x = \frac{V_t}{V_{tot}} \quad Eq. 25$$

where V_t is the amount of NH₃ that was absorbed/desorbed by SrCl₂ by time t ; V_{tot} is the total volume of NH₃ that was absorbed/desorbed by SrCl₂. The corrected flowrate FR_{corr} was calculated from the measured flowrate by taking into account the deviation between operating and calibrated pressure-temperature conditions. As the temperature of the gas passing through the

flowmeter was not measured, it was assumed constant, and hence the flowrate was corrected for pressure only.

The experiments were reproduced by the abovementioned model, which resulted in six simulations named as presented in Table 4.

Table 4. Performed simulations.

#	Experiment name	Simulation name	
		Absorption model	Desorption model
1	Comp + SS	1a	1d
2	Comp + Al	2a	2d
3	SrCl ₂ + Al	3a	3d

5.1.3.4 Neutron radiography

Neutron imaging experiments were carried out using two instruments. Experiment “Comp + SS” (see Table 3) has been performed on NeXT D50, the neutron imaging instrument located at the Institute Laue-Langevin (ILL) reactor in Grenoble, France [16], [17]. Using this beamline, the images were captured every second, and one image was produced from three consecutive images resulting in the acquisition time of 3 s. For the other two experiments, “Comp + Al” and “SrCl₂ + Al”, we have used NECTAR, the NEutron Computed Tomography And Radiography, situated at the FRM II neutron reactor at the Heinz Maier-Leibnitz Zentrum (MLZ), Germany [18]–[20]. In this case, the radiographs were collected every 27 s with the exposure time of 13 s. For more information on the instruments, the reader is referred to Supplementary information.

Simplified procedure of quantitative analysis of neutron radiography data used in this study is given in Supplementary information. This approach takes into account the contaminant component of the detected neutron beam [21], and gives more accurate results compared to the ones described in [9]. The kinetic curve was obtained for each hexagon as indexed in Figure 1(b), and the global reaction advancement was calculated as an average of the results obtained from the 12 hexagons.

5.1.4 Results and discussions

5.1.4.1 Parametric sweep

For the sensitivity analysis, the absorption and desorption models were computed for the following material properties: 1) thermal conductivity k_{comp} and 2) specific heat capacity $C_{p\ comp}$ of the composite material; 3) thermal conductivity k_{hc} and 4) specific heat capacity $C_{p\ hc}$ of the honeycomb half-disc material; 5) heat transfer coefficient between the composite material and the half-disc h_2 . We have used the simplest method of the sensitivity analysis, which requires varying parameter values one-at-a-time with the other parameters fixed at their initial values [22]. The initial values of the parameters can be found in [9]. For the evaluation of parameter sensitivity, we have calculated the sensitivity index (SI) for each parameter using the following formula [23]:

$$SI = \frac{D_{max} - D_{min}}{D_{max}} \cdot 100\% \quad Eq. 26$$

where D_{max} and D_{min} represent the maximum and minimum output values, respectively, resulting from varying the input over its entire range. In the present study, the output was assigned to a time required to complete 95% of absorption ($t_{a\ 95}$) or desorption ($t_{d\ 95}$). $t_{a(d)\ 95}$ was chosen as a criterion fixing the final power and efficiency of the system.

The parametric sweep was performed on $\frac{1}{4}$ of the geometry, presented in Figure 1(a), to save computational time.

Figure 2 illustrates the results of the study, presented as the dependency of $t_{a(d)\ 95}$ on a varied parameter. It is worth to note that Figure 2 does not include the results from the heat capacities, $C_{p\ comp}$ and $C_{p\ hc}$, because their SI 's are relatively low - below 5 % for the range 200 – 2000 J kg⁻¹ K⁻¹.

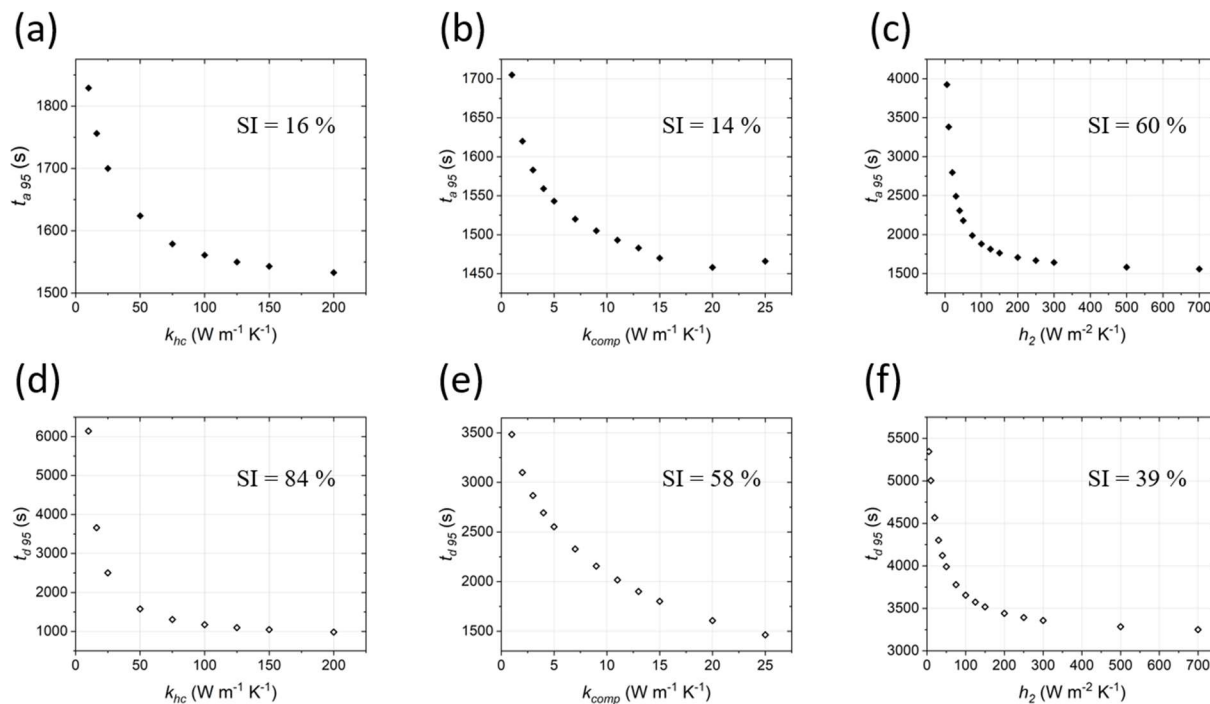


Figure 2. Results of parametric study: dependency of t_{a95} on (a) k_{hc} , (b) k_{comp} ; (c) h_2 and dependency of t_{d95} on (d) k_{hc} , (e) k_{comp} ; (f) h_2 .

All the curves from Figure 2 have the shape of an exponential decay function representing a falling curve that approaches, but never reaches an asymptote. This indicates that the increase in the parameter values have a substantial effect on the reaction rate up to a certain point, after which the impact becomes insignificant.

As can be seen from Figure 2(a-c), the heat transfer coefficient h_2 has the greatest influence on the absorption rate among all the studied parameters. It gives the highest SI, equal to 60 % for a range 5 - 700 $W m^{-2} K^{-1}$. When $h_2 < 200 W m^{-2} K^{-1}$, t_{a95} exhibits a strong dependence on h_2 (Figure 2(c)); however, further increase in h_2 has a limited effect on the absorption rate. The other two input parameters, k_{hc} and k_{comp} , are not heavily correlated to the output.

From Figure 2(d-f), one can notice that t_{d95} is sensitive to all the studied parameters. When comparing the values of SI , one can notice that the thermal conductivity of the heat exchanger k_{hc} is the major contributor to the speed of desorption, having a SI of 84 % for a range from 10 to 200 $W m^{-1} K^{-1}$. It is important to note that the increase in k_{hc} from 10 till 75 $W m^{-1} K^{-1}$ leads to 64 % gain in desorption time, while further increase gives remaining 20 %. The second important

parameter is the thermal conductivity of the composite k_{comp} (with no porosity) with the value of SI equal to 58 %. $t_{d\ 95}$ is sensitive to this parameter on the full range studied herein. The desorption rate is also sensitive to the change in heat transfer coefficient h_2 within a range from 5 to 200 $\text{W m}^{-2} \text{K}^{-1}$, and the difference between the two extreme points of the range is 36%. Further increase would not influence the reaction rate significantly.

Based on the results of the parametric sweep, the following recommendations on the enhancement of the sorption rates are to be made:

- 1) Make the heat exchanger of a material with the thermal conductivity higher than $75 \text{ W m}^{-1} \text{K}^{-1}$. Among other requirements, which the material should meet, there were also resistance to corrosion and price. The best fit to the aforementioned criteria is aluminum, as the thermal conductivity of its alloys varies between 150 and $200 \text{ W m}^{-1} \text{K}^{-1}$. Moreover, it is rather cheap and it shows good resistance to dry gaseous NH_3 . The characteristics of the selected alloy (3003-H18) are listed in Supplementary information.
- 2) Improve the thermal conductivity of the reactive bed. To increase the thermal conductivity of SrCl_2 , we have synthesized a composite material $\text{SrCl}_2 - \text{ENG}$ made of SrCl_2 and the heat conductive matrix of expanded natural graphite (ENG). The synthesis technique and characterization of the composite material is described in the section Material preparation and characterization. The composite is characterized with a relatively high effective thermal conductivity (see Figure 3) when compared with pristine SrCl_2 , which has a conductivity of $0.21 \text{ W m}^{-1} \text{K}^{-1}$ with the density of 798.3 kg m^{-3} [24].

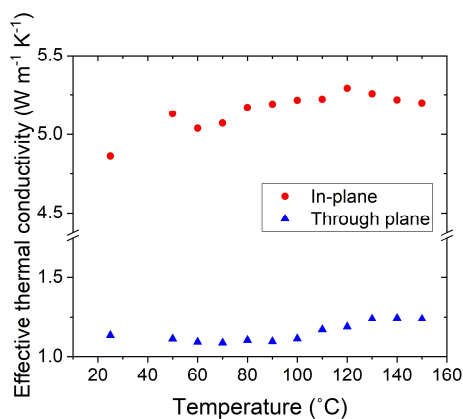


Figure 3. In-plane and through plane effective thermal conductivity of composite material as a function of temperature.

In the simulations with the composite material (see Table 4), the average values of the in-plane and through plane conductivities (k_{in} and k_{th}) over the measured temperature range were set as components of anisotropic conductivity k_{eff} as follows: x - and z -components are k_{in} , and y -component is k_{th} . The axes in the model geometry are shown in Figure 1(a). The average values of parallel and perpendicular thermal conductivities were found to be 5.15 and 1.16 W m⁻¹ K⁻¹, respectively. These values were assumed constant upon sorption, as the effective thermal conductivity of the composite material is several times higher compared to the one of SrCl₂-amine system.

- 3) Increase the heat transfer coefficient between the reactive bed and the heat transfer coefficient. No specific actions have been taken to address this point.

Based on the recommendation listed above, we have performed a set of experiments with the selected materials (the composite material and aluminum 3003-H18). For comparison, the materials with inferior heat transfer properties, such as pristine SrCl₂ and stainless steel 316), were also tested. The experiments are listed in Table 3 in the section Gas setup and experiments. During desorptions, the temperature of the heating element T_{he} was set to 100°C and during absorptions no heat sources/sinks were used. The results obtained from the experiments (flowrate and pressure curves) are presented in section Experimental results in Supplementary information.

5.1.4.2 Modeling results

As reported in Table 7 (see Supplementary Information), the average value of pressure during the experiments differs much, especially in case of the absorptions. To bring the experiments to same pressure conditions, we have first fitted the described above numerical models to the obtained from flowmeter experimental results and then run the simulations with the same pressure for absorptions ($p_{abs}=2.5$ bar) and desorptions ($p_{des}=1$ bar). The performed simulations are listed in Table 4.

Desorption results

For the desorption simulations, the unknown parameters were the desorption temperature T_{des} and the heat transfer coefficients between the sample and the heat exchanger h_2 . As mentioned above in Numerical model, T_{des} is lower than T_{he} (100°C) due to the heat resistance between the two contact surfaces. In simulation 1d, h_2 was set to 165 W m⁻² K⁻¹ – the value taken from the literature for similar system [8]. With this value, the model fits the experimental data well, when T_{des} is set to 70°C. Using this temperature, the values of h_2 for the simulations 2d and 3d were fitted to 20 and 40 W m⁻² K⁻¹, respectively. More than 8-fold difference between the values of h_2 for the same sample (composite material), but different simulations (1d and 2d) could be explained by the state of the material prior to cycling. While at the beginning of experiment “Comp + SS”, the sample has not been in contact with NH₃ before, in experiment “Comp + Al” the material has been cycled several times. It has been reported previously in [25] that the pristine pellets embedded in the cells of the heat exchanger expand during NH₃ absorption due to the difference in the densities of SrCl₂ and Sr(NH₃)₈Cl₂ and occupy the whole volume of the cells (see Figure 4). This appears to contribute a lot to improved contact between the sample and the heat exchanger walls.

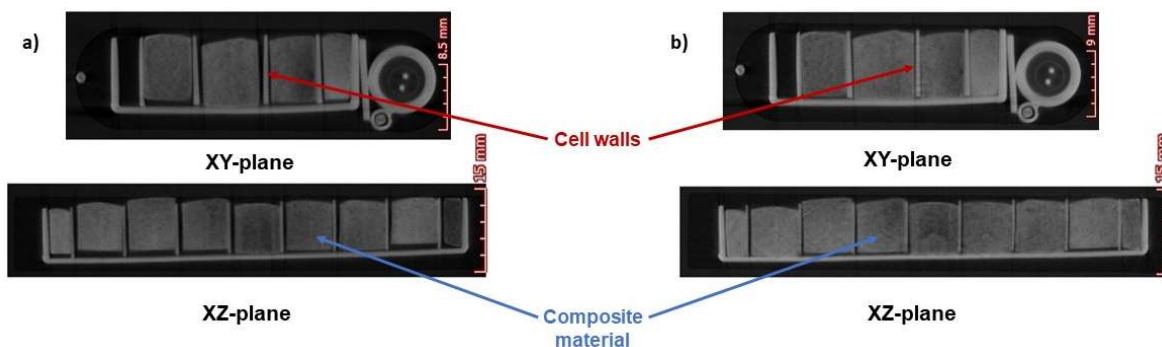


Figure 4. Two-dimensional images (XY- and XZ-planes) of the composite material (a) before cycling and (b) after cycling. The Figure is taken from Paper VI.

On the contrary, if the inserted material has been in contact with NH_3 , its geometry is well established and the cycling of the sample will not lead the enhancement of the heat transfer coefficient between the sample and the heat exchanger. This must be considered when one aims to improve the contact between the sample and the heat exchanger.

Figure 5 shows the comparison between the results from the simulations and experimental data obtained from flowmeter and neutron radiography. Figure 5(a) presents global reaction advancement curves and Figure 5(b-d) illustrates the results for some of the individual hexagons labelled as in Figure 1(b). The global kinetics curves from the numerical simulations is calculated as an average of the 12 hexagons indexed in Figure 1(b). The results for all the hexagons are presented in Figure 13 in Supplementary Information.

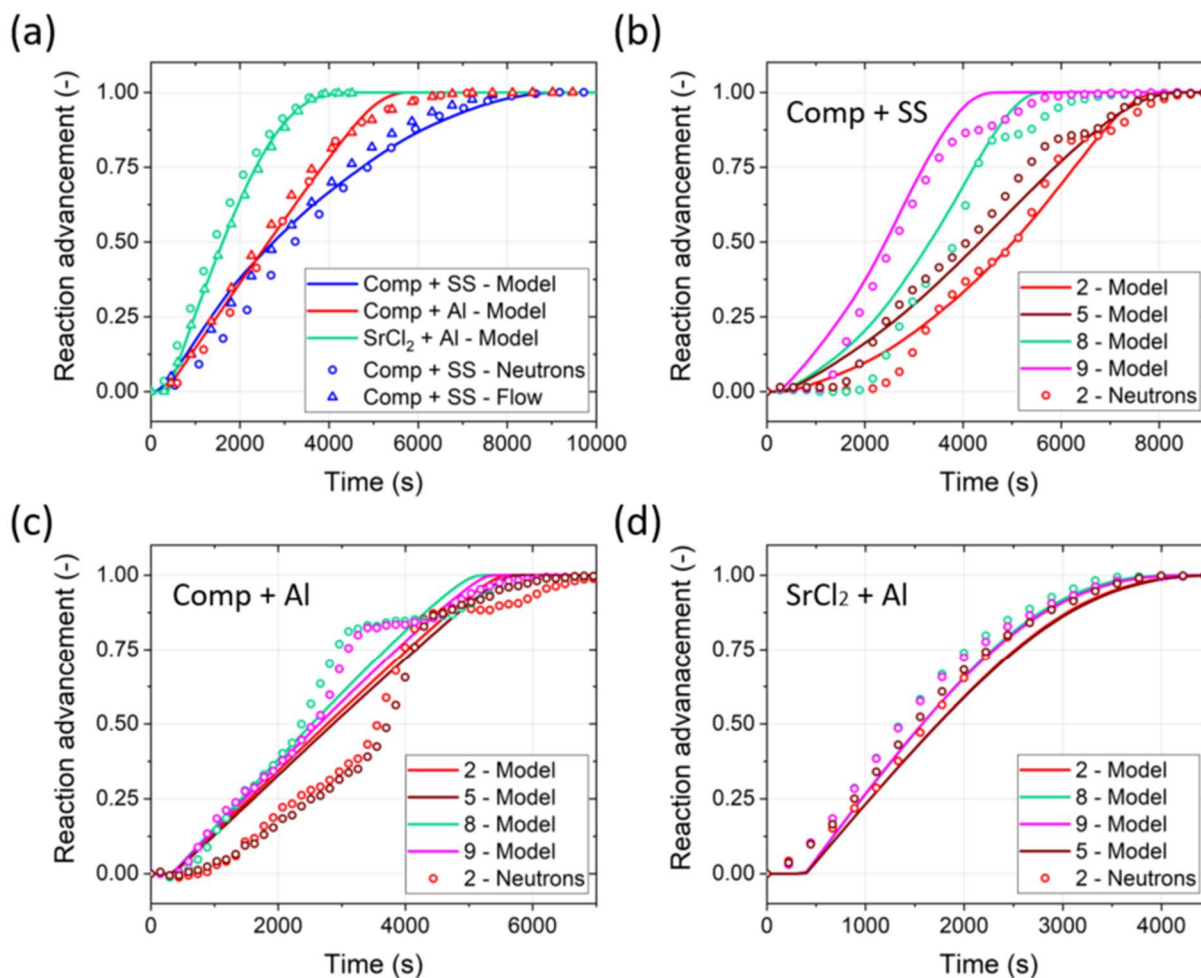


Figure 5. Comparison between model and experiment for desorption: (a) global reaction advancement curves from simulations (solid lines), flowmeter (triangles), and neutron radiography experiments (circles); (b-d) kinetic curves for individual hexagons from simulations (solid lines) and neutron radiography experiments (circles). Indexing of hexagons is shown in Figure 1(b).

The results from Figure 5(a) show a good agreement between the experimental data and the simulations on a global level. It should be noted that the absolute error between the flowmeter and neutron radiography global curves does not exceed 5 %.

If one looks at the results for individual hexagons (Figure 5(b-d)), one could see that the model captures the shape of the experimental curves only for non-impregnated salt (Figure 5(d)). In case of the composite material (Figure 5(b-c)), the desorptions occur in several step, and the model

represents one-step decomposition according to Eq. 1. Interestingly, the features on the curves are observed at the same degree of desorption for the two experiments. For example, the first deviation from a smooth line occurs, when the desorption advancement reaches 86 %, which corresponds to the diamine decomposing into the monoamine and NH_3 :



In a previous study [26], the presence of the diamine has been reported during the octaamine decomposition, but at higher pressures compared to the ones used in the present study. The fact that this step was not observed for the $SrCl_2$ powder bed at almost identical pressure-temperature conditions might indicate that the process of impregnation has changed the equilibrium parameters of the reaction in Eq. 27.

The second feature to notice, especially in Figure 5(c), is a knee at around 38 % of conversion, after which the reaction rate increased. This behavior may be explained by fast absorption of the heat by the sample due to the high thermal conductivity of the composite material. At the beginning of the process, the heat is consumed by the endothermic reaction occurring in the hexagons located closer to the heating element, and only a negligible heat could be transferred to the further ones. This hypothesis is supported by the fact that this feature is more pronounced in case of further hexagons 2 and 5, when compared to the closer hexagons 8 and 9. The model could not capture this feature because no limitation was set for the value of the heat flux in between the heating element and the honeycomb surface. In reality, this heat flux may be limited by the power sent to the heating element.

Absorption results

For the absorption simulations, we adjusted κ , the permeability, and d_p , the particle diameter for the composite material and $SrCl_2$ powder bed, respectively. The values of the heat transfer coefficient h_2 were taken from the desorption simulations, presented above. The value of κ were found to be $5 \times 10^{-16} \text{ m}^2$ for simulations 1a and 2a, and the particle diameter was calculated 200 nm for simulation 3a.

Figure 6 presents the comparison between the simulations and the experimental results.

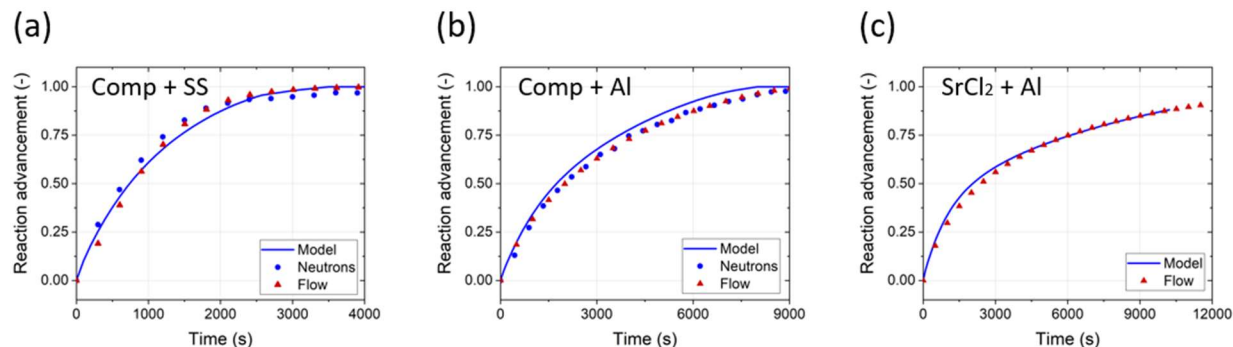


Figure 6. Comparison between model and experiment for absorption: global reaction advancement curves from simulations (solid lines), flowmeter (triangles), and neutron radiography experiments (circles) for (a) experiment “Comp + SS” and simulation 1d, (b) experiment “Comp + Al” and simulation 2d, and (c) experiment “SrCl₂ + Al” and simulation 3d. The results from neutron radiography are not available for “SrCl₂ + Al” experiment.

From Figure 6, one can notice that the results from the simulations are in line with the experimental data, on a global level. The results from individual hexagons have not been included, as the individual curves coincide with the global reaction curves and hence do not carry any additional information.

Common conditions

To compare the experimental results, we have computed the fitted models for same pressure ($p_{des} = 1$ bar and $p_{abs} = 2.5$ bar). To investigate the effect of the heat transfer coefficient between the sample and the heat exchanger h_2 , the simulations were also run for same pressure and h_2 ($165 \text{ W m}^{-2} \text{ K}^{-1}$).

The global kinetic curves retrieved for the desorptions and absorptions are presented in Figure 7(a) and (b), respectively.

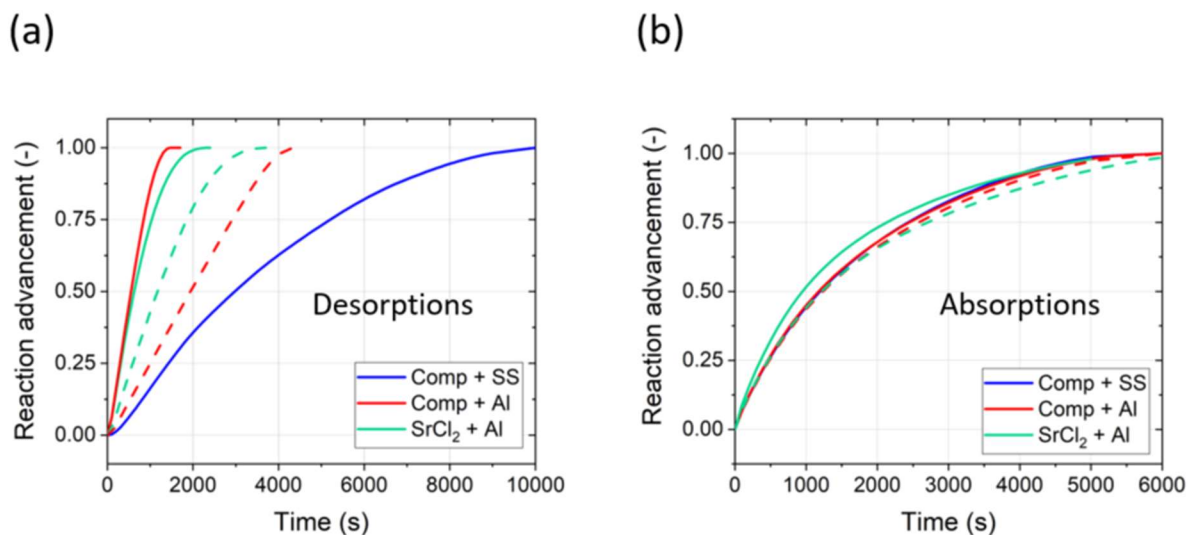


Figure 7. Global reaction advancement curves from absorption and desorption simulations run under same pressure (dashed line) and under same pressure and same $h_2=165 \text{ W m}^{-2} \text{ K}^{-1}$ (solid line). The two lines for experiments “Comp + SS” coincide.

From Figure 7, the values of $t_{d\ 95}$ and $t_{a\ 95}$ were extracted and listed in Table 5. As the specific amount of SrCl_2 is not the same for the three experiments, we have normalized it using the following formula:

$$\beta_{a(d)} = \frac{0.95 \cdot w_s \cdot \rho_{app,s}}{t_{a(d)\ 95}} \quad \text{Eq. 28}$$

Eq. 28 calculates the average rate of absorption or desorption of 1 kg of SrCl_2 from 1 m^3 of the reactive bed. The values of the average rate are presented in Table 5.

Table 5. Results for simulations calculated for same pressure (first) and same pressure and $h_2=165 \text{ W m}^{-2} \text{ K}^{-1}$ (second). The first and second positions are same for “Comp + SS”.

#	Experiment	$h_2, \text{ W m}^{-2} \text{ K}^{-1}$	$t_{d\ 95}, \text{ s}$	$\beta_d, \text{ kg m}^{-3} \text{ s}^{-1}$	$t_{a\ 95}, \text{ s}$	$\beta_a, \text{ kg m}^{-3} \text{ s}^{-1}$
1	Comp + SS	165	8140	0.048	4366	0.090
2	Comp + Al	20	3820 / 1193	0.103 / 0.329	4636 / 4314	0.085 / 0.091
3	SrCl_2 + Al	40	2766 / 1640	0.126 / 0.212	5198 / 4444	0.067 / 0.078

As can be observed from the desorption results obtained at same pressure but different h_2 (see Figure 7 and Table 5), experiment 2 with higher thermal conductivity of the reactive bed but lower h_2 exhibits slower desorption kinetics when compared to experiment 3. However, if h_2 would be the same for the two experiment, the reaction rate for experiment 1 would be the highest, as was predicted by the parametric study. This underlines the importance of taking into account the heat transfer coefficient when designing and building a thermochemical reactor. Interestingly, system 1 with a heat exchanger made of stainless steel has the lowest desorption rate among the three systems.

On the contrary to the desorption simulations, the absorption rate is higher for experiment 2 when compared to experiment 3 despite the fact that it is characterized with lower h_2 . It might be due to higher value of thermal conductivity of the composite material used for system 1, but as has been shown in the parametric study this parameter does not have a great effect on the absorption rate in comparison to h_2 . Another explanation could be that the absorption of NH_3 into the reactive bed is a diffusion-driven process, and the permeability of the reactive bed plays an important role in the absorption rate. This hypothesis is supported by the fact that the absorption rates of experiments 1 and 2 are almost similar for the same value of h_2 , even though the thermal conductivity of the samples in these two cases differs a lot.

5.1.5 Conclusion

The aim of this study was to perform a parametric study on the thermal properties of a reactive bed and a heat exchanger and confirm the study predictions with real-life tests. The parametric sweep was performed on a 3D model simulating sorption processes in a thermochemical heat storage reactor. As the experiments were executed at different conditions, we have fitted the model to the experimental data and carry out simulations for identical pressure-temperature conditions.

The parametric study revealed that factors limiting desorption rate, and hence the system efficiency, are the thermal conductivities of the reactive bed and heat exchanger. The desorption experiments confirmed this, but also demonstrated that increasing the values of the thermal conductivities without taking into account the contact between the reactive bead and the heat exchanger will not lead to the enhancement but deterioration of the system efficiency. One of

methods to make the contact between the surfaces better was shown to use pristine material for packing a reactor, as after several NH_3 cycles the pristine material will expand and occupy the whole reactive volume. In case of the absorption rate, the heat transfer between the sample and the heat exchanger was identified as its major contributor among the studied thermal parameters. This finding was supported by the absorption experiments; however, the experimental data has shown that the absorption is driven by NH_3 diffusion, which makes the permeability of the reactive bed critical parameter in case of the absorption rate.

In addition, it has been demonstrated that neutron radiography is a powerful tool for studying the spatio-temporal distribution of NH_3 within the reactive bed, which can bring valuable insights about the processes occurring inside the reactor.

5.1.6 Acknowledgements

This work is financially supported by NordForsk Nordic Neutron Science Programme via the Neutrons for Heat Storage (NHS) project (No. 82206). The authors thank neutron sources ILL and FRMII for the allocation of neutron radiation beam times, and particularly Lukas Helfen, Alessandro Tengattini, and Adrian Losko are acknowledged for experimental assistance. Additionally, the Danish Research Council is acknowledged for the financial support via Danscatt. Last but not least, the authors thank Hilde Larsson for giving valuable pieces of advice during modeling in COMSOL Multiphysics software.

5.1.7 References

- [1] A. Gil *et al.*, “State of the art on high temperature thermal energy storage for power generation. Part 1-Concepts, materials and modellization,” *Renew. Sustain. Energy Rev.*, vol. 14, no. 1, pp. 31–55, 2010.
- [2] M. Medrano, A. Gil, I. Martorell, X. Potau, and L. F. Cabeza, “State of the art on high-temperature thermal energy storage for power generation. Part 2-Case studies,” *Renew. Sustain. Energy Rev.*, vol. 14, no. 1, pp. 56–72, 2010.
- [3] S. Ayyappan, K. Mayilsamy, and V. V. Sreenarayanan, “Performance improvement studies in a solar greenhouse drier using sensible heat storage materials,” *Heat Mass Transf. und*

-
- Stoffuebertragung*, vol. 52, no. 3, pp. 459–467, 2016.
- [4] J. Pereira da Cunha and P. Eames, “Thermal energy storage for low and medium temperature applications using phase change materials - A review,” *Appl. Energy*, vol. 177, pp. 227–238, 2016.
- [5] I. Dincer and M. A. Ezan, *Heat Storage: A Unique Solution For Energy Systems*. 2018.
- [6] K. E. N’Tsoukpoe, T. Schmidt, H. U. Rammelberg, B. A. Watts, and W. K. L. Ruck, “A systematic multi-step screening of numerous salt hydrates for low temperature thermochemical energy storage,” *Appl. Energy*, 2014.
- [7] M. van der Pal and R. E. Critoph, “Performance of CaCl_2 -reactor for application in ammonia-salt based thermal transformers,” *Appl. Therm. Eng.*, vol. 126, pp. 518–524, 2017.
- [8] H. J. Huang, G. Bin Wu, J. Yang, Y. C. Dai, W. K. Yuan, and H. B. Lu, “Modeling of gas-solid chemisorption in chemical heat pumps,” *Sep. Purif. Technol.*, vol. 34, no. 1–3, pp. 191–200, 2004.
- [9] A. Karabanova *et al.*, “Neutron radiography for modeling thermochemical heat storage reactors: case study on $\text{SrCl}_2\text{-NH}_3$ system,” *J. Energy Storage - Submitt. June 2020*.
- [10] L. Jiang and A. P. Roskilly, “Thermal conductivity, permeability and reaction characteristic enhancement of ammonia solid sorbents: A review,” *Int. J. Heat Mass Transf.*, vol. 130, pp. 1206–1225, 2019.
- [11] A. Karabanova, P. Berdiyeva, M. van der Pal, R. E. Johnsen, S. Deledda, and D. Blanchard, “Importance of Using Intrinsic Kinetics in Modeling Thermochemical Heat Storage System: $\text{SrCl}_2\text{-NH}_3$ Case Study,” *Appl. Therm. Eng. - subm. July 2020*.
- [12] S. Mauran, P. Prades, and F. L’Haridon, “Heat and mass transfer in consolidated reacting beds for thermochemical systems,” *Heat Recover. Syst. CHP*, 1993.
- [13] L. Jiang, L. W. Wang, Z. Q. Jin, R. Z. Wang, and Y. J. Dai, “Effective thermal conductivity and permeability of compact compound ammoniated salts in the adsorption/desorption process,” *Int. J. Therm. Sci.*, vol. 71, pp. 103–110, 2013.
-

-
- [14] L. Jiang, R. Z. Wang, Y. J. Lu, A. P. Roskilly, L. W. Wang, and K. Tang, “Enquête sur l’utilisation de chlorure de strontium composite conducteur thermique innovant pour les machines de refroidissement à sorption à l’ammoniac,” *Int. J. Refrig.*, vol. 85, pp. 157–166, 2018.
- [15] L. W. Wang, Z. Tamainot-Telto, S. J. Metcalf, R. E. Critoph, and R. Z. Wang, “Anisotropic thermal conductivity and permeability of compacted expanded natural graphite,” *Appl. Therm. Eng.*, vol. 30, no. 13, pp. 1805–1811, 2010.
- [16] A. Tengattini *et al.*, “NeXT-Grenoble, the Neutron and X-ray tomograph in Grenoble,” *Nucl. Instruments Methods Phys. Res. Sect. A Accel. Spectrometers, Detect. Assoc. Equip.*, vol. 968, no. March, p. 163939, 2020.
- [17] C. Tötze, N. Kardjilov, N. Lenoir, I. Manke, S. E. Oswald, and A. Tengattini, “What comes NeXT? – High-Speed Neutron Tomography at ILL,” *Opt. Express*, vol. 27, no. 20, p. 28640, 2019.
- [18] T. Bücherl, C. Lierse Von Gostomski, H. Breikreutz, M. Jungwirth, and F. M. Wagner, “NECTAR - A fission neutron radiography and tomography facility,” *Nucl. Instruments Methods Phys. Res. Sect. A Accel. Spectrometers, Detect. Assoc. Equip.*, vol. 651, no. 1, pp. 86–89, 2011.
- [19] M. J. Mühlbauer *et al.*, “Neutron imaging with fission and thermal neutrons at NECTAR at MLZ,” *Phys. B Condens. Matter*, vol. 551, no. August 2017, pp. 359–363, 2018.
- [20] M. J. Mühlbauer *et al.*, “The Thermal Neutron Beam Option for NECTAR at MLZ,” *Phys. Procedia*, vol. 88, no. September 2016, pp. 148–153, 2017.
- [21] M. Tamaki, M. Oda, K. Takahashi, and W. Tanimoto, “Study on neutron imaging techniques and processings for developing quantitative neutron radiography,” vol. 377, pp. 102–106, 1996.
- [22] D. M. Hamby, “a Review of Techniques for Parameter Sensitivity,” *Environ. Monit. Assess.*, vol. 32, no. c, pp. 135–154, 1994.
- [23] L. R. Bauer and D. M. Hamby, “Relative Sensitivities of Existing and Novel Model
-

-
- Parameters in Atmospheric Tritium Dose Estimates,” *Radiat. Prot. Dosimetry*, vol. 37, no. 4, pp. 253–260, Aug. 1991.
- [24] L. Jiang, L. W. Wang, Z. Q. Jin, B. Tian, and R. Z. Wang, “Permeability and Thermal Conductivity of Compact Adsorbent of Salts for Sorption Refrigeration,” *J. Heat Transfer*, vol. 134, no. 10, p. 104503, 2012.
- [25] P. Berdiyeva, A. Karabanova, D. Blanchard, B. C. Hauback, and S. Deledda, “Sr(NH₃)₈Cl₂-Expanded Natural Graphite composite for thermochemical heat storage applications studied by in-situ neutron imaging,” *Int. J. Hydrog. Energy - Submitt. Sept. 2020*.
- [26] R. E. Johnsen, P. B. Jensen, P. Norby, and T. Vegge, “Temperature- And pressure-induced changes in the crystal structure of Sr(NH₃)₈Cl₂,” *J. Phys. Chem. C*, 2014.
- [27] S. Lysgaard, A. L. Ammitzbøll, R. E. Johnsen, P. Norby, U. J. Quaade, and T. Vegge, “Resolving the stability and structure of strontium chloride amines from equilibrium pressures, XRD and DFT,” *Int. J. Hydrogen Energy*, vol. 37, no. 24, pp. 18927–18936, 2012.
- [28] T. Roettinger, “PERFORMANCE TESTING AND EVALUATION OF SOLID ABSORPTION SOLAR COOLING UNIT,” vol. 61, no. 2, 1997.
- [29] C. A. Schneider, W. S. Rasband, and K. W. Eliceiri, “NIH Image to ImageJ: 25 years of image analysis,” *Nat. Methods*, vol. 9, no. 7, pp. 671–675, Jul. 2012.
-

5.1.8 Supplementary information

Table 6. Material properties and parameters.

Designation	Units	Value / Equation	Reference	
M_s	kg kmole ⁻¹	158.53	-	
M_1		175.561		
M_8		294.778		
M_{NH_3}		17.031		
ρ_s	kg m ⁻³	3108	ICSD collection code 18011	
ρ_1		2440	[27]	
ρ_8		1380	ICSD collection code 194517	
ρ_{matr}		2260	*	
C_{p1}	J kg ⁻¹ K ⁻¹	$649.8 + 3.524 \cdot T + 0.021 \cdot T^2$ $+ 0.00016 \cdot T^3$	[28]	
C_{p8}		$576.296 + 3.124 \cdot T + 0.07 \cdot T^2$ $+ 0.00005 \cdot T^3$		
$C_{p\,matr}$		720		**
$C_{p\,NH_3}$		$1.96 \cdot T + 1531$		Engineering Equation Solver (EES) 2016 database
k_{NH_3}	W m ⁻¹ K ⁻¹	$(0.138 \cdot T + 16.58) \cdot 10^{-3}$	Engineering Equation Solver (EES) 2016 database	
μ_{NH_3}	Pa s	$4 \cdot 10^{-8} \cdot T - 10^{-6}$		
ρ_{hc} (ss)	kg m ⁻³	7950	COMSOL Multiphysics 5.5 database	
ρ_{hc} (Al)		2730		
k_{hc} (ss)	W m ⁻¹ K ⁻¹	16.3		
k_{hc} (Al)		155		
$C_{p\,hc}$ (ss)	J kg ⁻¹ K ⁻¹	490		
$C_{p\,hc}$ (Al)		893		
ρ_{cell}	kg m ⁻³	2700		

k_{cell}	$\text{W m}^{-1} \text{K}^{-1}$	201	
$C_{p\ cell}$	$\text{J kg}^{-1} \text{K}^{-1}$	900	
T_{ini}	$^{\circ}\text{C}$	20	Experiment
T_{ext}	$^{\circ}\text{C}$	20	
p_{cal}	bar	1.01325	
h_1	$\text{W m}^{-2} \text{K}^{-1}$	5	

* <http://poco.com/Portals/0/Literature/Semiconductor/IND-109441-0115.pdf>

** <https://www.chem.wisc.edu/deptfiles/genchem/netorial/modules/thermodynamics/enthalpy/enthalpy3.htm>

5.1.8.1 Neutron instruments

Neutron imaging experiments were carried out using two instruments. One set of the experiments were performed on NeXT D50, the neutron imaging instrument located at the Institute Laue-Langevin (ILL) reactor in Grenoble, France [16], [17]. The instrument provides a beam of cold neutrons with a flux of up to $2 \times 10^8 \text{ cm}^{-2}\text{s}^{-1}$ at the sample position (collimation ratio L/D 400) with a spectrum of maximum intensity at 2.8 Å. During our experiments, the neutron beam was collimated with a pinhole of 23 mm diameter resulting in the collimation ratio L/D of 435. The images were captured every second by a detector consisting a 50 μm thick Gadox scintillator (field of view 10 cm \times 10 cm) and a CMOS camera (Hamamatsu Orca 4V2). One image was produced from three consecutive images resulting in the acquisition time of 3 s. The other instrument used in this study is NECTAR, the NEutron Computed Tomography And Radiography, situated at the FRM II neutron reactor at the Heinz Maier-Leibnitz Zentrum (MLZ), Germany [18]–[20]. A sample is exposed to a thermal neutron beam with a flux of up to $4.7 \times 10^7 \text{ cm}^{-2}\text{s}^{-1}$ at the sample position with a mean wavelength of 1.81 Å. The transmitted through the sample beam was captured by a detector setup composed of a 200 μm thick $^6\text{LiF} / \text{ZnS:Cu}$ scintillator and an Andor iKon-L CCD camera with a pixel size of 13.5 μm . The radiographs were collected on an area of 40 cm \times 40 cm every 27 s with the exposure time of 13 s.

5.1.8.2 Quantitative analysis of radiography data

For the quantitative analysis of the collected neutron radiography data, the raw images were normalized by flat-field (FF) and dark field (DF) images using ImageJ [29]:

$$T_{\theta} = \frac{I_{\theta-DF}}{FF-DF} \quad \text{Eq. 29}$$

where I_{θ} is the intensity of the transmitted beam in the raw image; T_{θ} the intensity of the transmitted beam in the normalized image.

While the dark field images correct for dark current in detector system, the flat-field images correct for inhomogeneities in beam-profile and in detector screen. The open beam and dark current images were taken prior to every absorption and desorption. After normalization, the stack of the normalized images were divided by the first image in case of absorption and by the last image in case of desorption to remove the contribution from the sample environment as well as from the monoamine ($\text{Sr}(\text{NH}_3)\text{Cl}_2$). Thus, the intensity of the beam in the divided images corresponds to neutrons transmitted through and scattered by NH_3 . This intensity I_t can be evaluated at time t as follows [21]:

$$I_t = I_0 e^{-\mu \cdot d} + I_s \quad \text{Eq. 30}$$

where I_0 is the intensity of the incident neutron beam; μ the linear attenuation coefficient of the sample; d the thickness of the sample; and I_s the overlapped contaminant component. The coefficient μ depends on the neutron wavelength together with the chemical composition and apparent density of the sample. In this study, it was assumed that the reaction occurs homogeneously in a fixed 1 cm thick reactive bed, and the amount of NH_3 present in the system is consistent with the reaction product $\text{Sr}(\text{NH}_3)_y\text{Cl}_2$, where y varies between 1 and 8. Thus, the linear attenuation coefficient, for a given neutron wavelength, is dependent only on the NH_3 density in the sample, which depends on the reaction advancement x and is calculated as follows:

$$\rho_{app_NH_3} = \frac{w_s \cdot \rho_{app_s} \cdot x \cdot N_{st} \cdot M_{NH_3}}{M_s} \quad \text{Eq. 31}$$

where w_s is the mass fraction of the salt in the composite material (for the pristine salt, it is equal to 1), ρ_{app_s} is the apparent density of the composite material, x is the reaction advancement, N_{st} is the stoichiometric ratio equal to 7; M_{NH_3} and M_s are the molar masses of NH_3 and SrCl_2 , respectively.

Based on the flowmeter readings, it was assumed that at the beginning and end of the sorption processes the amount of NH_3 corresponds to either $\text{Sr}(\text{NH}_3)\text{Cl}_2$ (no NH_3) or $\text{Sr}(\text{NH}_3)_8\text{Cl}_2$ (fully ammoniated state). For example, in the beginning of absorption there was no NH_3 present, which resulted in that the collected intensity was almost equal to the incident one. Based on this, the following expression was derived:

$$\frac{I_t}{I_1} = e^{-\mu_t \cdot d} + \frac{I_s(t)}{I_0} \quad \text{Eq. 32}$$

where I_1 is the collected intensity of the first image during NH_3 absorption, respectively.

While the first term on the right-hand side of Eq. 32 refers to the fraction of the beam transmitted through the sample, the second term corresponds to the scattered neutrons. In the following, the latter term will be referred as a contaminant term. Assuming maximum NH_3 loading in the end of absorption allows computing the maximum value of the contaminant term using the following formula:

$$\frac{I_s(t_{max})}{I_0} = \frac{I_t}{I_1} - e^{-\mu_{t_{max}} \cdot d} \quad \text{Eq. 33}$$

where t_{max} is time at the end of absorption and $\mu_{t_{max}}$ is linear attenuation coefficient of NH_3 corresponding to $\text{Sr}(\text{NH}_3)_8\text{Cl}_2$.

Thus, during absorption the contaminant term changes from 0 till its maximum. The dependency between the contaminant component and the reaction advancement can be described as follows:

$$\frac{I_s(t)}{I_0} = \frac{I_s(t_{max})}{I_0} \cdot (1 - (1 - x)^n) \quad \text{Eq. 34}$$

For desorption, the reverse procedure was applied.

For the analysis, several values of n were chosen (see Figure 8).

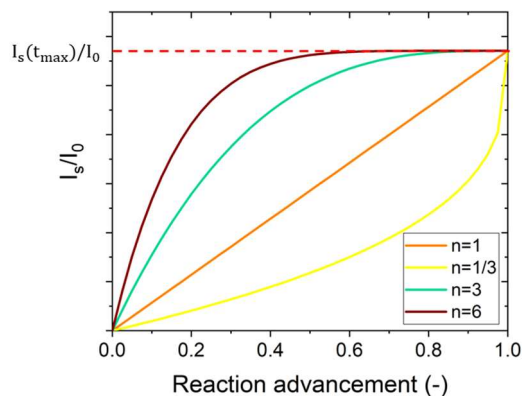


Figure 8. Dependency of $\frac{I_s(t)}{I_0}$ on reaction advancement for different values of n .

The reaction advancement as a function of $\frac{I_t}{I_1}$ is presented for the three sets of data in Figure 9: left - ILL-2020 (abs4, hexagon1), middle - FRM-II, ENG sample (abs2, hexagon 1), right – FRM-II, SrCl₂ sample (abs4, hexagon1).

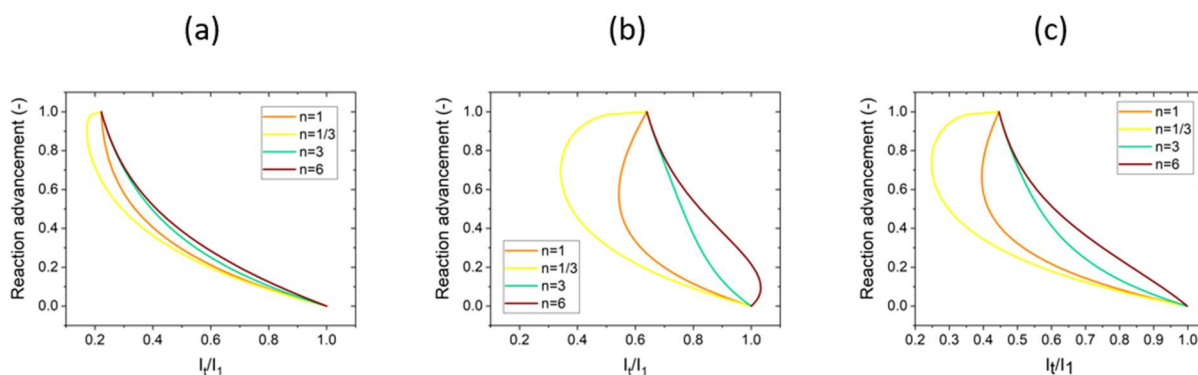


Figure 9. Dependency of reaction advancement on $\frac{I_t}{I_1}$ for different values of n and different absorption experiments: (a) “Comp + SS”, (b) “Comp + Al”, and (c) “SrCl₂ + Al”. The analysis was done for the 12 hexagons presented in Figure 1(b).

Based on the results presented in Figure 9, only those values of n were chosen, which gave dependencies, where each value of $\frac{I_t}{I_1}$ corresponds to only one value of the reaction advancement.

The results of the final calculations are shown below.

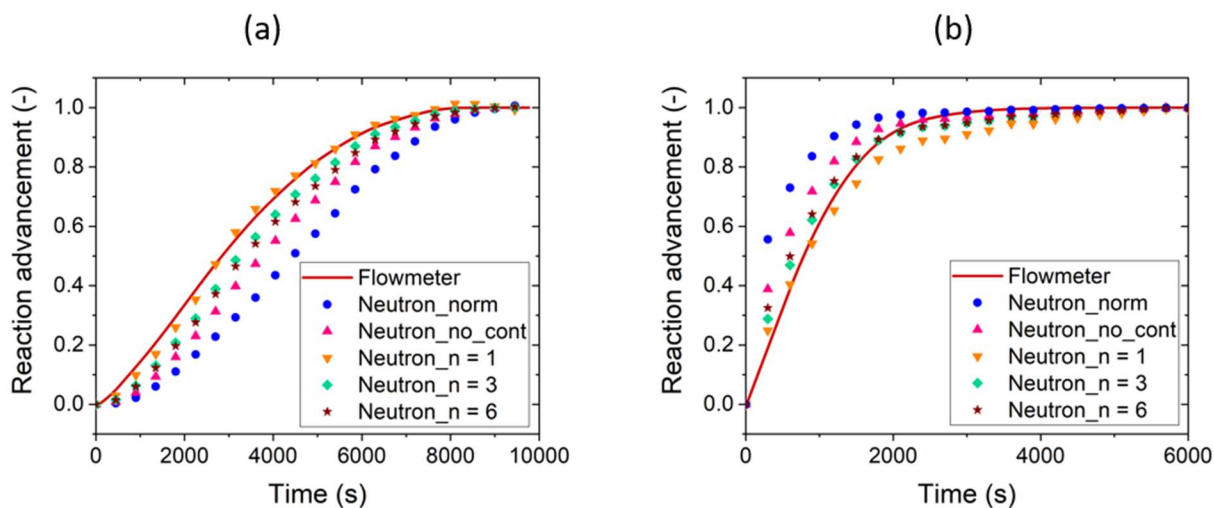


Figure 10. Results for experiment "Comp + SS": (a) desorption; (b) absorption. In the legend: 'Neutron_norm' is just normalized neutron data; 'Neutron_no_cont' is the neutron data recalculated without taking into account the contaminant component; 'Neutron_n=1' is the neutron data recalculated with taking into account the contaminant term that changes linearly; etc.

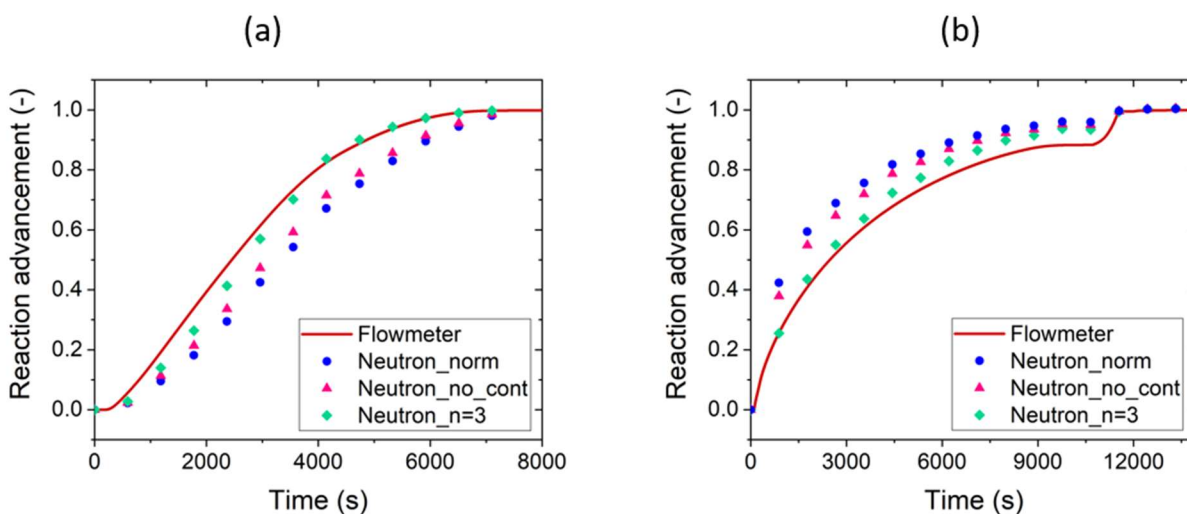


Figure 11. Results for experiment "Comp + Al": (a) desorption; (b) absorption. In the legend: 'Neutron_norm' is just normalized neutron data; 'Neutron_no_cont' is the neutron data recalculated without taking into account the contaminant component; 'Neutron_n=3' is the neutron data recalculated with taking into account the contaminant term that changes with cubic dependency.

5.1.8.3 Experimental results

Figure 12 illustrates the results from the absorption (a, c) and desorption (b, d) experiments.

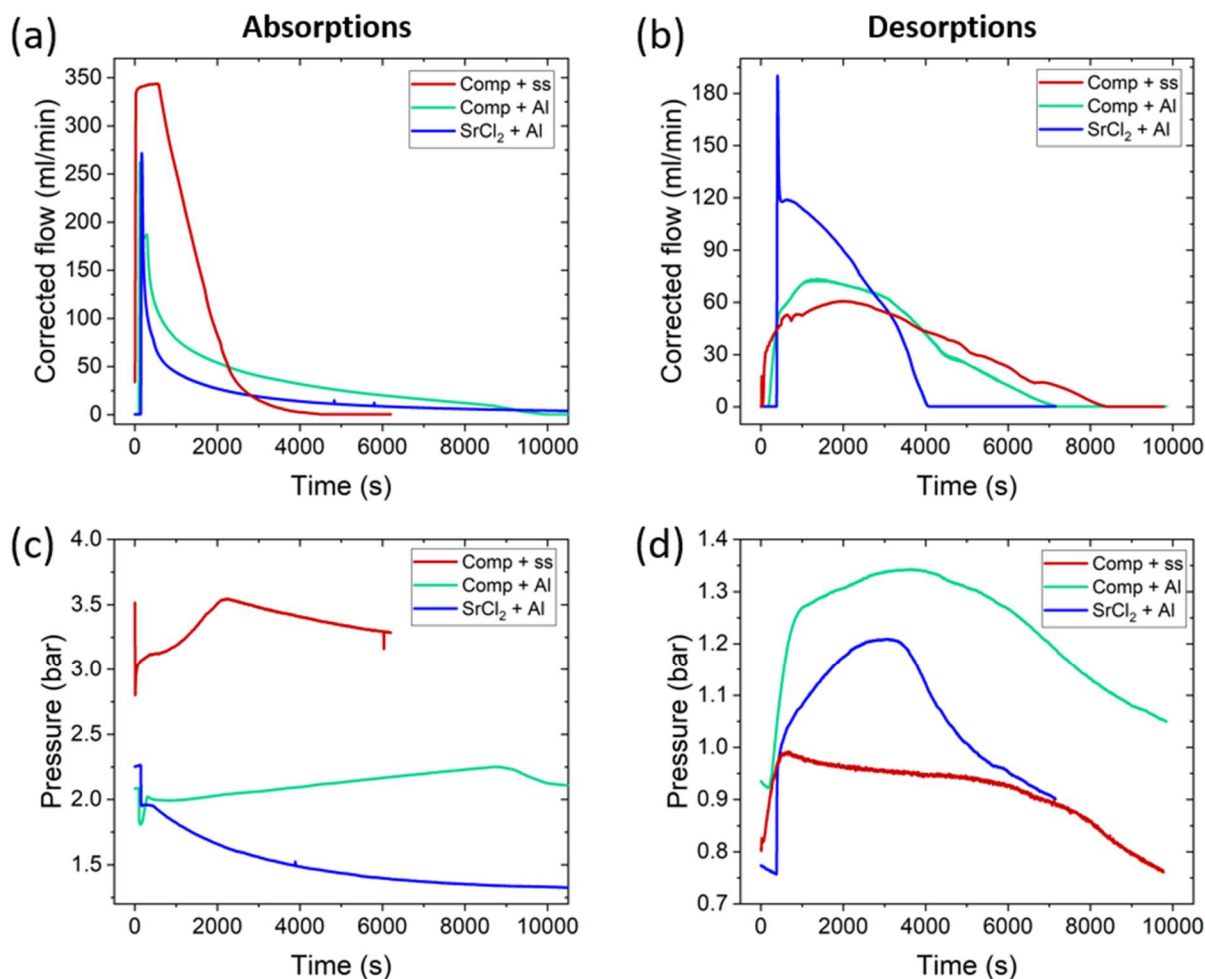


Figure 12. Experimental results: corrected flow as a function of time for (a) three absorption experiments and (b) three desorption experiments; pressure as a function of time for (c) three absorption experiments and (d) three desorption experiments.

The information extracted from Figure 12 was used for modeling. The curves from Figure 12(a, b), depicting dependencies of the corrected flow on time, were converted into global reaction advancement curves using Eq. 25 and compared with the model curves, as shown in Figure 5(a). From Figure 12(c, d), the average pressure values were found and used as an input for the simulations (see Table 7).

Table 7. Input parameters for absorption and desorption simulations – average pressure for all experiments.

Experiment	Average pressure (bar)	
	Absorption	Desorption
Comp + Al	2.1	1.27
SrCl ₂ + Al	Equation*	1.11
Comp + SS	3.35	0.92

* If $t \leq 4000$ s, then $p_{abs} = -5 \cdot 10^{-12} \cdot t^3 + 6 \cdot 10^{-8} \cdot t^2 - 0.0003 \cdot t + 2.076$; otherwise, $p_{abs} = -4 \cdot 10^{-13} \cdot t^3 + 1 \cdot 10^{-8} \cdot t^2 - 0.0001 \cdot t + 1.78$.

5.1.8.4 Desorption results

Table 8. Results from desorption simulations – fitted parameters and their values.

Simulation →	1d	2d	3d
Transition zone, s	100	100	100
Location, s	50	250	350
h_2 , W m ⁻¹ K ⁻¹	165	20	40

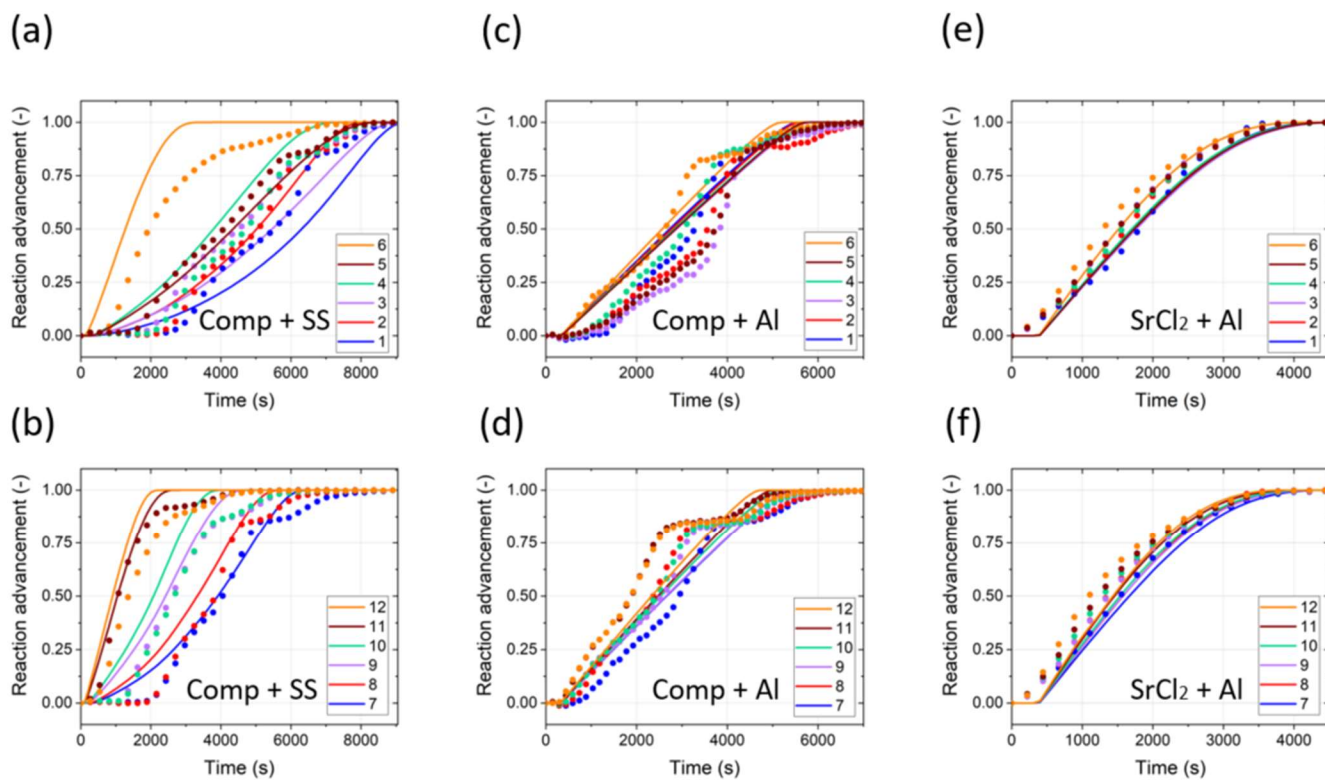


Figure 13. Comparison between desorption simulations and experimental results for individual hexagons indexed as in Figure 1(b): (a-b) experiment “Comp + SS” and simulation 1d; (c-d) experiment “Comp + Al” and simulation 2d; (e-f) experiment “SrCl₂ + Al” and simulation 3d.

5.2 Paper VI: $\text{Sr}(\text{NH}_3)_8\text{Cl}_2$ -Expanded Natural Graphite composite for thermochemical heat storage applications studied by *in-situ* neutron imaging

Perizat Berdiyeva^a, Anastasiia Karabanova^b, Didier Blanchard^b, Bjørn C. Hauback^a and Stefano Deledda^{a*}

^{a)} *Department for Neutron Materials Characterization, Institute for Energy Technology, P.O. Box 40, NO-2027, Kjeller, Norway*

^{b)} *Department of Energy Conversion and Storage, Technical University of Denmark, Fysikvej, DK-2800, Lyngby, Denmark*

* corresponding author

5.2.1 Abstract

This work presents an *in-situ* neutron imaging study of the ammonia sorption reaction in a SrCl_2 -Expanded Natural Graphite (ENG) composite loaded into a honeycomb-shaped stainless-steel scaffold and enclosed in a thermochemical heat storage (THS) reactor prototype. The performance of $\text{SrCl}_2/\text{Sr}(\text{NH}_3)_8\text{Cl}_2$ -ENG under different pressures and temperatures was investigated and the spatio-temporal content of ammonia was calculated from neutron radiograms. Quantitative image analysis revealed the formation of $\text{Sr}(\text{NH}_3)_8\text{Cl}_2$ upon ammonia uptake, while the desorption studies revealed a partial ammonia desorption resulting in the formation of the monoamine phase $\text{Sr}(\text{NH}_3)\text{Cl}_2$ via a stepwise release of ammonia. Neutron imaging also allowed the indirect evaluation of the stainless-steel honeycomb heat conductivity and showed that heat is transferred prevalently via the ENG matrix. Finally, neutron tomography of the reactor prototype was performed to ensure the stability of the THS system and composite material throughout the ammonia cycling experiments.

Key words

metal halide composites; thermochemical heat storage; ammonia sorption; neutron imaging

5.2.2 Introduction

Thermal energy storage and reutilization of the waste heat can give a significant contribution to reduce our carbon footprint. Different types of thermally driven materials and systems for both large and small scale applications have been developed in the past decade [1–4]. Among the various types of the thermal energy storage technologies, thermochemical heat storage (THS) systems have gained high interest and are considered as promising systems [5,6]. They can be operated using hydrates or ammines forming carbonates or metal halides for high, low or medium temperature storage, respectively. The salt-ammonia working pairs have shown high efficiency and cyclability compared to other solutions [7]. Besides, metal halide ammines have also been studied as potential hydrogen and ammonia storage materials [8–12].

The low temperature $\text{SrCl}_2\text{-NH}_3$ working pair has been extensively investigated by various techniques to characterize its kinetics, reaction pathways and cyclability [13–16]. The chemical reaction between SrCl_2 and NH_3 proceeds with the formation of $\text{Sr}(\text{NH}_3)_8\text{Cl}_2$ octammine at room temperature (RT) with a volume expansion of the material by up to 300 %. In the desorption process, NH_3 release generally results in the formation of $\text{Sr}(\text{NH}_3)\text{Cl}_2$ monoammine [13] at 40-50 °C under 1 bar of NH_3 . Alternatively, the formation of $\text{Sr}(\text{NH}_3)_2\text{Cl}_2$ diammine can precede the formation of monoammine under selected NH_3 pressures [14]. The full NH_3 desorption occurs above 150 °C against 1 bar of NH_3 . The desorption reaction results in a contraction of the material volume and formation of macro and microporous structures within the grains [17]. The extreme volume increase is the main drawback of most salt-ammonia based working pairs. If no precautions are applied, this behavior can limit their applications on account of system safety and drastically reduce the heat transfer because of the formed porous structure. Several studies have shown the possibility to circumvent the volume expansion problem in various salt-ammonia working pairs by mixing the salts with expanded natural graphite (ENG) and thus forming composites [18–22]. In addition, thermal studies showed up to 182 % increase in the thermal conductivity for $\text{SrCl}_2\text{-ENG}$ composites when compared to the pure salt [18]. While the ENG shows no affinity to NH_3 , [23], it can help to control the volume expansion in $\text{Sr}(\text{NH}_3)_8\text{Cl}_2$, by acting as a buffer.

The work presented here shows an *in-situ* neutron imaging study on a $\text{SrCl}_2\text{-ENG}$ composite placed in a stainless-steel honeycomb heat exchanger mounted inside a model THS reactor. The

honeycomb heat exchanger represents the basic unit of a THS reactor prototype. The full-size THS reactor will comprise eleven of these honeycomb discs with a total volume of 0.5 L. Neutron imaging offers the unique possibility to analyze the spatio-temporal ammonia content in the composite material due to the strong interaction of neutrons with hydrogen [24]. It is a powerful characterization method widely used for energy storage materials studies such as batteries, hydrogen storage systems and fuel cells [25–32]. Recently, similar neutron imaging experiments were conducted on the $\text{SrCl}_2/\text{Sr}(\text{NH}_3)_8\text{Cl}_2$ system within the same THS reactor prototype, and the fragility of the powder bed subjected to a large volume expansion was reported [33]. Furthermore, the deformation of the stainless-steel honeycomb due to the thermal expansion and mechanical stresses caused by the volume expansion during $\text{Sr}(\text{NH}_3)_8\text{Cl}_2$ formation was presented. On the contrary, our study reports a remarkable mechanical stability of SrCl_2 -ENG during NH_3 uptake and release with only slight expansion and contraction of the composite material, providing a homogeneous NH_3 uptake and showing excellent thermal conductivity. The hydrogen present in the ammonia molecule allows to detect the areas within the honeycomb, where $\text{Sr}(\text{NH}_3)_8\text{Cl}_2$ is formed, and here it is demonstrated for the first time how the NH_3 content in composite materials within a THS reactor can be calculated from neutron radiography images. Additionally, the heat released during NH_3 absorption reaction was monitored and the efficiency of the stainless-steel honeycomb serving as a heat exchanger and sample holder within the THS reactor is discussed. Complementary neutron tomography study revealed in-depth information about the honeycomb and the THS reactor, and the obtained results are compared to the previous neutron imaging study [33].

5.2.3 Experimental

5.2.3.1 Sample preparation

The SrCl_2 -ENG composite was prepared by impregnation of expanded natural graphite (ENG) sheets (from SGL Carbon, 95 % purity) with SrCl_2 (from AMMINEX, 99.9 % purity) by submerging the ENG into $\text{SrCl}_2 \cdot \text{H}_2\text{O}$ for 72 hours. Prior to the impregnation process, ENG was dried at 180 °C for 8 hours and then soaked into ethanol for 2 hours for reducing the surface tension between non-polar ENG and polar $\text{SrCl}_2 \cdot \text{H}_2\text{O}$ [34]. The impregnated ENG was then dried in an oven at 90 °C for 12 hours and further dehydrated in vacuum at 300 °C for 12 hours. Using this

impregnation method, a SrCl_2 -ENG composite with 76 wt% of SrCl_2 and 24 wt% of ENG was obtained. Hexagonal pellets with height of 10 mm were cut out from the SrCl_2 -ENG composite sheets.

5.2.3.2 THS set-up

The SrCl_2 -ENG composite pellets (total mass of 8.4 g) were loaded into a stainless-steel honeycomb half-disc containing a heating element with thermocouple (T_h) and a second thermocouple (T_s) to monitor the sample temperature during ammonia cycling. T_s was inserted to the top of the honeycomb and surrounded by stainless-steel walls with thickness of ~ 2.5 mm. The honeycomb half-disc was then inserted into the THS reactor, which was connected to an absorption/desorption rig (see Figure 1). The detailed parameters of the THS reactor are described elsewhere [33]. Prior to the neutron imaging experiment the sample was dried at 200 °C under dynamic vacuum for 3 hours. A reservoir with 100 g of $\text{Sr}(\text{NH}_3)_8\text{Cl}_2$ powder, denoted as the ‘ammonia reservoir’, served as the ammonia source and was connected to the THS reactor with stainless steel tubes. A flowmeter with a readout range of 0 – 200 ml min^{-1} was implemented between the THS reactor and the reservoir in order to monitor the NH_3 gas flow during cycling. A magnetic valve (M) connected to the THS reactor ensured a remote control of the NH_3 gas flow between SrCl_2 -ENG in the honeycomb and the reservoir. A pressure transducer (P) mounted between the flowmeter and the reservoir allowed a continuous monitoring of the pressure.

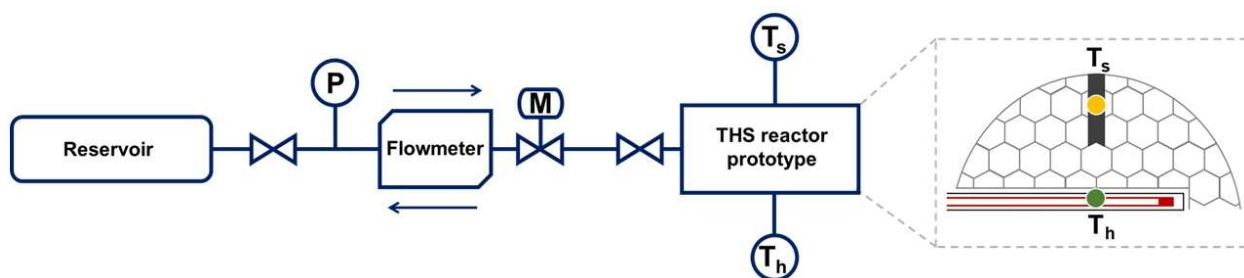


Figure 1. Left: Schematic view of the setup. P , T_h and T_s represent the points where the pressure, temperature of the heater and the sample temperature were monitored, respectively. M denotes the position of the magnetic valve. The arrows above and beneath the flowmeter show the NH_3 gas flow during the absorption and desorption, respectively. Right: Schematic of the honeycomb half-disc with marked positions of T_h and T_s . The heating element below the honeycomb is marked with red color.

The ammonia absorption in SrCl₂-ENG was achieved by heating up Sr(NH₃)₈Cl₂ in the ammonia reservoir, to release NH₃ into the setup, while the ammonia desorption was studied by heating ammoniated Sr(NH₃)₈Cl₂-ENG in the THS reactor at various temperatures. Such closed system ensured safe handling of NH₃ gas during the experiment.

5.2.3.3 Neutron Imaging set-up

The neutron imaging experiments were performed at the NeXT beamline (D50) [35] at the Institute Laue-Langevin (ILL) research reactor in Grenoble, France. A cold neutron beam with a flux of $1.5 \cdot 10^8$ n cm⁻² s⁻¹ was collimated by a 23 mm pinhole (L/D ~ 435) and transmitted through the sample. The sample was mounted in front of a Gadox scintillator screen with a field of view 10cm x 10cm and a thickness of 50 μm. The scintillated light was captured by a CMOS camera (Hamamatsu Orca 4V2) providing images with a time resolution of 1s. For three sequential radiography images, one average image was produced.

The radiography images were normalized and analyzed using ImageJ [36] and the transmission of the SrCl₂/Sr(NH₃)₈Cl₂-ENG composite material was calculated according to:

$$I = I_0 e^{-\mu x} \quad (1)$$

where I is the intensity transmitted through the sample, I_0 is the incident intensity, μ is the linear attenuation coefficient and x is the sample thickness.

The neutron transmission values of NH₃ absorbed in the composite material were obtained by dividing the overall stack of images by the first image (for absorption) or by the last image (for desorption) in order to remove the SrCl₂-ENG contribution from the images and to observe only absorbed or desorbed NH₃ in the radiogram. The mean transmission values for the NH₃ were obtained from selected hexagon-shaped areas within each cell of the honeycomb. The density of NH₃ was calculated according to:

$$\rho_{NH_3} = \frac{(\mu_{Sr(NH_3)_8Cl_2-EN} - \mu_{SrCl_2-ENG}) * M}{N_A * \sigma_{NH_3}} \quad (2)$$

where $\mu_{Sr(NH_3)_8Cl_2-ENG}$ is the attenuation coefficient of the ammoniated composite, μ_{SrCl_2-ENG} is the attenuation coefficient of the composite without ammonia, M is the molar mass of ammonia, N_A is Avogadro constant and σ_{NH_3} is the total neutron cross section of ammonia. The mass of ammonia m_{NH_3} is calculated from the density given by Equation-2 multiplied with the volume of NH_3 obtained from each radiogram. Then the gravimetric NH_3 content (wt%) in $Sr(NH_3)_xCl_2$ during absorption and desorption was calculated from:

$$x_{NH_3} = \frac{m_{NH_3}}{m_{NH_3} + m_{SrCl_2}} * 100\% \quad (3)$$

where m_{SrCl_2} is the mass of the $SrCl_2$ in the composite material in the initial state.

Neutron tomography of the composite material was carried out by rotating the THS reactor over a 360° range at 0.225° per step and resulting in 1600 projections (one image per step). The initial state, the absorbed and desorbed states of the composite material were scanned and reconstructed using XAct software [37] and visualized with VG Studio Max[®] software [38].

5.2.4 Results and discussions

5.2.4.1 Ammonia sorption and heat storage properties of the $SrCl_2$ -ENG composite in the THS system

In total four NH_3 absorption desorption cycles in the $SrCl_2$ -ENG composite were studied. Each absorption was followed by desorption with a dwell time to allow the THS reactor or the ammonia reservoir to cool down.

Absorption reactions were conducted at RT and at different NH_3 gas pressures. Figure 2a depicts the evolution of the NH_3 gas pressures during the four absorption processes. The first (Absorption-1, blue curve) and second (Absorption-2, red curve) absorption were performed at similar NH_3 pressures of ~ 2.5 bar which increased up to 2.7 bar due to the saturation of $Sr(NH_3)_8Cl_2$ -ENG while the NH_3 gas was still provided by the ammonia reservoir. The third absorption (Absorption-3, green curve) was achieved under 1.5 bar of NH_3 while the fourth absorption (Absorption-4, yellow curve) started at 3 bar of NH_3 . The pressure was then immediately increased up to 3.5 over 30 min by increasing the temperature of the ammonia reservoir.

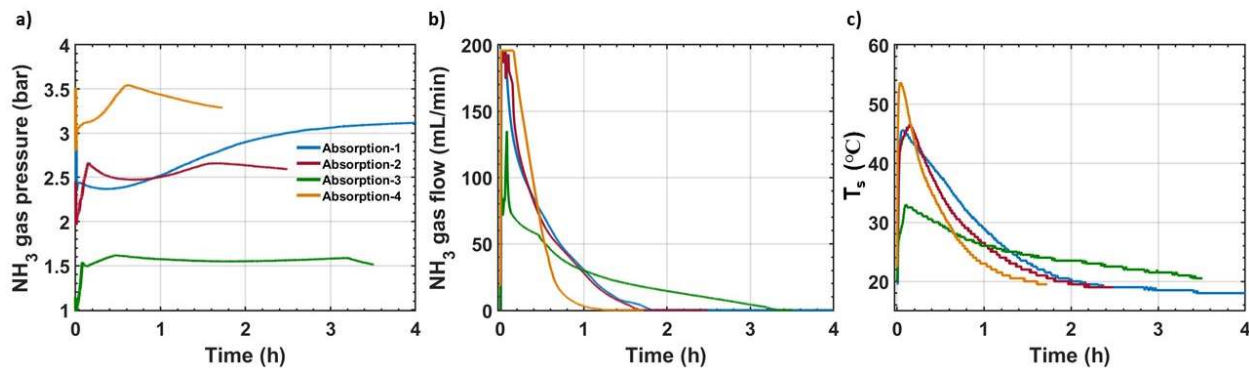


Figure 2. The parameters measured during absorption processes: a) NH₃ gas pressure, b) NH₃ gas flow and c) Sr(NH₃)₈Cl₂-ENG composite temperature, T_s.

The NH₃ gas flow during Absorption-1, -2 and -4 showed similar behavior with the flow increase up to 200 ml min⁻¹ at the very beginning of the experiment and then reduced. The NH₃ flow during Absorption-3 increased to 140 ml min⁻¹ and slowly reduced by the end of the absorption reaction of 3.2 hours. Due to the saturation of the flowmeter at its highest possible readout of 200 ml min⁻¹ during some absorption and desorption cycles (Figure 3b), the amount of ab-/desorbed NH₃ is underestimated, and therefore the total amount of NH₃ was not calculated from flowmeter data.

Heat is released during the Sr(NH₃)₈Cl₂ formation due to the exothermic absorption reaction. The temperature at the top of the honeycomb (T_s) was therefore recorded in order to evaluate the temperature increase during absorption. Figure 2c shows the temperatures measured as Sr(NH)₈Cl₂-ENG is formed during the absorption processes 1 to 4. At Absorption-1 and -2 (2.5 bar of NH₃) the thermocouple registered up to ~45 °C, while at 3 bar and 1.5 bar of NH₃ the temperature reached up to 55 °C and 32.5 °C, respectively.

The four NH₃ desorption processes were carried out under 0.8 bar of NH₃ and temperatures between 100 °C and 200 °C. Figure 3a shows the NH₃ pressure increase at the start of each desorption due to the released NH₃ which was then absorbed in the ammonia reservoir resulting in a subsequent pressure drop. The first (Desorption-1, blue curve) and the last (Desorption-4, yellow curve) desorption were conducted at the same temperature (200 °C). The pressure raised to 1.2 bar in 30 min, remained constant for a short time and then decreased.

During the second desorption (Desorption-2, red curve) at 150 °C, the pressure increases up to 1.1 bar, while for the third desorption (Desorption-3, green curve), conducted at the lowest temperature, 100 °C, the pressure increased only up to 0.95 bar.

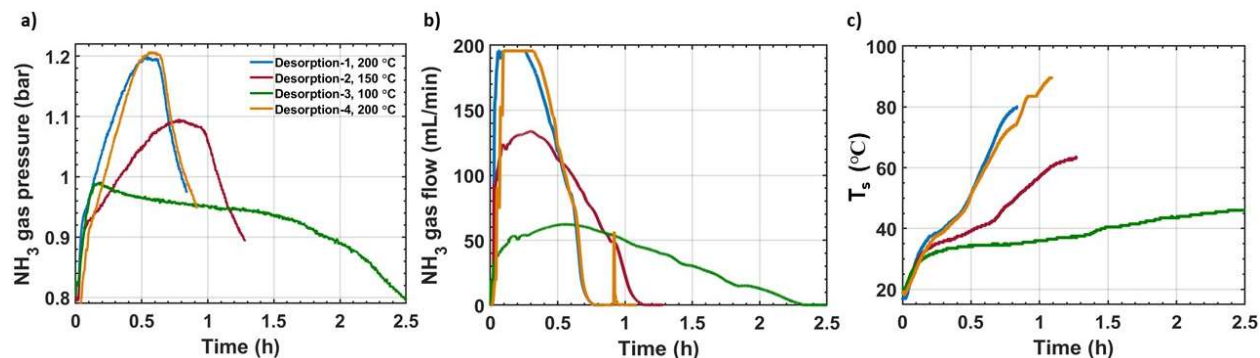


Figure 3. The parameters measured during desorption processes: a) NH_3 gas pressure, b) NH_3 gas flow and c) $\text{Sr}(\text{NH}_3)_8\text{Cl}_2$ -ENG composite temperature, T_s .

The temperature of the sample, T_s , was also measured during the desorption cycles at the top of the honeycomb to evaluate the heat distribution over the honeycomb area (Figure 3c). The highest T_s is 83 °C when the sample was heated at 200 °C (Desorption-1 and -4). The slight increase up to 90 °C in Desorption-4 was due to increasing the set temperature of the heating element to 230 °C at the end of the Desorption-4. At the lower desorption temperatures of 150 °C (Desorption-2) and 100 °C (Desorption-3), T_s reached only 63 °C and 43 °C, respectively. The difference in recorded temperature between the heating element and the thermocouple is mainly due to the distance between the heating element and the thermocouple. In addition, the heat distribution over the honeycomb area might be affected by the endothermic nature of the desorption reactions. It should be also noted that the thermocouple was positioned in between the ~2.5 mm stainless steel walls which might prevent reading the actual temperature of the sample during the sorption processes.

5.2.4.2 Neutron radiography

The four cycles of NH_3 absorption and desorption in the SrCl_2 -ENG composite under different temperatures and NH_3 pressures were investigated by *in-situ* neutron radiography. After the last desorption the sample was heated up to 230 °C under vacuum to remove all possible NH_3 left in the composite material. Due to the attenuation of neutron beam by hydrogen present in ammonia, the NH_3 uptake by SrCl_2 -ENG composite results in formation of dark areas in the radiograms, and

during the desorption the dark areas in the radiogram become brighter as a result of the ammonia release. The NH_3 absorption reaction was homogeneous over the honeycomb area (See Figure S1), but the desorption showed dependence of the heat transfer properties on the stainless-steel honeycomb.

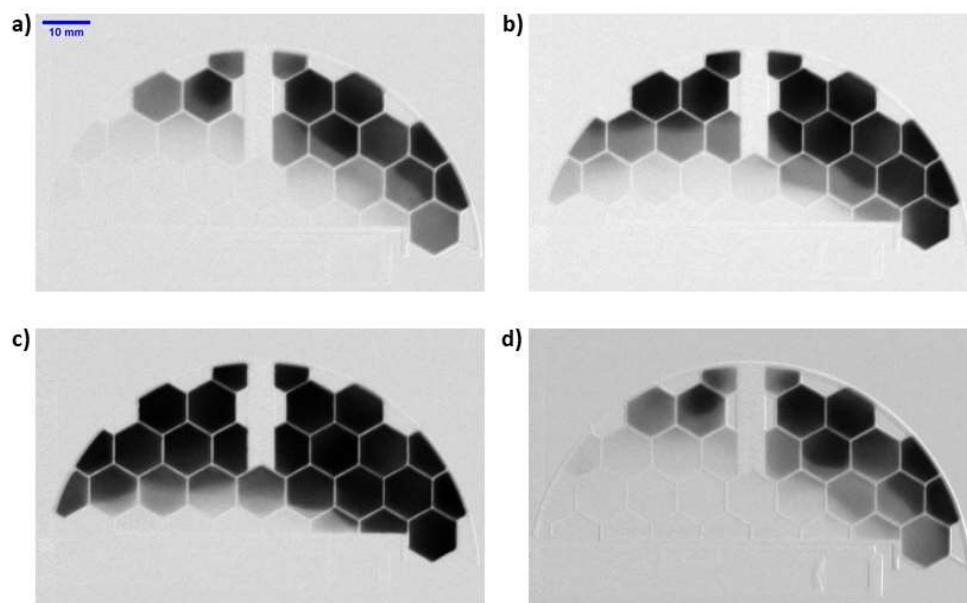


Figure 4. Series of normalized neutron radiography images after 30 min of a) Desorption-1 at 200 °C, b) Desorption-2 at 150 °C c) Desorption-3 at 100 °C and d) Desorption-4 at 200 °C.

Figure 4 shows the normalized radiography images after 30 min of the four desorption performed on $\text{Sr}(\text{NH}_3)_8\text{Cl}_2\text{-ENG}$ at different temperatures. The lower heating temperatures result in slower NH_3 release. The desorption of NH_3 starts from the areas of the honeycomb close to the heating element placed at its bottom, and thus showing the relatively poor heat conductivity of the stainless-steel honeycomb. In all four desorption cases, the NH_3 desorbed from each cell in the honeycomb is a result of the heat transferred through the composite material rather than the heated walls of the honeycomb cells.

For calculating the NH_3 content, several areas of the honeycomb were selected and numbered (see Figure S2). Figure 5a depicts a schematic view of the honeycomb with four cells marked as cell-3, -5, -7 and -12. The NH_3 contents of $\text{Sr}(\text{NH}_3)_8\text{Cl}_2$ formed in these selected cells calculated according to Eq. 3 are plotted as function of time in Figure 5b-i. For Absorption-1 (2.5 bar of NH_3)

the total NH_3 uptake reaches up to 45.7 wt% in cell-5 (Figure 5b) which is very close to the theoretical 46.2 wt% for a complete absorption. The NH_3 content in the cell-3, -7 and -12 reached 44.9 wt%, 45.1 and 43.5 wt%, respectively. Cell-12 shows the lowest NH_3 content throughout the cycling. This might be due to a slight inhomogeneity of the SrCl_2 content in the ENG matrix, which might differ from cell to cell and deviate from the overall value of 76 wt%. Finally, the ammoniated salt $\text{Sr}(\text{NH}_3)_8\text{Cl}_2$ represented 85 wt% of the composite, 15 wt% being the ENG and the gravimetric NH_3 capacity of the $\text{Sr}(\text{NH}_3)_8\text{Cl}_2$ -ENG composite evaluated to be of 38.8 wt%. The results for Desorption-1 at 200 °C (Figure 5c) show how the relative distance of the different cells from the heating element affects the desorption time. $\text{Sr}(\text{NH}_3)_8\text{Cl}_2$ in cell-5 and -12 desorbed NH_3 in 0.3-0.5 hours and for cell-7 and -3 in about 0.7 hours. Only 7 out of the 8 NH_3 moles were released and the monoamine was obtained with the NH_3 content kept as 5.4-5.7 wt%. The NH_3 wt% for monoamine was calculated relative to octamine. The sorption between $\text{Sr}(\text{NH}_3)\text{Cl}_2$ and $\text{Sr}(\text{NH}_3)_8\text{Cl}_2$ occurred in all the following cycles.

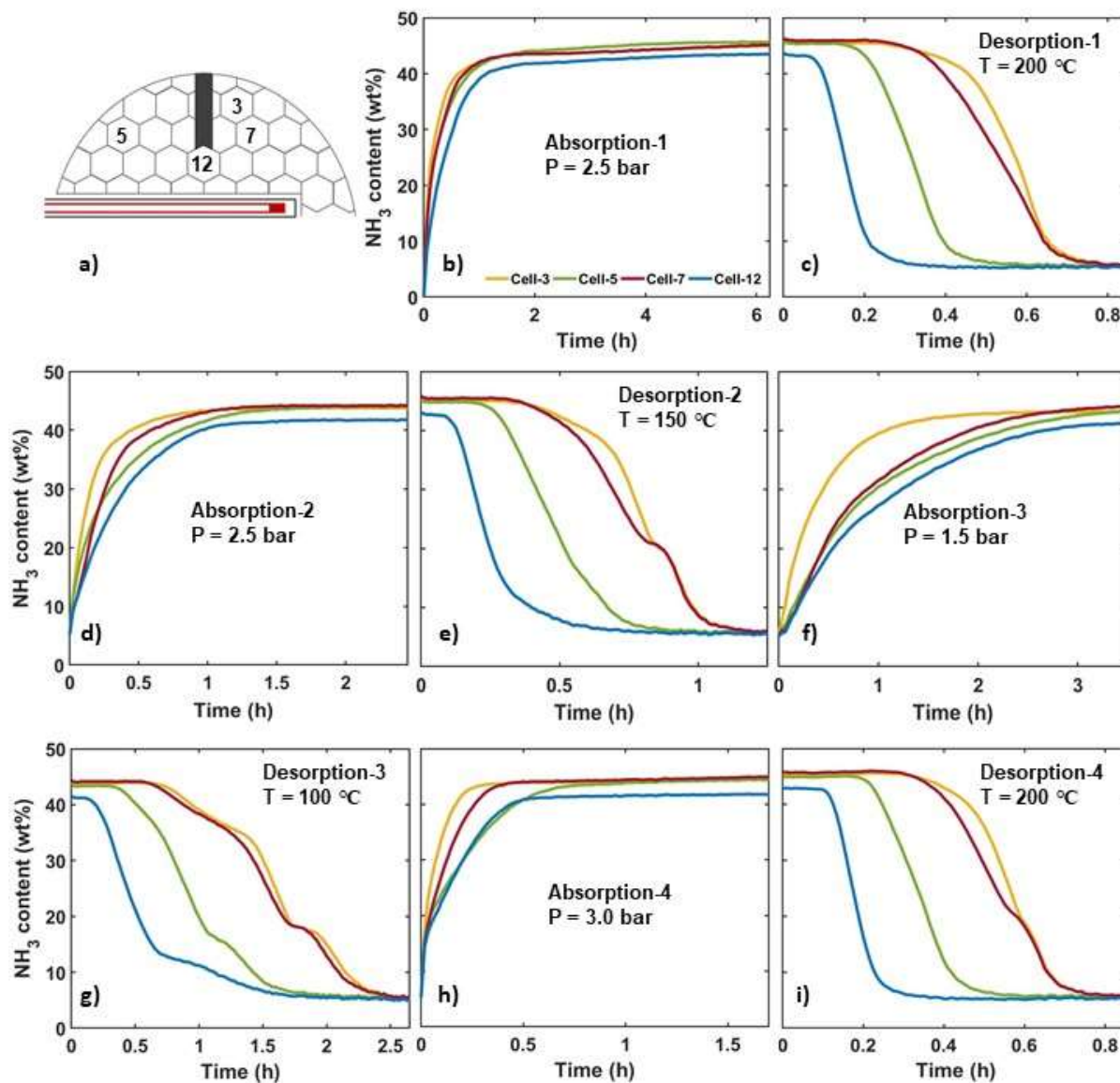


Figure 5. a) Schematic view of the honeycomb with the selected cells: cell 3 – yellow, cell 5 – green, cell 7 – red and cell 12 – blue. The heating element below the honeycomb is marked with red color. b-i) NH₃ content (wt%) in the selected cells during the absorption processes at RT and different pressures P , and during the desorption processes at pressure $P=0.8$ bar and different temperatures T . Absorption-2, -3 and -4 start from 5.4-5.8 wt%.

Therefore, Absorption-2 starts from 5.4-5.7 wt% and then 38.4 wt% of NH₃ was absorbed resulting in 44.6 wt% of ammonia in the salt at 2.5 bar (Figure 5d). After 2 hours, the absorption curves flatten out indicating saturation of the powder particles. The desorption at 150 °C (Desorption-2,

Figure 5e) shows that 7 moles of NH_3 are released within 1.15 hours and the desorption trend in each cell is the same as for the previous desorption. Absorption-3 at 1.5 bar of NH_3 resulted in a slow absorption process taking more than 3 hours due to the low NH_3 pressure (Figure 5f). The obtained NH_3 content reached up to 44.3 wt% in the cells. The following Desorption-3 at 100 °C resulted in the desorption of 7 moles of NH_3 in 2.5 hours (Figure 5g). The last cycle of the NH_3 sorption was performed at 3.0 bar for absorption of NH_3 reaching up to 45.6 wt% (Figure 5h) and desorption at 200 °C (Figure 5i).

The effect of the low heating temperature on the performance of the honeycomb during Desorption-2, -3 and -4 can be seen from plots in Figure 5e, g and i. At 0.8 hours of Desorption-2 ($T = 150$ °C), temporary slowdowns of the desorption for cells-3 and -7 were observed as “bumps” in the curves (Figure 5e). The desorption curves for cell-3, -5 and -7 (Figure 5g) contain two distinct “bumps”, and during Desorption-4 ($T = 200$ °C) the single “bump” in cell-3 and -7 appear at 0.55 hours. This is probably due to the endothermic nature of the desorption reaction and the heat dissipation within the honeycomb. It results in delayed heat transfer to the next cells and therefore slows down the ammonia release in the cells that are away from the heat source. However, the bumps in the desorption curves between 12 wt% and 20 wt% might also be the result of a multi-step desorption of NH_3 . The $\text{Sr}(\text{NH}_3)_8\text{Cl}_2$ octammine releases 7 moles of NH_3 followed by $\text{Sr}(\text{NH}_3)\text{Cl}_2$ monoammine formation at 40-50 °C under 1 bar of NH_3 [13]. However, this reaction has been reported to occur in two steps under selected NH_3 pressures and slow heating rates with the $\text{Sr}(\text{NH}_3)_2\text{Cl}_2$ diammine forming first and followed by the $\text{Sr}(\text{NH}_3)\text{Cl}_2$ monoammine [14]. The bumps observed at ~12 wt% might therefore correspond to the formation of the diamine. A similar NH_3 uptake and release behavior was observed for the other honeycomb cells not plotted here. These data are included in the Supplementary material (See Figure S3-S4). The slight mismatches of the NH_3 wt% values at the end of absorption and beginning of desorption curves are likely due to at least 30 minutes waiting time for cooling down the ammonia reservoir or the THS reactor in order to proceed with the next cycling step. During that cooling time no neutron radiography measurements were performed, and some NH_3 was likely reabsorbed or further desorbed before the start of the next sorption process.

Assuming the $\text{Sr}(\text{NH}_3)_8\text{Cl}_2$ octammine formation from SrCl_2 during Absorption-1 and only 7 moles of NH_3 were ab/desorbed during the following ab-/desorption reactions, following the

reaction $\text{Sr}(\text{NH}_3)_8\text{Cl}_2 \leftrightarrow \text{Sr}(\text{NH}_3)\text{Cl}_2 + 7\text{NH}_3$. During the desorption processes at temperature above or equal to 150 °C and against 0.8 bar of NH_3 (Figure 5 c, e and i) the full NH_3 desorption did not occur which is likely due to the poor heat conductivity of the stainless-steel honeycomb and loss of heat to the ambient via the THS reactor walls. Even with a heating temperature of 200 °C, the maximum temperature recorded at the honeycomb thermocouple (T_s) was 83 °C.

This was confirmed during our final neutron radiography experiment performed after Desorption-4 where the temperature was kept at 230 °C under dynamic vacuum for 15 min. The last NH_3 molecule was released from the sample (See Figure S5) and the radiography showed light gray image of intensity comparable to the one of the pristine samples. This suggests that the remaining NH_3 in the composite material might be the last mole of NH_3 .

5.2.4.3 Neutron Tomography

Three-dimensional images of the investigated sample were reconstructed from the neutron radiograms obtained during its rotation over 360° around its axis (See Figure S6). The information about the inner structure of the THS reactor prototype is acquired from the orthogonal planes of the 3D images, showing the arrangement of the hexagonal pellets of SrCl_2 -ENG composite within the cells of the honeycomb. Figure 6a shows the orthogonal view of the sample in the XY and XZ-planes before NH_3 cycling. A space between the pellets and the honeycomb walls can be seen in both planes, and thus allowing the pellets to expand and occupy the whole volume of the cells during the NH_3 absorption.

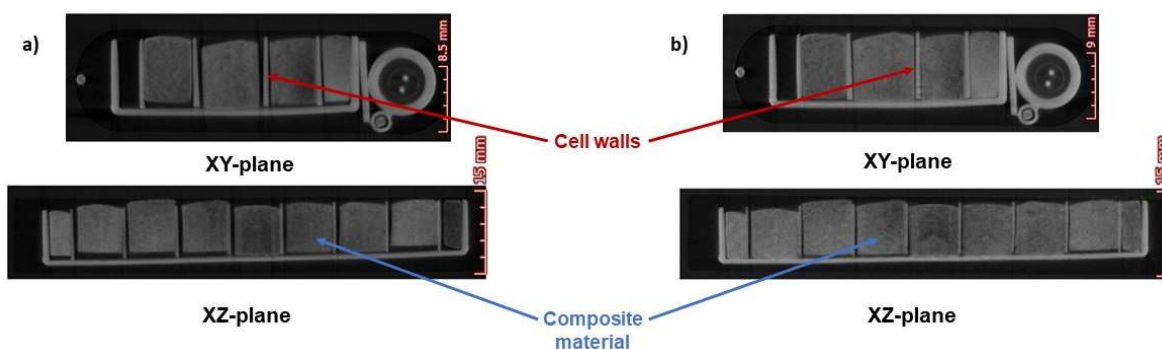


Figure 6. The XY (top row) and XZ-plane (bottom row) views of the a) initial SrCl_2 -ENG composite and b) $\text{Sr}(\text{NH}_3)\text{Cl}_2$ -ENG after cycling.

The ENG matrix in the composite acts as a buffer during NH_3 cycling limiting the expansion and contraction of SrCl_2 -ENG during NH_3 uptake and release, respectively. Figure 6b presents the XY and XZ-planes of the $\text{Sr}(\text{NH}_3)\text{Cl}_2$ -ENG after partial NH_3 desorption. Due to the NH_3 present in the salt, the pellets still occupy a large fraction of the available volume. It can also be noticed that the expansion of the composite in the axial directions (perpendicular to the honeycomb) is not limited by the walls of the honeycomb cells. This feature of the ENG is beneficial for the heat transfer between the active material and the honeycomb, and thus allowing to increase the efficiency of the THS reactor and the system.

5.2.4.4 Comparison with the previous work

In the previous neutron imaging study of the $\text{SrCl}_2/\text{Sr}(\text{NH}_3)_8\text{Cl}_2$ system within the same THS reactor prototype only qualitative analysis of the neutron radiography data was performed [33]. Some of the SrCl_2 powder had fallen out of the honeycomb during the sample mounting and volume expansion resulting in continuous changes of the SrCl_2 powder bed thickness, which could not be determined accurately and prevented any quantitative analysis [33]. A known thickness of the investigated area is needed for quantitative analysis of neutron radiography images (see Eq. 1). This was achieved in the present work by the confinement of SrCl_2 in the porous ENG matrix ensuring the stability of the SrCl_2 -ENG composite against external forces while allowing free expansion of the powder within the porous media. The composite material provided fast absorption and desorption processes compared to the previous study proving the improvement for the reaction kinetics when the salt is confined in porous ENG matrix. The desorption of 7 moles of NH_3 from $\text{Sr}(\text{NH}_3)_8\text{Cl}_2$ was complete within 4 hours at 100 °C, while desorption was completed within 2.5 hours in $\text{Sr}(\text{NH}_3)_8\text{Cl}_2$ -ENG composite.

Additionally, investigation of the heat transfer efficiency of the honeycomb and the spatio-temporal NH_3 concentration in the composite material during cycling in this study provides a valuable information about the efficient performance of the THS reactor. The presented neutron radiography results in this work will be compared with the numerical simulations from COMSOL Multiphysics modelling software. This modelling includes the NH_3 flow and heat transfer function of the honeycomb heat reactor which will provide high accuracy and close equivalence to the sorption reaction observed with neutron radiography.

Neutron tomography of the THS reactor prototype with $\text{SrCl}_2/\text{Sr}(\text{NH}_3)_8\text{Cl}_2$ system revealed the distortion of the honeycomb after NH_3 cycling, where the honeycomb back plate was bended due to the volume expansion of the sample [33]. In this work we note that the mechanical stresses on the honeycomb were minimized by confining the SrCl_2 in ENG matrix. Therefore, the mechanical stability of the stainless-steel honeycomb together with the limited expansion/contraction of the SrCl_2 -ENG composite make the investigated THS reactor a safe system for the future applications.

5.2.5 Conclusion

It is demonstrated that neutron imaging is a useful technique for determination of spatio-temporal NH_3 content in $\text{Sr}(\text{NH}_3)_8\text{Cl}_2$ -ENG composite pellets produced for thermochemical heat storage applications. ENG mixed with SrCl_2 showed excellent kinetics during the NH_3 absorption and desorption. The results from neutron radiography and tomography confirmed the mechanical stability of the SrCl_2 -ENG composite upon cycling. The stainless-steel honeycomb in which the pellets were embedded, showed a poor heat transfer efficiency during the desorption processes resulting in an inhomogeneous NH_3 desorption process. The heat release during exothermic $\text{Sr}(\text{NH}_3)_8\text{Cl}_2$ -ENG formation with the temperatures of up to $T = 55\text{ }^\circ\text{C}$ has been detected. The exothermic and endothermic NH_3 cycling monitored during *in-situ* neutron radiography revealed a high potential of the SrCl_2 -ENG composite materials for the low temperature thermochemical heat storage applications.

5.2.6 Acknowledgements

This work is financially supported by NordForsk Nordic Neutron Science Programme via the Neutrons for Heat Storage (NHS) project (No. 82206). The authors thank the ILL for the allocation of neutron radiation beam time via the experiments UGA-83 (10.5291/ILL-DATA.UGA-83) and DIR-196 (DOI: 10.5291/ILL-DATA.DIR-196) and particularly Lukas Helfen and Alessandro Tengattini for experimental assistance. Additionally, the Danish Research Council is gratefully acknowledged for the financial support via Danscatt.

5.2.7 Appendix A. Supplementary data

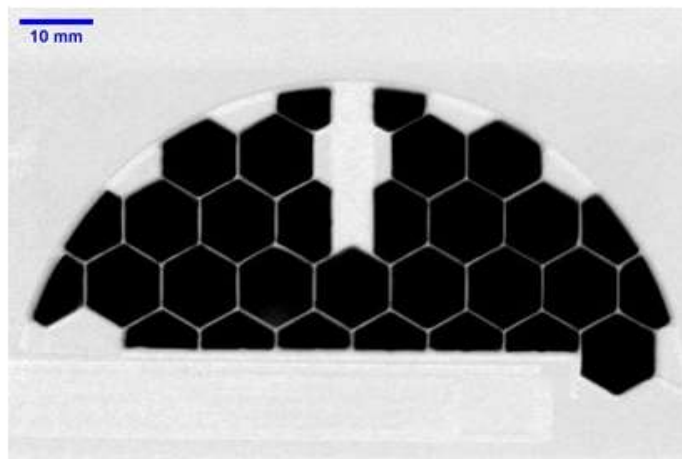


Figure S1. Neutron radiography image of the $\text{Sr}(\text{NH}_3)_8\text{Cl}_2\text{-ENG}$ after 6 hours of NH_3 absorption.

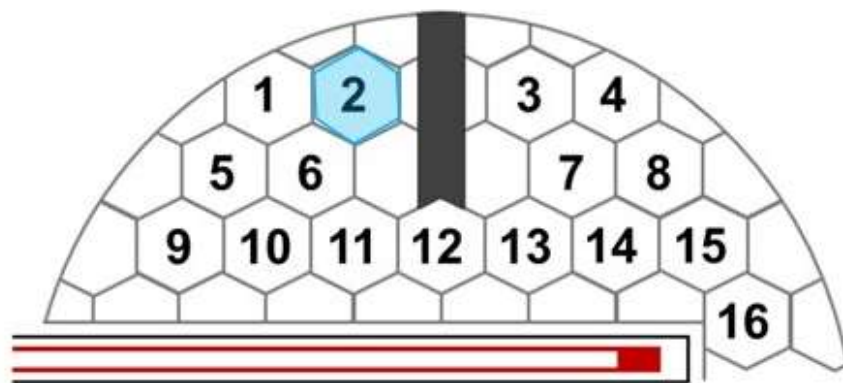


Figure S2. Schematic view of the honeycomb with numbered cells. The blue marked hexagon represents the area selected where NH_3 wt% is calculated. The heating element below the honeycomb is marked with red color.

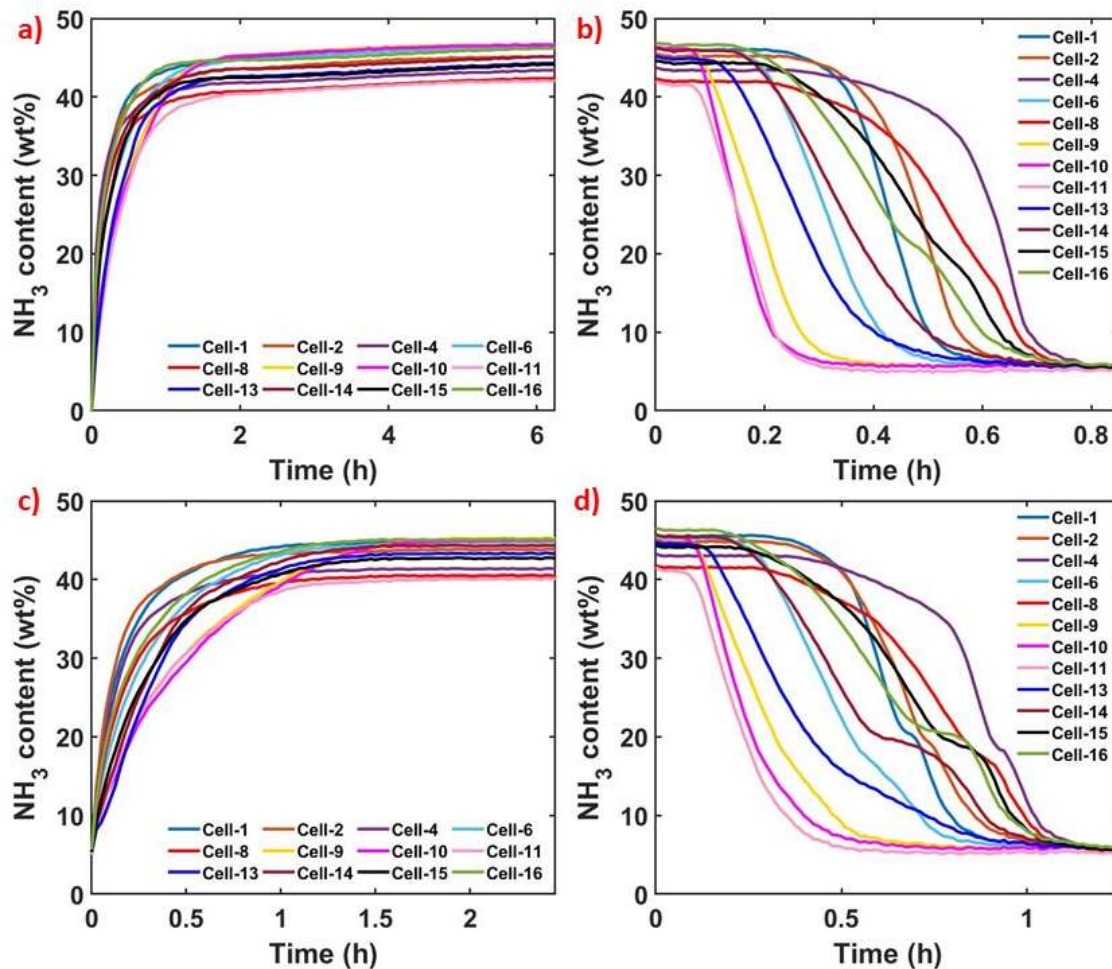


Figure S3. The NH_3 content (wt%) in selected cells during a) absorption-1 at $P = 2.5$ bar, b) desorption-1 at 200°C , c) absorption-2 at $P = 2.5$ bar and b) desorption-2 at 150°C . The absorption processes were conducted at RT and the desorption processes – at pressures $P=0.8$ bar of NH_3 .

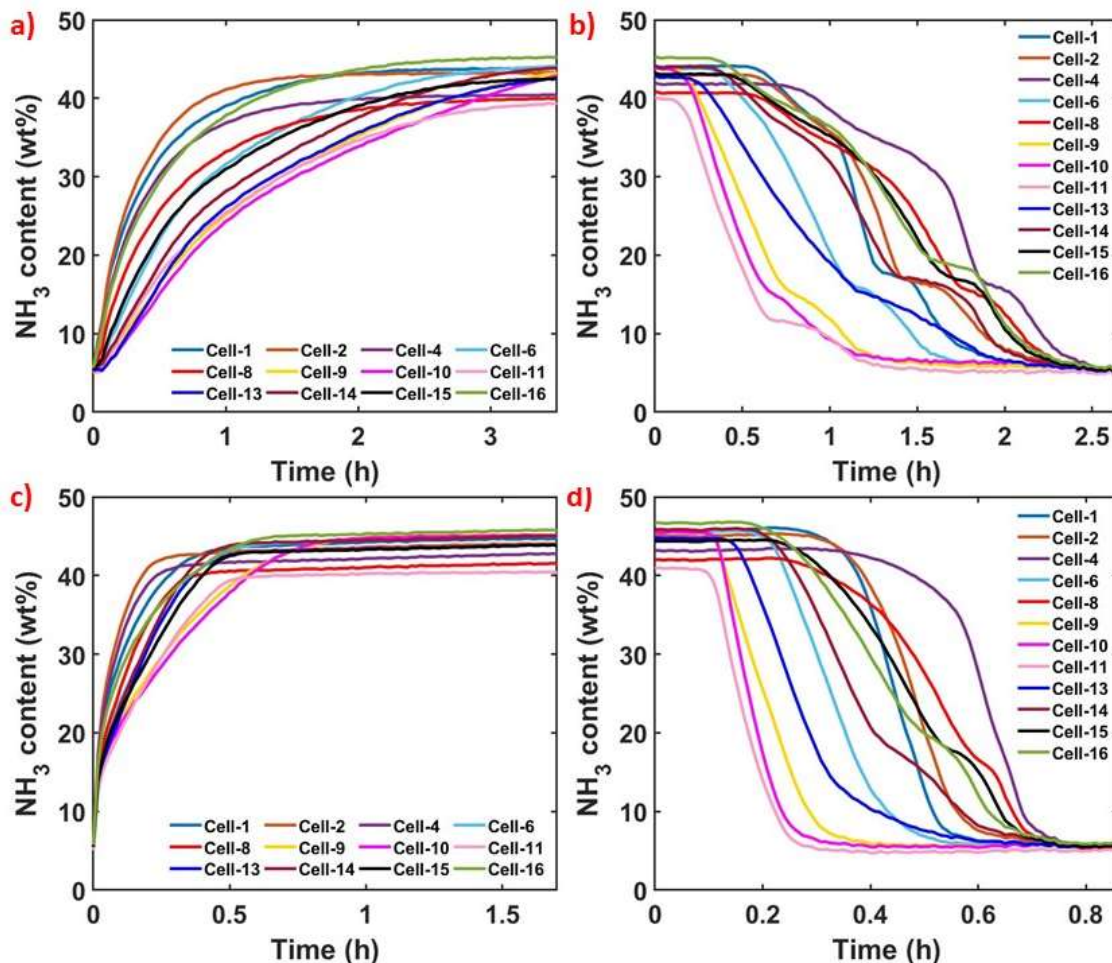


Figure S4. The NH_3 content (wt%) in selected cells during a) absorption-3 at $P = 1.5$ bar, b) desorption-3 at 100°C , c) absorption-4 at $P = 3.0$ bar and b) desorption-4 at 200°C . The absorption processes were conducted at RT and the desorption processes – at pressures $P=0.8$ bar of NH_3 .

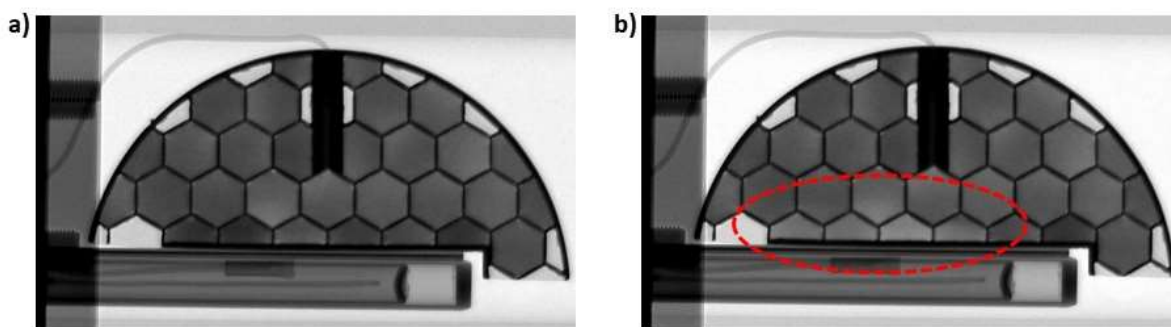


Figure S5. Neutron radiograph of the sample a) after desorption at 200°C and 1 bar of NH_3 and b) after desorption at 230°C under vacuum for 15 min. The red dotted circle shows the bright area from where the last mole of NH_3 is desorbed from $\text{Sr}(\text{NH}_3)\text{Cl}_2\text{-ENG}$ composite.

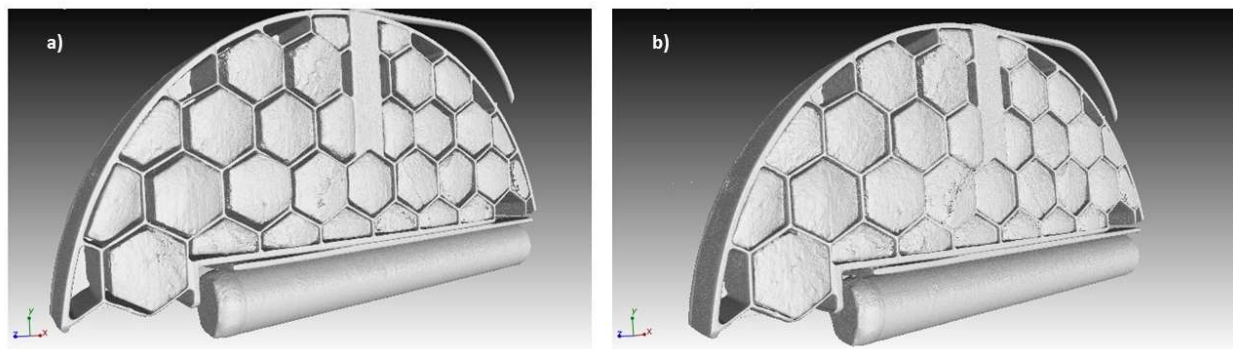


Figure S5. 3D image of a) $\text{SrCl}_2\text{-ENG}$ composite before NH_3 cycling and b) $\text{Sr}(\text{NH}_3)\text{Cl}_2\text{-ENG}$ after NH_3 cycling.

5.2.8 References

- [1] R. Parameshwaran, S. Kalaiselvam, S. Harikrishnan, A. Elayaperumal, Sustainable thermal energy storage technologies for buildings: A review, *Renewable and Sustainable Energy Reviews*. 16 (2012) 2394–2433. <https://doi.org/10.1016/j.rser.2012.01.058>.
- [2] A. Sharma, V.V. Tyagi, C.R. Chen, D. Buddhi, Review on thermal energy storage with phase change materials and applications, *Renewable and Sustainable Energy Reviews*. 13 (2009) 318–345. <https://doi.org/10.1016/j.rser.2007.10.005>.
- [3] T. D. Humphries, K. T. Møller, W.D. A. Rickard, M. Veronica Sofianos, S. Liu, C. E. Buckley, M. Paskevicius, Dolomite: a low cost thermochemical energy storage material, *Journal of Materials Chemistry A*. 7 (2019) 1206–1215. <https://doi.org/10.1039/C8TA07254J>.
- [4] K.T. Møller, D. Sheppard, D.B. Ravnsbæk, C.E. Buckley, E. Akiba, H.-W. Li, T.R. Jensen, Complex Metal Hydrides for Hydrogen, Thermal and Electrochemical Energy Storage, *Energies*. 10 (2017) 1645. <https://doi.org/10.3390/en10101645>.
- [5] D.N. Harries, M. Paskevicius, D.A. Sheppard, T.E.C. Price, C.E. Buckley, Concentrating Solar Thermal Heat Storage Using Metal Hydrides, *Proceedings of the IEEE*. 100 (2012) 539–549. <https://doi.org/10.1109/JPROC.2011.2158509>.
- [6] P. Pardo, A. Deydier, Z. Anxionnaz-Minvielle, S. Rougé, M. Cabassud, P. Cognet, A review on high temperature thermochemical heat energy storage, *Renewable and Sustainable Energy Reviews*. 32 (2014) 591–610. <https://doi.org/10.1016/j.rser.2013.12.014>.

- [7] T. Yan, Z.H. Kuai, S.F. Wu, Experimental investigation on a $\text{MnCl}_2\text{--SrCl}_2/\text{NH}_3$ thermochemical resorption heat storage system - ScienceDirect, 147 (2020) 874–883. <https://doi.org/10.1016/j.renene.2019.09.033>.
- [8] R.Z. Sørensen, J.S. Hummelshøj, A. Klerke, J.B. Reves, T. Vegge, J.K. Nørskov, C.H. Christensen, Indirect, Reversible High-Density Hydrogen Storage in Compact Metal Ammine Salts, *J. Am. Chem. Soc.* 130 (2008) 8660–8668. <https://doi.org/10.1021/ja076762c>.
- [9] A. Bialy, P.B. Jensen, D. Blanchard, T. Vegge, U.J. Quaade, Solid solution barium–strontium chlorides with tunable ammonia desorption properties and superior storage capacity, *Journal of Solid State Chemistry*. 221 (2015) 32–36. <https://doi.org/10.1016/j.jssc.2014.09.014>.
- [10] A. Tekin, J. S. Hummelshøj, H. S. Jacobsen, D. Sveinbjörnsson, D. Blanchard, J. K. Nørskov, T. Vegge, Ammonia dynamics in magnesium ammine from DFT and neutron scattering, *Energy & Environmental Science*. 3 (2010) 448–456. <https://doi.org/10.1039/B921442A>.
- [11] T. Vegge, R.Z. Sørensen, A. Klerke, J.S. Hummelshøj, T. Johannessen, J.K. Nørskov, C.H. Christensen, 19 - Indirect hydrogen storage in metal amines, in: G. Walker (Ed.), *Solid-State Hydrogen Storage*, Woodhead Publishing, 2008: pp. 533–564. <https://doi.org/10.1533/9781845694944.4.533>.
- [12] P. Berdiyeva, A. Karabanova, J.B. Grinderslev, R.E. Johnsen, D. Blanchard, B.C. Hauback, S. Deledda, Synthesis, Structure and NH_3 Sorption Properties of Mixed $\text{Mg}_{1-x}\text{Mn}_x(\text{NH}_3)_6\text{Cl}_2$ Amines, *Energies*. 13 (2020) 2746. <https://doi.org/10.3390/en13112746>.
- [13] R.E. Johnsen, P.B. Jensen, P. Norby, T. Vegge, Temperature- and Pressure-Induced Changes in the Crystal Structure of $\text{Sr}(\text{NH}_3)_8\text{Cl}_2$, *J. Phys. Chem. C*. 118 (2014) 24349–24356. <https://doi.org/10.1021/jp508076c>.
- [14] S. Lysgaard, A.L. Ammitzbøll, R.E. Johnsen, P. Norby, U.J. Quaade, T. Vegge, Resolving the stability and structure of strontium chloride amines from equilibrium pressures, XRD and DFT, *International Journal of Hydrogen Energy*. 37 (2012) 18927–18936. <https://doi.org/10.1016/j.ijhydene.2012.09.129>.
- [15] P. Bjerre Jensen, S. Lysgaard, U. J. Quaade, T. Vegge, Designing mixed metal halide amines for ammonia storage using density functional theory and genetic algorithms, *Physical Chemistry Chemical Physics*. 16 (2014) 19732–19740. <https://doi.org/10.1039/C4CP03133D>.

- [16] M. Kubota, K. Matsuo, R. Yamanouchi, H. Matsuda, Absorption and Desorption Characteristics of NH_3 with Metal Chlorides for Ammonia Storage, *Journal of Chemical Engineering of Japan*. adpub (2014). <https://doi.org/10.1252/jcej.13we294>.
- [17] H.S. Jacobsen, H.A. Hansen, J.W. Andreasen, Q. Shi, A. Andreasen, R. Feidenhans'l, M.M. Nielsen, K. Ståhl, T. Vegge, Nanoscale structural characterization of $\text{Mg}(\text{NH}_3)_6\text{Cl}_2$ during NH_3 desorption: An in situ small angle X-ray scattering study, *Chemical Physics Letters*. 441 (2007) 255–260. <https://doi.org/10.1016/j.cplett.2007.05.001>.
- [18] L. Jiang, L.W. Wang, Z.Q. Jin, R.Z. Wang, Y.J. Dai, Effective thermal conductivity and permeability of compact compound ammoniated salts in the adsorption/desorption process, *International Journal of Thermal Sciences*. 71 (2013) 103–110. <https://doi.org/10.1016/j.ijthermalsci.2013.03.017>.
- [19] B. Tian, Z.Q. Jin, L.W. Wang, R.Z. Wang, Permeability and thermal conductivity of compact chemical and physical adsorbents with expanded natural graphite as host matrix, *International Journal of Heat and Mass Transfer*. 55 (2012) 4453–4459. <https://doi.org/10.1016/j.ijheatmasstransfer.2012.04.016>.
- [20] L.W. Wang, Z. Tamainot-Telto, S.J. Metcalf, R.E. Critoph, R.Z. Wang, Anisotropic thermal conductivity and permeability of compacted expanded natural graphite, *Applied Thermal Engineering*. 30 (2010) 1805–1811. <https://doi.org/10.1016/j.applthermaleng.2010.04.014>.
- [21] J.H. Han, K.-H. Lee, Gas permeability of expanded graphite–metallic salt composite, *Applied Thermal Engineering*. 21 (2001) 453–463. [https://doi.org/10.1016/S1359-4311\(00\)00056-9](https://doi.org/10.1016/S1359-4311(00)00056-9).
- [22] M. van der Pal, R.E. Critoph, Performance of CaCl_2 -reactor for application in ammonia-salt based thermal transformers, *Applied Thermal Engineering*. 126 (2017) 518–524. <https://doi.org/10.1016/j.applthermaleng.2017.07.086>.
- [23] S. Wu, T.X. Li, R.Z. Wang, Experimental identification and thermodynamic analysis of ammonia sorption equilibrium characteristics on halide salts, *Energy*. 161 (2018) 955–962. <https://doi.org/10.1016/j.energy.2018.07.129>.
- [24] M. Strobl, I. Manke, N. Kardjilov, A. Hilger, M. Dawson, J. Banhart, Advances in neutron radiography and tomography, *J. Phys. D: Appl. Phys.* 42 (2009) 243001. <https://doi.org/10.1088/0022-3727/42/24/243001>.

-
- [25] N. Kardjilov, I. Manke, A. Hilger, M. Strobl, J. Banhart, Neutron imaging in materials science, *Materials Today*. 14 (2011) 248–256. [https://doi.org/10.1016/S1369-7021\(11\)70139-0](https://doi.org/10.1016/S1369-7021(11)70139-0).
- [26] N. Kardjilov, I. Manke, R. Woracek, A. Hilger, J. Banhart, Advances in neutron imaging, *Materials Today*. 21 (2018) 652–672. <https://doi.org/10.1016/j.mattod.2018.03.001>.
- [27] Ł. Gondek, N.B. Selvaraj, J. Czub, H. Figiel, D. Chapelle, N. Kardjilov, A. Hilger, I. Manke, Imaging of an operating $\text{LaNi}_{4.8}\text{Al}_{0.2}$ -based hydrogen storage container, *International Journal of Hydrogen Energy*. 36 (2011) 9751–9757. <https://doi.org/10.1016/j.ijhydene.2011.05.089>.
- [28] F. Heubner, A. Hilger, N. Kardjilov, I. Manke, B. Kieback, Ł. Gondek, J. Banhart, L. Röntzsch, In-operando stress measurement and neutron imaging of metal hydride composites for solid-state hydrogen storage, *Journal of Power Sources*. 397 (2018) 262–270. <https://doi.org/10.1016/j.jpowsour.2018.06.093>.
- [29] P. Boillat, E.H. Lehmann, P. Trtik, M. Cochet, Neutron imaging of fuel cells – Recent trends and future prospects, *Current Opinion in Electrochemistry*. 5 (2017) 3–10. <https://doi.org/10.1016/j.coelec.2017.07.012>.
- [30] A. Senyshyn, M.J. Mühlbauer, K. Nikolowski, T. Pirling, H. Ehrenberg, “In-operando” neutron scattering studies on Li-ion batteries, *Journal of Power Sources*. 203 (2012) 126–129. <https://doi.org/10.1016/j.jpowsour.2011.12.007>.
- [31] W.J. Weydanz, H. Reisenweber, A. Gottschalk, M. Schulz, T. Knoche, G. Reinhart, M. Masuch, J. Franke, R. Gilles, Visualization of electrolyte filling process and influence of vacuum during filling for hard case prismatic lithium ion cells by neutron imaging to optimize the production process, *Journal of Power Sources*. 380 (2018) 126–134. <https://doi.org/10.1016/j.jpowsour.2018.01.081>.
- [32] C. Tötze, I. Manke, A. Hilger, G. Choinka, N. Kardjilov, T. Arlt, H. Markötter, A. Schröder, K. Wippermann, D. Stolten, C. Hartnig, P. Krüger, R. Kuhn, J. Banhart, Large area high resolution neutron imaging detector for fuel cell research, *Journal of Power Sources*. 196 (2011) 4631–4637. <https://doi.org/10.1016/j.jpowsour.2011.01.049>.
- [33] P. Berdiyeva, A. Karabanova, M.G. Makowska, R.E. Johnsen, D. Blanchard, B.C. Hauback, S. Deledda, In-situ neutron imaging study of NH_3 absorption and desorption in SrCl_2
-

within a heat storage prototype reactor, *Journal of Energy Storage*. 29 (2020) 101388.

<https://doi.org/10.1016/j.est.2020.101388>.

[34] Y. Wang, C.H.F. Peden, S. Choi, Catalyst of a metal heteropoly acid salt that is insoluble in a polar solvent on a non-metallic porous support and method of making, US6815392B2, 2004. <https://patents.google.com/patent/US6815392B2/en> (accessed April 26, 2020).

[35] C. Tötzke, N. Kardjilov, N. Lenoir, N. Lenoir, I. Manke, S.E. Oswald, A. Tengattini, A. Tengattini, What comes NeXT? – High-Speed Neutron Tomography at ILL, *Opt. Express*, OE. 27 (2019) 28640–28648. <https://doi.org/10.1364/OE.27.028640>.

[36] C.A. Schneider, W.S. Rasband, K.W. Eliceiri, NIH Image to ImageJ: 25 years of image analysis, *Nature Methods*. 9 (2012) 671–675. <https://doi.org/10.1038/nmeth.2089>.

[37] Radioscopy & Tomography systems | RX Solutions, Rx-Solutions. (n.d.). <https://www.rxsolutions.fr/x-act> (accessed May 11, 2020).

[38] VGSTUDIO MAX: High-End Software for CT Data, Volumegraphics.Com. (n.d.). <https://www.volumegraphics.com/en/products/vgstudio-max.html> (accessed May 11, 2020).

6 Conclusion and Outlook

The presented thesis was performed within the frame of the Scandinavian project “Neutrons for Heat Storage” with the main objective to model and build a cost-effective and compact thermochemical heat storage system, of 2-3 kWh capacity, for the recovery of low-grade waste heat. The presented research focused on the development and validation of a numerical model of a thermochemical reactor utilizing a reversible reaction between solid SrCl_2 and gaseous NH_3 . In addition, the most sensitive parameters of the thermochemical reactor were to be determined.

In the first chapter of the thesis, the kinetic parameters of the sorption reactions between SrCl_2 solid and NH_3 gas were obtained using a Sieverts type apparatus at constant pressures and temperatures. In the attempt to measure the intrinsic reaction rates, i.e. rates not biased by the heat and mass transfer phenomena, the kinetic experiments were performed on a composite material made of the sorbent, SrCl_2 , inserted into the pores of the heat-conductive matrix of expanded natural graphite (ENG). Furthermore, we used the optimal mass of the composite material, to ensure that the effect of the heat and mass transfer on the chemical reaction rates is maximally eliminated, while conserving good accuracy in the measurements. In contrast to the presented work, kinetic parameters for SrCl_2 - NH_3 systems found in literature were characterized on bulky samples, where the impact of the mass-dependent phenomena, namely heat and mass transfer, is unavoidable. This is the main difference between the present kinetic study and the others reported in literature. The obtained kinetic equations were found to predict the experimental data, used for the determination of the kinetic parameters, over a wide pressure-temperature range. Moreover, they were successfully validated against other experimental datasets, unlike the literature rate equations, which were shown to deviate largely. This underlines the significance of using intrinsic kinetic parameters for the accurate modelling of thermochemical reactions.

In the second chapter, the obtained kinetics parameters were used for developing a numerical three-dimensional (3D) model of the absorption and desorption of NH_3 by SrCl_2 amines. Besides the chemical reaction rates, the absorption and desorption models also included heat and mass transfer physics, characterized by material properties taken from literature. The results from the models were successfully validated against the experimental data obtained from neutron radiography. In

this work, neutron radiography was used for the purpose of model validation for the first time on such system. Unlike conventional methods of model validation that provide limited information on the reaction front, neutron radiography allows following the amount of hydrogen and hence ammonia at each point of the sample at relatively small time step (less than 30 s, in our case). This feature makes this technique unique for studying systems utilizing hydrogen-bearing sorbates, e.g. NH_3 , H_2 , H_2O , CH_3OH etc. After the models were validated against neutron radiography, the absorption model was successfully crosschecked using the temperature and flowmeter readings.

Finally, the models were used for the identification of the most critical parameters for the reactor efficiency and performance. Among the studied parameters there were specific heat capacities and thermal conductivities of the reactive bed and the heat exchanger as well as the heat transfer coefficient between the reactive bed and the heat exchanger. The results of the study indicated that the parameters having the highest impact on the desorption and the absorption rates are thermal conductivities of the reactive bed and the heat exchanger and the heat transfer coefficient, respectively. To validate and supplement the results of the sensitivity analysis, we carried out sorption experiments combined with neutron radiography studies on materials with inferior and superior thermal conductivities (stainless steel and pure SrCl_2 vs. aluminum and SrCl_2 -ENG composite material). The experiments were found to confirm the results from the sensitivity analysis, but some additional information was revealed. For example, it was shown that the heat transfer coefficient plays an important role in the desorption rate, specifically in case of high thermal conductivities, and should not be neglected when designing the reactor. From the absorption experiments, the absorption was found to be mainly driven by fluid dynamics with the permeability as the most influencing parameter.

Even though the main objectives of the PhD project were achieved, several issues remain to study and to deepen developing a simulation tool for predicting the behavior of thermochemical processes.

For example, the intrinsic kinetic trends of the working pair SrCl_2 - NH_3 obtained on a Sievert's type apparatus using isothermal programs should be crosschecked using other instruments, e.g. thermogravimetric analysis and differential scanning calorimetry machines, as well as other programs, e.g. isothermal heating. To the best of our knowledge, this comparison has never been

done before; however, it would be relevant, as it would reveal the effect of used instrument and program on the values of kinetics parameters and would help researchers build a common ground in regard to the identification of intrinsic kinetic parameters.

Regarding the study on the validation of the model, first, one has to develop a more detailed and accurate procedure for the treatment of radiography data. Especially for the treatment of the scattering component. Even though the quantitate neutron radiography data is in a good agreement with the results from the flowmeter readings (see Chapter V, Paper V), more theoretical background is to be included.

Then, there are some improvements of the reactor prototype that should be implemented. For example, additional thermocouples should be installed in the reactor prototype. Minimum two temperature sensors should measure the temperature of the reactive bed at different points, to provide sufficient information on the evolution of the heat front within the sorbent. Then, two other temperature sensors should be welded on the surface of the heating element at different points, giving an opportunity to check that the temperature of the heating element is equal to the set temperature (in our case, 100°C) and uniform along the full length. Another way of confirming the uniformity of the heating element temperature under an uneven load will be to use an infra-red camera during the sorption experiments. In addition, one has to experimentally determine the value of the heat transfer coefficient between the aluminum cell and the ambient environment, accounting for losses to the ambient environment. The way of doing this in case of the desorption experiments would be to measure the electricity use of the heating element and then to subtract the heat required for heating up the cell and for the desorption. For the absorption experiments, one could calculate it using Grashof and Reynolds numbers and the temperature of the aluminum cell wall. This experimental data would be extremely useful, when building a model for its validation.

Regarding the improvement of the reactor prototype, future efforts should be directed towards the optimization of the heat transfer coefficient between the reactive bed and the heat exchanger, consequently maximizing the absorption and desorption rates. In this regard, appropriate technologies should be identified to increase the heat transfer coefficient. Some of the methods are listed below:

1. Thermal treatment, where the honeycomb and reactive bed are cooled before placing them together so when they are at the room temperature any gaps are compressed;
2. Mechanical pressure treatment where the composite material is compressed after placement;
3. Use of adhesives or filler to reduce the gaps: for example, a thermal glue to bond the two surfaces;
4. Surface preparation: roughing or smoothing the surface to improve the contact;
5. Growing composite materials on the surface, e.g. carbon fibers.

Moreover, the developed numerical model should be used not only for the determination of the critical model parameters, but also for the identification of the optimal reactor design. We are looking forward to confronting the model against experimental data obtained from the two reactor prototypes that has been build and currently are under commissioning at Technical University of Denmark and Royal Institute of Technology (Stockholm, Sweden). Furthermore, to confirm that the established model is valid for not only SrCl₂-NH₃ working pair but also for other materials, sorption experiments involving other sorbents and sorbates should be performed.

7 Supplementary Information

7.1 Paper VII: Small Angle Neutron Scattering Characterization of Composite SrCl₂-ENG for Thermochemical Heat Storage

Anastasiia Karabanova¹, Kenneth Dahl Knudsen², Perizat Berdiyeva², Michel van der Pal³,
Stefano Deledda², Rune E. Johnsen¹, Didier Blanchard¹

¹*Department of Energy Conversion and Storage, Technical University of Denmark, 2800 Kgs. Lyngby, Denmark;*

²*Department for Neutron Materials Characterization, Institute for Energy Technology, 2027 Kjeller, Norway;*

³*TNO Energy Transition, 1755 LE Petten, The Netherlands.*

7.1.1 Abstract

This work presents an in-situ nanoscale structural characterization of the composite material SrCl₂-Expanded Natural Graphite during ammonia absorption and desorption, using small angle neutron scattering (SANS) together with X-ray powder diffraction and sorption measurements. For the processing of the composite material SANS patterns, we developed and implemented two methods, which showed comparable results. The study allowed following the evolution of the SrCl₂ particles and the nanopores inside the particles during five sorption cycles. The structural changes were compared to the absorption and desorption kinetic measurements, allowing analyze qualitatively the impact of the structural changes on the material properties, such as thermal conductivity and permeability.

Keywords: SANS, composite SrCl₂-ENG, thermochemical heat storage, kinetic measurements, structural evolution.

7.1.2 Introduction

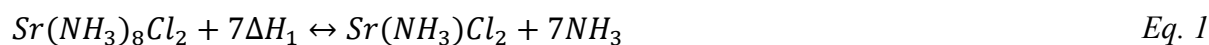
According to recent studies, low-grade waste heat, of temperature below 100°C, accounts for more than 45% of the global primary energy consumption [1]. Thermochemical heat storage is a promising technology for overcoming the problem of the waste heat because thermochemical materials offer high energy density with nearly no heat losses [2]. However, before wide market implementation, some limitations of the technology must be overcome. Thermochemical heat storage is based on a reversible reaction between mainly solid sorbents and gaseous sorbates, such as ammonia, water, or hydrogen. During the sorption reactions, the solid sorbents exhibit volume expansion and contraction [3], as well as agglomeration phenomena causing limitations to gas diffusion [4]. In addition to this, the sorbent materials are poor heat conductors, as their effective thermal conductivity is reported to vary between 0.1 and 1.3 W m⁻¹ K⁻¹ [5]. To overcome the abovementioned challenges, the thermochemical salts can be mixed with porous matrices, among which the most extensively studied are vermiculite ([6]–[9]), activated carbon ([6], [10]), silica gel ([11], [12]), and expanded natural graphite (ENG) ([10], [13]–[15]). For a thorough literature review on the matrices for composite materials, the reader is referred to the work of Jarimi et al. [16]. In particular, ENG has been identified as one of the best matrix materials to significantly improve heat and mass transfer within the reactive bed, as it has high in-plane thermal conductivity and permeability [17]. Moreover, ENG acts as a stabilizer for the salt particles and thus prevents the expansion of the reactive bed, which could be detrimental for the system safety [18].

Employing the composite materials in energy storage systems requires good understanding of the heat and mass transfer properties, such as thermal conductivity and permeability, for the accurate design and optimization of a thermochemical reactor. These transport properties are directly related to the structural features of the material, and they can be modelled and predicted, if the material morphology is known. For example, in the paper by Olives and Mauran [19], the authors reviewed the models of heat transfer in porous media and then suggested a new model for the composite material Impex-m [20] (ENG-MnCl₂) on the basis of the thermal tortuosity and real cross-section. The proposed relation was validated with experimental results obtained from the graphite matrix alone and the Impex-m composite in the anhydrous state (no ammonia present), whereas the comparison for the material in ammoniated states was not performed. However,

knowledge on how the structure of the composite material evolves during ammonia cycling as well as from cycle to cycle is important to broaden the model application.

Until now, studies on nanostructural changes of thermochemical materials, in particular metal halides, during the reaction with ammonia have been scarcely reported. In 2007, Jacobsen et al. [21] examined structural changes during the decomposition of $\text{Mg}(\text{NH}_3)_6\text{Cl}_2$ using in-situ small angle X-ray scattering (SAXS) supported by results from X-ray powder diffraction (XRPD) and the Barrett, Joyner, and Halenda (BJH) method. The authors showed that during heating the formation and agglomeration of spherical $\text{Mg}(\text{NH}_3)_2\text{Cl}_2$ crystallites and the development of a tubular pore structure occurs. The same process of decomposition of $\text{Mg}(\text{NH}_3)_6\text{Cl}_2$ with respect to pore size distribution was investigated in another research by Hummelshøj et al. in 2005 [22]. Pore size distribution for different degree of ammonia desorption was also studied for other metal chlorides – MnCl_2 , CaCl_2 , and NiCl_2 – in the paper by Sørensen et al. in 2008 [23]. To the best of our knowledge, no study on the structural changes in composite materials during ammonia sorption has been reported; however, the results from the aforementioned studies provide a relevant background to investigate this further.

In the present paper, the evolution of the nanostructure of the composite material containing ENG and SrCl_2 during ammonia sorption has been studied using small angle neutron scattering (SANS), together with XRPD and sorption measurements. The sorption reactions are described by the following equations:



In addition, the microstructure of the material has been investigated with scanning electron microscopy (SEM).

7.1.3 Experimental

7.1.3.1 Sample preparation

Expanded natural graphite (ENG) in the form of a board (apparent density $\rho_{\text{ENG}} = 75 \text{ kg/m}^3$) supplied by SGL Carbon was used as a host matrix for the synthesis of the composite material.

Strontium chloride SrCl_2 (purity >98%) was delivered by Amminex. The composite material was prepared by an impregnation method. First, dehydrated ENG board (120°C , 8 h) was immersed into ethanol for two hours to decrease the surface tension between the non-polar ENG and a polar aqueous SrCl_2 solution. The board was subsequently placed in the SrCl_2 solution (33.3 % wt.) for 72 h, after which the impregnated board was dried in a ventilated oven at 90°C for 12 h to ensure that there was no retained water left. Finally, the sample was dried in a vacuum furnace at 300°C for 12 h to eliminate the water absorbed by the salt crystals. The synthesized material had the following characteristics: mass content of SrCl_2 was 72 % wt.; apparent density was 550 kg/m^3 . The sample used in the neutron experiments had the shape of a rectangular plate with the following dimensions: length 30 mm, width 9 mm, and thickness 1 mm.

7.1.3.2 Gas setup and its operation

The schematic of the barometric Sievert's type apparatus used in-situ for the SANS experiments is shown in Figure 1.

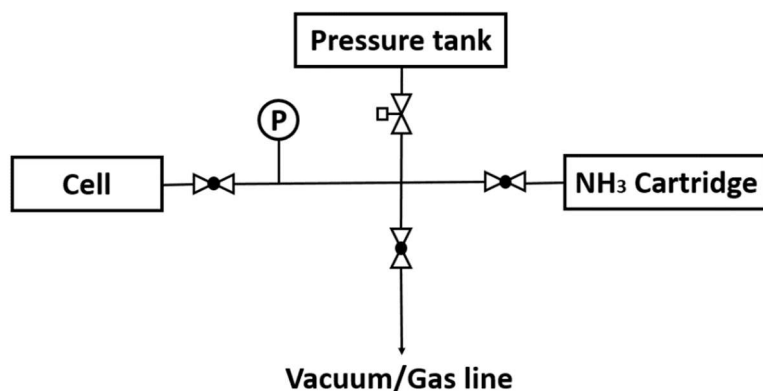


Figure 1. Simplified schematic of experimental setup for SANS studies. P represents a pressure transducer.

The experimental apparatus consists of a sample cell, a pressure tank, an NH_3 cartridge, and a vacuum pump. All the components of the system are connected with stainless steel tubing of 3.18 mm inner diameter, forming a calibrated volume of 513 ml. The NH_3 cartridge is a source of NH_3 , as it contains ammoniated SrCl_2 and releases NH_3 when heated. A heater is in-built in the cartridge and connected to an adjustable power supply.

For keeping track of the pressure in the calibrated volume during sorption processes, the setup is equipped with a pressure transducer. Detecting pressure change in the system gives an opportunity to calculate the amount of NH_3 moles absorbed or desorbed by one mole of SrCl_2 with the following formula:

$$\theta = \frac{n_{\text{NH}_3}}{n_s} = \frac{\Delta p \cdot V / R \cdot T}{m_s / M_s} \quad \text{Eq. 3}$$

where n_{NH_3} is the amount of ammonia absorbed/desorbed by the amount of the salt n_s ; Δp is the absolute value of the pressure change during absorption/desorption; V is the calibrated volume; R is the gas constant; T is the temperature of gaseous ammonia in the calibrated volume; m_s and M_s are the mass and the molar mass of the salt.

The in-house fabricated cell is made of aluminum, since this material is almost transparent for neutrons. The estimated loss over the 1 mm thick aluminum walls is below 1%. The schematic of the cell is shown in Figure 2.

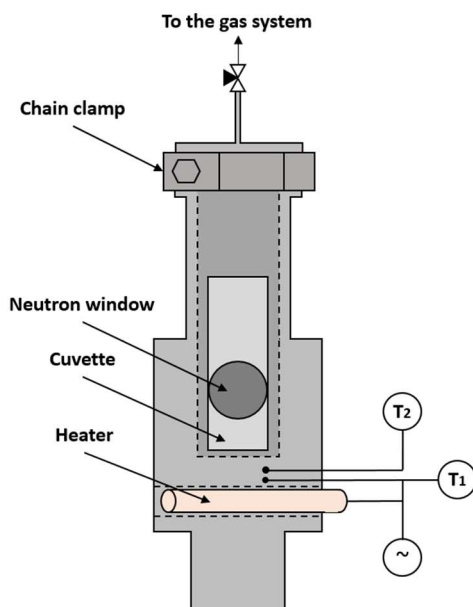


Figure 2. Schematic of the cell for the SANS studies. T_1 is a thermocouple measuring input temperature for the temperature controller and T_2 is a thermocouple metering the temperature around the sample area.

The cell is equipped with a heater connected to a temperature controller (Hart Scientific, model 2200). The input temperature to the controller comes from a K-type thermocouple T_1 , slotted in one of the two side ports in the cell. The other port is occupied with a K-type thermocouple T_2 , metering the temperature close to the sample area. Taking into account high thermal conductivity of aluminum and the composite material, the temperature of the sample was assumed equal to the one measured with T_2 . The cell accommodates a rectangular quartz cuvette of 45 mm in length, 12.5 mm in width, 3 mm in total thickness with 1 mm path length (Starna Scientific, type 1.30/Q/1), with the sample inside. Prior to the experiment, the sample was left in a vacuum furnace at 300°C for 12 h to eliminate the water absorbed by SrCl_2 during the process of fabrication (see also section on sample preparation). After that, the cuvette with the dehydrated sample was placed into the cell, and the cell was connected to a closed needle valve via a chain clamp. To ensure that the sample was not contaminated with water, all the operations were performed in a glove-box under controlled atmosphere, where the level of water was maintained below 0.5 ppm. Then the cell was connected to the rest of the system via a Swagelok fitting and placed into a pre-aligned position in the neutron beam, ensuring that the 7 mm beam hit the center of the sample window (12 mm in diameter) without touching the edges of the cuvette.

Prior to the sorption experiments, the system was evacuated until the pressure was below 10^{-5} bar.

7.1.3.3 X-ray diffraction measurements

To determine the average crystallite size and lattice strain of SrCl_2 before and after impregnation, XRPD patterns of the composite material and pristine SrCl_2 samples were collected using a Rigaku Smart Lab diffractometer in the Bragg-Brentano configuration (Cu K_α , $\lambda = 1.5418 \text{ \AA}$). To avoid contamination of the hydrophilic samples with atmospheric water, the samples were placed in an in-house designed and fabricated gas-tight sample holder with a Kapton window.

Using the PowderPlot software, the peaks of SrCl_2 were fitted and their width β was determined. After that, a Williamson-Hall plot analysis was performed, where both size- and strain-induced broadenings were deconvoluted using the following formula:

$$\beta_T \cdot \cos\theta := \varepsilon \cdot (4\sin\theta) + \frac{K\lambda}{D} \quad \text{Eq. 4}$$

where β_T is the total sample broadening; θ is the scattering angle corresponding to peak position; ε is the strain; K is the shape factor equal to 1 for spherical crystals; λ is the wavelength of X-ray beam; D is the average crystallite size.

The total sample broadening was calculated as follows:

$$\beta_T = \sqrt{\beta^2 - \beta_I^2} \quad \text{Eq. 5}$$

where β_I is the instrumental broadening determined with the Cagliotti formula $\beta_I \sqrt{U \cdot \tan^2 \theta + V \cdot \tan \theta + W}$. The parameters U , V , and W were determined using a standard sample LaB₆, which show no crystallite or strain broadening.

7.1.3.4 Scanning electron microscopy

The microstructure of the composite material as well as the distribution of SrCl₂ within the composite was studied using scanning electron microscopy (SEM) imaging and energy-dispersive X-ray (EDX) spectroscopy on (producer, model of the instrument). Two cubic pieces of the composite material with side 5 mm was separately mounted in an epoxy resin, finely polished, and then coated with carbon. The cross section surface of one of the specimens revealed the in-plane structure of the material, while the other showed through-plane arrangement of ENG sheets and SrCl₂ particles.

7.1.3.5 Small angle neutron scattering measurements

Instruments and data treatment

In-situ SANS measurements during the absorption/desorption processes between gaseous NH₃ and the SrCl₂-ENG composite were carried out at two instruments – Larmor [24] and vSANS at the neutron facilities ISIS (UK) and NIST (USA), respectively.

The SANS configuration in the Larmor instrument allows to cover a wide q range of approximately 0.0035 – 0.6686 Å⁻¹ thanks to the time-of-flight setup at ISIS with a broad wavelength band of 0.9-13 Å. This resulted in relatively fast data collection, useful when studying process dynamics. The acquisition time to obtain scattering and transmission patterns was 1088 and 274 s, respectively. A transmission pattern was collected after each scattering experiment resulting in the average total time of 1423 s (including read out and computer processing), or approx. 24 min, to

acquire one data point. The obtained data set was reduced following a standard procedure in the Mantid software [25], which automatically takes into account the sample transmission and subtracts the contributions from the cell and the cuvette.

During the beamtime at vSANS, the q range was shifted towards lower q -values, resulting in a q range of 0.0017 - 0.155 Å⁻¹, allowing to investigate larger features of the system compared to the ISIS experiment. In this case, scattering and transmission measurements took 600 and 100 s, respectively. One transmission measurement was performed after the acquisition of three scattering patterns, which resulted in 662 s on average, or approx. 11 min, for measuring one data point. The obtained data was reduced in Igor Pro 7 using vSANS procedures available at NIST.

In SANS measurements, the observed intensity scales with the contrast term, which is calculated as the difference of scattering length densities squared:

$$I(q) \sim (\rho_1 - \rho_2)^2 \quad \text{Eq. 6}$$

where ρ_1 and ρ_2 are the scattering length densities of a studied material and the surrounding medium, respectively.

Note that although X-rays would give better nominal contrast for SrCl₂ with respect to the carbon matrix, we have in this work employed neutrons due to the advantage they give for doing in-situ measurements through a solid, pressurized cell, adapted to the experimental absorption/desorption setup. Furthermore, thanks to high incoherent neutron cross-section of hydrogen, one can directly follow the content of hydrogen and hence ammonia in the sample during absorption and desorption. Finally, neutrons are characterized with high penetration power, giving the possibility to study bulky samples, more representative for potential applications. These points are, in fact, essential features of the present investigations.

In order to evaluate the contribution of each component of the system, which contains both the composite material (combination of studied materials) and gaseous NH₃ (medium), the neutron scattering length densities of the different components were listed in Table 1.

Table 1. Scattering length density (SLD) of each component of the system with sample 1.

Compound	SLD ($\times 10^{-6} \text{ \AA}^{-2}$)
NH ₃ (liquid)	-0.40
NH ₃ (gas at 2.5bar)	-0.01
SrCl ₂	3.03
Sr(NH ₃)Cl ₂	2.04
Sr(NH ₃) ₈ Cl ₂	0.32
C (ENG)	7.02

Based on Table 1, the contrast terms for ENG and Sr(NH₃)_zCl₂ ($0 \leq z \leq 8$) with respect to voids filled with gaseous NH₃ at 2.5 bar are 49.4×10^{-12} and $9.2 \times 10^{-12} \text{ \AA}^{-2}$ ($z = 0$) or lower ($z \geq 1$), respectively. Therefore, the contribution from ENG to scattering patterns of the composite material is more than 5 times higher than the contribution from SrCl₂ amines. Thus, to study the features related to SrCl₂ ammine system one has to subtract the contribution of the graphite from the total composite material signal, which can be carried out in two ways:

1. “Pristine method”: the scattering pattern of pristine ENG, the graphite prior to impregnation, is subtracted from the composite material patterns. Here the structure of ENG was assumed to remain unchanged after the synthesis.
2. “Impregnated method”: The scattering pattern of the impregnated ENG is subtracted from the composite patterns. The signal of the impregnated ENG is calculated as the difference between the signals of the composite material before NH₃ cycling and pristine SrCl₂. Pristine SrCl₂ is SrCl₂ powder as used for the synthesis of the composite material. When implementing this approach, SrCl₂ particles were assumed to have the same structure before and after impregnation.

In the “pristine method”, when subtracting the graphite contribution, one has to be cautious because the amount of graphite inside the scattering volume for the pure ENG sample may be slightly different than the amount of ENG in the same volume for the composite sample, due to possible differences in packing in the two cuvettes. However, this will typically be just an overall

scaling of the data in the y-direction, and should not affect the profile of the data, which is the most important for our purposes.

Given that both methods rely on assumptions that cannot be avoided, but are very difficult to evaluate explicitly, we have implemented both approaches and then compared the two sets of results. Any systematic error in either of the two methods is then likely to appear in this comparison.

Data analysis

The scattering data was analyzed using a Guinier/power-law approach as proposed by Beaucage and Schaefer [26]. This approach implements a unified equation, which is a sum of Guinier and Porod regimes from n interrelated structural levels:

$$I(q) = \sum_{i=1}^N G_i \exp\left(-\frac{q^2 R_{g,i}^2}{3}\right) + B_i \exp\left(-\frac{q^2 R_{g,(i+1)}^2}{3}\right) \left(\frac{q}{(\operatorname{erf}(q R_{g,i}/\sqrt{6}))^3}\right)^{-P_i} \quad \text{Eq. 7}$$

where $I(q)$ is the scattered intensity as a function of q ; q is the scalar of the momentum transfer vector or scattering vector; G is the exponential pre-factor; R_g is the radius of gyration; B is the pre-factor specific to the power law scattering; and P is the power characterizing the form of the structural level. If the level is represented by smooth spheres, surface fractals, discs or rods, then the value of power is 4, $3 < P < 4$, 2, or 1, respectively.

The SANS data from the ISIS experiment was initially modelled by a 2-level expression:

$$I(q) = G_1 \exp\left(-\frac{q^2 R_{g,1}^2}{3}\right) + B_1 \exp\left(-\frac{q^2 R_{g,2}^2}{3}\right) \left(\frac{q}{(\operatorname{erf}\left(\frac{q R_{g,1}}{\sqrt{6}}\right))^3}\right)^{-P_1} + \quad \text{Eq. 8}$$

$$G_2 \exp\left(-\frac{q^2 R_{g,2}^2}{3}\right) + B_2 \left(\frac{q}{(\operatorname{erf}(q R_{g,2}/\sqrt{6}))^3}\right)^{-P_2}$$

In Eq. 8, the first two terms represent scattering from $\text{Sr}(\text{NH}_3)_2\text{Cl}_2$ particles and the last two terms represent the signal from a porous structure formed inside the particles. In order to not overparameterize the model, and since we do not have information for this system saying that particles and pores have an average shape significantly different from that of spheres, both the particles and the pores were assumed to be represented by smooth spheres, and hence P_1 and P_2 were set to 4.

An analysis using Eq. 8 assumes that the characteristic sizes are sufficiently separated to be deconvoluted from the experimental scattering pattern, implying also the need for a relatively wide q -range. If the structural sizes approach each other or partly overlap, such a 2-level approach may give inaccurate results, and a 1-level model will be a better representation of the data, having fewer correlated parameters:

$$I(q) = G \exp\left(-\frac{q^2 R_g^2}{3}\right) + B \left(\frac{q}{\left(\operatorname{erf}\left(\frac{q R_g}{\sqrt{6}}\right)\right)^3}\right)^{-P} \quad \text{Eq. 9}$$

The data from NIST reached a very low q -value ($q = 0.0017 \text{ \AA}^{-1}$), thus allowing to probe sizes significantly larger than the individual particles, and it was found necessary to include in the model a large-scale R_g (named $R_{g,0}$) to accommodate the contribution from features in this size range. On the other hand, the high- q limit ($q = 0.155 \text{ \AA}^{-1}$) was lower than that of the ISIS data, wherefore it was not possible to distinguish properly the signals from the particles and the pores inside these particles (cf. comment above). The data obtained from the NIST experiment were therefore also fitted using 2-level model, where the first level ($R_{g,0}$) corresponds to scattering from features larger than the individual particles and the second level (R_g) represents the combined signal from the salt particles and the pores:

$$I(q) = G_0 \exp\left(-\frac{q^2 R_{g,0}^2}{3}\right) + B_0 \exp\left(-\frac{q^2 R_g^2}{3}\right) \left(\frac{q}{\left(\operatorname{erf}\left(\frac{q R_{g,0}}{\sqrt{6}}\right)\right)^3}\right)^{-P_0} + G \exp\left(-\frac{q^2 R_g^2}{3}\right) + B \left(\frac{q}{\left(\operatorname{erf}\left(\frac{q R_g}{\sqrt{6}}\right)\right)^3}\right)^{-P} \quad \text{Eq. 10}$$

Please note that the second part of Eq. 10 describes the same structural level as Eq. 9.

To determine particle size distribution, the polydispersity index, PDI , was calculated as follows [27]:

$$PDI = \frac{B \cdot R_g^4}{1.62 \cdot G} \quad \text{Eq. 11}$$

The value of PDI is equal to unity for monodisperse spherical particles, and the coefficient of 1.62 serves for normalization. The value of the PDI increases with an increase in dispersity and asymmetry of the structural entities.

7.1.4 Results

7.1.4.1 Sorption kinetics

During the first round of experiments (ISIS), the rectangular plate of the composite material (160 mg) was subjected to five NH_3 cycles, equivalent to five absorptions and five desorptions. Figure 3 shows the results of the measurements with kinetic and pressure curves for the five absorptions (a-b) and desorptions (c-d).

All the absorptions were carried out at room temperature under NH_3 atmosphere. The pressure dynamics with the initial pressure value for each absorption is presented in Figure 3(b). One could observe that initial pressure for the first three absorptions is same and equal 2.52 bar. The last two absorption (Absorption 4 and Absorption 5) were performed at higher pressure - 2.92 and 3.05 bar, respectively, in order to check the change in the absorption rate with the increase in pressure. Desorption tests were performed by heating the sample from room temperature to 100°C with a constant heating rate (HR). HR was 1 K/min for the first four desorptions and reduced to 0.2 K/min for Desorption 5, as indicated in Figure 3(c). The initial pressure during the first three desorptions as well as Desorption 5 was around atmospheric pressure (see Figure 3(d)), whereas Desorption 4 started from 0.71 bar before evacuation of the system at 100°C . Taking into account the equilibrium curves for $\text{Sr}(\text{NH}_3)_8\text{Cl}_2$ - $\text{Sr}(\text{NH}_3)\text{Cl}_2$ and $\text{Sr}(\text{NH}_3)\text{Cl}_2$ - NH_3 systems [28], one could conclude that Desorption 4 was fully complete with no NH_3 present at the end of the reaction, while the other desorptions were partially complete with one mole of NH_3 per mole of SrCl_2 left.

From Figure 3(a) one can see that the amount of absorbed NH_3 during Absorption 1 and Absorption 5 (calculated with Eq. 3) reached around 8 mole/mole of SrCl_2 ($\pm 3\%$), and the other absorptions gave 7 mole/mole of SrCl_2 ($\pm 3\%$), which is consistent with the reactions stoichiometry (Eq. 1 and Eq. 2). In addition, all the desorptions achieved the theoretical value of 7 mole/mole of SrCl_2 at the first desorption step.

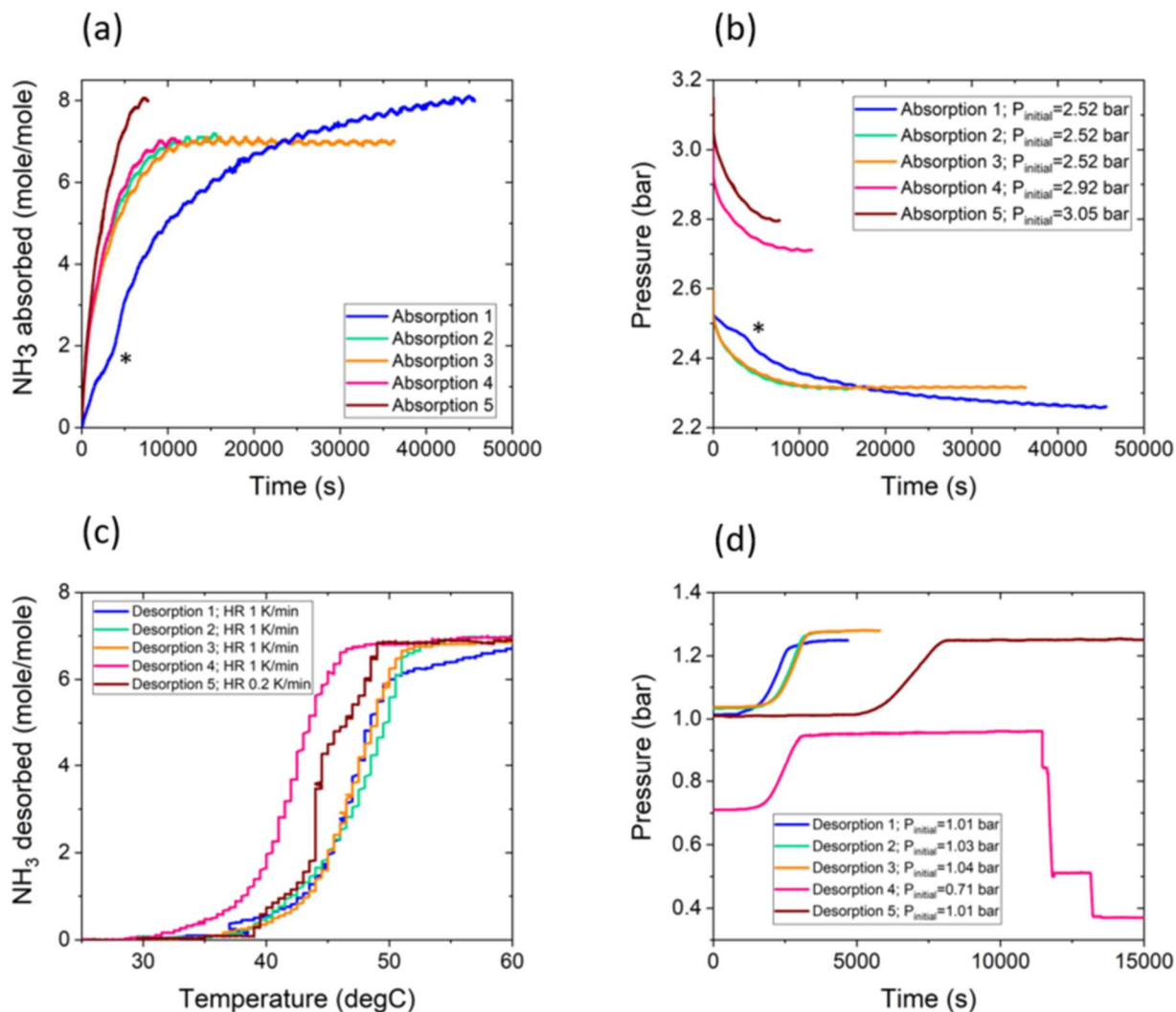


Figure 3. Results of the kinetic measurements: (a) absorption kinetic curves for five cycles; (b) pressure curves for five absorptions. In the legend, $P_{initial}$ refers to NH_3 pressure at the beginning of absorption. (c) desorption kinetics curves for five cycles. In the legend, HR corresponds to heating rate. The second desorption step during Desorption 4 is not shown. (d) Pressure curves for five desorptions. In the legend, $P_{initial}$ refers to NH_3 pressure at the beginning of the desorption. (*: Crack appeared in the cuvette wall).

Absorption results

At the beginning of Absorption 1, the cuvette split at the sides due to the expansion of the sample, which is indicated with a small knee in Figure 3(a) and (b). The crack in the cuvette did not cause any displacement of the sample and hence did not prevent the experiment from being performed

(note that the cuvette is fully enclosed by an aluminum chamber). In fact, the breakage helped speed up the sorption reactions thanks to the increase in the contact area between the sample and gaseous NH_3 .

At the beginning of NH_3 cycling, gaseous NH_3 moves within the reactive bed freely thanks to the porous structure of the ENG matrix, but it takes some time for the gas to diffuse into the pristine particles of SrCl_2 . The diffusion of the gas into the salts particles results in a change in the salt nanostructure, followed by a stabilization. This process is seen during the first three absorptions performed under same NH_3 pressure, 2.52 bar (see Figure 3(b)). For example, Absorption 1 proceeds much slower compared to Absorption 2, while the kinetic curve of Absorption 3 almost coincides with the one of Absorption 2. It is worth noting here that the pristine salt particles are expected to have an initial porous structure, developed during the dehydration of absorbed water molecules prior to the experiment.

From Figure 3(b), it can also be noticed that the increase in initial pressure by 0.4 bar in case of Absorption 4 resulted in insignificant increase of the reaction rate (Figure 3(a)) when compared to the previous absorptions, while further pressure rise by 0.13 bar led to considerably faster Absorption 5. The reason for this could be the restructuring of the system during fully complete desorption (Desorption 4, cf. Figure 3(d)) prior to Absorption 5.

Desorption results

Figure 3(c) illustrates the dependency of the amount of desorbed NH_3 per mole of SrCl_2 on the temperature of the sample. As seen from the plot, the first three desorptions started at around 37°C , but the kinetics curve of Desorption 1 (blue curve) has a different shape compared to the ones of Desorption 2 and Desorption 3 close to the end of the reaction. This deceleration in the rate of Desorption 1 by the end of the reaction is likely to be associated with the completion of the nanostructural changes. Desorption 4 (pink curve) is characterized with the starting temperature 7 degrees lower than the previous cycles, as well as with faster kinetics due to the decrease in initial pressure (cf. Figure 3(d)). In the case of Desorption 5, the reaction starts at almost the same point as the first three desorptions (same initial pressure), but the kinetics rate is faster thanks to the lower heating rate leading to more uniform temperature distribution within the sample.

It is worth noting that the desorption temperature of 37°C observed at 1 bar of NH₃ atmosphere is the same as the one reported by Bialy et al. [29] for pure SrCl₂. This suggests that the equilibrium conditions for SrCl₂ were not affected by the impregnation of the salt particles into the ENG matrix.

7.1.4.2 XRD

The XRPD patterns obtained on the two samples – the composite material and pristine SrCl₂ – are presented in Figure 4(a), and the results of the Williamson-Hall method for the two samples are shown in Figure 4(b).

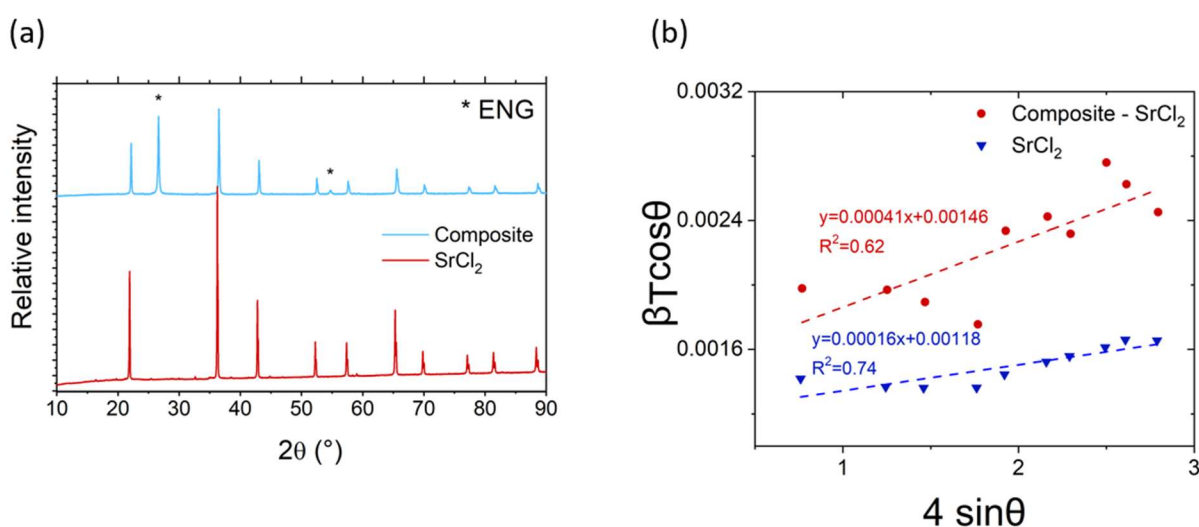


Figure 4. XRPD patterns (a) and Williamson-Hall plots (b) of the composite material and pristine SrCl₂.

From Figure 4(a), it can be observed that the peaks of SrCl₂ coincide for the two samples, confirming that the cubic phase of the SrCl₂ remains unchanged after the process of impregnation. However, one can observe that the peaks are broader for the impregnated salt. This indicates that the SrCl₂ crystallites became smaller and the lattice strain increased. This is supported by the results presented in Figure 4(b), where the slope (reverse crystallite size) and intercept (strain) in the Williamson-Hall plot for the composite material are larger compared to the ones for the pristine SrCl₂. The values of the crystallite size and strain were extracted from Figure 4(b), and the summary of the results are shown in Table 2.

Table 2. Results from the Williamson-Hall plot analysis.

Sample	D, nm	ϵ	R_g (sphere), nm
Composite – SrCl ₂	106	4.07×10^{-4}	41
Pristine SrCl ₂	131	1.61×10^{-4}	51

According to the results presented in Table 2, the size of the SrCl₂ crystallites decreased from 131 to 106 nm after impregnation. With the assumption that the crystallites are spherical on average, the radius of gyration was calculated using $R_g = \sqrt{\frac{3}{5}} \cdot R$. After impregnation, the lattice strain increased from 1.61×10^{-4} to 4.07×10^{-4} .

7.1.4.3 SANS

Data presentation

In order to perform the comparison between the “pristine method” and “impregnated method”, described previously, Figure 5 presents log-log plots of the ISIS scattering data processed using both methods. The results from the subtraction of the pristine ENG (“pristine method”) and impregnated ENG (“impregnated method”) are shown in Figure 5(a-b) and (c-d), respectively. Figure 5(a) and (c) show log-log plots of neutron scattering from SrCl₂ ammine system prior to NH₃ cycling (start) and at the end of five desorptions. Please note that before NH₃ cycling (start) and at the end of desorption 4 (des 4 - end) there is deammoniated salt present in the system, and at the end of the other desorptions, the chemical composition in the system is SrCl₂ monoamine. Figure 5(b) and (d) illustrate patterns collected at the end of the five absorptions, with SrCl₂ octaammine present.

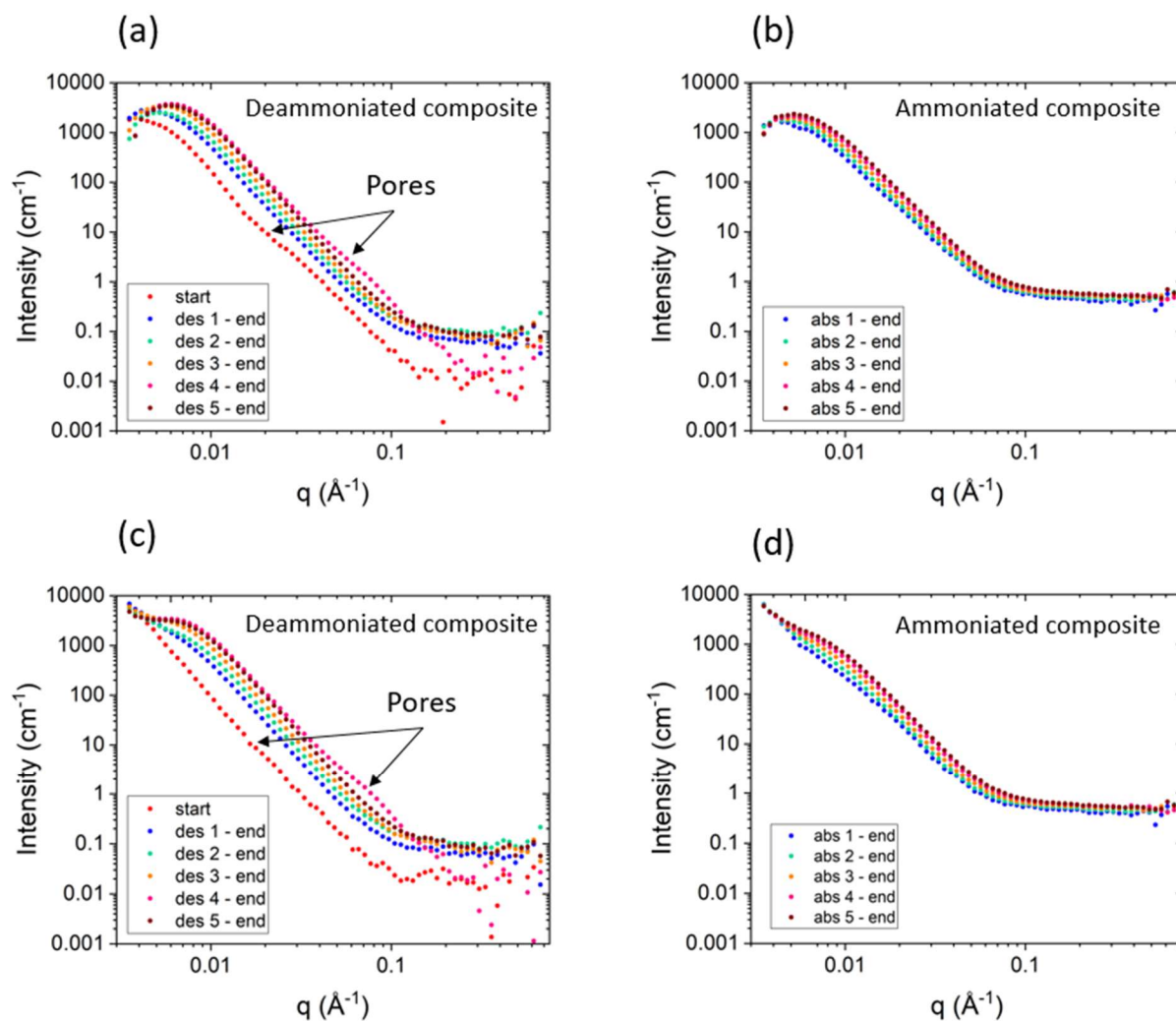


Figure 5. Log-log plots of neutron scattering data obtained at Larmor (ISIS). The data was processed using (a-b) pristine and (c-d) impregnated methods. (a) and (c) present patterns obtained prior to NH₃ cycling (start) and at the end of desorptions (des # - end). (b) and (d) depict scattering patterns taken at the end of the absorptions.

As shown in Figure 5, the scattering patterns obtained using the two methods show comparable shapes over the whole q -range except in the low q -region (< 0.006 Å⁻¹). This is a confirmation that the separation of the contribution from the SrCl₂ particles from the ENG matrix is reasonable to a first approximation, although errors cannot be fully disregarded. In fact, the discrepancy seen at the lowest q may be attributed to the difference between the patterns of the pristine materials, pristine ENG and SrCl₂. For example, at low q , the pristine SrCl₂ gives a strong upturn, indicating

that there are large salt particles present outside of the experimental q -range, whereas the pristine ENG pattern shows a plateau, making it possible to extract information about the size of the pores in the non-impregnated graphite matrix. The fitting of the 1-level model (Eq. 9) to the pristine ENG pattern gave a P value close to 4, suggesting smooth spherical features with the radius of gyration of around 35 nm and PDI 8.8. Similar results were obtained for the pristine ENG from the NIST dataset with P set to 4: $R_g = 33$ nm and PDI = 6.3. This R_g can be attributed to the pores in the ENG matrix prior to impregnation.

Taking into account the slight difference between the results from the two methods in the lowest q -range, the q -range below 0.006 \AA^{-1} was not included during the fitting of the unified equation to the scattering patterns.

The profiles illustrated in Figure 5 have two features: a plateau at low q ($< 0.01 \text{ \AA}^{-1}$) and a bump in the middle q -range (from 0.02 to 0.1 \AA^{-1}). While the plateau at low q can be attributed to large structures, most probably to the salt particles, the knee in the middle q -range must be related to the porous structure within the particles, as previously reported in literature for the MgCl_2 -ammine system [21], [22]. The knee is clearly visible for the profile of the fully deammoniated sample prior to cycling ("start"), but less so after the different desorptions. However, at the end of desorption 4, a new knee appears at a higher q -value (near $q = 0.1 \text{ \AA}^{-1}$). We relate this to a population of smaller nanopores existing in the fully deammoniated sample only. Note that, as mentioned previously, desorption 4 was complete with no NH_3 present at the end of the reaction, while the other desorptions were only partially complete with one mole of NH_3 per mole of SrCl_2 left.

It should be noted that the plateau corresponding to the salt particles started to appear only after the fifth scattering pattern during the first absorption run, i.e. after approx. 1 hour (as described in the experimental section), a pattern was collected every 24 min), when using the "impregnated method" for data reduction. This is because the contribution from the low- q regime of the pristine SrCl_2 had a significant effect on the composite material patterns. Considering this, one has to be aware of the overestimation of the particles size at the beginning of absorption 1, when using the "impregnated method". Hence, the initial dimensions of the different features (particles and pores) were in the following determined using the "pristine method".

If one looks at the evolution of the profiles from cycle to cycle, the general trend is that scattering patterns are shifted up and towards higher q , indicating an increase in the specific surface area and decrease in the characteristic sizes. In addition, the more the sample is cycled, the steeper the curve slope becomes (see Figure 5(b, d)), which suggest that the features become either less asymmetric, or more monodisperse, or both. The same tendency was noted within a cycle: the higher the NH_3 loading in the sample, the steeper the curve slope. This qualitative inspection of the data is a useful starting point for the quantitative analysis presented in the next section.

Data fitting

ISIS data

As a starting point for the quantitative analysis, the 2-level model expressed as Eq. 8 was fitted to the composite material profile measured prior to NH_3 cycling (pristine method). The results are presented in Figure 6.

The different characteristic sizes extracted here were 38 nm ($R_{g,1}$) and 12 nm ($R_{g,2}$), with the error calculated to approx. ± 1 nm, based on the assumption that the implemented model is a sufficiently accurate representation of the investigated system. The first structural level with $R_{g,1}$ of around 38 nm can be assigned to the salt particles, since the size is similar to that found previously for the crystallites, determined by XRPD studies (see Table 2). The crystallization taking place after impregnation leads to crystallites that are smaller than the pristine ones (cf. Table 2). The resemblance between the R_g -value found from SANS (38 nm) and that of equivalent spherical particles based on XRPD data (41 nm), makes it reasonable in the following to use the assumption that these particles are on average near spherical ($P = 4$), although there may be some polydispersity present. The second structural level, associated with the internal pores [22], has been already reported in SAXS studies conducted by Jacobsen et al. [21]. These authors regarded the pores as intrinsically cylindrical, but modelled only the radius of the cylinder with $P = 4$ and omitted the contribution from the length of the cylinder with $P = 1$, arguing that the signal from the length was not discernible from the salt crystallites. Considering the similarity of the MgCl_2 -amine and SrCl_2 -amine systems, and to keep the number of parameters manageable given the limited resolution in the SANS data, we have implemented the same approach in the current study.

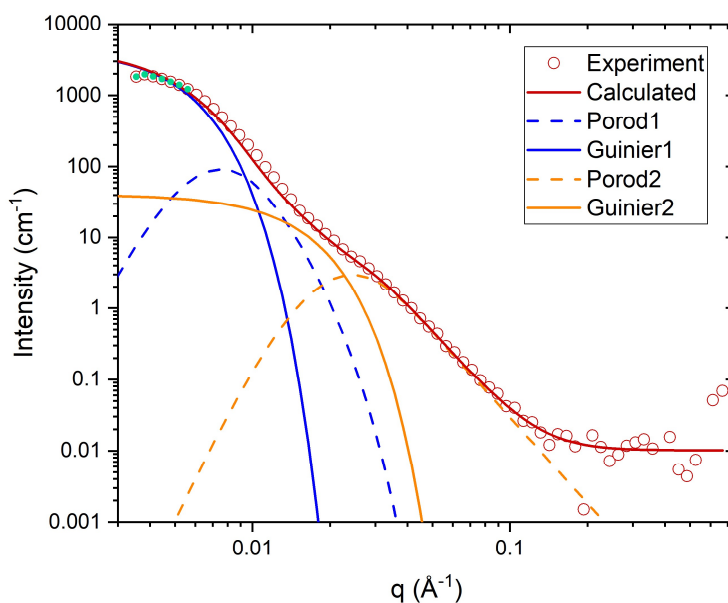


Figure 6. Fit of Eq. 8 to impregnated SrCl_2 prior to NH_3 cycling: $R_{g,1}=376 \text{ \AA}$, $\text{PDI}_1=3.9$, $R_{g,2}=124 \text{ \AA}$, $\text{PDI}_2=10.3$. Method of processing: pristine. Only the data points marked with a hollow symbol were included in the fitting. The different contributions (Guinier, Porod) to the total pattern are also shown.

Using the results from the first pattern as initial parameters, the 2-level model (Eq. 8) was fitted to the ISIS data set (except the fully deammoniated sample at the end of desorption 4) processed using the “pristine method”. Figure 7 illustrates the results. For convenience, Figure 7(a) shows a series of consecutive kinetic curves for five absorptions and five desorptions. Figure 7(b) and (c) depicts the evolution of the radius of gyration for the particles $R_{g,1}$ and the pores $R_{g,2}$, respectively.

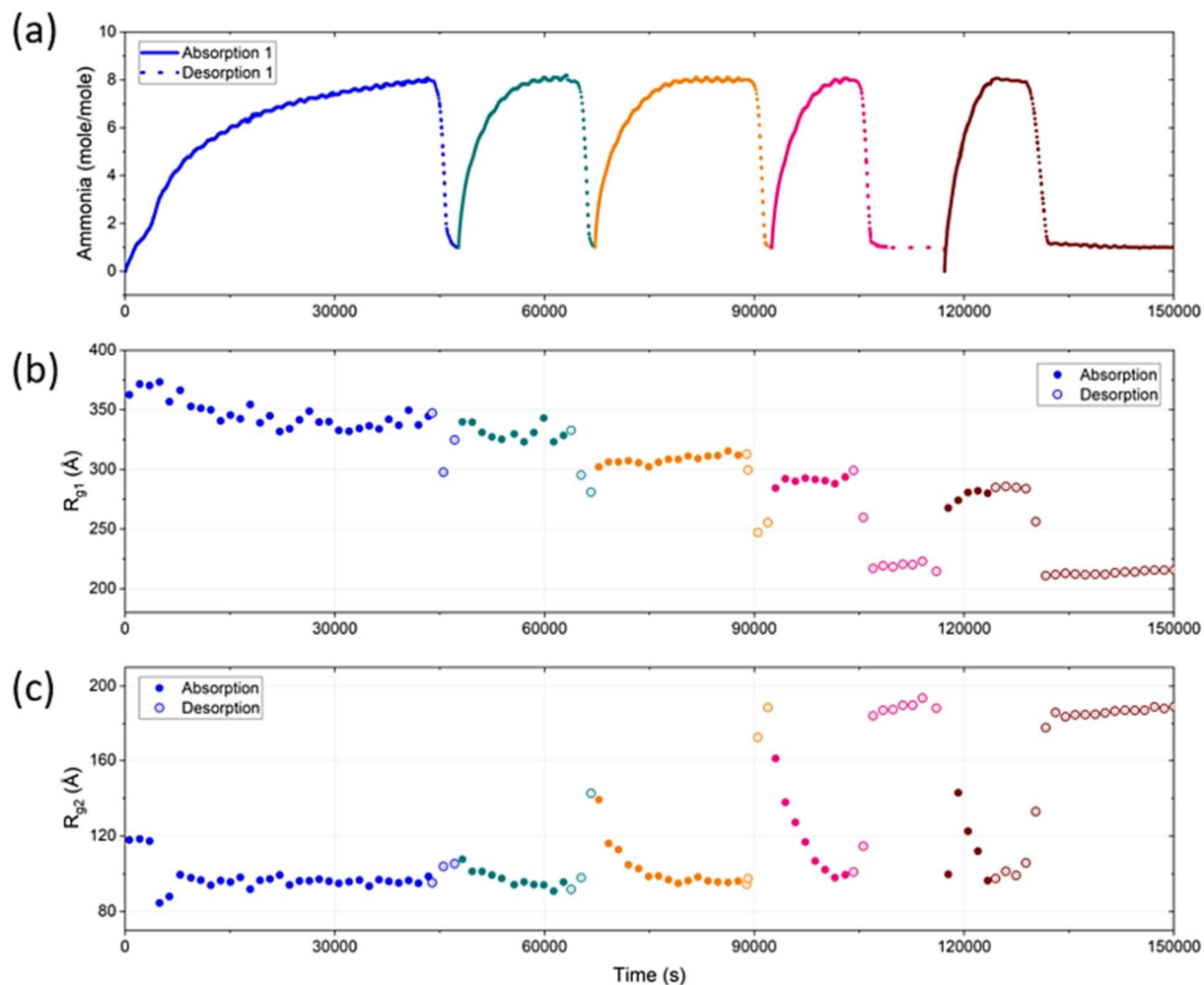


Figure 7. Results from the fitting of 2-level model (Eq. 8) to ISIS data set processed using “pristine method”: (a) kinetic curves of consecutive absorptions (solid line) and desorptions (dotted line); (b) the evolution of radius of gyration of SrCl_2 particles $R_{g,1}$ during 5 absorptions (filled circles) and 5 desorptions (hollow circles); (c) the evolution of radius of gyration of pores $R_{g,2}$ inside salt particles during 5 absorptions (full circles) and 5 desorptions (hollow circles).

From cycle to cycle, the salt particles and pores exhibit a systematic increase and decrease in size; this would be expected to give an evolution also in the specific surface area. Indeed, as shown earlier (cf. Fig. 5), the surface area was found to increase continuously with cycling.

Within one sorption cycle, the pores become smaller during absorption and bigger during desorption (see Figure 7(c)), which is consistent with previous results reported in literature [21],

[22]. In case of the salt particles, they decrease in size during absorption 1, stabilize during absorption 2 (within the accuracy of the measurements), and increase slightly in size during the last three absorptions. The reduction in size found during absorption 1 could be explained by the crystallites experiencing partial fracture due to ammonia diffusion [30]. Upon the subsequent cycles, the expansion during absorption and contraction during desorption might be attributed to the difference in true density of the ammoniated and deammoniated salt. Interestingly, these findings are not supported by the results from the paper of Jacobsen et al. [21], where the authors have reported that during heating the $\text{Mg}(\text{NH}_3)_2\text{Cl}_2$ crystallites grow due to the formation of agglomerates. This difference between the results from the present study and literature is likely due to the presence of the ENG matrix in the composite material, which hinders the agglomeration of the particles during sorption processes [31].

The polydispersity index (*PDI*) connected with $R_{g,1}$ and $R_{g,2}$ were found to increase during absorption and decrease during desorption, indicating that in ammoniated state the particles and pores are characterized with higher polydispersity and more asymmetric shape (see also S 1 in Supplementary information). This is in agreement with the study conducted by Jacobsen et al. [21].

The same trends and dependencies as described above were observed for the results obtained using the “impregnated method” presented in S 2 in Supplementary information. This suggests that the method of data processing does not affect the results, except for the beginning of absorption 1, as mentioned above.

After desorption 1, the two characteristic sizes started to converge toward the same value, having only a gap of 50 Å by the end of the desorption 3 (cf. Figure 7(b) and (c)). As mentioned above, in this case, the model cannot properly separate the two features due to the limited information content in the scattering pattern, and the 1-level model is more relevant. We therefore reanalyzed the data with a 1-level approach (data reduced with the “pristine method”), thus extracting information about the average particle/pore structural development during cycling. These results are presented in Figure 8.

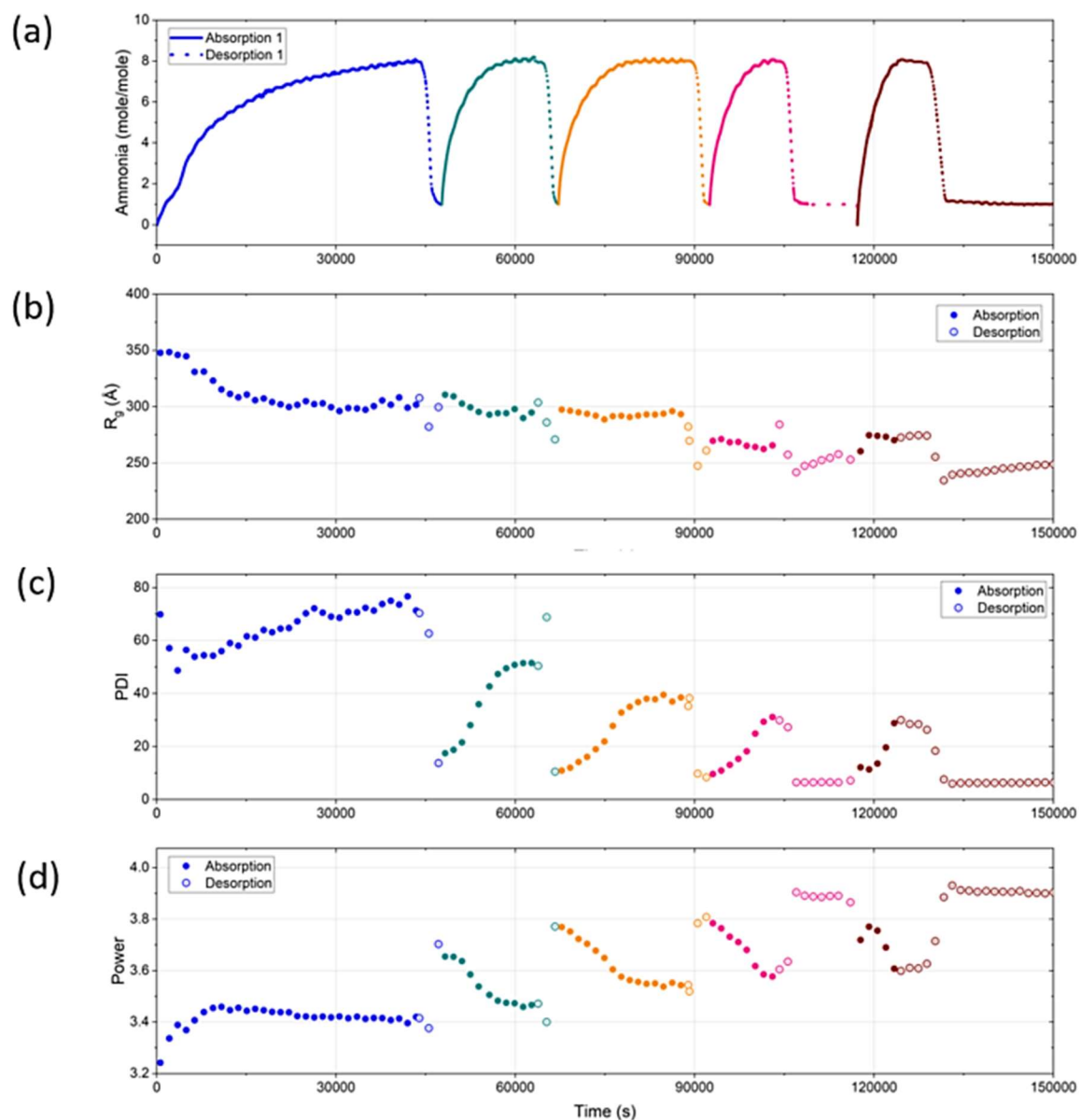


Figure 8. Results from the fitting of 1-level model (Eq. 9) to ISIS data set processed using “pristine method”: (a) kinetic curves of consecutive absorptions (solid line) and desorptions (dotted line); the evolution of (b) R_g , (c) PDI, and (d) power during 5 absorptions (filled circles) and 5 desorptions (hollow circles).

Figure 8 presents this combined evolution of the particles and pores. After five sorption cycles, the characteristic size R_g was reduced from 350 down to 250 Å, indicating that the combined structural level reflects particles. In addition, the PDI decreased from around 80 to 6 and the power

P increased from 3.2 to 3.9. This is equivalent to a continuous development towards a system of rather smooth, spherical entities. As expected, the results from the “impregnated method” (see S 3 in Supplementary information) show similar trends.

NIST data

Since the experimental configuration at NIST experiment allows access to lower q -values, in addition to the previously reported structures (salt particles and pores), a larger feature with $R_{g,0} > 80$ nm was detected. This structural level was assumed to originate from the ENG, as the salt particles appear to be stabilized by the matrix. However, to confirm this, more information is needed. The composite material NIST profiles treated with the “pristine method” are presented in S 4 in Supplementary information.

To analyze the NIST data, we have applied the 2-level model (see Eq. 10) with the smaller structural level originating from both particles and pores (see Figure 9), cf. also the Theory section.

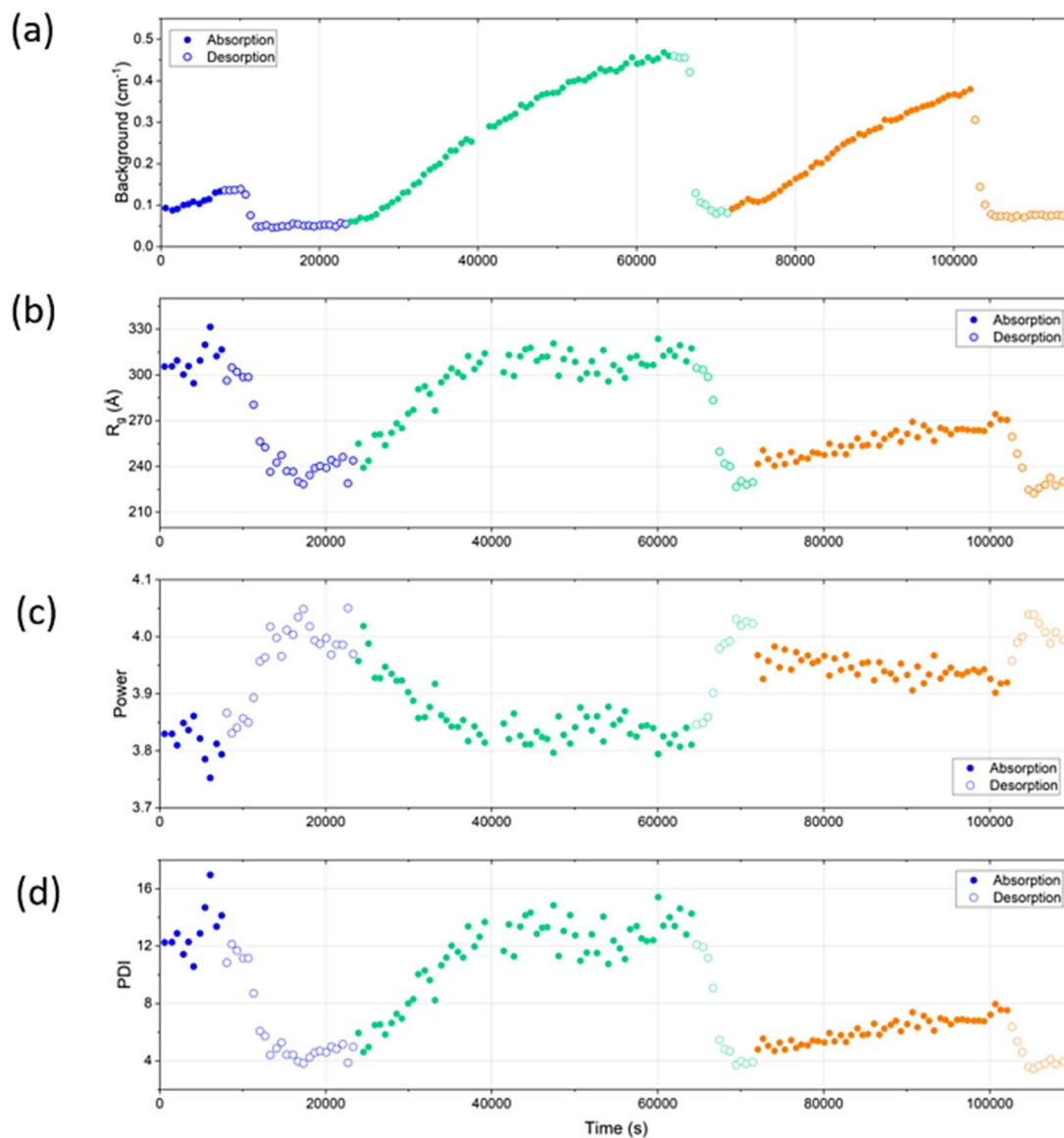


Figure 9. Results from the fitting of 2-level model (Eq. 10) to NIST data set processed using “pristine method”: evolution of (a) background, (b) R_g , (c) power, and (d) PDI during 3 absorptions (filled circles) and 3 desorptions (hollow circles)

For these data, the progression of the sorption reactions is followed as the dependency of the background on the reaction time (see Figure 9(a)). The high- q background level is a direct probe of hydrogen and hence ammonia in the sample, since incoherent neutron scattering contribution from hydrogen is about 50 times larger than from SrCl₂, and the contribution from carbon is practically zero. The evolution of the parameters R_g , P , and PDI for three sorption cycles is also

shown in Figure 9. The results are similar to the ones described for the ISIS data fitted to the 1-level model. This indicates that the obtained results are reproducible not only for the two methods of data processing but also for different instruments.

SANS and sorption kinetics

By comparing SANS results with kinetic tests, one can correlate structural changes with the rate of the sorption processes. For example, it has been shown that during the five desorptions (see Figure 3) the reaction rate is same, suggesting that the structural changes described above do not influence the desorption rate. Since the desorption is a heat driven process, defined by the ability of the reactive bed to conduct heat, one might claim that the thermal conductivity of the composite material is not affected by the morphological changes. For absorption, the evolution in the composite nanostructure has an impact on the absorption rate only in case of the first absorption, when the crystallites break down due to ammonia diffusion. Further decrease in the particle size and increase in the pore size during three subsequent absorptions (absorption 2-4) did not cause any change in the absorption rate. However, after the fully completed desorption 4, the absorption proceeded significantly faster, which may be explained by the appearance of an additional porous structure within the salt particles. Thus, to increase the absorption rate, one must cycle the material at least once. It worth noting that the sorption experiments have been performed on a sample of a relatively small mass (160 mg), which might have affected the observations, as the heat and mass transfer are mass-dependent phenomena.

7.1.4.4 SEM

The morphology of the composite material and the distribution of the elements within the composite material were examined using SEM and EDX techniques, respectively. Figure 10 shows SEM images of the in-plane structure of the composite material taken at magnification of 220 (a) and 1000 (b).

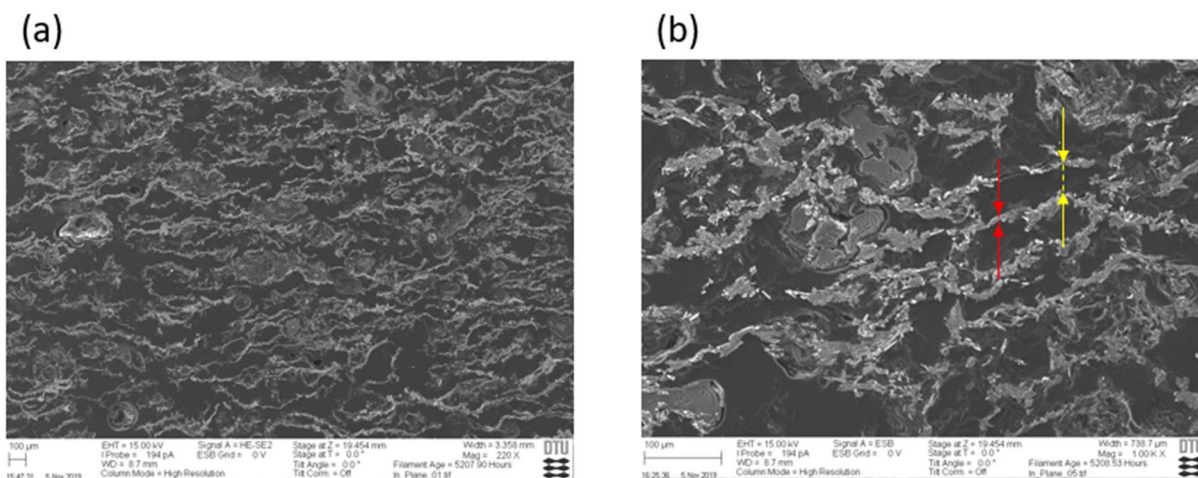


Figure 10. SEM images of in-plane cross-section of the composite material (a) magnification 220; (b) magnification 1000. The thickness of the ENG particles is shown in red, and the distance between the ENG particles is indicated in yellow.

As seen from Figure 10, the ENG particles exhibit vermiculite (plate) structure and form an interconnected network, which provides an enhanced thermal behavior to the composite materials. The average size (thickness) of the particles is around 10-20 μm , while the average distance between the two adjacent particles (pore size) is about 50 μm . The thickness of expanded graphite particles and the pore size obtained in the current study is consistent with the previously reported values. For example, in 2020 Zhao *et al.* [32] studied the morphology of three types of expanded natural graphite for phase change materials application. In this study, the thickness of the particles was found to be in the range between 1 and 400 μm , and the pore size was reported to vary from 27 to 243 μm depending on graphite type.

Figure 11 depicts elemental maps of SEM images from Figure 10.

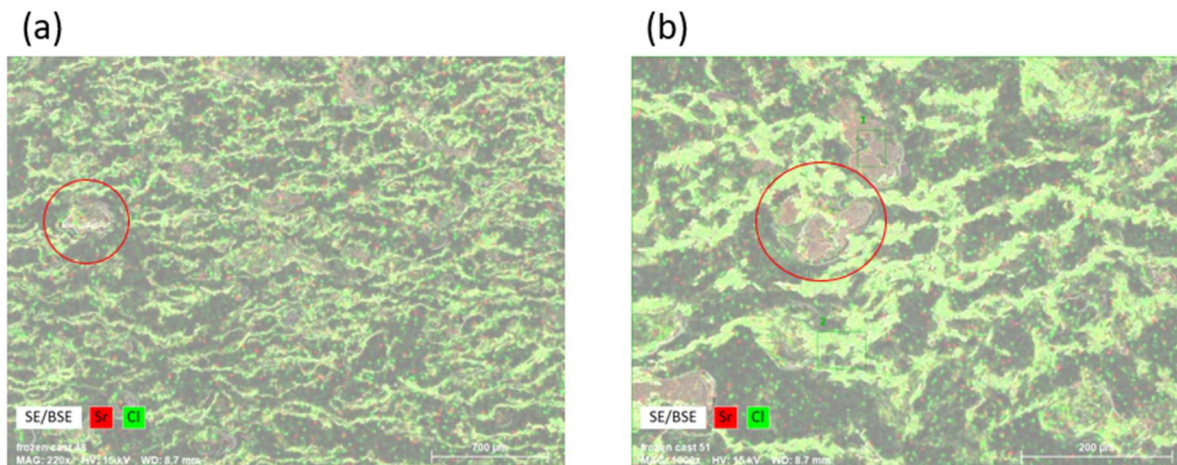


Figure 11. EDS maps of in-plane cross-section of the composite material taken at magnification of (a) 220; (b) 1000.

From Figure 11(a), one could observe that SrCl_2 particles are evenly distributed within the ENG matrix, which is confirmed by the image taken at higher magnification in Figure 11(b). The ratio between Cl and Sr atoms in most of the areas was determined to be two ($\pm 5\%$), which represents stoichiometry; however, in the regions highlighted by the red circles (see Figure 11), the concentration of Cl element was twice as less as the theoretical one. This could be explained by the formation of SrCO_3 agglomerates due to the presence of CO_3^{2-} ions in the water used for the synthesis.

7.1.5 Conclusion

The focus of the present paper was on studying the evolution of the nanostructure of the composite material SrCl_2 -Expanded Natural Graphite (ENG) upon ammonia sorption. Moreover, the obtained structural information was coupled with the information on the sorption kinetics. While structural changes were investigated with small angle neutron scattering (SANS) technique in the q range $1.7 \times 10^{-3} - 0.67 \text{ \AA}^{-1}$, the sorption kinetic curves were retrieved using a barometric Sievert's type apparatus. The *in-situ* SANS experiments were performed at instruments Larmor@ ISIS (the UK) and vSANS@ NIST (the US).

For the analysis of the SANS data, we have developed and implemented two methods of data processing – “pristine method” and “impregnated method”. The two methods have shown comparable results, indicating that both can be used for treating the composite material data. In addition, the SANS results were reproduced on the two instruments.

The structural studies have shown the existence of three structural levels, among which the medium and smallest features corresponds to SrCl_2 particles and nanopores within the particles, respectively. The largest level was assumed to originate from ENG matrix; however, to confirm this, more information is required. After five sorption cycles, the particles and pores shrink and expand, respectively. These structural changes were shown not to affect the desorption rate, but absorption rate during the first cycle.

7.1.6 Acknowledgements

This work is financially supported by NordForsk Nordic Neutron Science Programme via the Neutrons for Heat Storage (NHS) project (No. 82206). The authors thank neutron sources ISIS (the UK) and NIST (the US) for the allocation of neutron radiation beam times. Beamline scientists Leide Cavalcanti (ISIS), Robert Dalgliesh (ISIS), Adam Washington (ISIS), Yun Liu (NIST) and Cedric Gagnon (NIST) are acknowledged for experimental assistance. Additionally, the Danish Research Council is acknowledged for the financial support via Danscatt.

7.1.7 References

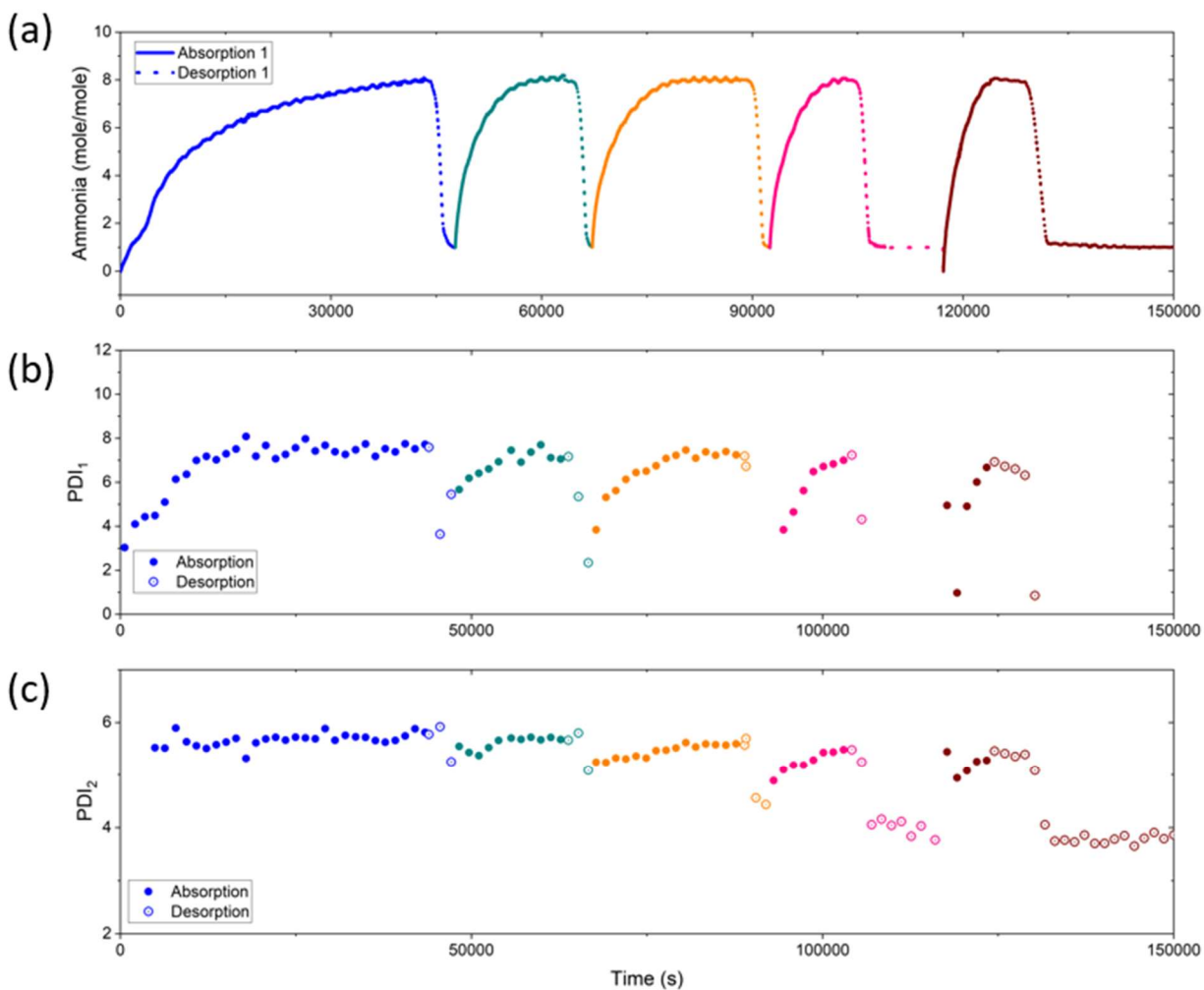
- [1] C. Forman, I. K. Muritala, R. Pardemann, and B. Meyer, “Estimating the global waste heat potential,” *Renew. Sustain. Energy Rev.*, vol. 57, pp. 1568–1579, 2016.
- [2] D. Aydin, S. P. Casey, and S. Riffat, “The latest advancements on thermochemical heat storage systems,” *Renew. Sustain. Energy Rev.*, vol. 41, pp. 356–367, 2015.
- [3] P. Berdiyeva, A. Karabanova, M. G. Makowska, and R. E. Johnsen, “In-situ neutron imaging study of NH_3 absorption and desorption in SrCl_2 within a heat storage prototype reactor,” *J. Energy Storage*, vol. 29, no. December 2019, p. 101388, 2020.
- [4] A. Tekin *et al.*, “Ammonia dynamics in magnesium ammine from DFT and neutron

- scattering,” *Energy Environ. Sci.*, vol. 3, no. 4, pp. 448–456, 2010.
- [5] A. Fopah Lele, K. E. N’Tsoukpoe, T. Osterland, F. Kuznik, and W. K. L. Ruck, “Thermal conductivity measurement of thermochemical storage materials,” *Appl. Therm. Eng.*, 2015.
- [6] S. P. Casey, J. Elvins, S. Riffat, and A. Robinson, “Salt impregnated desiccant matrices for ‘open’ thermochemical energy storage - Selection, synthesis and characterisation of candidate materials,” *Energy Build.*, vol. 84, pp. 412–425, 2014.
- [7] D. Aydin, S. P. Casey, X. Chen, and S. Riffat, “Novel ‘open-sorption pipe’ reactor for solar thermal energy storage,” *Energy Convers. Manag.*, vol. 121, pp. 321–334, 2016.
- [8] A. Sapienza, I. S. Glaznev, S. Santamaria, A. Freni, and Y. I. Aristov, “Adsorption chilling driven by low temperature heat: New adsorbent and cycle optimization,” *Appl. Therm. Eng.*, vol. 32, no. 1, pp. 141–146, 2012.
- [9] A. D. Grekova, L. G. Gordeeva, and Y. I. Aristov, “Composite ‘LiCl/vermiculite’ as advanced water sorbent for thermal energy storage,” *Appl. Therm. Eng.*, vol. 124, pp. 1401–1408, 2017.
- [10] M. M. Druske *et al.*, “Developed materials for thermal energy storage: Synthesis and characterization,” *Energy Procedia*, vol. 61, pp. 96–99, 2014.
- [11] H. Wu, S. Wang, and D. Zhu, “Effects of impregnating variables on dynamic sorption characteristics and storage properties of composite sorbent for solar heat storage,” *Sol. Energy*, vol. 81, no. 7, pp. 864–871, 2007.
- [12] I. A. Simonova, A. Freni, G. Restuccia, and Y. I. Aristov, “Water sorption on composite ‘silica modified by calcium nitrate,’” *Microporous Mesoporous Mater.*, vol. 122, no. 1–3, pp. 223–228, 2009.
- [13] S. Mauran, P. Prades, and F. L’Haridon, “Heat and mass transfer in consolidated reacting beds for thermochemical systems,” *Heat Recover. Syst. CHP*, vol. 13, no. 4, pp. 315–319, 1993.
- [14] L. Jiang, L. W. Wang, Z. Q. Jin, R. Z. Wang, and Y. J. Dai, “Effective thermal conductivity
-

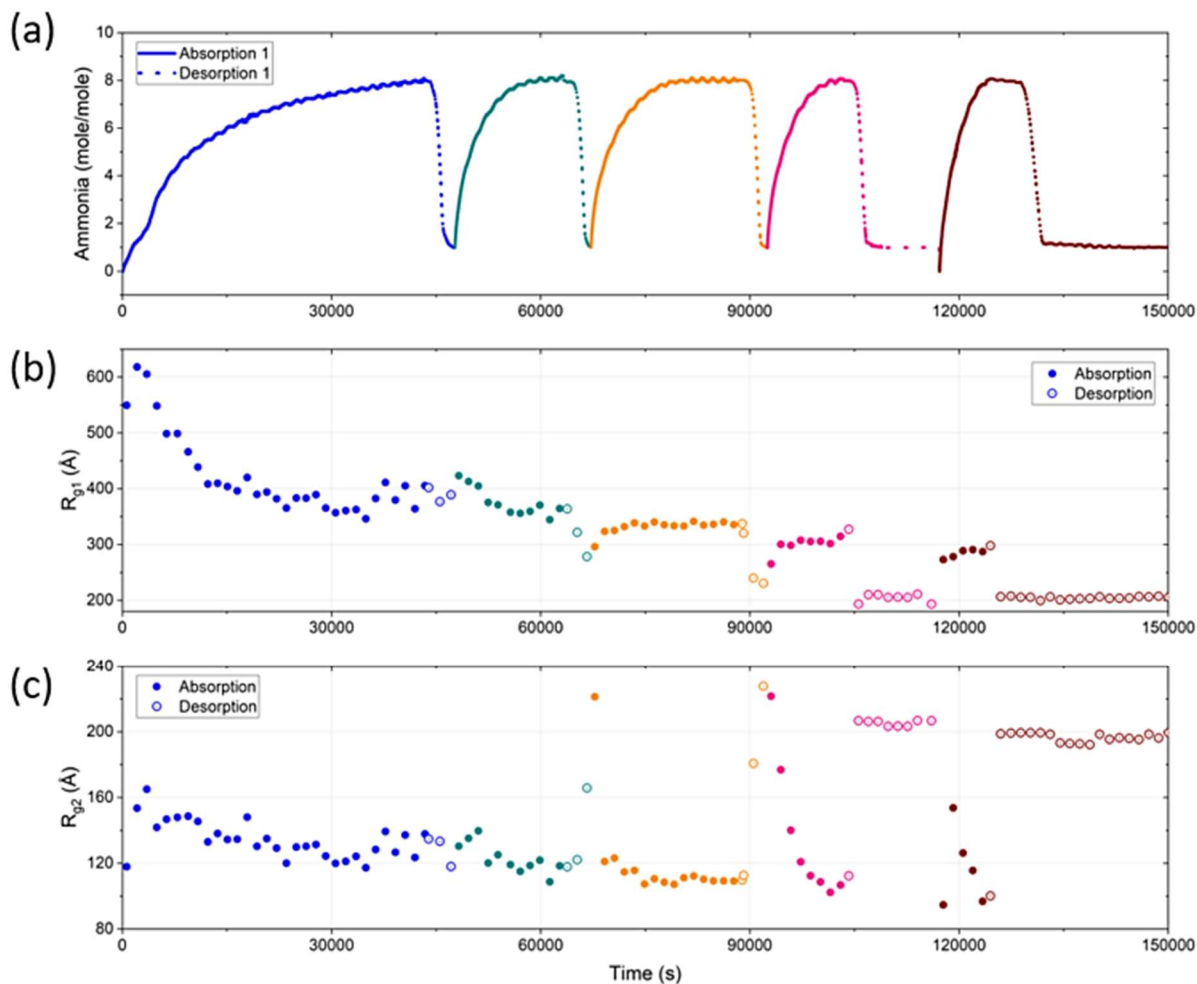
- and permeability of compact compound ammoniated salts in the adsorption/desorption process,” *Int. J. Therm. Sci.*, 2013.
- [15] L. Jiang, R. Z. Wang, Y. J. Lu, A. P. Roskilly, L. W. Wang, and K. Tang, “Enquête sur l’utilisation de chlorure de strontium composite conducteur thermique innovant pour les machines de refroidissement à sorption à l’ammoniac,” *Int. J. Refrig.*, vol. 85, pp. 157–166, 2018.
- [16] H. Jarimi, D. Aydin, Z. Yanan, G. Ozankaya, X. Chen, and S. Riffat, “Review on the recent progress of thermochemical materials and processes for solar thermal energy storage and industrial waste heat recovery,” *Int. J. Low-Carbon Technol.*, vol. 14, no. 1, pp. 44–69, 2019.
- [17] L. Jiang, L. W. Wang, Z. Q. Jin, B. Tian, and R. Z. Wang, “Permeability and Thermal Conductivity of Compact Adsorbent of Salts for Sorption Refrigeration,” *J. Heat Transfer*, 2012.
- [18] M. van der Pal and R. E. Critoph, “Performance of CaCl_2 -reactor for application in ammonia-salt based thermal transformers,” *Appl. Therm. Eng.*, vol. 126, pp. 518–524, 2017.
- [19] R. Olives and S. Mauran, “A highly conductive porous medium for solid-gas reactions: Effect of the dispersed phase on the thermal tortuosity,” *Transp. Porous Media*, vol. 43, no. 2, pp. 377–394, 2001.
- [20] C. Mauran, S., Lebrun, M., Prades, P., Moreau, M., Spinner, B. and Drapier, “No Title,” 777.537, 1991.
- [21] H. S. Jacobsen *et al.*, “Nanoscale structural characterization of $\text{Mg}(\text{NH}_3)_6\text{Cl}_2$ during NH_3 desorption: An in situ small angle X-ray scattering study,” *Chem. Phys. Lett.*, 2007.
- [22] J. S. Hummelshøj, R. Z. Sørensen, M. Y. Kustova, T. Johannessen, J. K. Nørskov, and C. H. Christensen, “Generation of nanopores during desorption of NH_3 from $\text{Mg}(\text{NH}_3)_6\text{Cl}_2$,” *J. Am. Chem. Soc.*, vol. 128, no. 1, pp. 16–17, 2006.
- [23] R. Z. Sørensen *et al.*, “Indirect, reversible high-density hydrogen storage in compact metal ammine salts,” *J. Am. Chem. Soc.*, vol. 130, no. 27, pp. 8660–8668, 2008.

- [24] S. M. Bennington, “Instruments on the ISIS second target station,” *Nucl. Instruments Methods Phys. Res. Sect. A Accel. Spectrometers, Detect. Assoc. Equip.*, vol. 600, no. 1, pp. 32–34, 2009.
- [25] O. Arnold *et al.*, “Mantid - Data analysis and visualization package for neutron scattering and μ SR experiments,” *Nucl. Instruments Methods Phys. Res. Sect. A Accel. Spectrometers, Detect. Assoc. Equip.*, vol. 764, pp. 156–166, 2014.
- [26] G. Beaucage and D. W. Schaefer, “Structural studies of complex systems using small-angle scattering: a unified Guinier/power-law approach,” *J. Non. Cryst. Solids*, vol. 172–174, no. PART 2, pp. 797–805, 1994.
- [27] G. Beaucage, H. K. Kammler, and S. E. Pratsinis, “Particle size distributions from small-angle scattering using global scattering functions,” *J. Appl. Crystallogr.*, vol. 37, no. 4, pp. 523–535, 2004.
- [28] G. Walker, Ed., *Solid-State Hydrogen Storage. Material and Chemistry*. Woohed Publishing Limited and CRC Press LLC, 2008.
- [29] A. Bialy, P. B. Jensen, D. Blanchard, T. Vegge, and U. J. Quaade, “Solid solution barium-strontium chlorides with tunable ammonia desorption properties and superior storage capacity,” *J. Solid State Chem.*, vol. 221, pp. 32–36, 2015.
- [30] S. Lysgaard, A. L. Ammitzbøll, R. E. Johnsen, P. Norby, U. J. Quaade, and T. Vegge, “Resolving the stability and structure of strontium chloride amines from equilibrium pressures, XRD and DFT,” *Int. J. Hydrogen Energy*, 2012.
- [31] L. Jiang, L. W. Wang, and R. Z. Wang, “Investigation on thermal conductive consolidated composite CaCl_2 for adsorption refrigeration,” 2014.
- [32] Y. Zhao *et al.*, “Expanded graphite – Paraffin composite phase change materials: Effect of particle size on the composite structure and properties,” *Appl. Therm. Eng.*, vol. 171, no. February, p. 115015, 2020.

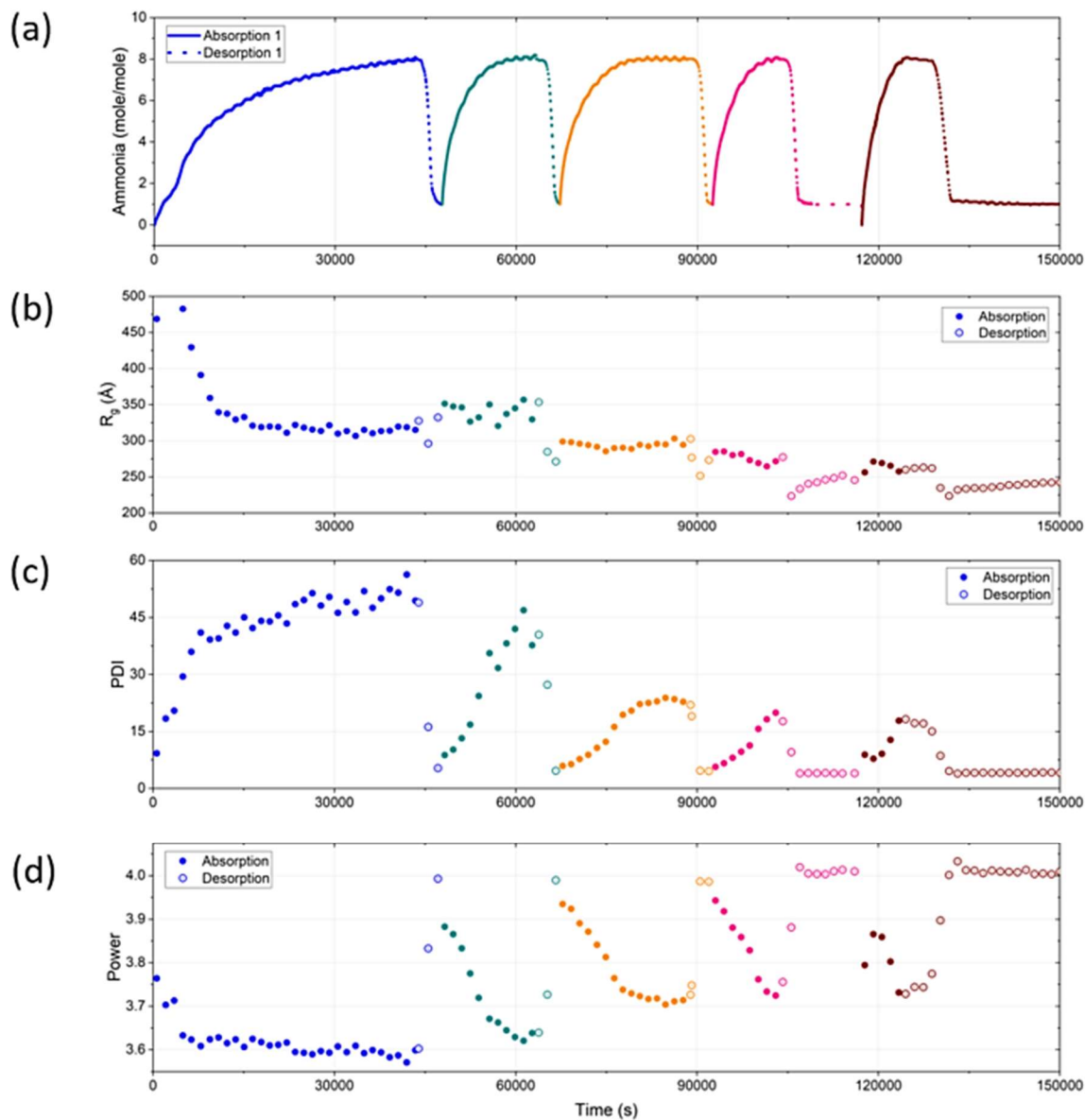
7.1.8 Supplementary information



S 1. Results from the fitting of 2-level model (Eq. 8) to ISIS data set processed using “pristine method”: (a) kinetic curves of consecutive absorptions (solid line) and desorptions (dotted line); (b) the evolution of PDI of SrCl₂ particles PDI₁ during 5 absorptions (filled circles) and 5 desorptions (hollow circles); (c) the evolution of PDI of pores PDI₂ inside salt particles during 5 absorptions (full circles) and 5 desorptions (hollow circles).

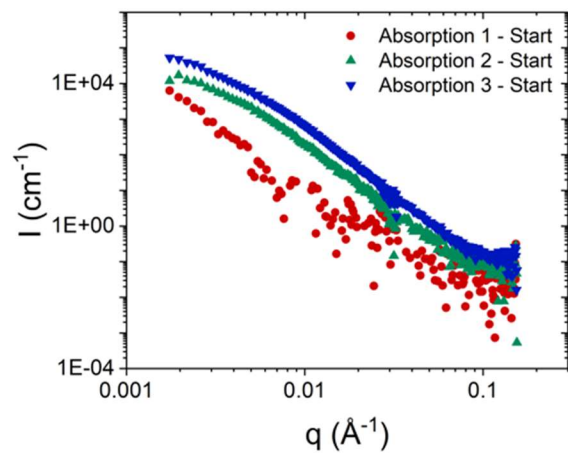


S 2. Results from the fitting of 2-level model (Eq. 8) to ISIS data set processed using “impregnated method”: (a) kinetic curves of consecutive absorptions (solid line) and desorptions (dotted line); (b) the evolution of radius of gyration of SrCl_2 particles during 5 absorptions (filled circles) and 5 desorptions (hollow circles); (c) the evolution of radius of gyration of pores inside salt particles during 5 absorptions (full circles) and 5 desorptions (hollow circles).

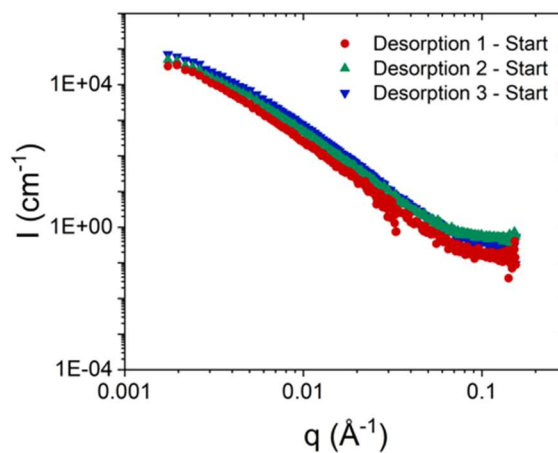


S 3. Results from the fitting of 1-level model (Eq. 9) to ISIS data set processed using “impregnated method”: (a) kinetic curves of consecutive absorptions (solid line) and desorptions (dotted line); the evolution of (b) R_g , (c) PDI, and (d) power during 5 absorptions (filled circles) and 5 desorptions (hollow circles).

(a)



(b)



S 4. NIST scattering patterns of composite materials treated with “pristine method” at the start of (a) three absorptions and (b) three desorptions.

7.2 Paper VIII: Numerical Design of a Reactor-Heat Exchanger Combined Unit for Ammonia-SrCl₂ Thermochemical Storage System

Saman N. Gunasekara¹, Stefano Soprani², Anastasiia Karabanova², Viktoria Martin¹ and Didier Blanchard²

¹ *Department of Energy Technology, KTH Royal Institute of Technology, Stockholm (Sweden).*

² *Department of Energy Conversion and Storage, Technical University of Denmark (DTU), Roskilde (Denmark).*

7.2.1 Abstract

This work presents the design of a reactor-heat exchanger combined unit using COMSOL transient simulations in 2D for a thermochemical storage (TCS) system of NH₃-SrCl₂ (absorption-desorption of SrCl₂·NH₃ and SrCl₂·8NH₃). TCS with NH₃-metal halide reactions is emerging, with many packed-bed reactors often incorporating salt with expanded graphite (EG) to improve thermal conductivity. Similarly, a packed-bed reactor is chosen here using SrCl₂-EG composite, for a reaction pressure of 8 bar, accommodating desorption above 82 °C and absorption below 79 °C. The aim here is to find a simple and cost-effective reactor-heat exchanger (HEX) combined unit to store 0.5 kWh heat (1.1 kg of SrCl₂·NH₃ forming 1.8 kg of SrCl₂·8NH₃). From several HEX configurations, the first configuration is modelled here. This contains three reaction media cylinders (a composite of 87.5% w/w of SrCl₂·8NH₃ in EG) sandwiching two units of tube-in-tube (TinT) HEXs. A stationary study for the heat transfer fluid (HTF) velocity analysis is coupled with a time-dependent study for the reaction phenomena, respectively for the salt-alone and salt-EG composite. For 15 hours reaction time, the reaction advancement (above 0.85) was enhanced significantly in the salt-EG composite, which was only above 0.55 for the salt-only case. The reaction progression is the slowest in the bottom of the innermost reaction media, where the HTF temperature is the lowest. Thus, an additional HEX unit along the center-axis of the reactor appears suitable to reduce the reaction time. As next, the effect of HEX thickness, number of TinT units, as well as other reactor-HEX configurations will be analyzed to choose the optimal setup.

7.2.2 Introduction

Thermal energy storage (TES) is a key technology in enabling more efficient and effective management of energy systems, by facilitating peak shaving and load shifting (Barzin, Chen, Young, & Farid, 2015), harvesting waste thermal energy (Chiu et al. 2016, Fujii et al. 2019), and renewable energy sources integration, particularly with solar energy (Frazzica and Freni 2017, Valverde et al. 2017). Thermochemical storage (TCS) systems storing the heats of reversible chemical reactions are an attractive type of TES, with, very high storage densities that offer temperature-flexible design. TCS systems are mainly two-fold based on the operating mechanism: using adsorption, or absorption. Among the absorption-based TCS systems involving non-water reaction pairs, many employ the reaction between NH_3 and a metal halide such as SrCl_2 , MnCl_2 , CaCl_2 , BaCl_2 , MgCl_2 , and NH_4Cl_2 (Erhard, Spindler, and Hahne 1998, Li et al. 2009, Bao et al. 2012, NagaMalleswara Rao, Ram Gopal, and Bhattacharyya 2013, Li, Wang, and Yan 2015, Kuwata et al. 2016, Soprani 2016, Li et al. 2016, Jiang et al. 2016, Mofidi and Udell 2017, Al-Zareer, Dincer, and Rosen 2017). As the thermal conductivity of these salts are considerably low, to improve heat transfer and thus reaction kinetics inside the reactors, incorporating the metal halide into e.g. expanded graphite (EG) matrices have also been analyzed (Bao et al. 2012, Li et al. 2009, Li et al. 2010, Jiang et al. 2016, Mofidi and Udell 2017). The evaluated reactor configurations include e.g. simple packed-beds with an axial flow of NH_3 in (NagaMalleswara Rao et al., 2013), (Li et al., 2016), a packed-bed using stainless-steel (SS) honeycomb disks containing salt with NH_3 flow through the disks (Soprani, 2016), a permeable piston-controlled packed-bed (Mofidi & Udell, 2017), among others. These heat exchanger (HEX) configurations so far are of simple construction, e.g.: an HTF bath where the reaction media pipes are immersed (Erhard, Spindler, and Hahne 1998); an annular jacket coupled with a center-line HEX (Bao et al. 2012, NagaMalleswara Rao, Ram Gopal, and Bhattacharyya 2013); a double-pipe HEX (Li, Wang, and Yan 2015, Li et al. 2016); an HTF bath adjacent to a packed bed of reactants (Kuwata et al. 2016); a W-tube HEX (Soprani 2016); as an annular HEX (Jiang et al. 2016) or a heating rod (Mofidi and Udell 2017) along the center-axis of packed bed.

With this background, the aim of this study is to present new knowledge on the combined reactor-HEXs configurations that significantly improve the heat transfer properties and reaction kinetics of NH_3 -metal halide TCS systems. Specifically, out of several new HEX configurations in combine with an EG matrix for better heat transfer will be explored through numerical simulations, with reaction advancement (a), as well as temperature and ammonia velocity evolution within the reactor as performance criteria. This is expected to achieved through transient 2D simulations with COMSOL Multiphysics (COMSOL Inc., 2019), for the NH_3 - SrCl_2

system involving the absorption/desorption between $\text{SrCl}_2 \cdot \text{NH}_3$ and $\text{SrCl}_2 \cdot 8\text{NH}_3$. With these COMSOL numerical simulations, it is here expected to determine the optimal reactor-heat exchanger configuration for improved reaction kinetics in the system, starting with the presented configuration and comparisons to be made with some other configurations in continuation.

7.2.3 Methodology

The considered chemical reaction of the system NH_3 - SrCl_2 is detailed in (eq. 1). This reaction has a reaction enthalpy (ΔH) and entropy (ΔS) of $41.4 \text{ kJ mol}_{\text{NH}_3}^{-1}$ and $230 \text{ J mol}^{-1} \text{ K}^{-1}$ (Lysgaard et al., 2012) respectively. For the targeted heat storage capacity of 0.5 kWh (i.e., 1800 kJ), the stoichiometric amount of NH_3 needed is 43.48 mol, to react with 6.21 mol (i.e., 1.09 kg) of $\text{SrCl}_2 \cdot \text{NH}_3(\text{s})$ to produce 6.21 mol (i.e., 1.83 kg) of $\text{SrCl}_2 \cdot 8\text{NH}_3(\text{s})$. The equilibrium conditions are chosen according to the Van't Hoff's equation (Soprani 2016, Lysgaard et al. 2012), at 8 bar pressure, with absorption at 79 °C and desorption at 82 °C.



7.2.3.1 Reactor sizing

To realize aim of finding an optimal reactor-HEX configuration, several specific configurations are chosen, with better HEX-configurations, e.g. as compared to state-of-the-art as summarized in section 7.2.2. From these chosen alternatives, as the first step, a cylindrical packed-bed reactor (vessel in SS 316) is considered herein. This is embedding $\text{SrCl}_2 \cdot 8\text{NH}_3$ -EG composite in three respective cylindrical blocks sandwiched between two annular tube-in-tube (TinT) heat exchangers in Al, as shown in Figure 1. These dimensions along the indicated parameters are explained and summarized in Table 1, which were calculated using the following data. The simplicity for cost-effective manufacturing of this combined unit has been a priority in choosing this particular reactor-HEXs configuration here. Thus, e.g. the reactor vessel diameter and thickness were chosen within existing commercial stainless steel pipe dimensions from (Damstahl, 1998) suitable for the system pressures (allowing a safety margin as well). The employed expanded graphite (EG) boards are from (SGL CARBON GmbH, 2019).

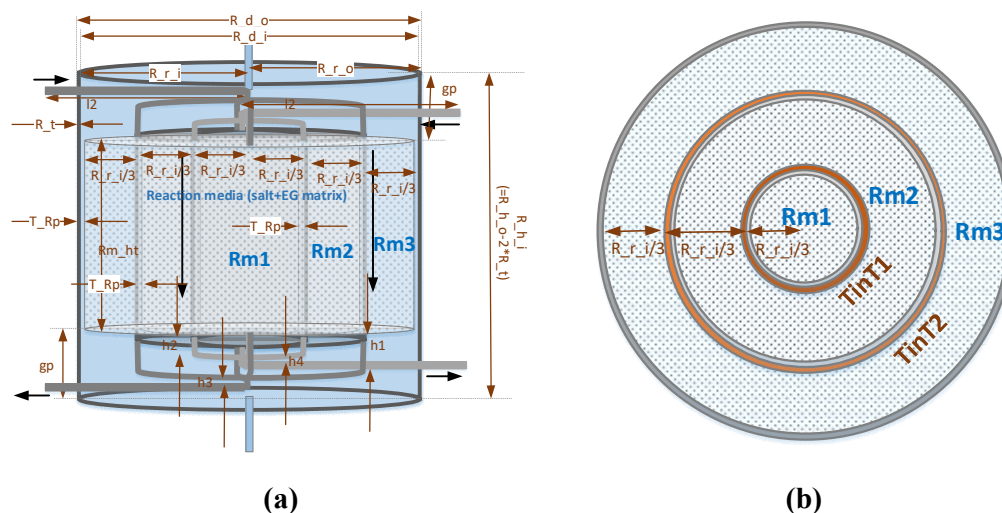


Figure 1. The chosen reactor-Heat Exchanger configuration and dimensions (Rm: reaction media, TinT: tube-in-tube HEX)

The required amount of reaction media (Rm), i.e., the salt-EG board composite, was calculated based on own experimental data (conducted at DTU) for salt compression tests into Sigratherm (SGL) EG boards L 20/1500 (SGL CARBON GmbH, 2019). The tests indicated that this SrCl_2 -EG composite (bulk density of 820 kg m^{-3}) can be made successfully to contain 79% w/w SrCl_2 (molar mass: $158.52 \text{ g mol}^{-1}$). After ammoniation tests, the density of this composite became 1380 kg m^{-3} , thus accounting for 87.5% w/w of $\text{SrCl}_2 \cdot 8\text{NH}_3$. With a bulk density of 1000 kg m^{-3} of $\text{SrCl}_2 \cdot 8\text{NH}_3$ (Soprani 2016, Lysgaard et al. 2012), the required EG board volume of L 20/1500 type is thus found to be 0.00152 m^3 (for 0.5 kWh energy storage capacity). To accommodate any compacting inhomogeneity, it was decided to use 30% more volume of the board, thus accounting for 0.00198 m^3 ($\sim 2 \text{ l}$). As during the experiments, neither the salt compacting nor ammoniation expanded the volume of the EG board from the original size, this volume corresponds to the total volume of the reaction media, i.e., the salt-EG composite. There, the reaction media height was chosen iteratively to achieve a reaction media volume to match this 130% of the EG volume. This chosen height results in real reaction media volume of 0.00210 m^3 , which is therefore sufficient (as it is greater than 0.00198 m^3). The volume fraction of $\text{SrCl}_2 \cdot 8\text{NH}_3$ and EG in this media is 0.952 and 0.0476 (excluding pore volume), respectively.

Table 1. The chosen reactor-heat exchanger dimensions

Parameter	Value	Unit	Description
R_r_o	84.15	mm	Reactor external radius (Damstahl, 1998). $R_{d_o}=2 \cdot R_{r_o}$
R_t	2.6	mm	Reactor wall thickness (Damstahl, 1998).
R_r_i	81.55	mm	Reactor internal radius (Damstahl, 1998). $R_{d_i}=2 \cdot R_{r_i}$
HEX_d_i	4	mm	Heat exchanger tubing internal diameter (Swagelok, 2019)
HEX_d_o	6	mm	Heat exchanger tubing external diameter (Swagelok, 2019)
l2	94.15	mm	Length of the HEX tube inlet and outlet horizontal pieces, assumed,
T Rp	0	mm	The gaps between each reactor component (e.g. reaction media and TinT walls), assumed negligible.
TinT1_r	27.18	mm	Tube-in-in-tube 1 (inner) HEX radius, to the center of the HEX annulus
TinT2_r	54.37	mm	Tube-in-in-tube 2 (outer) HEX radius, to the center of the HEX annulus
TinT_t	2.6	mm	Wall thickness of each TinT cylindrical tube, assumed = R_t
HEX_t	5	mm	The effective HEX thickness (for heat transfer fluid flow) of each TinT
TinT1_ro	37.38	mm	The outer radius (including HEX walls and HEX_t) of TinT1 cylinder
TinT1_ri	27.2	mm	The inner radius (excluding HEX walls and HEX_t) of TinT1 cylinder
TinT2_ro	64.57	mm	The outer radius (including HEX walls and HEX_t) of TinT2 cylinder
TinT2_ri	54.4	mm	The inner radius (excluding HEX walls and HEX_t) of TinT2 cylinder
Rm1_r	27.2	mm	The radius of the inner reaction media cylinder
Rm2_r	54.4	mm	The outer radius of the middle reaction media cylinder
Rm3_r	81.6	mm	The outer radius of the outer reaction media cylinder
Rm_v_1.3	0.00198	m ³	Total volume of reaction media required for 1.3% EG volume (1.98 l)
Rm_ht	140.0	mm	Reaction media height, iteratively calculated to obtain the required reaction media volume
HEX_h	140.0	mm	Assumed as the same as Rm_ht
Rm1_v	0.000325	m ³	The volume of inner reaction media cylinder
Rm2_v	0.000685	m ³	The volume of middle reaction media cylinder
Rm3_v	0.001091	m ³	The volume of outer reaction media cylinder
Rm_v_calc	0.002102	m ³	The total real volume of the reaction media (=Rm1_v+ Rm2_v+ Rm3_v)
h1	105.0	mm	Heights of the vertical parts of the HEX inlet and outlets to/from TinT2
h2	35.0	mm	Heights of the vertical parts of the HEX inlet and outlets to/from TinT1
h3, h4	25.0	mm	Heights of the vertical HEX inlet/outlet connectors to/from TinT1 and TinT2
Gp	80	mm	Empty reaction vessel spaces above and below reaction media, assumed
R_hi	305.2	mm	Total reactor height, inner
R_ho	310.4	mm	Total reactor height, outer
R_Vt	0.006905	m ³	Total reactor volume (6.91 l)

7.2.3.2 Reactor-heat exchanger numerical simulation using COMSOL

The transient simulations using COMSOL (finite element modelling), version 5.4, are performed on the reactor, considering only the active parts of the reactor: the three reaction media cylinders, the two TinT units and the reactor vessel just constrained to their heights. For computational simplicity, this reactor drawn in 3D as shown in Figure 2 (a) and (b), was then modelled in 2D for an axisymmetric cross-section shown in Figure 2 (c), by-default halved by COMSOL along the axis as in Figure 2 (d). In the present work, only desorption is modelled, where absorption is expected to be studied eventually. In Figure 2, the fluid inlets and outlets are indicated using arrows, where red represents the heat transfer fluid (HTF) and blue represents NH₃. Here only the NH₃ direction during desorption is shown, which originates within the reaction media and flows

out of it as shown, from the top. For the absorption case, this NH_3 flow will be reversed, which will then flow into the reaction media from the bottom.

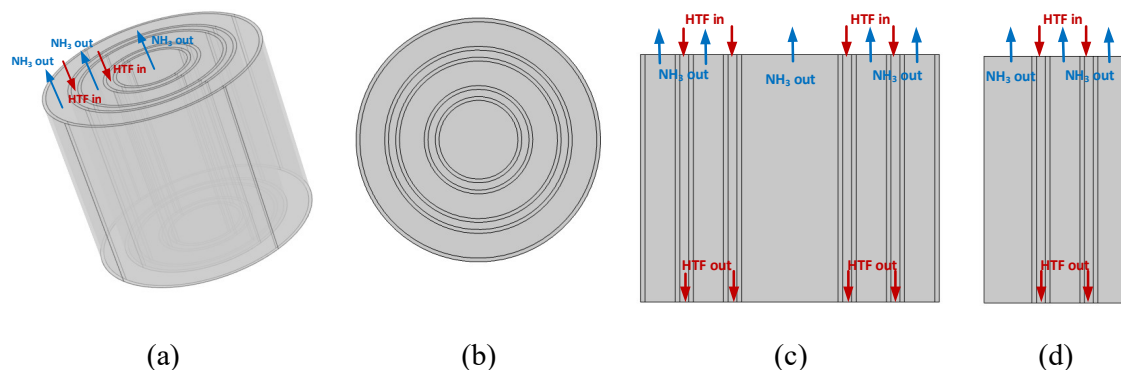


Figure 2. The reactor-HEX geometry modelled in COMSOL: (a) the 3D geometry in full, (b) from the top, (c) the 2D axisymmetric cross-section of this 3D geometry, and (d) a half (divided along the axis) of this 2D geometry.

The transient simulations are conducted through a stationary study for the HTF flow inside the HEXs and a time-dependent study on the reaction, heat transfer and gas flow phenomena. These are performed considering the desorption case, so far, for an HTF inlet temperature of $90\text{ }^{\circ}\text{C}$. The flow-field obtained from the stationary study (*spf.U*) is used as an input to the time-dependent study. The HTF considered is a silicon oil (Therm 180 (Lauda, 2019)) circulated in the HEXs using Lauda ECO Gold thermostat baths with an average volumetric flow rate of 0.183 l s^{-1} (a half of the maximum of 0.37 l s^{-1}). Therefore, the HTF flow regime is turbulent (with Reynolds numbers considerably above 2900) already at the inlets of each TinT units, with average and maximum velocities of 354 m s^{-1} and 709 m s^{-1} (TinT1, 517 mm^3 cross-section) and 192 m s^{-1} and 385 m s^{-1} (TinT2, 953 mm^3 cross-section). Thus, the stationary study is constructed using the *Turbulent flow module* ($k\text{-}\epsilon$ type) in COMSOL for the HTF flow within the HEX units.

In the time-dependent study, the involved physics (i.e., chemical kinetics and heat and mass transfer) of the reaction domains are solved in COMSOL, employing partial differential equations (PDEs), as shown in (eq. 2)-(eq. 7), using the respective physics modules: *heat transfer in porous media*, *domain ODEs and DAEs*, and *free and porous media flow*. In particular, these describe: heat transfer in all domains beside the salt bed (eq. 2), heat transfer in the porous salt-ammonia media (eq. 3), the chemical reaction rate (eq. 4), fluid flow in the salt-Al mesh porous media ((eq. 5) and (eq. 6)), and the fluid flow of the desorbed NH_3 gas (eq. 7). In (eq. 2), ρ is the density, c_p is the specific heat capacity at constant pressure, k is the thermal conductivity, T is the temperature and \mathbf{u} is the flow field, equal to 0 in the solid domains. In (eq. 3) and (eq. 4), $da(t)/dt$ is the reaction advancement rate, N_s is the number of stoichiometric amount of reacting NH_3 (mol/volume), ΔH

is the reaction enthalpy, k_{0a} and k_{0d} are the respective Arrhenius pre-exponential factors for absorption and desorption, E_a and E_d are the respective absorption and desorption activation energies, $a(t)$ is the reaction advancement, m_a and m_d are the respective kinetic coefficients of absorption and desorption, p_{eq} is the equilibrium pressure, and p is the reactor pressure. In (eq. 5) and (eq. 6), ε is the porosity of the salt, ρ is NH_3 density, Q_{br} is the mass of source/sink, MW_{NH_3} is NH_3 molecular weight, μ is the dynamic viscosity of NH_3 , k_D is the hydraulic permeability of salt, β_F is the Forcheimer drag factor, and F is the domain forces (neglected). In (eq. 7), ρ is NH_3 density, μ is the dynamic viscosity of NH_3 , p is the pressure, \mathbf{u} is the velocity field, F is the forces that NH_3 gas is subject to (which are neglected). The hydraulic permeability of the salt k_D is calculated using the Carman-Kozeny equation as shown in (eq. 8), where the salt particles are assumed spherical with a diameter d_p of 0.5 mm.

$$\rho c_p \frac{\partial T}{\partial t} + \rho c_p \mathbf{u} \cdot \nabla T + \nabla(-k \nabla T) = 0 \quad (\text{eq. 2})$$

$$(\rho c_p)_{eff} \frac{\partial T}{\partial t} + \rho c_p \mathbf{u} \cdot \nabla T + \nabla(-k_{eff} \nabla T) \pm \frac{da(t)}{dt} N_s \cdot \Delta H_{des} = 0 \quad (\text{eq. 3})$$

$$\frac{da(t)}{dt} = k_{0a,d} \exp\left(-\frac{E_{a,d}}{RT}\right) (1 - a(t))^{m_{a,d}} \left(\frac{p_{eq} - p}{p_{eq}}\right) \quad (\text{eq. 4})$$

$$\frac{\partial \varepsilon \rho}{\partial t} + \nabla \cdot (\rho \mathbf{u}) = Q_{br}; \quad Q_{br} = \pm \frac{da(t)}{dt} N_s \cdot MW_{\text{NH}_3} \quad (\text{eq. 5})$$

$$\rho \frac{\partial \mathbf{u}}{\partial t} = \nabla \cdot \left[-p \mathbf{I} + \frac{\mu}{\varepsilon} (\nabla \mathbf{u} + (\nabla \mathbf{u})^T) - \frac{2\mu}{3\varepsilon} (\nabla \cdot \mathbf{u}) \mathbf{I} \right] - \left(\frac{\mu}{k_D} + \beta_F |\mathbf{u}| + \frac{Q_{br}}{\varepsilon^2} \right) \mathbf{u} + \mathbf{F} \quad (\text{eq. 6})$$

$$\rho \frac{\partial \mathbf{u}}{\partial t} + \rho (\mathbf{u} \cdot \nabla) \mathbf{u} = \nabla \cdot \left[-p \mathbf{I} + \mu (\nabla \mathbf{u} + (\nabla \mathbf{u})^T) - \frac{2}{3} \mu (\nabla \cdot \mathbf{u}) \mathbf{I} \right] + \mathbf{F}; \quad \frac{\partial \rho}{\partial t} + \nabla \cdot (\rho \mathbf{u}) = 0 \quad (\text{eq. 7})$$

$$k_D = \frac{\varepsilon^3}{180(1 - \varepsilon)^2} d_p^2 \quad (\text{eq. 8})$$

A time step of 30 seconds and a total simulation time of 15 hours are used. These simulations, starting with coarse mesh sizing, were repeated for normal and fine mesh sizes, while obtaining consistent results. Therefore, fine mesh size is chosen as a representative enough mesh size. The porosity ε of the salt ($\text{SrCl}_2 \cdot 8\text{NH}_3$) alone is used as 0.28264 (for its true and bulk densities respectively of 1394 kg m^{-3} and 1000 kg m^{-3} (Soprani 2016, Lysgaard et al. 2012)). Whereas, the porosity ε of the $\text{SrCl}_2 \cdot 8\text{NH}_3$ -EG composite is used as 0.30213 (for the density of graphite 2260 kg m^{-3} (Graphite, 2015) and the density of graphite in the EG board 75 kg m^{-3} (SGL CARBON GmbH, 2019)). The corresponding volume fractions of $\text{SrCl}_2 \cdot 8\text{NH}_3$ and EG in the composite

(excluding the pore-volume) are thus 0.952 and 0.0476. The effective thermal conductivity of the composite was calculated as a volume average of the thermal conductivity of each material. Thermal conductivity of each salt was approximated to $1.1 \text{ W m}^{-1} \text{ K}^{-1}$ as per available data from literature (Jiang et al. 2013). The in-plane and through-plane thermal conductivities of graphite of the EG board were found to be respectively $26 \text{ W m}^{-1} \text{ K}^{-1}$ and $10.5 \text{ W m}^{-1} \text{ K}^{-1}$ by linear projection of the data from (SGL CARBON GmbH, 2019) for the compacted new density of EG: 172 kg m^{-3} (for 21 w/w% graphite in the composite with bulk density of 820 kg m^{-3}). The main simulation was performed considering the salt-EG composite. To analyze the influence of the EG in the heat transfer enhancement, a simulation trial was, in-addition, conducted for the case of salt-only, thus excluding EG (thus considering that the entire volume of 0.00210 m^3 to be filled with $\text{SrCl}_2 \cdot 8\text{NH}_3$ with a porosity ε of 0.30213). The property data of Al, SS and HTF Therm 180 were used from COMSOL standard materials library, assuming bulk solid Al, SS AISI 4340.1 and Silicon (liquid).

The initial temperature of the HTF fluid is set to $90 \text{ }^\circ\text{C}$, while the initial temperature of the reaction media, HEX Al walls, and the SS reactor walls are also assumed to be at room temperature ($25 \text{ }^\circ\text{C}$). The initial pressure of the reactor is set to be 8 bar, and of the HEX is set to be 1 bar. The reaction advancement a , which is defined as zero for the condition where the salt is fully saturated with NH_3 (which should, upon complete desorption reach 1). The initial velocity field of NH_3 is assumed null (i.e, 0 m s^{-1}), while the flow rate of the HTF at the HEX inlet is considered to be 0.183 l s^{-1} . The velocity at the walls was considered null and the reactor casing to be adiabatic.

7.2.4 Results and discussion

The numerical simulation results obtained of the TCS reactor for desorption during 15 hours are discussed in this section. Indeed, a combined study of both desorption and absorption is important to draw general conclusions on reaction kinetics and, mass and heat transfer, and therefore absorption analysis will be a key future step. In the present desorption modelling, the stationary study yielded the velocity profile of the HTF inside the two HEX units, as detailed in section 7.2.4.1. By employing the resultant HTF velocity profile into the time-dependent study, the reaction progression behavior within this TinT HEXs-based reactor configuration is analyzed within the considered 15 hours of reaction time, along the temperature evolution, velocity of NH_3 evolution and reaction advancement in sections 7.2.4.2-7.2.4.4. These results are shown for several chosen time steps as examples at 0 s, 900 s, 1800 s, 3600 s (1 h), 10800 s (3 h), 18000 s (5 h), 36000 s (10 h) and 54000 s (15 h).

7.2.4.1 Heat exchanger velocity profile The velocity profiles of the HTF (in the turbulent regime) within the two TinT HEXs found through the stationary study are shown in Figure 3; in (a) on the chosen 2D cross-section and in (b) on a projection of this cross-section into two thirds of the 3D reactor. The flow direction is identified with black and red arrows, respectively in the 2D and the 3D profiles. The velocity of the HTF lies within a range of 0.17-0.27 m s⁻¹, as results indicate. The specific turbulent flow profile from this stationary study $spf.U$ as in Figure 3 is fed into the consecutive time-dependent study of the reaction.

7.2.4.2 Reactor temperature profiles

The temperature evolution inside the considered part of the reactor during desorption is shown at the chosen example time-steps in-terms of isothermal contours in the 2D cross-section as in Figure 4, and in-terms of temperature regions in the 3D projection as in Figure 5. By the end of the total 15 hours of reaction time, the considered reactor+HEX unit has reached temperatures of 88.80-89.97 °C, implying that the system has reached nearly isothermal conditions (for the employed HTF inlet temperature of 90 °C). As seen, the temperature inside the reactor evolves faster and closer to the HEX walls, and more so at the HTF inlets. With time, the temperature profile in the reactor becomes somewhat asymmetric, evolving into increasingly higher temperature regions at the outer reaction media cylinders as compared to the innermost reaction media cylinder. This can be reasoned with the larger thickness (i.e., the distance heat transfer needs to occur) of the innermost reaction media cylinder and which therefore has higher thermal mass as compared to the outer reaction cylinders.

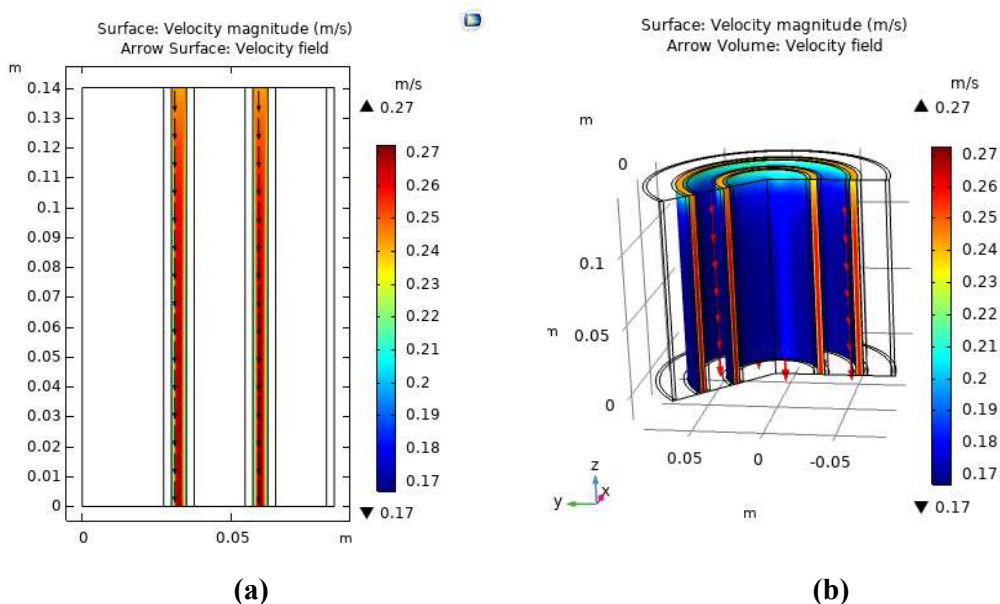


Figure 3. The velocity profiles of the HTF (a) in 2 D (b) in 3D (the arrows indicate the flow direction)

7.2.4.3 Reactor – NH₃ flow during desorption

NH₃ flow velocity inside the reactor during desorption propagation can be seen in Figure 6, with the flow direction identified with red arrows located where NH₃ leaves the reaction media. The flow velocity of NH₃ varies in each reaction media region, however, as can be seen, lies within a range of 0 m s⁻¹ to a maximum of 1.85×10^{-3} m s⁻¹ during the considered reaction period of 15 hours. The 0 m s⁻¹ occurs at initial conditions as well as in the regions that have completely desorbed with time. As also can be seen, the velocity evolution is also dominating at the HTF inlet side (top of the reactor), while the two outer-cylinders of reaction media undergo more desorption as compared to the innermost reaction media. These results imply that e.g. an additional HEX tube that could run along the center axis of the reactor could significantly improve the reaction rate, particularly within the innermost reaction media cylinder.

7.2.4.4 Reaction advancement

The reaction advancement (a) is shown along the employed 15 hour time-period in a 3D projection of the reactor in Figure 7. Analogous to the temperature and NH₃ velocity evolution within the reactor, the reaction (desorption in this study) advancement also occurs more at outer reaction cylinders, with somewhat lesser within the innermost reaction media cylinder. These results also therefore confirm the significance of an additional HEX component along e.g. the center-axis of the reactor. The reaction advancement has reached 0.85 or above in the entirety of

reaction media during these 15 hours. For 100% desorption (i.e., to reach $a=1$ in the entirety of reaction media), longer time will be required, as reaction will slow-down with further advancement. This is however excluded herein, as the main purpose of the study is to analyze the effects of the HEX geometry and the EG in improving reaction kinetics.

The simulations conducted for the case of using salt-alone (i.e., no EG) yielded a reaction advancement of only 0.55 and above at the end of the total 15 hours' reaction time, which is therefore slightly lower than the case with EG. These final reaction advancements are compared in Figure 8, respectively for the composite with EG (a) and without EG (i.e., purely salt) (b). Indeed, even if combining the salt with EG enhances heat transfer, it the same time creates compromises in either the available storage capacity of the TCS or the mass transfer rate as either the amount of salt or the porosity decreases for a given reactor volume. With this type of numerical simulations as in this work, finding the best compromise between heat and mass transfer can be effectively identified.

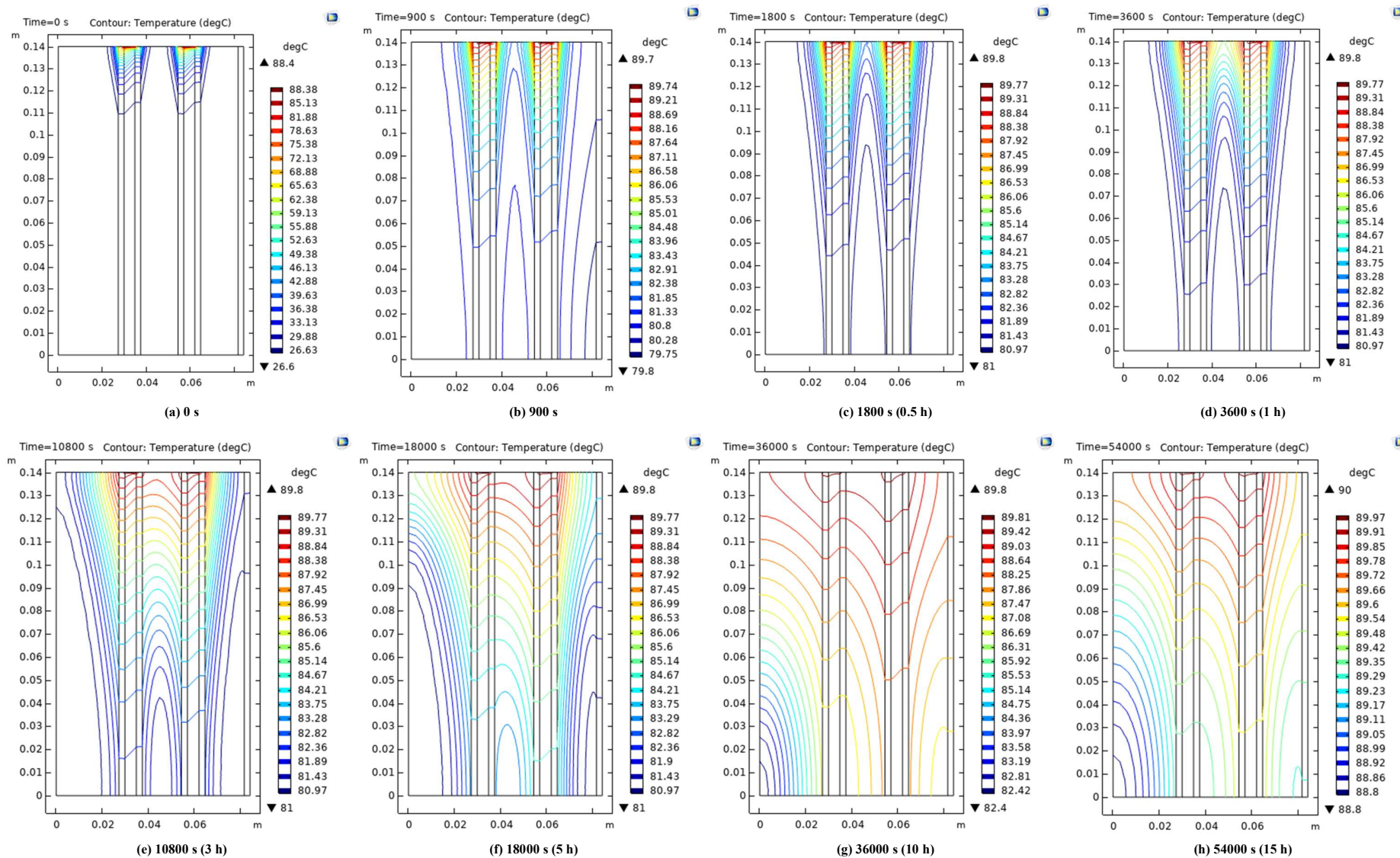


Figure 4. The temperature evolution in the reactor during desorption in terms of isothermal contours from 0-54000 s (15 hours), in (a)-(h)

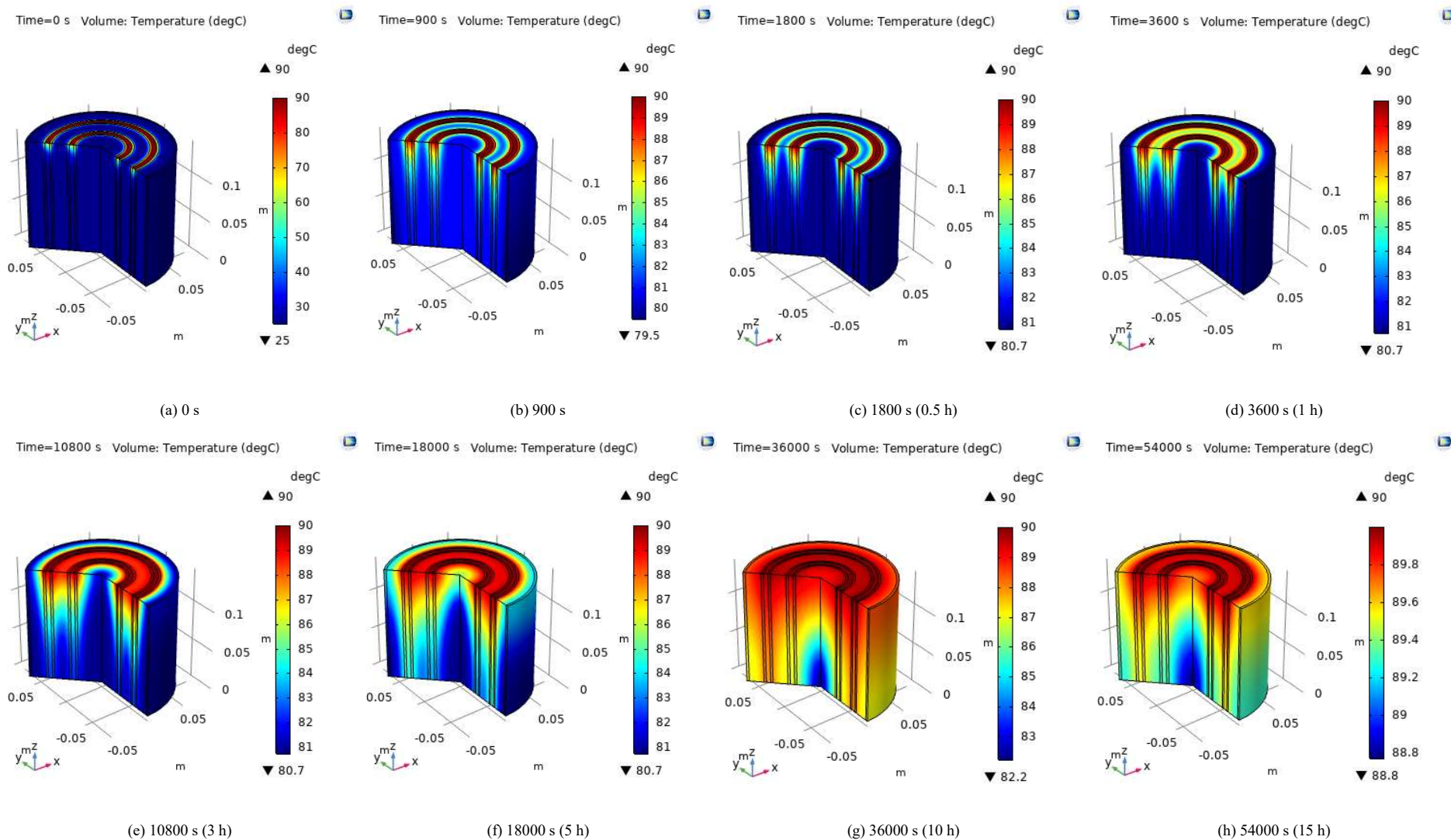


Figure 5. The temperature evolution in the reactor during desorption in-terms of temperature regions projected in 3D, from 0--54000 s (15 hours), in (a)-(h)

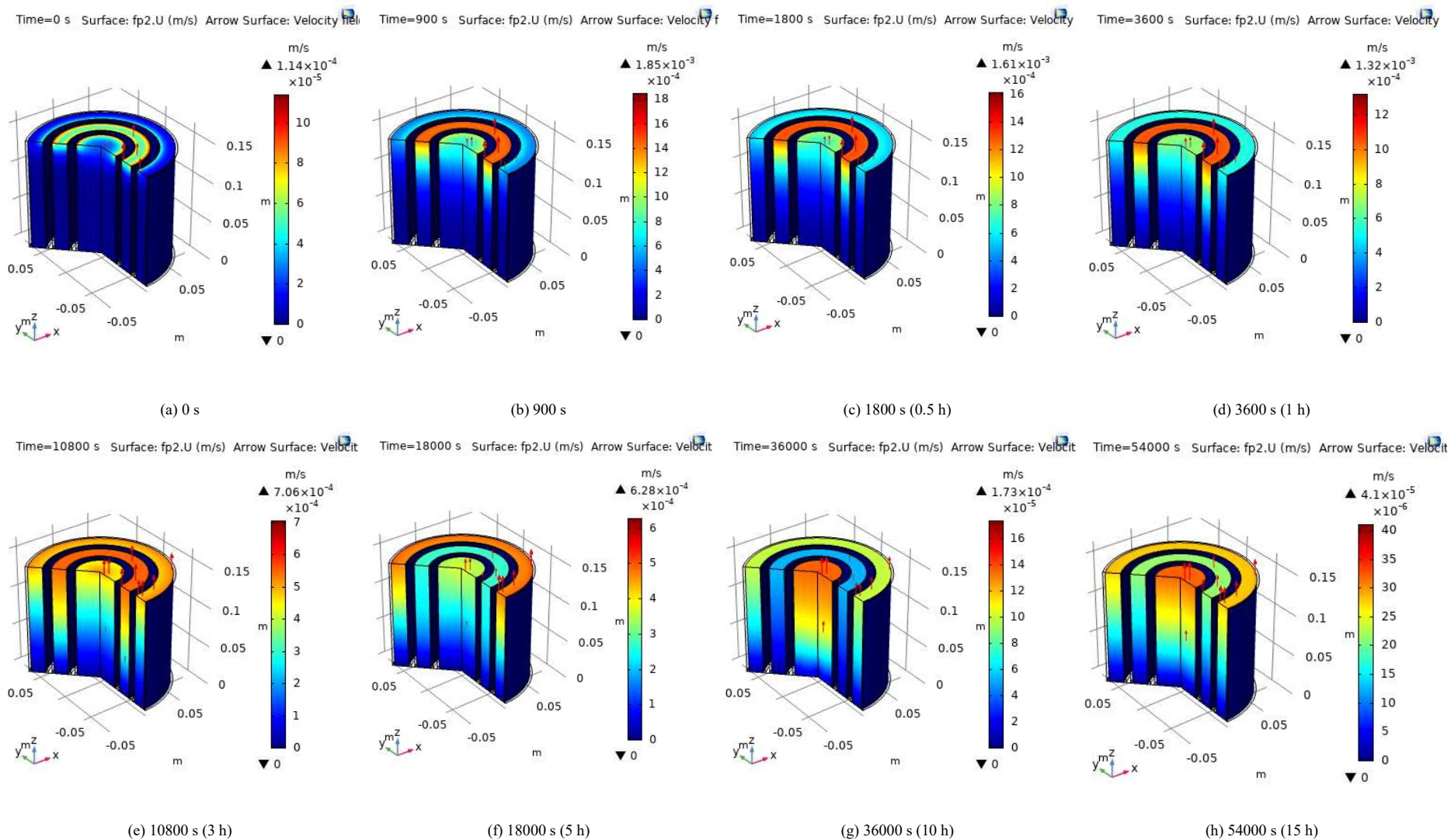


Figure 6. The velocity evolution of NH_3 produced during desorption in the reactor projected in 3D, from 0–54000 s (15 hours), in (a)–(h)

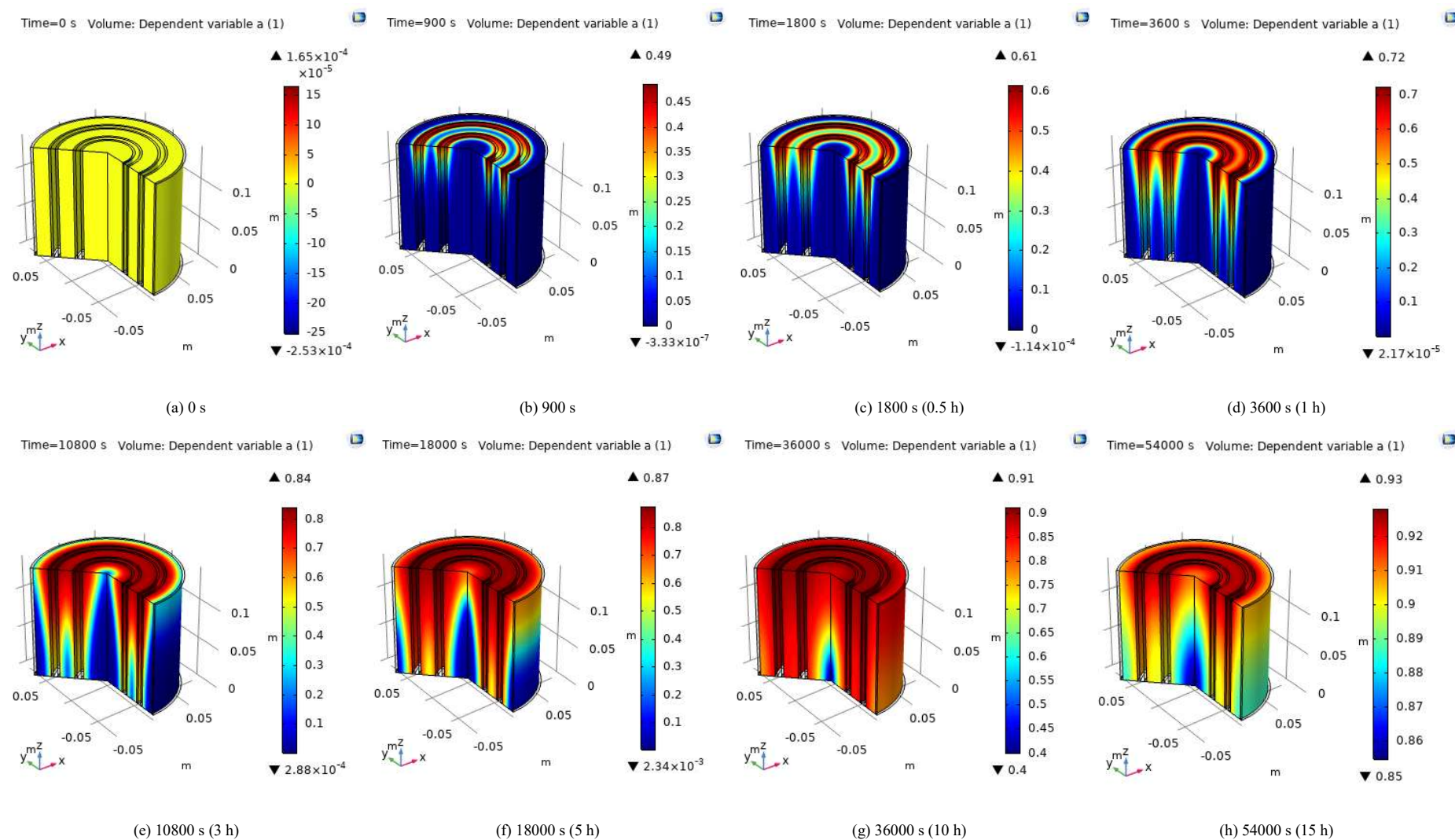


Figure 7. The reaction advancement in desorption projected in 3D, from 0--54000 s (15 hours), in (a)-(h)

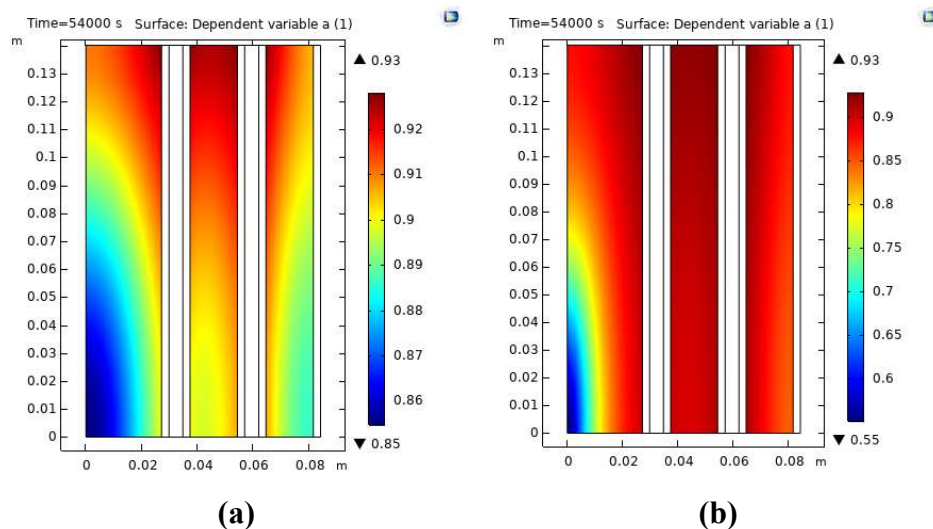


Figure 8. The reaction advancements at the end of total 15 hours, for (a) with EG and (b) without EG

7.2.5 Concluding remarks

Numerical modeling of a reactor-heat exchanger combined unit of a TCS system in COMSOL in 2D, for the reversible chemical reaction between $\text{SrCl}_2 \cdot \text{NH}_3$ and $\text{SrCl}_2 \cdot 8\text{NH}_3$ is conducted with the aim of finding an optimal configuration of a reactor-HEX unit. The 2 l (effective volume) packed-bed reactor is designed to store 0.5 kWh of heat above $\sim 81^\circ\text{C}$ at or below 8 bar during desorption. The transient simulations in COMSOL results describe the heat and mass transfer, reaction kinetics and fluid flow phenomena for this reactor employing a composite of $\text{SrCl}_2 \cdot 8\text{NH}_3$ and EG (with volume fractions 0.665 and 0.0332) combined with two TinT HEX sections to provide the required heat of desorption. The employed volume fraction of graphite manages to improve the reaction advancement significantly. For instance, for a total of 15 hours reaction time, the reaction advancement for the salt-EG composite reaches above 0.85 whereas when the salt-alone was used (i.e., excluding EG) this is only above 0.55. The two TinT units contribute to reasonable heat transfer within the reactor, while, the results imply that if an additional unit of HEX is installed along the center-axis of the reactor, the reaction time can be further reduced. This work exemplifies the effectiveness of this new and simple HEX-configuration in improving the reaction kinetics, accommodating better heat exchange between the HTF and reaction media, as compared to the current state-of-the-art of HEXs for NH_3 -metal halide reaction-based TCS systems. As future

work, the effects of effective HEX thickness and number of TinT units (including one along the center-axis of the reactor), reversing the HTF flow direction, as well as the other chosen reactor+HEX configurations will be analyzed through similar numerical simulations. Thereby, the optimal reactor-HEX configuration will be chosen to construct in a bench-scale TCS system at KTH. This is expected to work as a test-bed for the TCS technology using this chemical reaction system, for different operating conditions including solar-thermal heat storage.

7.2.6 Acknowledgments

The authors acknowledge Nordforsk for funding this research project: Neutrons for Heat Storage (NHS).

7.2.7 References

Al-Zareer, M., Dincer, I., & Rosen, M. A. (2017). Heat Transfer and Thermodynamic Analyses of a Novel Solid-Gas Thermochemical Strontium Chloride-Ammonia Thermal Energy Storage System. *Journal of Heat Transfer*, 140(February), 1–17.

<https://doi.org/10.1115/1.4037534>

Bao, H. S., Wang, R. Z., Oliveira, R. G., & Li, T. X. (2012). Resorption system for cold storage and long-distance refrigeration. *Applied Energy*, 93, 479–487.

<https://doi.org/10.1016/j.apenergy.2011.12.022>

Barzin, R., Chen, J. J. J., Young, B. R., & Farid, M. M. (2015). Peak load shifting with energy storage and price-based control system. *Energy*, 92, 505–514.

<https://doi.org/10.1016/j.energy.2015.05.144>

Chiu, J. N. W., Castro Flores, J., Martin, V., & Lacarrière, B. (2016). Industrial surplus heat transportation for use in district heating. *Energy*, 110, 139–147.

<https://doi.org/10.1016/j.energy.2016.05.003>

COMSOL Inc. (2019). COMSOL-Multiphysics simulation just got better, faster, more accessible. Retrieved March 21, 2019, from <https://www.comsol.se/>

Damstahl. (1998). *Driftstryck för rostfria rör*. Retrieved from

<https://www.damstahl.se/globalassets/downloads-130x185/sverige/downloads/driftstryck->

for-rostfria-ror..pdf

- Erhard, A., Spindler, K., & Hahne, E. (1998). Test and simulation of a solar powered solid sorption cooling machine. *International Journal of Refrigeration*, 21(2), 133–141. [https://doi.org/10.1016/S0140-7007\(97\)00065-0](https://doi.org/10.1016/S0140-7007(97)00065-0)
- Frazzica, A., & Freni, A. (2017). Adsorbent working pairs for solar thermal energy storage in buildings. *Renewable Energy*, 110, 87–94. <https://doi.org/10.1016/j.renene.2016.09.047>
- Fujii, S., Horie, N., Nakaibayashi, K., Kanematsu, Y., Kikuchi, Y., & Nakagaki, T. (2019). Design of zeolite boiler in thermochemical energy storage and transport system utilizing unused heat from sugar mill. *Applied Energy*, 238, 561–571. <https://doi.org/10.1016/j.apenergy.2019.01.104>
- Graphite, P. (2015). Properties and Characteristics. In *Properties and Characteristics of Graphite- For industrial applications*. Retrieved from <http://poco.com/Portals/0/Literature/Semiconductor/IND-109441-0115.pdf>
- Jiang, L., Wang, L. W., Jin, Z. Q., Wang, R. Z., & Dai, Y. J. (2013). Effective thermal conductivity and permeability of compact compound ammoniated salts in the adsorption/desorption process. *International Journal of Thermal Sciences*. <https://doi.org/10.1016/j.ijthermalsci.2013.03.017>
- Jiang, L., Wang, L. W., Liu, C. Z., & Wang, R. Z. (2016). Experimental study on a resorption system for power and refrigeration cogeneration. *Energy*, 97, 182–190. <https://doi.org/10.1016/j.energy.2015.12.128>
- Kuwata, K., Masuda, S., Kobayashi, N., Fuse, T., & Okamura, T. (2016). Thermochemical Heat Storage Performance in the Gas/Liquid-Solid Reactions of SrCl₂ with NH₃. *Natural Resources*, 07(11), 655–665. <https://doi.org/10.4236/nr.2016.711052>
- Lauda. (2019). *LAUDA Heat transfer liquids - Thermostats, Circulation chillers, Water baths*. Lauda-Koenigshofen.
- Li, T. X., Wang, R. Z., Kiplagat, J. K., & Chen, H. (2010). Experimental study and comparison of thermochemical resorption refrigeration cycle and adsorption refrigeration cycle. *Chemical Engineering Science*, 65(14), 4222–4230.
-

<https://doi.org/10.1016/j.ces.2010.04.022>

- Li, T. X., Wang, R. Z., Wang, L. W., & Kiplagat, J. K. (2009). Study on the heat transfer and sorption characteristics of a consolidated composite sorbent for solar-powered thermochemical cooling systems. *Solar Energy*, *83*(9), 1742–1755.
<https://doi.org/10.1016/j.solener.2009.06.013>
- Li, T. X., Wang, R. Z., & Yan, T. (2015). Solid-gas thermochemical sorption thermal battery for solar cooling and heating energy storage and heat transformer. *Energy*, *84*, 745–758.
<https://doi.org/10.1016/j.energy.2015.03.040>
- Li, T. X., Xu, J. X., Yan, T., & Wang, R. Z. (2016). Development of sorption thermal battery for low-grade waste heat recovery and combined cold and heat energy storage. *Energy*, *107*, 347–359. <https://doi.org/10.1016/j.energy.2016.03.126>
- Lysgaard, S., Ammitzbøll, A. L., Johnsen, R. E., Norby, P., Quaade, U. J., & Vegge, T. (2012). Resolving the stability and structure of strontium chloride amines from equilibrium pressures, XRD and DFT. *International Journal of Hydrogen Energy*, *37*(24), 18927–18936. <https://doi.org/10.1016/j.ijhydene.2012.09.129>
- Mofidi, S. A. H., & Udell, K. S. (2017). Study of Heat and Mass Transfer in $\text{MgCl}_2/\text{NH}_3$ Thermochemical Batteries. *Journal of Energy Resources Technology*, *139*(3), 032005.
<https://doi.org/10.1115/1.4035750>
- NagaMalleswara Rao, K., Ram Gopal, M., & Bhattacharyya, S. (2013). Analysis of a $\text{SrCl}_2 - \text{NH}_3$ solid sorption refrigeration system. *International Journal of Low-Carbon Technologies*, *10*(4), 365–373. <https://doi.org/10.1093/ijlct/ctt046>
- SGL CARBON GmbH. (2019). *SIGRATHERM L and LN - Graphite lightweight board for thermal management*. Retrieved from SGL CARBON GmbH
- Soprani, S. (2016). *MODELING – TES system based on $\text{SrCl}_2 - \text{NH}_3$* . Roskilde.
- Swagelok. (2019). 304 / 304L and 316 / 316L Seamless , Instrumentation Grade Tubing. Retrieved from Product Specification PDF website:
<https://www.swagelok.com/en/catalog/Product/Detail?part=SS-T6M-S-1.0M-6ME>

Valverde, J. M., Barea-López, M., Perejón, A., Sánchez-Jiménez, P. E., & Pérez-Maqueda, L. A. (2017). Effect of Thermal Pretreatment and Nanosilica Addition on Limestone Performance at Calcium-Looping Conditions for Thermochemical Energy Storage of Concentrated Solar Power. *Energy and Fuels*, 31(4), 4226–4236.
<https://doi.org/10.1021/acs.energyfuels.6b03364>